



Titre: Additive Manufacturing of Terahertz Waveguide Components for THz
Title: Sensing and Communications

Auteur: Yang Cao
Author:

Date: 2021

Type: Mémoire ou thèse / Dissertation or Thesis

Référence: Cao, Y. (2021). Additive Manufacturing of Terahertz Waveguide Components for
Citation: THz Sensing and Communications [Thèse de doctorat, Polytechnique Montréal].
PolyPublie. <https://publications.polymtl.ca/9956/>

 **Document en libre accès dans PolyPublie**
Open Access document in PolyPublie

URL de PolyPublie: <https://publications.polymtl.ca/9956/>
PolyPublie URL:

**Directeurs de
recherche:** Maksim A. Skorobogatiy
Advisors:

Programme: Génie physique
Program:

POLYTECHNIQUE MONTRÉAL

affiliée à l'Université de Montréal

**Additive Manufacturing of Terahertz Waveguide Components for THz
Sensing and Communications**

YANG CAO

Département de génie physique

Thèse présentée en vue de l'obtention du diplôme de *Philosophiæ Doctor*

Génie physique

Décembre 2021

© Yang Cao, 2021.

POLYTECHNIQUE MONTRÉAL

affiliée à l'Université de Montréal

Cette thèse intitulée :

**Additive Manufacturing of Terahertz Waveguide Components for THz
Sensing and Communications**

présentée par Yang CAO

en vue de l'obtention du diplôme de *Philosophiæ Doctor*

a été dûment acceptée par le jury d'examen constitué de :

Yves-Alain PETER, président

Maksim SKOROBOGATIY, membre et directeur de recherche

Juan Nicolas QUESADA MEJIA, membre

Tsuneyuki OZAKI, membre externe

DEDICATION

I would like to dedicate this thesis to my beloved families for their unconditional love and support

ACKNOWLEDGEMENTS

I would like to thank the following people, without whom I would not have been able to complete this research.

First, I want to express my deepest gratitude to my supervisor, Prof. Maksim Skorobogatiy, for offering me the opportunity to pursue my scientific dream. His consistent support and guidance made this four-years challenging research an inspiring and unforgettable experience for me. Besides valuable knowledge and in-depth insights in THz science, the firm belief and rigorous standard in scientific exploration I learned from him will benefit my entire life.

I also want to thank Prof. Yves-Alain Peter, Prof. Tsuneyuki Ozaki, and Prof. Nicolas Quesada for accepting to judge and comment this thesis.

I want to thank Prof. Thomas Gervais for his efforts and expertise in our development of the terahertz fluid sensor.

I would like to thank all my friends and colleagues in Engineering Physics department at Polytechnique Montréal. Especially, I want to thank Dr. Kathirvel Nallappan, Dr. Hichem Guerboukha, Guofu Xu, Raphael Henri, Quentin Chapdelaine, Dr. Hang Qu, Dr. Xin Lu, and Dr. Jingwen Li for their invaluable discussion and assistance in my research together with the happiness we shared. I want to thank Francis Boutet, Jean-Paul Levesque, and Yves Leblanc for their professional technical assistance in all my projects.

Finally, I dedicate this thesis to my family. To my parents, they planted the seed of exploration in my heart when I was a child and devoted all their efforts to take care of my growth. To my fiancée Dr. Yun Li, her accompany and encouragement help me to get through every difficult moment in the past four years. Also to all my family members for their unconditional love and support.

RÉSUMÉ

Les ondes térahertz allant de 0.1 à 10 THz occupent la dernière portion relativement sous-utilisée du spectre électromagnétique. Située à la transition entre les régions de l'électronique et de la photonique, le « trou des THz » (*THz gap*) a retenu beaucoup d'attention pour ses potentielles applications en détection, communication, imagerie et spectroscopie au cours des dernières décennies. Afin de faire passer ces technologies THz de la théorie à la pratique, les guides d'onde THz efficaces pour diriger et manipuler les faisceaux est une des pièces manquantes du casse-tête. Cependant, en raison de l'impossibilité d'utiliser des solutions électroniques et photoniques conventionnelles telles que des lignes de transmission métalliques ou fibres en silice dans le régime THz, un manque de normes universelles pour la conception et fabrication de ces composants maintient les guides d'onde THz au stade du développement.

En considérant que l'échelle d'un guide d'onde est typiquement comparable à la longueur d'onde de l'onde guidée, soit de 3 mm à 30 μm dans le cas du rayonnement THz, les techniques de fabrication additive (*additive manufacturing* (AM)), dont la résolution est en constante amélioration, sont devenues graduellement une solution prometteuse pour fabriquer des guides d'ondes THz avec une structure 3D compliquée ainsi que des détails sous-longueur-d'onde. Ceci a rendu possible de nouvelles avancées en conception et fabrication de guides d'ondes THz. Dans cette étude, nous nous concentrons sur les fibres diélectrique THz et guides d'ondes plasmoniques imprimés en 3D. Le premier objectif primaire est le développement d'un capteur fluide en temps réel conçu avec une fibre diélectrique de Bragg à bande interdite photonique (*photonic bandgap* (PBG)) en THz. Un second objectif est le développement de composants optiques THz et de circuits basés sur les guides d'ondes plasmoniques à deux fils pour la communication THz.

Cette thèse débute avec une revue de la littérature scientifique sur les sujets touchés par les guides d'ondes THz en détection et communication, ainsi que sur l'application d'imprimantes 3D à la fabrication de guides d'onde THz. D'abord, quatre types de guides d'onde THz utilisés couramment, soit les fibres polymères, les guides d'onde plasmoniques, les guides d'onde rectangulaires et les guides d'onde planaires en silicium, sont brièvement discutés selon leurs mécanismes de guidage et les techniques de fabrication applicables. Ensuite sont discutés les applications des guides d'onde THz dans les domaines de la détection et de l'imagerie. En termes

de détection, l'accent est mis sur plusieurs concepts de capteurs THz basés sur des guides d'onde, ainsi que sur le développement et les applications potentielles de guides d'onde de Bragg à PBG. On analyse ensuite les rôles potentiels de guide d'onde THz classique et rapporte une revue de littérature de leurs applications en communication THz. En particulier, le développement du guide d'ondes plasmonique à deux fils et l'implémentation du multiplexeur d'insertion-extraction (*add-drop multiplexer* (ADM)) en THz pour le multiplexage par répartition de fréquence. Finalement, la littérature des techniques conventionnelles de AM et leurs applications dans le champ de la fabrication de guides d'onde THz est présentée.

Par la suite, la conception et la méthode de fabrication de capteurs à base de guides d'onde de Bragg à PBG et de guides d'ondes plasmoniques quasi bifilaires (*quasi-two-wire plasmonic waveguide components*) sont détaillées. Un système de spectroscopie THz à onde continue (CW) qui est utilisé tout le long de cette thèse pour caractériser expérimentalement les guides d'onde imprimés en 3D est également brièvement introduit également.

Ensuite, trois démonstrations sont faites afin d'atteindre les deux objectifs primaires.

En premier lieu on développe et fabrique un capteur fluide basé sur un guide d'onde de Bragg à PBG pour détection chimique et biologique sans contact, qui opère en modalité de détection par résonance pour contrôler la variation de l'indice de réfraction (RI) d'analytes liquides circulant à travers un canal intégré dans la gaine du guide d'onde. Ce capteur est fabriqué d'une pièce en utilisant l'impression 3D par modélisation par déposition fusionnée (*fused deposition modeling*) (FDM) sans traitement supplémentaire. En raison de l'anticroisement entre la relation de dispersion du mode fondamental guidée dans le noyau et d'un état de défaut dans le réflecteur à perte dû à l'existence d'un analyte liquide, un pic de perte du mode peut être trouvé près de la fréquence d'accord de phase parmi les bandes interdites du réflecteur du guide d'ondes. Expérimentalement, en utilisant un guide d'onde de Bragg à PBG avec une longueur optimisée pour assurer un guidage efficace d'un seul mode et des pertes de propagation limitées, on observe un creux dans l'amplitude et un changement rapide de phase, dont la position spectrale est linéairement dépendante de la partie réelle du RI de l'analyte avec une sensibilité calculée de ~ 110 GHz/RIU à partir du spectre de transmission normalisé. De plus, on effectue une analyse de la réponse dynamique du capteur fluide et confirme sa capacité de détection en temps réel d'un liquide.

En second lieu, on propose un guide d'ondes THz plasmonique à deux fils et un circuit optique pour la communication THz. Le guide d'ondes plasmonique quasi bifilaire ainsi conçu, formé de deux fils métalliques parallèles suspendu à l'intérieur d'une enceinte diélectrique protectrice de taille microscopique, est fabriqué par combinaison d'impression 3D par stéréolithographie (SLA) et de dépôt de métaux par chimie humide. Par la suite, une étude numérique et expérimentale en profondeur du guide d'onde à deux fils est menée. Ce guide d'onde à faibles pertes et dispersion peut fournir une plateforme versatile pour développer des composants THz passifs pour l'analyse de signaux en télécommunication THz. Pour la fabrication, on développe le réseau de Bragg (*waveguide Bragg gratings*) (WBGs) à deux fils avec des réseaux fabriqués par emboutissage à chaud de feuille de métal. De plus, la nature modulaire de l'impression 3D permet l'intégration optique 3D des composants THz développés avec un haut degré de reconfigurabilité, ce qui est impossible pour la plupart des composants micro-ondes et optiques utilisant des méthodes de fabrication standard. En addition, on démontre deux types de circuits plasmoniques THz, incluant un séparateur/multiplexeur en forme d'Y et un prototype d'ADM.

En troisième lieu, on propose un ADM à quatre ports basé sur les guides d'onde plasmonique quasi bifilaire, avec pour objectif de permettre un multiplexage par répartition en fréquence qui exploite davantage la large et dérégulée région des THz et multiplie la capacité de transmission de données des réseaux de communication THz basés sur des liaisons à canal unique. On développe un WBG à deux fils avec des variations périodiques dans la section transversale de chaque fil et des coupleurs latéraux composés de deux guides d'onde à deux fils en contact. Par la suite, en combinant ces deux éléments capables de manipuler des faisceaux THz large bande dans les domaines spectraux et spatiaux, un circuit d'ADM à deux fils avec l'élément crucial de coupleur directionnel à grilles est développé afin de permettre la suppression et l'ajout simultanés d'ondes porteuses THz. L'étude numérique et expérimentale de deux ADM opérant à une fréquence de porteur de charge de ~ 140 GHz, soit un qui est optimisé pour l'extraction et l'autre optimisé pour une performance équilibrée entre l'extraction et l'insertion.

Finalement, on conclut cette thèse en discutant les limitations de techniques de AM utilisée pour la fabrication de composants THz et l'optimisation correspondante, et aussi en mettant l'accent sur le potentiel de ces guides d'onde dans les liaisons THz.

ABSTRACT

The terahertz band ranging from 0.1-10 THz occupies the last relatively underutilized part of the electromagnetic spectrum. Placed in the switching region between electronics and photonics, the “THz gap” has garnered attention for potential applications in sensing, communications, imaging, and spectroscopy during the past decades. To transform the THz technology from theory to practice, the efficient THz waveguide component for THz beam steering and manipulating is one of the missing pieces of the puzzle. However, due to the unavailability of conventional electronics and photonics solutions such as metal transmission lines and silica fibers in the THz range, the lack of universal design standards and fabrication routes has trapped THz waveguide components in the development stage.

Considering that the waveguide scale is typically comparable to the wavelength of light, spanning from 3 mm to 30 μm for THz radiation, additive manufacturing techniques incorporating continuously improving resolution have gradually become a promising solution to reproduce THz waveguides with complicated 3D structures and subwavelength features. This has led to the possible realization of new advances in the design and fabrication of THz waveguide components. In this study, we focused on 3D printed THz dielectric fibers and plasmonic waveguides. Among the primary objectives was the development of a real-time fluidic sensor based on a THz photonic bandgap Bragg dielectric fiber. While another was the development of THz optical components and circuits based on two-wire plasmonic waveguides for THz communication.

We begin this thesis with a scientific literature review on subjects of the involvement of THz waveguide components in THz sensing and communications, as well as applications of 3D printing in THz waveguides. First, four types of commonly used THz waveguides, that is, polymer fibers, plasmonic waveguides, rectangular waveguides, and waveguides on planar silicon substrates, are briefly discussed along with their guiding mechanisms and applicable manufacturing techniques. Subsequently, we shift the focus to applications of THz waveguide components in the field of THz sensing and communications. In terms of sensing, several THz waveguide-based sensor designs, as well as the development and potential application of photonic bandgap Bragg waveguides have been discussed. We then analyze the potential roles of classic THz waveguides coupled with a literature review of their applications in THz communications. In particular, the development of

two-wire plasmonic waveguides and the implementation of THz add-drop multiplexer for frequency division multiplexing was focused upon. Finally, conventional additive manufacturing techniques and their applications in THz waveguide component fabrication from the literature have been presented.

Next, the design and manufacturing process of THz photonic bandgap Bragg waveguide-based sensors and quasi-two-wire plasmonic waveguide components have been detailed. A continuous-wave THz spectroscopy system that is employed throughout this thesis to experimentally characterize 3D printed THz waveguide components is briefly introduced as well.

Consequently, we turn to two primary objectives with three demonstrations.

First, we developed and fabricated a photonic bandgap Bragg waveguide-based fluidic sensor for non-contact chemical and biological sensing, which operates in resonant sensing modality to monitor the refractive index change of liquid analytes flowing through the fluidic channel that is integrated into the waveguide cladding. This sensor is fabricated in a single run using fused deposition modeling 3D printing without post-processing. Owing to the anticrossing between the dispersion relationship of the fundamental core-guided mode and a lossy reflector defect state caused by the existence of liquid analyte, a modal loss peak can be found near the phase-matching frequency among the waveguide reflector bandgaps. Through experiments, using a photonic bandgap Bragg waveguide with an optimized length to ensure effective single-mode guidance and limited propagation loss, we observed amplitude dip and rapid phase change, whose spectral position is linearly dependent on the real part of the analyte refractive index with a derived sensitivity of ~ 110 GHz/RIU, on complex normalized transmission spectra. Moreover, we performed an analysis of the dynamic response of the fluidic sensor and confirmed its capacity for real-time monitoring of the flowing liquid.

Second, we proposed two-wire THz plasmonic waveguide components and optical circuits for THz communication. The designed underlying quasi-two-wire THz waveguide, which features two metalized parallel wires suspended inside a protective micro-sized dielectric enclosure, was fabricated using a combination of stereolithography 3D printing and wet chemistry metal deposition techniques. Subsequently, an in-depth numerical and experimental study of the proposed two-wire waveguide was conducted. This low-loss low-dispersion waveguide can

provide a versatile platform to develop passive THz components for signal processing in THz communications. Further, for the implementation, we developed two-wire waveguide Bragg gratings with paper-based metal gratings fabricated via a hot stamping technique. Moreover, the modular nature endowed by 3D printing enables the 3D optical integration of the developed THz components with a high degree of reconfigurability, which is impossible for most microwave and optical components using standard manufacturing methods. We demonstrated two types of complex THz plasmonic circuits, including a Y-shaped splitter/multiplexer and a prototype of an add-drop multiplexer.

Third, we proposed four-port THz add-drop multiplexers based on the proposed stereolithography 3D printed quasi-two-wire waveguide to enable frequency division multiplexing that can further exploit the vast unregulated THz band and multiply the data-throughput capacity of THz communication networks based on single-channel links. We developed high-reflectivity two-wire waveguide Bragg gratings featuring periodic variations in the cross section of one wire and side couplers featuring two touching two-wire waveguides. Thereafter, combining these two elements capable of manipulating broadband THz light in the spectral and spatial domains, two-wire add-drop multiplexer circuits with the crucial element of a grating-loaded directional coupler were developed to allow both channel dropping and adding of THz carrier waves simultaneously. Furthermore, numerical and experimental study of two optimal add-drop multiplexer designs for operation at ~ 140 GHz carrier frequency, that is, one with optimized drop action, and the other exhibiting balanced drop/add performance, were conducted.

Finally, we concluded this thesis by discussing the limitations of the employed additive manufacturing techniques in THz waveguide component fabrication and the corresponding optimization, and also highlighting the potential of two-wire waveguides in THz links.

TABLE OF CONTENTS

DEDICATION	III
ACKNOWLEDGEMENTS	IV
RÉSUMÉ.....	V
ABSTRACT	VIII
TABLE OF CONTENTS	XI
LIST OF TABLES	XV
LIST OF FIGURES.....	XVI
LIST OF SYMBOLS AND ABBREVIATIONS.....	XIX
LIST OF APPENDICES	XXII
CHAPTER 1 INTRODUCTION.....	1
1.1 Context and challenges.....	2
1.2 General motivation and organization of this thesis	3
CHAPTER 2 LITERATURE REVIEW.....	6
2.1 Review of classic THz waveguides.....	6
2.2 Review of THz waveguide components for THz sensing.....	9
2.2.1 THz waveguide-based sensor.....	10
2.2.2 Hollow-core PBG Bragg waveguide.....	12
2.3 Review of THz waveguide components for THz communication.....	14
2.3.1 Involvement of THz waveguides in THz communications.....	15
2.3.2 THz two-wire plasmonic waveguide.....	17
2.3.3 ADM for THz frequency division multiplexing communication.....	20
2.4 Additive manufacturing techniques in THz waveguide fabrication.....	22
CHAPTER 3 METHODOLOGY	29

3.1	THz waveguide component fabrication using 3D printing techniques	29
3.1.1	Fabrication of THz PBG Bragg waveguide-based sensor using FDM 3D printing...	29
3.1.2	Fabrication of THz two-wire plasmonic circuits using SLA 3D printing.....	31
3.2	Numerical simulation	34
3.3	Experimental setup to characterize THz waveguide components.....	35
3.3.1	CW-THz spectroscopy system.....	35
3.3.2	Photonics-based THz communication system.....	36
CHAPTER 4 ARTICLE 1: ADDITIVE MANUFACTURING OF RESONANT FLUIDIC SENSORS BASED ON PHOTONIC BANDGAP WAVEGUIDES FOR TERAHERTZ APPLICATIONS		38
4.1	Introduction	38
4.2	Theoretical analysis of the THz hollow-core Bragg waveguides	41
4.2.1	Hollow-core Bragg waveguide with a perfectly periodic reflector.....	41
4.2.2	Hollow-core Bragg waveguide with a defect in the reflector	45
4.3	Fabrication of the hollow-core THz Bragg waveguides using FDM and SLA techniques	47
4.4	Characterizing of the hollow-core THz Bragg waveguide-based sensors using CW-THz spectroscopy	50
4.4.1	Choosing the optimal length of the hollow-core Bragg waveguide.....	52
4.5	The performance of the THz PBG Bragg waveguide-based fluidic sensor	54
4.5.1	Amplitude detection modality	56
4.5.2	Phase detection modality.....	58
4.5.3	Real time RI monitoring using fluidic sensor	61
4.6	Conclusion.....	65

CHAPTER 5 ARTICLE 2: ADDITIVE MANUFACTURING OF HIGHLY RECONFIGURABLE PLASMONIC CIRCUITS FOR TERAHERTZ COMMUNICATIONS..67

5.1	Introduction	68
5.2	Two-wire waveguides	72
5.2.1	The design of the micro-encapsulated two-wire waveguide	72
5.2.2	The fabrication of the micro-encapsulated two-wire waveguide	77
5.3	Optical characterization of the 3D printed two-wire waveguide components	80
5.3.1	Straight two-wire waveguides	80
5.3.2	Two-wire waveguide bends	82
5.3.3	Two-wire waveguide Bragg gratings	85
5.4	The THz plasmonic circuits	91
5.4.1	THz splitter/multiplexer	91
5.4.2	THz add-drop multiplexer (ADM).....	93
5.5	Conclusion.....	95

CHAPTER 6 ARTICLE 3: ADD DROP MULTIPLEXERS FOR TERAHERTZ COMMUNICATIONS USING TWO-WIRE WAVEGUIDE BASED PLASMONIC CIRCUITS

6.1	Introduction	97
6.2	Results	101
6.2.1	Two-wire waveguide-based Bragg grating	101
6.2.2	Two-wire waveguide-based directional coupler circuit	104
6.2.3	Grating-loaded side couplers for ADMs	107
6.2.4	Characterization of ADMs using THz communication system	112
6.3	Discussion	115

6.4	Methods.....	116
6.4.1	Fabrication of two-wire waveguide components	116
6.4.2	Characterization of two-wire WBGs.....	116
6.4.3	Characterization of side coupler section	118
6.4.4	Characterization of two-wire ADM circuits using CW-THz spectroscopy system.....	118
6.4.5	Characterization of ADM circuits using THz communication system	119
6.4.6	Numerical simulation	121
CHAPTER 7	GENERAL DISCUSSION.....	123
7.1	Limitation of employed manufacturing techniques and further optimization.....	123
7.2	Application of 3D-printed two-wire waveguide in THz communications.....	126
CHAPTER 8	CONCLUSION	128
REFERENCES	131
APPENDIX	148

LIST OF TABLES

Table 2.1 Reported classic THz waveguides	27
---	----

LIST OF FIGURES

Figure 2.1 The reported THz PBG Bragg waveguides	13
Figure 2.2. THz two-wire waveguide.....	18
Figure 2.3 The reported THz ADM designs	21
Figure 3.1 The cross-sectional view of THz PBG Bragg waveguide-based resonant sensor	30
Figure 3.2 The cross-sectional view of micro-encapsulate two-wire waveguides.....	33
Figure 3.3 The layer composition of a hot stamping foil which is reprinted from Ref. [181]	34
Figure 3.4 The free-space THz optical path in CW-THz spectroscopy for characterization.....	36
Figure 4.1 Numerical simulation of THz PBG Bragg waveguide	43
Figure 4.2 Numerical simulation of THz PBG Bragg waveguide with a defect in the reflector ...	45
Figure 4.3 Photos of 3D printed THz PBG Bragg waveguide	47
Figure 4.4 PBG Bragg waveguide-based THz fluidic sensor	51
Figure 4.5 Spectral performance of THz PBG Bragg waveguides with different lengths.....	54
Figure 4.6 Sensing using amplitude detection modality	56
Figure 4.7 Sensing using phase detection modality	60
Figure 4.8 Real-time monitoring analyte RI change using PBG Bragg waveguide-based sensor.	64
Figure 5.1 Design of micro-encapsulated two-wire waveguide.....	75
Figure 5.2 Characterization of straight micro-encapsulated two-wire waveguides	79
Figure 5.3 Micro-encapsulated two-wire waveguide bends.....	84
Figure 5.4 Paper-based two-wire waveguide Bragg gratings	89
Figure 5.5 Two-wire waveguide-based coupler.....	92
Figure 5.6 Two-wire waveguide-based ADM.....	94
Figure 6.1 Schematic of the proposed four-port ADM circuit (top part is not shown) comprising a grating-loaded side coupler placed between two Y splitters.....	100

Figure 6.2 Numerical and experimental studies on the two-wire WBGs.....	102
Figure 6.3 Numerical and experimental studies on two-wire directional coupler circuit	104
Figure 6.4 Numerical study on the grating-loaded side coupler sections	108
Figure 6.5 Power transmittances of grating-loaded side couplers and insertion losses of complete ADM circuits.....	110
Figure 6.6 Experimental study of two-wire ADM circuits for THz communications	112
Figure 7.1 Experimental study of two-wire waveguides for THz communications	126
Figure A. 1 The measurement of complex RI of 3D printed PLA plates	149
Figure A. 2 Measurement of RI of fluidic analytes for THz sensing.....	150
Figure B. 1 Micro-encapsulated two-wire waveguide in another design.....	151
Figure B. 2 The transverse modal electric field distribution $ E_t $ of the fundamental mode of the micro-encapsulated two-wire waveguides	152
Figure B. 3 The transverse electric field distribution $ E_t $ of the fundamental mode of a micro-encapsulated two-wire waveguide	153
Figure B. 4 Experimental setup to characterize two-wire waveguides	154
Figure B. 5 Numerical simulation of paper-based two-wire WBG.....	157
Figure B. 6 Experimental setup to characterize THz coupler	158
Figure B. 7 Characterization of two-wire ADM circuit.....	159
Figure C. 1 The design of two-wire WBGs	160
Figure C. 2 Numerical simulation results of directional coupler circuit.....	162
Figure C. 3 Characterization of two-wire Y splitters	163
Figure C. 4 Numerical simulation results of 35mm-long grating-loaded side coupler sections containing 20 periods with $A=1.03$ mm, $H=0.21$ mm, and different L_d^{in} computed using Eq. 6.1	165

Figure C. 5 Numerical transmittances (by power) of the 35mm-long grating-loaded side coupler sections containing gratings featuring different numbers of periods with $\Lambda=1.03$ mm, $H=0.21$ mm, and $L_d^{in}=1.5$ mm computed using Eq. 6.1 at Plane 2 for Through port	166
Figure C. 6 Eye diagram for the noise level of the THz communication system	169
Figure C. 7 The CW-THz spectroscopy system to characterize two-wire WBGs.....	170
Figure C. 8 The CW-THz spectroscopy system to characterize the directional coupler and ADM circuits.	171
Figure C. 9 Schematic of the photonics-based THz communication system to characterize THz ADM circuits.....	171
Figure C. 10 Numerical simulation of two-wire WBGs	172

LIST OF SYMBOLS AND ABBREVIATIONS

α	Absorption loss coefficient
Λ	Grating period length
c	Speed of light in vacuum
β	Propagation constant
D	Dispersion
ε	Dielectric constant
n_{eff}	Modal effective refractive index
S	Longitudinal flux
v_g	Group velocity
λ	Wavelength
ω	Frequency
3D	Three-dimensional
ABS	Acrylonitrile butadiene styrene
ADM	Add-drop multiplexer
AM	Additive manufacturing
ARROW	Anti-resonant reflecting optical waveguide
ASK	Amplitude shift keying
BER	Bit error rate
CAD	Computer-aided design
CNC	Computer numerical control
CW	Continuous wave
DFB	Distributed feedback

DLP	Digital light processing
DOF	Degree of freedom
EDFA	Erbium-doped fiber amplifier
FDM	Fused deposition modeling
FEFD	Finite element frequency domain
FEM	Finite element method
FFT	Fast Fourier transform
FWHM	Full width at half maximum
F-P	Fabry-Perot
Gbps	Gigabit per second
GVD	Group velocity dispersion
IBC	Impedance boundary condition
IR	Infrared
LNA	Low noise amplifier
MEMS	Micro-electro-mechanical systems
MS	Movable section
MZI	Mach–Zehnder interferometer
OAM	Orbital angular momentum
TDS	Time-domain spectrometer
TEM	Transverse electromagnetic
THz	Terahertz
PBG	Photonic bandgap
PEC	Perfect Electrical Conductor
PC	Photonic crystal

PCL	Plano-convex lens
PDM	Polarization division multiplexing
PLA	Polylactic acid
PM	Parabolic mirror
PMC	Perfect magnetic conductor
PML	Perfect matched layer
PRNS	Pseudorandom bit sequence
PSK	Phase-shift keying
PPWG	Parallel-plate waveguide
RI	Refractive index
RIU	Refractive index unit
SLA	Stereolithography
SLM	Selective laser melting
SLS	Selective laser sintering
SNR	Signal-to-noise ratio
SPP	Surface plasmon polariton
TIR	Total internal reflection
UV	Ultraviolet
WBG	Waveguide Bragg grating
WDM	Wavelength division multiplexing
WS	Waveguide section
ZBD	Zero bias Schottky detection

LIST OF APPENDICES

Appendix A	Supplementary material for: Additive manufacturing of resonant fluidic sensors based on photonic bandgap waveguides for terahertz applications	148
Appendix B	Supplementary material for: Additive manufacturing of highly reconfigurable plasmonic circuits for terahertz communications.....	151
Appendix C	Supplementary material for: Add drop multiplexers for terahertz communications using two-wire waveguide based plasmonic circuits.....	160
Appendix D	Scientific contributions.....	173

CHAPTER 1 INTRODUCTION

Waveguides, owing to their ability to guide electromagnetic radiation along designed geometrical paths, play an important role in both photonics and electronics. In addition to realizing point-to-point connections, waveguides also provide a versatile platform to develop various components with useful functions to manipulate the propagated electromagnetic wave along its way [1]. Exploiting advantages in transmission efficiency and structural universality, well-developed silica fiber and hollow conductive metal pipes are ubiquitous in the infrared and microwave regimes, respectively. However, both these types of waveguides are not perfectly suitable for the emerging THz regime that ties the discontinuity between the world of optics at high frequency and that of electronics at low frequency.

Owing to the difficulty in access using both conventional optical and electronic methods, the THz band ranging from 0.1 – 10 THz was the last remaining scientific gap in the electromagnetic spectrum before the development of ultrafast lasers in the late 1980s [2, 3]. Aided by the unique optical properties of THz waves, the past decades have witnessed a plethora of technological advances in THz generation and detection [4, 5], which have laid the foundation for potential applications of THz light, including medical diagnostics [6], chemical and biological sensing [7, 8], and wireless communication [9]. At present, the output power of commercial THz sources operating below 1 THz can reach several watts. However, when employing free-space propagation, the intrinsically strong atmospheric attenuation and highly directional beam profile pose challenges of efficiently exploiting the generated THz wave in practical applications [10]. In contrast, the THz waveguide can guide THz light in a controlled environment and protect it from external disturbances. Moreover, by replacing the bulk optics, THz waveguide components can thrust the development of compact THz circuits. Therefore, the involvement of THz waveguide components is a promising trend in THz technology [11].

Benefiting from optics and electronics solutions, THz waveguides in various forms, including planar waveguides on silicon wafers [12, 13], together with three-dimensional (3D) fibers in optically transparent polymers, rectangular waveguides, and plasmonic waveguides in metal, have been proposed [14-16]. However, they exhibit certain performance limitations, typically arising from two detrimental factors: material absorption and fabrication imperfection [1]. Despite functioning well in IR and microwave, polymers and metals usually feature high material

absorption in the THz regime. Consequently, THz waveguides are designed to confine THz radiation in the lossless dry gas around its hosting material, which places a stringent requirement on the surface finish to reduce scattering loss caused by defects. Considering that the scale of the waveguide is usually comparable to its operating wavelength, fiber draw synthesis and MEMS, which are commonly utilized for infrared optics, can be employed to manufacture THz waveguides having much larger scales with a satisfactory definition. However, the requirement of costly high-end facilities and multi-stage fabrication processes results in the conventional techniques being an unpreferred option in the THz regime in some cases. In contrast, in the past decade, owing to continuous advances in hardware and materials, the cost-effective AM technique has gradually become a promising solution to produce modules with complicated 3D structures with ease and precision [17], thus democratizing the routine laboratory research in THz optical components.

1.1 Context and challenges

The emergence of the AM technique has led to a revolution in the design and fabrication of THz waveguide components, as it allows the creation of geometries that were unattainable using traditional methods, such as internal porous structures. Due to the almost fully automated manufacturing process, the highly accessible AM technique enables the rapid prototyping of designed THz optics without the need for machining expertise. Exploiting the advantage of the resolution and consistency of manufacturing, the AM technique can also ensure the reproduction of stereotypical THz waveguide components with high precision and efficiency in the future.

However, the extensive application of the AM technique in THz waveguide components is hindered by certain intrinsic defects, such as the restriction on the size of THz waveguide components posed by the build volume of the 3D printer, the scarcity of applicable printing materials featuring low material absorption in the THz band, as well as the requirement of post-processing (e.g., cleaning and polishing for SLA 3D printing). At present, the AM technique is used primarily for THz dielectric fibers with simple and uniform cross-sections, and rarely for THz waveguide components with complex structures. Considering that the general trend of THz technology involves employing waveguide components with advanced functions and reconfigurable optical circuits assembled by modular waveguide components in various practical applications, the

utilization of the AM technique to fulfill such demands is of particular importance, which is the main objective of this thesis.

Specifically, in this thesis, we explore the practical applications of 3D printed THz waveguide components in THz sensing and communications. In terms of THz sensing, the analyte is usually placed away from waveguide-based sensors to mitigate the impact of its presence on the insertion loss [18]. It usually requires underlying THz waveguides to feature weak modal confinement, causing the sensing to be susceptible to noise. To find practical applications, it is necessary to develop a THz waveguide that enables efficient interaction between its tightly confined modal field and analyte that is placed in a controlled environment, thereby rendering the THz waveguide design and fabrication challenging. Regarding THz communications, wireless links have been primarily focused upon, where THz emitters and receiver arms are usually assembled using discrete bulky free-space THz optics. More reliable and compact THz communication networks are expected for practical applications, which can be achieved with the involvement of THz waveguides. With proper design, THz waveguides can provide a universal platform to develop waveguide components and optical circuits enabling advanced signal processing functionalities. However, developing a target waveguide that features small loss and dispersion, high coupling coefficients with THz sources and other optical devices, as well as modular nature is challenging.

1.2 General motivation and organization of this thesis

The main objective of this thesis is to explore the applications of THz waveguide components enabled by efficient AM techniques in the field of THz sensing and communication.

In Chapter 2 of this thesis, we present a detailed review of classic THz waveguides and their applications in the field of THz sensing and communication, as well as the involvement of AM techniques in THz waveguide fabrication. In particular, we focused on the research and development of PBG Bragg fibers, two-wire plasmonic waveguides, and THz ADMs, which are the three main sub-topics of this thesis.

Chapter 3 introduces the methodology of this study. We begin by indicating the design and fabrication of the proposed THz waveguides, that is, the PBG Bragg waveguide and micro-

encapsulated two-wire plasmonic waveguide. Further, a CW-THz spectroscopy system and a THz communication system for optical characterization are introduced.

The following three chapters are the main contributions of this study. Two independent issues in THz sensing and communications with the shared objective of exploring the application of 3D printed THz waveguide components have been addressed.

Chapter 4 is based on “Additive manufacturing of resonant fluidic sensors based on photonic bandgap waveguides for terahertz applications (2019),” which was published in *Optics Express* [19]. THz fluidic sensors are powerful tools for detecting liquid analytes for applications in the fields of biology and chemistry. Its performance in terms of sensitivity, resolution, response time, and stability are primarily determined by the employed optical device. In this chapter, we developed a THz fluidic sensor based on an FDM 3D printed PBG Bragg waveguide, aiming at real-time monitoring of the RI variation of flowing liquid with high sensitivity in a non-contact manner. The geometrical design based on numerical simulation, selection of proper fabrication methods, and experimental characterization of this sensor has been elaborated. Appendix A provides further details related to this chapter.

Chapter 5 is based on “Additive manufacturing of highly reconfigurable plasmonic circuits for terahertz communications (2020),” which was published in *Optica* [20]. With proper design, THz waveguides can interconnect discrete free-space THz devices to build THz links where THz carrier waves propagate in highly controlled environments, and also provide a versatile platform to develop optical components for signal processing. Therefore, the enrollment of THz waveguides opens up new opportunities for THz communication network design. In this chapter, we propose a novel type of modular quasi-two-wire THz plasmonic waveguide using the SLA 3D printing technique to achieve these goals. First, an in-depth study of waveguide design and fabrication has been presented. Subsequently, the implementation of waveguide components (e.g., WBGs), and reconfigurable THz plasmonic circuits (ex, Y couplers, and ADM prototypes) based on the underlying waveguide for THz communications were demonstrated. Appendix B reproduces the Supplementary Material of [20] and is related to this chapter.

Chapter 6 is based on “Add drop multiplexers for terahertz communications using two-wire waveguide-based plasmonic circuits (2021),” which is currently under revision considering peer

reviewers' comments that we received from Nature Communications. The THz frequency division multiplexing scheme, which exploits the light property in frequency, enables the mux/demux of independent data streams, thus paving a way toward THz communication networks with ultra-high data rate targets of Tbps. In this chapter, we proposed a THz ADM circuit, which is the enabling element of this multiplexing scheme, based on the modular 3D printed two-wire waveguide demonstrated in Chapter 5. First, we presented the development of two-wire waveguide-based Bragg gratings and directional couplers. Thereafter, theoretical and experimental study on ADMs with the crucial block of a grating-loaded side coupler, which is the conjunction of these two elements, was introduced comprehensively. Appendix C reproduces the Supplementary Information of [21] and is related to this chapter.

Chapter 7 provides certain complementary details of the previous chapters and indicates future research directions and perspectives. The limitations of AM techniques in THz waveguide fabrication and the corresponding further optimization have been elaborated. In addition, we discuss the applicability of the two-wire plasmonic waveguide in THz links.

CHAPTER 2 LITERATURE REVIEW

A scientific review of THz waveguide components and their applications in THz sensing and communications has been presented in this chapter. We begin by introducing the guiding mechanisms and fabrication routes of several types of most commonly used THz waveguides. Subsequently, we overview the research on THz sensing with particular attention to the development of THz waveguide-based sensors and hollow-core PBG Bragg waveguides. Further, we briefly review the potential applications of different types of THz waveguides in THz communication systems. The research and development of two-wire plasmonic waveguides and ADMs, which are believed to be vital to THz communication networks, were focused upon. Finally, the advantages, limitations, and applications of various AM techniques in THz waveguide component fabrication have been discussed.

2.1 Review of classic THz waveguides

Currently, free-space propagation is usually used in THz systems exploiting the advantage of the low-loss atmospheric transmission window [22]. In contrast, despite having a larger transmission loss, the THz waveguide enables the guidance and manipulation of THz radiation in a compact, flexible, and highly controllable environment. The tight modal confinement required by THz sensing, as well as stable signal propagation that is isolated from the external environment required by THz communications can be realized using THz waveguides with proper designs. Moreover, the THz waveguide can serve as the basis for passive and active optical components with various functionalities (e.g., WBG, coupler, and antenna), thus promoting the development of THz optical circuits. Therefore, the study of THz waveguides is important in THz science.

Because THz waves occupy the gap between the IR and microwave range in the electromagnetic spectrum, the design and fabrication of the corresponding waveguide components can benefit from both the well-developed photonic and electronic fields. Several classic THz waveguides are listed in Table 2.1.

As a photonic solution, THz dielectric fibers, whose concept is adapted from the silica fiber for the mid-IR range [23], have been proposed. Because of the lower material absorption compared to that of other common materials in the THz regime, most THz fibers are composed of polymers [24]. Solid-core fibers, such as subwavelength fibers [25, 26] and suspended core fibers [27, 28], usually

transmit THz radiation in the air surrounding the polymer core by total internal reflection (TIR). The transmission loss and dispersion of these fibers are also directly proportional to those of the hosting materials [14], and the optimal diameter of the solid core must be selected to achieve a trade-off between the tight modal confinement and low transmission loss of the transmitted THz light. For various THz photonic crystal fibers, the THz radiation falling in a specific band can be confined to the central hollow core by photonic bandgap (PBG) [29, 30] or antiresonance effects [31, 32]. In contrast to broadband solid-core fibers showcasing simple structures, THz photonic crystal fibers typically feature highly designable porous cross sections. Theoretically, the designed fiber can be used in various applications in THz fields (e.g., fluidic and film sensing [33, 34], as well as birefringence, polarization maintenance, and orbital angular momentum multiplexing for THz communications [35-37]). However, reproducing the complicated structure of THz photonic crystal fibers using conventional fiber-drawing techniques is a challenge. In contrast, AM has emerged as a superior method for fabricating THz dielectric waveguides in recent years.

The planar silicon substrate, which has been extensively studied in microwave fields, can serve as a versatile platform for THz signal transmission and processing because of the low material absorption and dispersion of silicon, coupled with a similar standard in design and manufacturing in the THz band [38]. Relied on TIR, photonic bandgap, or topology insulation, THz light can travel along the designed optical path on a planar substrate [13, 39, 40]. With the capability of integrating discrete THz elements (e.g., high-Q resonators [41, 42], diplexers [39, 43], and multiplexers [44]) on a monolithic chip, the silicon substrate can serve as the basis to develop compact THz communication systems [45]. However, the inherent 2D nature makes it difficult for silicon circuits to perform 3D integration. The applicability and scalability of waveguides built on silicon substrates in THz systems are restricted owing to the unattainable out-of-plane inter-chip connectorization and coupling with free-space THz optical devices. Currently, microfabrication is the only conventional manufacturing technique suitable for THz silicon substrates to achieve desired micrometer-sized features. However, the required high-end fab infrastructure and multi-stage fabrication process set a high threshold for laboratory research on this type of THz waveguide.

As the dimensional scaled-down version of an extensively used waveguide structure in microwave communication systems, the THz rectangular metal waveguide can confine THz waves within a specific band in the hollow core by TIR [46]. Conventional THz rectangular metal waveguides are

obtained via CNC milling with a satisfactory surface finish [47, 48]. Whereas, to obtain those for high operation frequency or having deeply subwavelength internal structures, one usually needs to resort to the combination of MEMS and silicon wafers [49]. In recent years, technical improvements in terms of processing precision and applicable materials have enabled the AM technique as an alternative solution, particularly for THz rectangular waveguides designed for low operation frequencies (below 300 GHz).

The THz plasmonic waveguide, which is another metallic solution, enables the propagation of broadband THz radiation with low transmission loss and dispersion. Compared with rectangular waveguides, classic THz plasmonic waveguides are weakly frequency-dependent and enable various designs and functionalities (e.g., Y coupler and ring resonator on a planar slab [50, 51], as well as a wire plasmonic waveguide-based RI sensor [52]). In THz plasmonic waveguides, the SPP wave is excited by the interaction between the incident THz radiation and the collective oscillation of free electrons in the metal, and subsequently propagates along the metal/dielectric interface with its modal electric field mainly distributed in the dielectric [1]. Therefore, the guidance properties of the THz SPP wave are highly reliant on the characteristics of the dielectric, which is lossless dry air in most cases. In addition, it is also affected by the ohmic loss and surface finish of the metal. THz plasmonic waveguides with simple structures (e.g., PPWG [53, 54]) are usually obtained by CNC machining. While the THz spoof SPP waveguides with subwavelength features on the surface are built on silicon wafers by optical lithography and metal sputter deposition techniques [55, 56]. For the aforementioned techniques, it is prohibitively difficult to fabricate THz plasmonic waveguides with complicated three-dimensional structures or internal truss structures. In contrast, their substrates can be obtained employing AM techniques with ease and precision. It was found that the performance of SLA 3D-printed dielectric supports with optically thick metal layer deposition is equivalent to the conventional THz plasmonic waveguide [57].

In conclusion, various types of THz waveguides have been developed by adapting the concepts of electronic and photonic solutions. In the subsequent sections of this chapter, we will shift the focus to THz waveguide and waveguide components with advanced functionalities for THz sensing and communications. We will review the development of THz waveguide-based sensing and PBG Bragg waveguide in Chapter 2.2, the application of THz waveguides, particularly two-wire

plasmonic waveguides in THz communications, and the research on THz ADM for frequency division multiplexing in Chapter 2.3.

2.2 Review of THz waveguide components for THz sensing

Owing to the existence of fingerprints of certain macromolecules, high penetrability, and low photon energy, THz waves offer new possibilities for the characterization and detection of substances. For example, tracking the spectral position of absorption lines in the THz range that are associated with intramolecular and intermolecular vibrations can be used to identify amino acids for biomedical and pharmaceutical applications [58]. In addition, compared with the commercial X-ray scanner, the non-invasive and non-ionizing THz radiation provides a superior solution for security checks by exploiting the advantage of personal healthcare and privacy protection [59, 60].

In addition to the aforementioned material characterizations using a free-space THz beam path, THz sensing can be implemented with the assistance of THz optical devices to detect the change in analytes. With a proper design, the THz optical device can enable efficient light-matter interaction in a designable and flexible form, thus resulting in the high stability and sensitivity of THz sensing [61]. Metamaterials are among the most promising platforms [62]. The resonant structures, such as split-ring resonators [63] and metallic mesh [64], on the engineered thin film, can generate singularities on the spectrum of the transmitted free-space THz beam, whose spectral position reflects the variation in analytes placed nearby. Owing to the high sensitivity and the minute amount of required sample, THz metamaterial-based sensors have found applications in biomolecular [65] and microfluidic [66, 67] detection. However, due to the stringent requirements for machining errors, fabricating THz metamaterials with micro-sized features is challenging. Even the SLA 3D printing, which has the finest resolution among various AM techniques, is incapable of manufacturing THz metamaterials with high resonant frequencies [68]. Moreover, as it is exposed in free space, the performance of the metamaterial-based THz sensor is easily affected by external disturbances, thus limiting its practical applications in complex environments.

In contrast, because most of the designs can be realized by various AM techniques and the THz light is confined in a controlled environment, THz waveguides can provide a cost-effective and reliable platform for THz sensing with sufficient light-matter interaction length. According to the

type of base, most of the reported THz waveguide-based sensors can be categorized as metallic plasmonic waveguide-based and dielectric fiber-based sensors. The development of these two types of sensors is described in detail below.

2.2.1 THz waveguide-based sensor

The PPWG and spoof plasmonic waveguides with corrugated surfaces are THz plasmonic waveguides that have been frequently employed for THz sensing. In [69], a micro-sized groove inscribed on a metal plate served as a resonant cavity integrated into the PPWG. Tracking the resonant frequency on the transmission spectra in the range of 0.25-0.3 THz can enable detection of the change in the RI of liquid analytes that fill this groove (N-alkanes) with a sensitivity of 95 GHz/RIU. Using a similar structure, multichannel microfluidic sensing with sensitivities over 170 GHz/RIU was realized by two independent resonant cavities in PPWG [70]. In addition, the PPWG-based THz TDS system outperforms the conventional free-space system in thin-film characterization owing to its enhanced sensitivity [71, 72]. The fingerprints on transmission spectra can be tracked to probe the analyte deposited on the waveguide plates; thus, it is particularly suitable for detecting hazardous samples of a small amount (e.g., explosive solids [73], pharmaceutical and organic compounds [74], and biological molecules [75]). With a similar working principle, the characterization of lactose powder was also implemented using a metal wire-based TDS system in [76]. For THz spoof plasmonic waveguides, by tracking the cut-off frequency of the spoof SPP mode, which manifests as an amplitude decline in the transmission spectrum and an amplitude dip in the reflection spectra, the microliter-volume liquid or powdered analytes that are placed in the deeply subwavelength structure (in grooves or between ridges) can be detected with sensitivities of up to hundreds of GHz/RIU [77-80]. In summary, THz plasmonic waveguide-based sensors show great potential in detecting and characterizing analytes in small amounts owing to the tight confinement of THz radiation in the vicinity of the metal surface.

Regarding the THz dielectric fiber, although THz photonic crystal fiber provides a flexible platform for THz sensing theoretically [81-83], most designs to date have been impractical because of the difficulty in introducing the analyte inside their internal porous structure and controlling the resultant light-matter interaction. Currently, THz dielectric fiber-based sensing is mainly utilized based on waveguides with the simplest structures, that is, the solid-core subwavelength fiber and

hollow-core tube waveguide, using the evanescent wave and the resonance occurring in the engineered microstructures.

Featuring a larger penetration depth than that of mid-infrared light, the evanescent field of THz wave enables detection of large targets such as cells and bacteria (sizes of 0.5-10 μm), leading to new opportunities in biosensing. Using the interaction between the probed analytes covering the fiber surface and the THz evanescent wave, the non-resonant sensing, where the transmission loss of a suspended-core fiber is correlated with the concentration of the bacterial that encompasses its central core [84] has been proposed. In addition, resonant sensing, where the spectral position of the dispersion dip changes with the RI of the liquid analyte in which the subwavelength fiber is immersed [18], has been proposed as well. In other implementations, resonant sensors based on a hollow-core THz tube waveguide were developed to detect the thickness of a thin film [18] and the RI of the powder in a porous absorbent layer that serves as the waveguide outer cladding [85]. Furthermore, with similar geometry and working mechanism, solid-core silicon fiber- and silica hollow-core tube waveguide-based THz sensors have also been proposed [85, 86].

Another commonly used type of THz dielectric waveguide-based sensing relies on the resonance of artificially engineered micro-sized structures. Compared with the evanescent wave of the THz waveguide having a smooth geometry, the designed waveguide components facilitate stronger localization of the THz radiation, thus allowing enhanced light-matter interaction and detection sensitivity. A Bragg grating based on THz polymer fiber, a concept adapted from the optical regime, was developed in [85]. In addition to serving as a band-stop filter in THz communications, the proposed solid-core fiber with a periodic sequence of laser-inscribed notches was used to monitor paper quality in [87]. Once being placed on top of the paper stacks, the resonant frequency of the THz fiber Bragg grating decreased with an increase in paper thickness because of the stronger localization of the fundamental guided mode in the paper rather than the air. In [88], a similar THz sensor was developed on a polymer hollow-core tube waveguide. The quantity changes of the liquid analyte placed in the periodic grooves that are etched on the waveguide outer surface result in a shift in the resonant frequency with a sensitivity of 50 GHz/ μl .

It was found that in most reported THz waveguide-based sensors, the probed analyte was exposed, or that placing the analyte inside the waveguide to enable controllable light-matter interaction was challenging. Therefore, THz detection is susceptible to external disturbances and noise associated

with irrelevant parameters of the analyte (e.g., the change in analyte amount when monitoring the variation of the analyte RI). Due to the limited structural flexibility of the aforementioned waveguides, developing THz sensors based on other types of waveguides could be a promising solution for practical applications. Enabled by 3D printing techniques, the THz PBG Bragg waveguide was selected and studied in this thesis. In the following sections, its development and applications have been reviewed.

2.2.2 Hollow-core PBG Bragg waveguide

The hollow-core PBG Bragg waveguide, which has been demonstrated as a THz fluidic sensor in this thesis, is a specific type of hollow-core photonic crystal fiber. Featuring a hollow core surrounded by a sequence of bilayers with periodically alternating RI, the PBG Bragg fiber can confine and guide THz radiation in the reflective bands owing to the occurrence of constructive interference in the cladding region. Theoretically, the spectral position of the bandgap can be tuned arbitrarily by a suitable combination of the RI and thickness of the bilayer. In this case, the optimal size of the hollow core must be selected to enable efficient coupling with a Gaussian beam, achieve low modal loss, and facilitate single-mode operation [89, 90].

In the mid-IR range, PBG Bragg fibers are usually fabricated using fiber drawing techniques. The fiber preform can be obtained by co-rolling two films in different materials [91] or depositing two types of materials on a hollow-core tube [92]. However, in most cases, preprocessing is time-consuming (e.g., heating for over a week to consolidate the preform), and fiber drawing is challenging because of the difficulty in adjusting multiple parameters (e.g., furnace temperature, pressurization to maintain the hollow core, and spinning roll speed) to obtain a fiber with a small geometrical deviation from the designed one [91]. Consequently, the complicated manufacturing process limits the application of this type of fiber to a certain degree. Currently, considering the advantages of low transmission loss and large mode area for single-mode operation, most reports of mid-IR PBG Bragg fiber have focused on the application of high-power laser delivery [93, 94]. From the perspective of sensing, the PBG Bragg waveguide is rarely used owing to the existence of various cost-effective alternatives. In [95-97], PBG Bragg waveguides were employed to detect the RI change of the liquid analyte that filled the central core by tracking the spectral position of the transmission peak and monitoring the output amplitude at this frequency. In [98], using the

anticrossing phenomenon enhanced by squeezing the fiber core, the thickness change in the thin film deposited on the inner surface of the PBG Bragg fiber core was detected. In addition, a weak-light-confined PBG Bragg waveguide was used as a multi-parameter sensor to detect changes in the external environment, that is, temperature by resonant sensing and liquid level by non-resonant sensing [92].

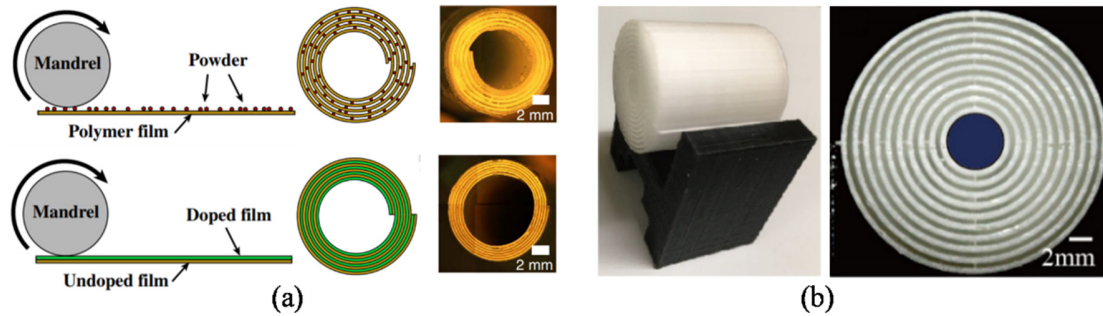


Figure 2.1 The reported THz PBG Bragg waveguides

(a) The polymer/air one that is obtained by rolling polymer film with powders on top, and the polymer one that is obtained by co-rolling thin bilayer film. Reprinted from [99]. (b) The resin/air one that is fabricated by SLA 3D printing. Reprinted from [100].

Because the layer thickness and hollow-core dimensions are comparable to the wavelength of the transmitted light, the scale of the PBG Bragg waveguides for THz radiation is on the millimeter level, thereby enabling the applicability of various manufacturing methods in addition to the conventional fiber drawing. In [99], a polymer/air THz PBG Bragg fiber was obtained by rolling a thin polymer film around a mandrel. Powders that are randomly laid on top of this film serve as spacers between two neighboring polymer layers in the fiber cladding. Another polymer fiber was obtained by rolling a bilayer film. Moreover, PBG Bragg waveguides with bandgaps in the sub-THz range can also be manufactured using FDM, SLA, and DLP 3D printing techniques [19, 100, 101] (see Fig 2.1 (a)). Compared to fiber drawing, the aforementioned manufacturing methods are highly efficient and accessible. With more applicable materials, a high RI contrast in the cladding region is achievable, thus endowing the THz PBG Bragg waveguide with high modal confinement and low radiation loss. In [102], by employing different guiding mechanisms (TIR, bandgap, and antiresonance effect), a ferroelectric PVDF/lossless PC Bragg fiber supporting broadband transmission (1.0-3.0 THz) was proposed. For THz PBG Bragg waveguide-based sensing, due to

the larger scale of the hollow core compared with the mid-IR ones, placing the powered analyte inside is simpler. In [100], by tracking the resultant anticrossing frequency on transmission spectra, thin-film sensing using a spinning 3D printed THz Bragg fiber was reported with a surface sensitivity of 0.1 GHz/ μm . It is noted when using the anticrossing phenomenon of the PBG Bragg waveguide with a defect for sensing, a higher sensing resolution can be achieved by placing the analyte further away from the hollow core. Compared with the conventional waveguides with solid cladding, the 3D printed polymer/air PBG Bragg waveguide could integrate the analyte (defect) inside the cladding region (see Fig 2.1 (b)). In [19], we proposed a 3D printed PBG Bragg waveguide with a built-in fluidic channel to monitor the RI change of the flowing liquid analyte in real-time. This work is detailed in Chapter 4 of this thesis.

2.3 Review of THz waveguide components for THz communication

In the era of data explosion, the almost vertical growth in data traffic drives the communication industry to continuously pursue more efficient data transfer. Currently, owing to the difficulty in further improving the spectral efficiency, one general development trend of wireless communication is to shift the carrier wave toward a higher frequency to exploit the band with a larger bandwidth [103]. In the past decade, with the evolution from 4G to 5G, the data rate of mobile communication has increased by two orders of magnitude to several gigabits per second. However, owing to the rapid development of smart terminals and the emergence of new applications (e.g., surreal virtual reality and the Internet of Everything) [104], the overcrowded microwave frequency band is not sufficient to meet the bandwidth demand in the foreseeable future. Therefore, the THz band, which contains an extensive unregulated spectrum, has attracted great attention for the development of ultra-high-speed communication networks. A few medium-distance high-bitrate THz wireless links have been demonstrated in the laboratory (e.g., 132 Gbps data transfer over 3.8 m [105]). Benefiting from low-loss atmospheric transmission windows, most of those reported have employed THz carrier frequency below 0.5 THz.

However, due to the considerable moisture absorption and highly directional beam profile of THz wave, the negative impact of atmospheric weather conditions (e.g., rain, fog, and snow), and the necessity of precisely aligning THz transmitter and receiver modules (particularly under dynamic scenarios) restrict the practical applications of THz wireless links. In addition, the lack of powerful

THz sources and sensitive THz receivers also poses many challenging problems for THz communication networks, such as minimizing the interference between independent channels [106]. Therefore, to build a reliable and efficient THz link in complicated environments, instead of employing discrete optical elements for THz beam steering in free space, it is preferable to adopt an integrated solution based on THz waveguides to enclose the THz signal in highly controlled environments. In addition to simple data transmission, THz waveguides can serve as versatile platforms for THz signal processing, routing, and multiplexing [107]. Moreover, we believe that the THz circuits obtained by assembling waveguide components with various functionalities can provide new perspectives on THz communication network designs. In the subsequent sections, we briefly summarize the application and potential of the above-mentioned four types of classic THz waveguides (see Table 2.1) and the corresponding waveguide components in THz communication systems.

2.3.1 Involvement of THz waveguides in THz communications

Rectangular waveguides have been extensively employed in commercial microwave communication systems. The operation frequency can be theoretically shifted to the THz range by shrinking the scale of the well-developed passive waveguide components. In terms of guiding THz signals in communication systems, in addition to employing straight or curved rectangular waveguides with a cm-level length to interconnect THz devices, the rectangular waveguide-based coupler can split and combine THz signals with a small insertion loss (e.g., 2 dB in the 110-170 band [108]), and the flared rectangular waveguide antenna can efficiently transmit/collect broadband THz signals from/into THz transmitters/receivers. Further, THz bandpass filters for signal processing were developed by integrating intercoupling cavity resonators inside rectangular waveguides [109, 110]. Although featuring a high coupling coefficient with most commercial THz sources (e.g., uni-traveling-carrier photodiode and Schottky diode), THz rectangular waveguides, particularly those with micro-sized scales for high operation frequencies, usually feature high transmission loss and dispersion. In addition, fabricating the micro-structured waveguide components using conventional metal machining or AM techniques is a challenging task. Therefore, the rectangular waveguide usually plays the simple role of interconnects in THz communication systems.

Compared with THz rectangular waveguides, the mass and scale of THz waveguides on silicon substrates are orders of magnitude smaller, thereby enabling the miniaturization of THz circuits. Benefiting from various guidance mechanisms (see Table 2.1), THz signal routing along complex geometrical paths with small insertion loss and dispersion is achievable on a silicon substrate [12, 13, 40]. Further, several conventional passive THz optical components, such as high-Q cavities [41, 42], couplers [43], and antennas [111], can be built on substrates for THz communications. Moreover, allowing the co-integration of electronic and photonic circuits, coupled with hybrid and heterogeneous integration of active III–V materials, active THz elements (e.g., THz generation and detection modules) can be integrated on a silicon wafer [45]. In conclusion, the silicon substrate provides a versatile integration platform for THz waveguiding and manipulation, and thus has great potential in intra/inter-chip THz links.

In contrast to micro-sized optical elements on silicon substrates for short-distance THz communication, the THz dielectric fiber and plasmonic waveguides usually feature a much larger scale and thereby fit for links with a longer distance. With high structural flexibility and relaxed demand in fabrication tolerances, these two types of THz waveguides can be fabricated using the emerging AM techniques in most cases, thereby lowering their threshold entering into production. Although they have great potential in THz communications, owing to the lack of a universal design standard, heretofore THz dielectric fiber- and plasmonic waveguide-based components are usually proposed as independent elements without overall planning of circuits that can be integrated into THz communication systems.

THz dielectric fibers with simple structures, namely, solid-core subwavelength fibers [26], suspended-core fibers [112], hollow-core tube waveguides [113], and porous fibers [114], have been used to establish moderate-distance THz links. Compared to the free-space link, these meter-level links are efficient in terms of power consumption and suitable for data transfer in the scenario where the direct line-of-sight link is not available (e.g., circumventing obstacles in a compact inter-vehicular environment). Further, as complementary components for THz fiber links, Y-splitters and 1×3 multimode interference splitters were developed based on 3D printed PS solid-core subwavelength fibers [115]. In another 3d-printed implementation [116], our research group demonstrated a dispersion compensator by introducing a Bragg grating into a hollow-core tube waveguide. Consequently, it was found that a single-mode operation with highly negative

dispersion could be obtained near the bandgap edge by suppressing one supported mode and opening a bandgap for another mode.

Regarding plasmonic waveguides, compared with those having a single-conductor structure (e.g., metal wire and strip), PPWGs and two-wire waveguides featuring tighter modal confinement are expected to provide reliable platforms for waveguiding and manipulating THz carrier waves in communication systems. The PPWG, composed of two parallel and smooth metal plates separated by an air gap, was first proposed in 2001 [117] and is still a hot topic in THz science. In terms of THz communication, although its supported TEM mode features low modal loss and negligible dispersion theoretically, the PPWG tends to be used for short-distance links (cm-level [118]) and signal processing owing to the engineering challenges in the manufacturing and maintenance of waveguides with long lengths. A PPWG-based broadband T-junction 1×2 power splitter was developed in [119]. Further, the power-split ratio of the two output ports can be adjusted by laterally moving a triangular-shipped septum in the vicinity of the T-junction. Based on this component, the same research group proposed an electrically tunable splitter, where the output port of the THz light that is launched into this device is switchable by actuating liquid metal components placed around the T-junction [120]. In addition, the PPWG supports two orthogonal linearly polarized modes (TE_1 and TEM) that can be efficiently excited by conventional THz sources without interference [121]. Therefore, it is promising to enroll PPWGs in THz polarization division multiplexing (PDM) communication networks.

Another THz plasmonic waveguide that has attracted significant attention is the two-wire waveguide, which is among the primary research topics of this study. In the next subsection, we review its development and applications in THz communications in detail.

2.3.2 THz two-wire plasmonic waveguide

A THz plasmonic waveguide featuring a single cylindrical metal wire was first proposed by Mittleman's group in 2004 [122]. Primarily distributed in the dry air surrounding the wire, THz radiation in a coaxial ring-shaped mode can propagate with low transmission loss and negligible dispersion. However, the supported radially polarized Sommerfeld wave differs from the linearly polarized THz radiation launched by the majority of THz sources, thus resulting in a low coupling coefficient. In addition, owing to the weak modal confinement, the metal wire plasmonic

waveguide is susceptible to environmental disturbances and suffers high radiation loss with a slight bend. Although the required geometrical flexibility can be realized by depositing a dielectric layer (e.g., polyurethane [123]) on the metal wire, a substantial increase in transmission loss and dispersion is observed as an expense, which limits its applications in THz communication links.

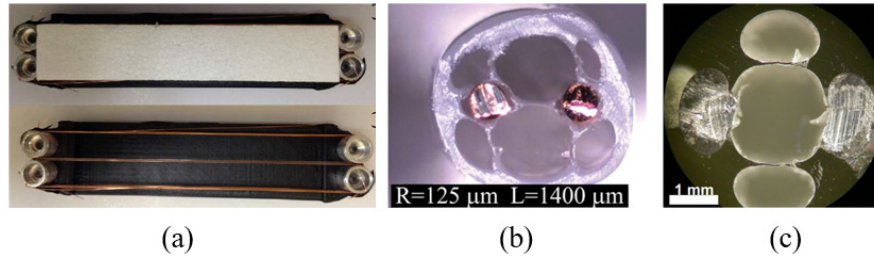


Figure 2.2. THz two-wire waveguide

(a) The two-wire waveguide protected by porous plastic foam. Reprinted from [124]. (b) The hybrid two-wire waveguide where two wires are inserted into a micro-structured hollow-core dielectric fiber. Reprinted from [124]. (c) The hybrid two-wire waveguide fabricated by drawing a polymer preform containing metal wires. Reprinted from [125].

Proposed in 2009 [126], two parallel conductive wires in the form of a TV-antennas cable, which are adapted from the twin-lead cable for RF signal transmission, emerged as promising THz waveguides for THz communications. The TEM mode, which is primarily distributed in the air gap between the two conductors, shares symmetry with standard THz photoconductive antennas, thereby enabling efficient modal excitation [124]. An active two-wire waveguide was proposed in [127], wherein THz radiation was directly generated within the waveguide structure by inserting photoconductive antennas between the two wires.

Moreover, compared with a single wire, the higher structural flexibility leads to new opportunities for two-wire waveguides considering device tunability. Modal field contraction has been realized by a two-wire waveguide featuring a pair of slowly tapered elliptical wires with a constant distance between two wires [128], as well as the one with a gradually narrowing air gap [129, 130]. The resultant beam shaping results in ease of coupling with other THz devices (e.g., PPWG) and enhanced energy flow density, while also enabling time-domain integration of broadband THz pulses for THz communications. Further, in another implementation [131], a frequency-tunable

two-wire waveguide-based Bragg grating was demonstrated by inserting a micromachined paper grating into the air gap between two wires.

Although it allows THz light guidance and manipulation, owing to the exposed air gap and the difficulty in aligning two parallel wires, the practical application of standing-alone two-wire waveguides in THz communications is limited. Consequently, to benefit from the outstanding optical properties and simultaneously ensure structural stability, several designs with the classic two-wire waveguides being embedded in dielectric claddings have been proposed. In [124], our research group reported a two-wire waveguide design wherein two metal wires were protected by porous plastic foam and stretched by cumbersome holders at their two ends (see Fig. 2.2 (a)). In [132], following the insertion of two metal wires into the micro-structured cladding of a dielectric hollow-core fiber, a hybrid two-wire waveguide was proposed (see Fig. 2.2 (b)). In addition, a waveguide with a similar design was also fabricated by drawing a Zeonex preform containing indium wires (see Fig. 2.2 (c)) [125]. However, the modal electric field of the THz SPP wave supported by classic two-wire waveguides reaches its maximum intensity at a position close to the wires. For such hybrid two-wire waveguides, although the modal field is predominately confined in the central hollow core of the fibers, the existence of a lossy dielectric in the gap to fix wires can still considerably influence the guided THz SPP wave in a negative manner.

Recently, we proposed a 3D-printed micro-encapsulate two-wire waveguide exhibiting two wires suspended in dry air and encapsulated by a dielectric cage [20]. Without the intrusion of leaky material in the air gap between the two wires, the designed waveguide features low transmission loss and GVD. In addition, butt-coupling between Ws and other THz devices with low insertion loss can be realized by this waveguide owing to its modular nature. Moreover, with outstanding structural flexibility and stability enabled by AM techniques, this two-wire plasmonic waveguide can serve as a versatile platform to develop various waveguide components (e.g., WBG, splitter, and directional coupler) and highly reconfigurable plasmonic circuits (e.g., ADM circuit) for THz communication links. In Chapters 5 and 6 of this thesis, we present detailed information on the proposed two-wire plasmonic waveguide and circuits.

2.3.3 ADM for THz frequency division multiplexing communication

Based on the ultra-high bit rate data transmission via a single channel [133-135], the linear growth of the data throughput capacity of THz communication networks can be realized by exploiting various DOFs of THz light, including polarization [136, 137], frequency [43, 120, 138, 139], and OAM [140]. In contrast to the THz PDM system, wherein a dual-channel link is created with two orthogonally polarized carrier waves, THz multiple-channel links can be created by adapting multiplexing schemes using the latter two efficient DOFs. In addition, although OAM multiplexing theoretically outperforms frequency division multiplexing in terms of channel capacity and spectral efficiency, it is still in the nascent stage. In contrast, frequency division multiplexing is a well-developed technique whose derived orthogonal frequency division multiplexing has been extensively used in 4G/5G communication, thus showing a higher prospect of realizing terahertz multiplexing communication in the near future.

In the frequency division multiplexing scheme, the ADM is the enabling element that adds (extracts) one (or a few) signals to (from) the existing data stream. In the optical regime, ADMs are typically built on silica-based planar lightwave circuits and fiber arrays using a combination of mature frequency-selective optical elements (e.g., ring resonator, phase-shifted grating, Bragg grating, and arrayed waveguide grating), and wideband light-guiding elements (e.g., circulator, and coupler) [141-145]. However, owing to the lack of universal and reliable technical routes in the THz regime, the THz ADM is still in its early development, with only a few demonstrations presented based on planar silicon substrates and PPWG.

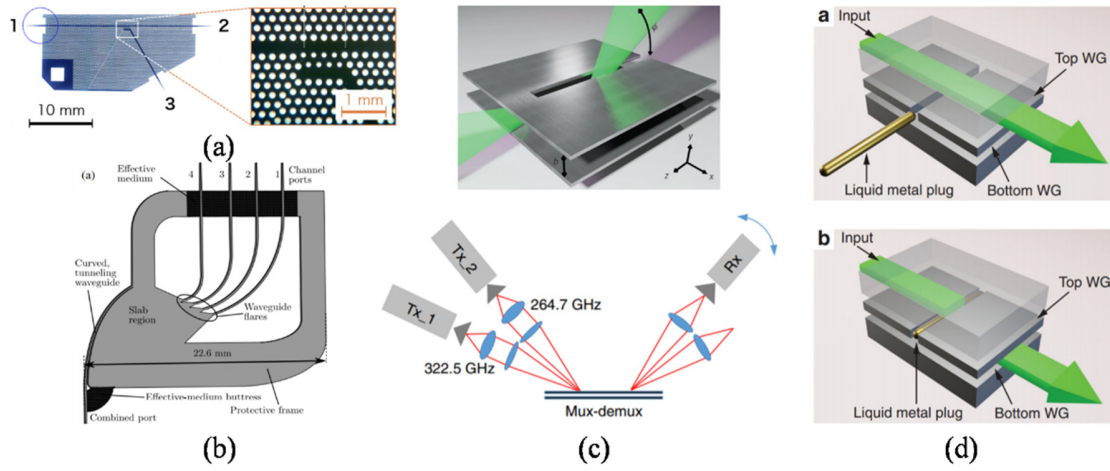


Figure 2.3 The reported THz ADM designs

(a) A diplexer on a silicon substrate. Reprinted from [39]. (b) The curved tunneling silicon slab waveguides. Reprinted from [44]. (c) The leaky-wave antenna built on PPWG. Reprinted from [138]. (d) The stacked PPWGs containing electrically actuated liquid metals. Reprinted from [120].

Nagatsuma's group reported a THz ADM built on a slab silicon substrate containing two adjacent photonic crystal waveguides in 2016 (see Fig. 2.3 (a)) [39, 43]. Carefully tailoring the coupling length aided in the realization of channel dropping via directional coupling of the narrowband THz carrier frequency within the photonic bandgap. In another silicon substrate-based THz ADM design that was proposed recently [44], wherein THz carrier waves tunneled from a curved micro-scale silicon waveguide to an adjacent curved silicon slab via evanescent fields. Subsequently, beam focusing of THz signals in different carrier frequencies at various positions on the slab was realized by the constructive interference of leaked waves from each point along the curved slab boundary. Finally, the THz signal in multiple channels was guided to distinct linear-flared waveguide structures featuring different flares (see Fig. 2.3 (b)). Further, the leaky-wave radiation was also applied by PPWGs to develop THz ADMs in [138, 139]. In this design, the angle of emission and reception of THz light from the slot of the PPWG is frequency-dependent. Therefore, the channel dropping and adding could be conducted in a broad THz spectral range (see Fig. 2.3 (c)). Nevertheless, as a free-space component, this ADM has a stringent alignment requirement, integrating it into compact THz circuits is challenging. In another implementation [120], the coupling between two vertically stacked PPWGs through gaps in the shared metal plate was used

for THz channel dropping. Capillaries are inserted into these gaps, where the liquid metal that is immersed in the liquid electrolyte move along the channel by applying a small voltage. The desired THz carrier frequency could be switched between the Through and Drop ports owing to the placement of liquid metal inside or outside the waveguides (see Fig. 2.3 (d)).

Compared to the aforementioned THz ADMs based on deformed PPWGs and silicon substrates having complicated structures, the conjunction of THz waveguide components that are capable of splitting/combining THz carrier frequencies in spectral and spatial domains, a concept adopted by most optical ADMs, is a simpler and more flexible solution. Featuring low transmission loss and dispersion, high coupling coefficient with the THz sources, and modular nature, the 3D-printed micro-encapsulated two-wire waveguide provides a versatile platform to develop reconfigurable THz plasmonic circuits [20]. A three-port ADM prototype composed of a Y-coupler and an external Bragg grating was proposed in [20] and Chapter 5. Another tunable four-port ADM design with the key building block of a grating-loaded directional coupler was developed and applied in THz communications in Chapter 6.

2.4 Additive manufacturing techniques in THz waveguide fabrication

Owing to the flexibility in design and continuously improving processing resolution, 3D printing has emerged as a promising method that can substitute conventional fiber drawing, CNC machining, and even advanced microfabrication techniques to fabricate THz waveguide components in certain cases. In contrast to these traditional subtractive manufacturing routes, where the desired model is obtained by the removal of the redundant parts from bulk, the designed 3D model is built layer by layer from scratch using AM techniques. Since its development in the 1980s, the AM technique has been applied in various fields, such as industrial manufacturing [146], biomedical science [147], and artistic creation [148]. In electronic fields, with continuous technological innovation, the application of 3D printing has expanded from the microwave [149-151] to the THz regime, which requires finer minimum features. In the THz spectral range, in addition to the aforementioned waveguide components, the AM technique has also been employed in the fabrication of various quasi-optical components and devices, such as antennas [152], metamaterials [68], spiral phase plates [153], polarizers [154], and GRIN lenses [155]. In this section, we reviewed the conventional AM techniques and their applications in the fabrication of THz waveguide components.

Among various AM techniques, FDM, which was first proposed in the early 1990s [156] is currently the most commonly used technique because of its cost-effective infrastructure and raw materials, coupled with the single-step and environmentally friendly manufacturing process [157]. The thermoplastic filament is heated, softened, and extruded through the nozzle, and subsequently deposited on the build platform layer by layer to form the designed 3D structure. The overall print quality depends primarily on the nozzle size, which ranges from 0.2 to 0.8 mm in diameter for most commercial printers. The resultant resolution of hundreds of micrometers and surface roughness of tens of micrometers restricts the application of FDM 3D printing in THz rectangular and plasmonic waveguides, where the geometrical defect of this scale significantly affects the transmitted THz light. Currently, the FDM 3D printing is used mainly to fabricate THz dielectric fiber components with an operation frequency below 0.5 THz [17].

Although certain conventional FDM 3D printing materials (e.g., ABS and PMMA) exhibit relatively high material absorption in the THz range [24], these amorphous materials are capable of solidifying homogeneously and bonding tightly after extrusion from the nozzle, thus resulting in a small geometrical deviation of the obtained prints from the designed ones. Therefore, together with PLA which features high strength, stiffness, and printability, these materials are suitable for the fabrication of THz hollow-core photonic crystal fibers with complicated cross-sectional shapes. For instance, J. Yang *et al.* designed and manufactured a THz Kagome fiber featuring an average transmission loss of 0.01 cm^{-1} for 0.2-1.0 THz [31]. In another implementation [32], hollow-core nested antiresonant nodeless fibers designed for short-reach THz applications were fabricated. Considering that the electric field distribution of the fundamental mode supported by these fibers is primarily in the central hollow core, the material absorption of the hosting polymer has a negligible influence on the transmission loss.

In contrast, certain semi-crystalline thermoplastics (e.g., HDPE and PP) exhibit much lower material absorption [24]. However, owing to their low self-adhesion characteristics, when using these non-standard 3D printing materials, adjusting the printing parameters to avoid wrapping and cracking of built models during cooling is a challenging task [158]. Because it is difficult to avoid the deformation of 3D printed THz hollow-core fibers with porous structures, these 3D printing materials are primarily used in the production of THz solid-core fibers with relatively plain designs. By trial and error, our research group fabricated a THz suspended-core fiber featuring a rotationally

symmetrical cross section with a single section length of 25 cm. Owing to the low material absorption of PP ($\sim 0.006 \text{ cm}^{-1}$ at $\sim 128 \text{ GHz}$), the transmission loss of the fabricated THz fiber is $\sim 2 \text{ dB/m}$ [28]. Moreover, similar to the production using an optical fiber draw tower, a THz solid core fiber was manufactured by a heated extruder of an FDM 3D printer together with a spinning spooling wheel in [26]. Furthermore, using a nozzle with a complicated internal structure, THz suspended- and hollow-core antiresonant polymer fibers were also obtained using this method [159, 160].

The SLA, invented in the 1980s, was the first AM technique reported [161]. With the capability of reproducing highly detailed prototypes with satisfactory accuracy, the SLA is among the most popular 3D printing technologies that have been extensively employed in industrial manufacturing [162]. In SLA 3D printing, the designed module is fabricated by curing the photosensitive resin to pattern its cross sections layer by layer using UV radiation. Further, DLP, another vat photopolymerization technology, functions on the same working principle. The primary difference between the DLP and SLA is the source of UV radiation. For the former, stationary UV light from a projector simultaneously cures the photosensitive resin on the entire printing layer. To realize the latter, the UV laser was steered by two galvanometers, and the focused beam spot moves linearly from point to point to trace the desired pattern on one layer. However, despite the resultant lower printing speed, the XY-axis resolution of SLA 3D printing depending on the laser beam spot is usually higher than that of DLP, which is determined by the voxel size of the projector on the building platform, thus allowing the fabrication of objects with smaller minimum features.

Nevertheless, for most affordable desktop SLA and DLP 3D printers, the finest XY-resolution and layer thickness are of the order of tens of micrometers, which is less than one-tenth of the wavelength of the sub-THz wave. Moreover, the surface finish of the fabricated model is of the order of hundreds of nanometers, which is orders-of-magnitude lower than that of other AM prints. Therefore, both the SLA and DLP techniques enable the fabrication of THz devices with high geometrical accuracy. In addition to the hollow core THz dielectric fibers [100, 101], these two types of AM techniques have also found application in THz rectangular and plasmonic waveguide components with the assistance of metallization [20, 57, 163, 164]. Despite the somewhat large material absorption of the cured resin in the THz spectral range (over 1 cm^{-1} for THz light with operation frequency over 0.2 THz), the 3D printed dielectric structure serves as the mechanical

support of the conductive layer in the proposed waveguide components, and thereby has a minor influence on the transmission of the THz radiation, whose electric field is primarily distributed in the lossless dielectric (dry air).

To fabricate THz rectangular waveguide components, in addition to metalizing the DLP 3D printed dielectric support, the SLS and SLM 3D printing techniques provide another straightforward solution, namely the desired structure can be directly formed by fusing alloy or metal powder without postprocessing. In [165], THz rectangular waveguides with operation frequency in the D-band (110-170 GHz) and H-band (220-235 GHz) were fabricated using SLM 3D printing, during which the powdered particles were continuously placed at the top of the powder bed and selectively fused by a laser to form the cross sections of the desired object layer by layer. The main differences between SLS and SLM include the raw materials and structure of prints. SLS 3D printing is prone to processing plastic, ceramic, and certain specific kinds of alloys (e.g., stainless steel, and AlSi₁₀Mg). The pulsed carbon dioxide laser heats the powder to the temperature at which the grains are fused at the molecular level to achieve prints with controllable porosity. Metals and alloys are suitable for SLM 3D printing, where a CW ytterbium fiber laser is usually used to fully melt the powder into a homogeneous part, thus resulting in nearly full-density prints.

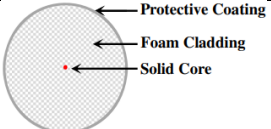
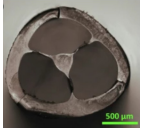
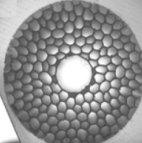
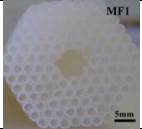


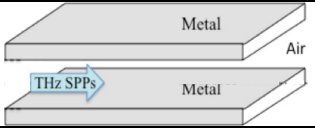
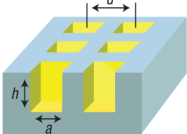
Despite the existence of more types of applicable materials, high resolution, which is on the order of tens of micrometers, and free of support for prints, compared with the FDM and SLA ones, SLS and SLM 3D printers are rarely used in routine laboratory research because of the high cost and risk brought by their integrated high-power laser modules. Currently, affordable commercial desktop printers are prone to process dielectrics with low melting temperatures (e.g., nylon [166]), which limits their application in the manufacturing of THz metallic waveguide components.

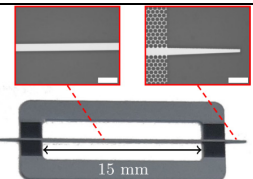
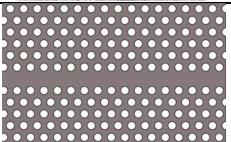
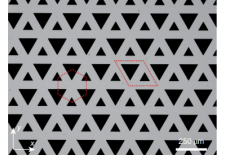
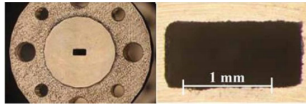
In conclusion, both FDM and SLA (DLP) 3D printing are popular AM techniques that have been extensively used in THz waveguide component fabrication. They outperform traditional machining methods in terms of accessibility and cost of infrastructure and raw materials, as well as the universality and consistency of manufacturing, thus facilitating the reproduction of THz waveguide components. However, the limitations in applicable materials and building volume, as well as the requirement for higher resolution and post-processing (e.g., metallization) still hinder the creation of THz waveguide components. We believe that with further technical innovations in the field of materials, hardware, and processes, such as multi-material 3D printing [167], 3D printing using

smart materials (4D printing) [168], and two-photon lithography [169, 170], the AM technique can enable a more novel design of THz waveguide components.

In this thesis, using FDM and SLA 3D printing techniques, we proposed a PBG Bragg waveguide-based THz fluidic sensor (see Chapter 4) and two-wire plasmonic circuits for THz communications (see Chapters 5 and 6), respectively.

Table 2.1 Reported classic THz waveguides

Waveguide	Material	Fabrication technique	Guiding mechanism	Example	Schematic
Dielectric waveguide (fiber)	Dielectric mainly polymers silicon [171]	Fiber drawing or Additive manufacturing	TIR	Subwavelength fiber [26]	
				Suspended-core fiber [154]	
			Photonic bandgap	Photonic bandgap fiber [172-174]	
			Antiresonance	Kagome fiber [175]	
Plasmonic waveguide	Metal Or Silicon substrate with metal coating Or Polymer support with metal coating	CNC machining Or Microfabrication Or Additive manufacturing	SPP	Metal wires [122, 176]	
				Goubau line [177]	
				PPWG [178]	
			Spoof SPP	Structured metal surface [179]	

Waveguide	Material	Fabrication technique	Guiding mechanism	Example	Schematic
Waveguide on a planar silicon wafer	Silicon	Microfabrication	TIR	Unclad waveguide [13]	
			Photonic bandgap	PC waveguide [39]	
			Topology insulation	Valley hall photonic crystal [40]	
Rectangular waveguide	Metal or Dielectric support with metal coating	CNC machining or Additive manufacturing	TIR	Rectangular waveguide [165]	

Reprinted from [26, 154,173,175,177,178,179,13,39,40, and 165]

CHAPTER 3 METHODOLOGY

In this chapter, we briefly describe the general methodology used in this thesis. We begin by discussing the design principles and fabrication techniques of THz PBG Bragg waveguide-based sensors and two-wire plasmonic circuits. Subsequently, we briefly introduce numerical simulations of the proposed THz waveguide components and circuits. Finally, we present the experimental setup that was used for characterization. Detailed descriptions of the experimental setup, characterization, as well as numerical simulation models, can be found in Chapters 4.4, 6.4, and Appendix B.

3.1 THz waveguide component fabrication using 3D printing techniques

Among various 3D printing techniques, FDM and SLA have been extensively used in the fabrication of THz waveguide components. In this work, desktop 3D printers exploiting these two printing techniques (Raised 3D Pro and Asiga Pro 2) were used to manufacture PBG Bragg waveguide-based fluidic sensor and reconfigurable two-wire plasmonic circuits, respectively. As a preprocessing procedure for 3D printed THz optical components, the corresponding 3D CAD models were sliced into multiple layers with a fixed thickness along the printing direction using the specific pre-programming software (ideaMaker for FDM 3D printing, and Asiga Composer for SLA 3D printing).

3.1.1 Fabrication of THz PBG Bragg waveguide-based sensor using FDM 3D printing

Fig 3.1 shows a schematic for the cross-sectional view of the proposed THz PBG Bragg waveguide, where the square hollow core is surrounded by ten PLA/air bilayers. When launched into the hollow core of a PBG Bragg waveguide, the THz light with operation frequency falling within the bandgap can be confined in the core and guided through the waveguide with a small insertion loss. Whereas, the THz light with an operation frequency outside the bandgap will leak out through the cladding region.

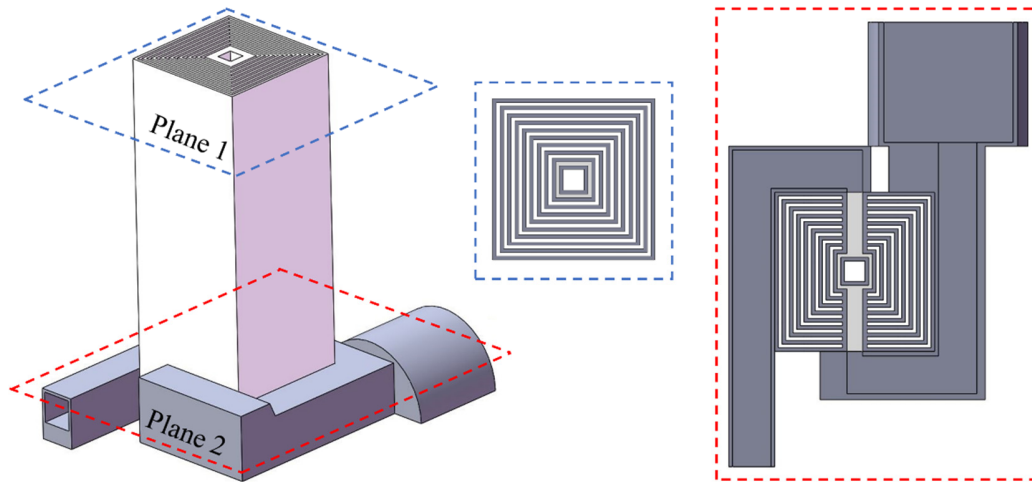


Figure 3.1 The cross-sectional view of THz PBG Bragg waveguide-based resonant sensor

To mitigate the influence of noise on resonant sensing, the spectral position of the bandgap of the PBG Bragg waveguide was set in the range of 0.2 – 0.3 THz due to the absence of water vapor absorption peak in this spectral range. Further, by numerical simulation using the 2D model in COMSOL Multiphysics, the layer thickness and core size were set to 0.8 and 4.5 mm, respectively, to allow the few-mode operation and high coupling coefficient with the focused THz light in a CW-THz spectroscopy system for characterization. By comparing waveguides with different lengths (see Chapter 4.4.1), a 10 cm-long PBG Bragg waveguide that enables an effective single-mode operation with minimal insertion loss was selected as the platform to implement resonant sensing.

Further, based on the PBG Bragg waveguide, the air layer close to the hollow core was selected to fill the liquid analytes, thus facilitating the strong anticrossing phenomenon for THz sensing. In experiments, this layer was sealed at both ends and connected to an external fluidic channel. Driven by gravity, the liquid analyte injected into the fluidic channel can flow through this layer. The fluidic channel section that passes through the cladding region can also fix the relative position of each PLA layer (see Fig 3.1), thus ensuring the structural stability of the PBG Bragg waveguide while having a small impact on the photonic bandgap.

A THz fluidic sensor composed of a PBG Bragg waveguide and a fluidic channel was fabricated using the FDM 3D printer along the waveguide length in a single shot. The entire component was fabricated using a 0.4 mm nozzle operating at 215 °C together with 1.75 mm-diameter PLA filaments. The softened polymer was extruded and deposited onto the heat bed to form the raft.

Subsequently, by displacing the nozzle in space, the desired PBG Bragg waveguide-based sensor with a satisfactory definition was built on the raft layer by layer. During 3D printing, the heat bed was maintained at 60 °C to mitigate the surface wrapping. It is noted that a high filling ratio and a small layer thickness were required to ensure the airtightness of the manufactured fluidic channel and avoid the leakage of liquid analyte when it flows through at the expense of the long manufacturing time (~20 hours). The resultant low porosity led to a significant increase in the RI of the PLA layer in the PBG waveguides (see Appendix A.1). In addition, compared with the numerical one with ideal geometry, the 3D-printed PBG Bragg waveguide features a larger scattering loss, which is primarily due to the surface roughness.

Moreover, FDM 3D printing was also employed to fabricate various holders, clamps, and containers for the convenience of characterizing the proposed THz components in this thesis.

It is noted that the designed PBG Bragg waveguide-based sensor is achievable by CNC machining in plastic theoretically. However, manufacturing this complicated 3D model containing a built-in fluidic channel penetrating the fiber reflector as integrity is a challenging task that requires high-end multi-axis CNC machine and machining expertise. An alternative route that includes post-machining assembly of discrete components is easily accessible, but inadvisable, which is because that the structural integrity and shape perfection is of importance to avoid the leakage of liquid analyte flowing through the fluidic conduit and to ensure the appearance of bandgap which is sensitive to the small geometrical deviation from the design.

3.1.2 Fabrication of THz two-wire plasmonic circuits using SLA 3D printing

SLA is another extensively used rapid prototyping technique for THz optical component fabrication. By curing the photosensitive resin to form the desired 2D pattern with a fixed thickness, the 3D object is successively constructed layer by layer. In each period of SLA 3D printing, the building platform moves vertically to immerse the top of the fabricated 3D model into the uncured resin in the printing tray. Thereafter, the UV laser scans and selectively solidifies the liquid resin to form a new layer.

The resolution of SLA 3D printing, which is determined by the chemical characteristics of the photosensitive resin and the beam spot size of the UV laser, is superior to that of the FDM.

Therefore, SLA 3D printing can endow the manufactured 3D objects with finer definitions in most cases. Moreover, compared with the SLA 3D printed two-wire waveguide, which is highly consistent with the design, the deformation, rough surface, and internal defect result in significantly greater transmission loss of the FDM 3D-printed ones. Although the cured photosensitive resin exhibits larger material absorption than the PLA in the THz spectral range [100], the electric field distribution of the SPP wave supported by the proposed micro-encapsulated two-wire waveguide was mainly confined in the air gap between two wires with a small portion leaking into the lossy dielectric enclosure. Therefore, compared with FDM, SLA 3D printing using photosensitive resin is more suitable for the fabrication of the substrate of micro-encapsulated two-wire plasmonic circuits.

Fig. 3.2(a) shows a schematic cross-sectional view of the proposed micro-encapsulated two-wire waveguide, based on which the THz plasmonic circuits were developed. For the convenience of subsequent metallization, the waveguide dielectric support was divided into two complementary parts to be fabricated separately. Although it is a time-consuming process (~ 12 hours for 6cm-long straight two-wire waveguide sections), each part must be printed along the waveguide propagation direction to achieve a satisfactory definition (see Fig. 3.2(b)). In contrast, when printing along the radial direction, the collapse of the deeply subwavelength pillar connecting the wire and enclosure, and the mismatch of the two halves of the enclosure resulted in severe deformation of the assembled dielectric support (see Fig. 3.2(c)). Consequently, to reduce the fabrication time, several parts were printed using the SLA 3D printer simultaneously and the entire two-wire waveguide component was assembled with complementary parts using the alignment features on the enclosure. Additionally, it is noted that the end facet of each 3D-printed part must be carefully polished and flattened. In experiments, we found that the debris of the tree-like support structure and inclined end facet resulted in an increasing coupling loss between WSs and with other THz component devices.

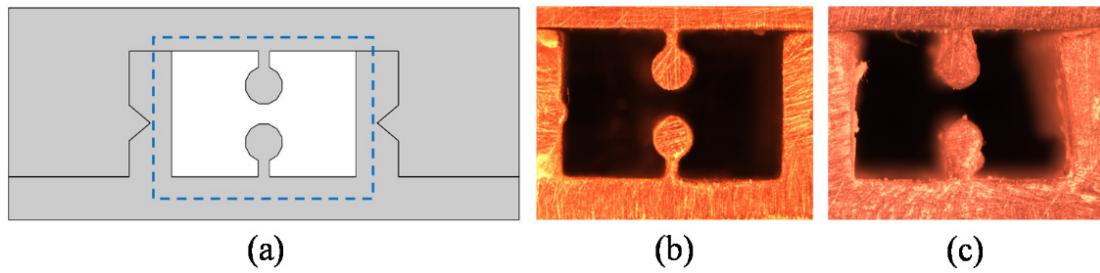


Figure 3.2 The cross-sectional view of micro-encapsulate two-wire waveguides

(a) The schematic diagram. Photos of the end facet (in the blue dotted region in Fig 3.2 (a)) of dielectric supports of straight two-wire waveguides that were printed along (b) the waveguide propagation direction and (c) the radial direction of the waveguide using an SLA 3D printer.

Following the post-processing and polishing, the SLA 3D-printed dielectric support of two-wire waveguide components was metalized using the wet chemistry deposition technique. After protecting the inner wall surface of the enclosure, a silver layer with a thickness of tens of micrometers was deposited on the exposed cylindrical wire support. Finally, we used the V-shaped grooves and ridges imprinted on the side wall of the enclosure to assemble two complementary parts into a two-wire WS, and then developed a two-wire plasmonic circuit by connecting multiple WSs with the assistance of alignment and connection elements imprinted on the end facet of the enclosure.

It is noted that the all-metal structures obtained by CNC machining can be an interesting alternative to the partially metalized 3D printed resin support developed in this work. However, the all-metallic encapsulation of the two-wire waveguides can pose significant challenges due to the presence of a large number of higher-order, relatively low-loss modes that can cause multi-mode interference effects and bring about additional noise and artifacts to the operation of two-wire circuits. This is because a hollow metallic encapsulation cage is essentially a heavily multimode rectangular waveguide that supports relatively low-loss modes even when two metallic wires are placed inside. Another alternative route where the polymer support fabricated by CNC machining is partially metalized is theoretically feasible, and the obtained structure is expected to perform as the desired THz plasmonic components. However, from the fabrication point of view, CNC machining is considerably more difficult than 3D printing as the deeply sub-mm features of the waveguide support and grating structure, as well as the 3D complexity of models.

The hot stamping technique is another metallization technique that allows rapid prototyping of metalized patterns on a planar substrate with ease and precision [180]. It was employed in this thesis to fabricate paper-based two-wire WBGs (see Chapter 5.3.3).

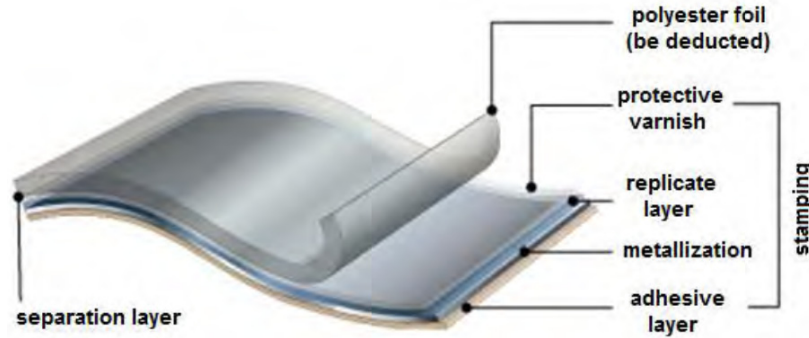


Figure 3.3 The layer composition of a hot stamping foil which is reprinted from Ref. [181]

First, the pattern of the designed metalized periodic stripes was printed onto both sides of the paper substrate using a high-resolution office laser printer. Thereafter, the paper substrate was sandwiched between two hot-stamping foils whose composition is shown in Fig. 3.3. When passing through the laminator [26], the adhesive layer (thermoplastic resin) of hot stamping foil bonded to the toner on the paper substrate under heat and pressure, thus selectively depositing the polymer/metal film on the printed pattern. Further, the resolution of the hot stamping technique was mainly determined by the printer resolution and paper quality. In experiments, it was found that by characterizing the fabricated Bragg grating using the CW-THz spectroscopy system, the width difference in designed periodic stripes below 10 μm could be distinguished.

3.2 Numerical simulation

In this thesis, a numerical study of PBG Bragg waveguides and two-wire waveguide components was conducted using the finite element frequency domain (FEFD) module of the commercial software COMSOL Multiphysics. The effective refractive index, modal loss, and electric field distribution of modes supported by waveguide components featuring a uniform cross section were computed using the 2D mode solver tool. The bending loss of two-wire waveguide bends, which have the same cross-section along the tangential direction of the waveguide, was computed using the axisymmetric 2D solver tool. Further, the transmission and reflection coefficients of two-wire WBGs, directional couplers, and ADM circuits were obtained by computing the scattering matrix

coefficients of the defined ports in the corresponding 3D numerical modules. It is noted that the computation cell of the waveguide components containing symmetry planes was simplified using the PEC and PMC boundary conditions. With a proper design, the resultant half or quarter module derived the same numerical simulation results as that of a complete module within a much shorter computation time.

3.3 Experimental setup to characterize THz waveguide components

3.3.1 CW-THz spectroscopy system

The optical properties of the proposed PBG Bragg waveguides and two-wire plasmonic circuits proposed in this thesis were characterized using a CW-THz spectroscopy system. Compared with the THz TDS system, which is another important tool in THz spectroscopic studies, CW-THz spectroscopy provides spectral information over a somewhat narrower bandwidth within a longer data collection time. However, owing to the much higher spectral resolution (50 MHz), the CW-THz spectroscopy system is perfectly suitable for detecting the spectral singularity position of PBG Bragg waveguide-based resonant sensors, as well as the operation bandwidth of two-wire WBGs and ADMs. Moreover, the THz beam path in the CW-THz spectroscopy system can be easily modified by changing the configuration of free-space optical components without affecting the rest of the system, thus allowing the characterization of THz waveguide components with arbitrary shapes (e.g., The 90° waveguide bends with different bend radii) and advanced functionalities (e.g., THz ADMs).

In the CW-THz spectroscopy system (Toptica photonics), we mixed fiber radiation from two tunable distributed feedback (DFB) lasers with slightly different emission wavelengths in the IR C-band. A 50:50 fiber coupler was used to split the signal obtained into emission and detection arms. The THz radiation corresponding to the beat frequency between these two DFB lasers was generated in the photomixer (under bias voltage). A similar photomixer (without bias) and a lock-in amplifier were used to detect the recollimated THz beam. Further, to measure the complex transmission spectra of the THz waveguide components placed inside the spectroscopy system, the THz frequency was scanned by continuously varying the emission wavelengths of the two DFB lasers via adjusting the temperature of the Bragg grating in each laser cavity. Meanwhile, a phase

measurement was performed using an optical delay line in the form of a polarization-maintaining fiber wound onto piezoelectric elements at every frequency [182-184]. The configurations of the free-space THz components to characterize the PBG Bragg waveguides and two-wire plasmonic circuits were different, as shown in Figs. 3.4(a) and 3.4(b), respectively. Compared with the latter configuration, the former one possessed the ability to mitigate the interference of the standing wave on the measured transmission spectra for sensing at the expense of difficulty in alignment and limited application scope. A detailed description of the experimental setup configuration and characterization can be found in Chapters 4.4, 6.4, and Appendix B.

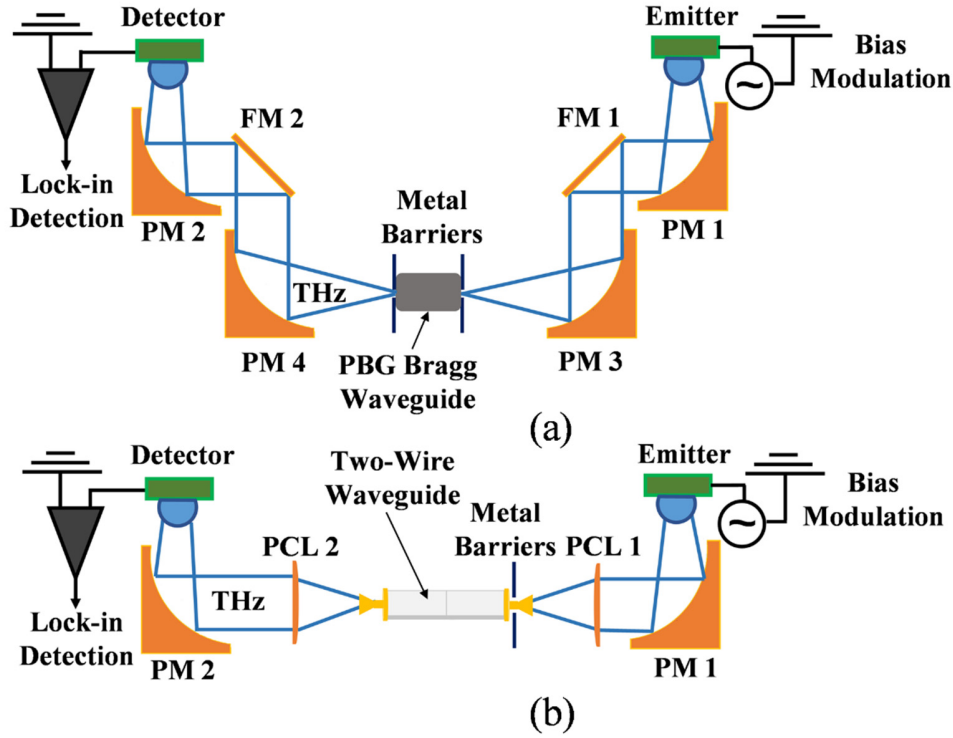


Figure 3.4 The free-space THz optical path in CW-THz spectroscopy for characterization
 (a) PBG Bragg waveguide-based resonant sensor, and (b) Two-wire plasmonic circuits.

3.3.2 Photonics-based THz communication system

The two-wire ADM circuit proposed in this thesis (see Chapter 6) was characterized using an in-house photonics-based THz communication system to explore its potential application in the field of THz FDM communications [26, 185]. The modulated THz carrier waves were generated using

a pseudorandom bit sequence (PRBS) with a pattern length of $2^{31} - 1$ as the baseband signal source. Consequently, the eye pattern and BER response of THz signals with different bit rates propagating through THz ADM circuits were recorded. The experimental setup is shown and briefly discussed in the methodology section in Chapter 6.

CHAPTER 4 ARTICLE 1: ADDITIVE MANUFACTURING OF RESONANT FLUIDIC SENSORS BASED ON PHOTONIC BANDGAP WAVEGUIDES FOR TERAHERTZ APPLICATIONS

Yang Cao¹, Kathirvel Nallappan^{1,2}, Hichem Guerboukha¹, Thomas Gervais¹,
and Maksim Skorobogatiy¹

¹Génie physique, Polytechnique Montréal

²Génie électrique, Polytechnique Montréal

Optics Express, vol. 27, no. 20, p. 27663-27681 (2019)

Abstract: A hollow-core Bragg waveguide-based resonant fluidic sensor operating in the terahertz frequency band is studied. A fused deposition modeling 3D printing technique with a Polylactic Acid filament is employed to fabricate the sensor where the liquid analyte is flowing in the microfluidic channel integrated into the waveguide cladding. The fluidic channel supports a resonant defect state which is probed spectrally using the core-guided mode of the Bragg waveguide. CW-THz spectroscopy is used to characterize the fluidic sensor. The measured signal amplitude shows a dip in the transmission spectrum, while the measured phase shows a sharp change in the vicinity of the anticrossing frequency whose spectral position depends strongly on the real part of the analyte refractive index. The sensor spectral response is further optimized by tailoring the waveguide length and position of the defect layer. Consistent with the results of numerical modeling, the measured sensor sensitivity is ~ 110 GHz/RIU, while the sensor resolution ~ 0.0045 RIU is limited by the parasitic standing waves in the spectrometer cavity. We believe that the proposed fluidic sensor opens new opportunities in applied chemical and biological sensing as it offers a non-contact measurement technique for monitoring refractive index changes in flowing liquids.

4.1 Introduction

The terahertz (THz) frequency band (100 GHz – 10 THz, wavelengths 3 mm – 30 μ m) holds great promise for non-destructive imaging, industrial sensing, and process monitoring due to relative transparency of many important dielectric materials, low photon energy (especially important for

bio-applications), as well as unique spectral fingerprints of numerous materials in this spectral range [186].

From the point of view of optical sensing, enabled by the efficient light-matter interaction, the change in the RI of the analyte under investigation can be probed by monitoring the variation in the properties of the optical beam, such as absorption, resonance, transmission, and scattering. Besides straightforward applications in the field of chromatography that analyzes nonfluorescent samples lacking strong chromophores [187], as the correlation between the RI and other physical and chemical characteristics of analytes, optical sensing can also find various applications in biomedical diagnoses, food industries, and environmental monitoring. Compared with other sensing strategies where the analyte information is converted from electrochemical, piezoelectrical, acoustic, or calorimetric signals, optical sensing can exploit not only the analyte properties but also various principles and configurations of optical sensors, thus enabling real-time and remote analysis with attenuated external disturbance and high sensitivity.

In particular, monitoring of the refractive index (RI) of fluids using THz waves has attracted much interest due to various important applications, such as probing the binding state of the nucleic acids [188], monitoring the conformational change and interaction of the proteins [189], as well as detecting pesticides and antibiotics [190, 191]. Compared with other optical methods (ex. relying on evanescent wave or surface plasmon resonance, and non-resonant sensing), a more sensitive detection strategy for monitoring liquid analyte RI relies on tracking the position of spectral singularities caused by the resonant excitation of a certain optical defect state by the probing THz wave [192]. Either the signal amplitude or phase can be used in such experiments, with phase being, generally, the most sensitive parameter for the detection of small changes in the analyte RI. Such resonant THz fluidic sensors have been so far realized using metamaterials and waveguide structures with or without photonic crystal reflectors [69, 70, 88, 193, 194].

In metamaterial-based sensors, artificially-engineered micrometer-sized inclusions are patterned on a planar substrate and subsequently brought close to liquid analytes. The electromagnetic response of the metamaterial is then probed to monitor the shift of the metamaterial resonant frequency, which can then be related to changes in the thickness and/or RI of the liquid analyte. The best sensitivities measured to date using this methodology are ~ 50 GHz/ μm and ~ 700 GHz/RIU for sensors operating at relatively high (3.5 THz and 1.5 THz) frequencies [193, 194].

Due to high sensor sensitivities, the range of measured thickness and RIs are limited to $\sim 10\ \mu\text{m}$ and ~ 1 RIU, respectively. Unfortunately, as the size of elemental features (such as split-ring resonators) can be as small as $\lambda/5 = 60\ \mu\text{m}$ at 1 THz, one has to resort to the relatively costly microfabrication techniques to fabricate metamaterial-based sensors operating at such high frequencies, while such small features remain out of reach for most AM systems.

In contrast, waveguide-based sensors can be fabricated using simpler geometries and more cost-effective techniques. Thus, in [69], a parallel-plate waveguide (PPWG) with a 1mm gap was used to probe resonantly the RI of liquid analytes filling the groove that was inscribed onto the surface of a waveguide hollow core. The groove featured a rectangular cross section with a width and depth of $\sim 400\ \mu\text{m}$, and functioned as a resonant cavity for the THz wave propagating perpendicularly to it. A sensitivity of $\sim 90\ \text{GHz/RIU}$ was measured in the $0.27 - 0.3\ \text{THz}$ frequency range, and offered ~ 0.3 RIU measurement range. The same research group then proposed a multichannel structure with similar architecture for multi-sample detection [70]. Furthermore, in [88], a hollow-core tube-shaped THz waveguide with a grating (period $300\ \mu\text{m}$) inscribed on its outer surface that also contained liquid analyte was employed as a fluidic sensor featuring sensitivity of $\sim 50\ \text{GHz}/\mu\text{L}$ at $\sim 0.6\ \text{THz}$. Changes in the grating RI impacted the transmission properties of the core-guided THz wave of the ARROW waveguide. Changes in the analyte RI can then be extracted from changes in the frequency of maximal transmission efficiency through the tube waveguide.

Among all the resonant sensors of RI, hollow-core photonic bandgap (PBG) Bragg waveguides offer many practical advantages including simplicity and flexibility of design and fabrication [195], high sensitivities, ease of integration into sensing systems, integration of microfluidics directly into the waveguide structure, as well as operation range from visible-near-IR [95, 97, 98] to THz spectral range [100]. By introducing a geometrical or RI defect inside the waveguide periodic reflector, a spectral singularity in the transmitted spectra is introduced at the frequency of anticrossing between the dispersion relations of the core-guide mode and the mode supported by the defect in the reflector [196, 197]. Thus, integrating a fluidic channel inside of a PBG waveguide reflector allows real-time resonant monitoring of the analyte RI by tracking the position of the anticrossing frequency that normally manifests itself as a narrow dip in the waveguide transmission spectrum.

From the device fabrication and system design point of view, THz sensing components operating below ~ 0.5 THz are relatively easy to fabricate due to large wavelengths in the THz band, and they also profit from relatively low atmospheric absorption (no major water vapor absorption peaks at lower frequencies) thus forgoing the need for nitrogen enclosures. It is, therefore, no surprise that 3D printing that offers $50 - 400 \mu\text{m}$ resolutions even when using low-cost tabletop systems has emerged as one of the prime tools for rapid, cost-effective fabrication of the THz components for operation at lower THz frequencies [57, 100, 115, 116, 198, 199].

In this work, we present theoretical analysis and experimental study of a THz hollow-core Bragg waveguide-based resonant fluidic sensor. The spectral position of the waveguide reflector bandgap and anticrossing frequency of its fundamental mode with that of a reflector defect state are first studied numerically using finite element COMSOL Multiphysics software. Then, we explore several fabrication strategies for such sensors using fused deposition modeling (FDM) and stereolithography (SLA) techniques, and comment on their comparative advantages and disadvantages. We then experimentally optimize the sensor by choosing the proper waveguide length and the optimal position of the reflector defect, as well as comment on the limitations in the sensor resolution posed by the accuracy of AM techniques used in sensor fabrication. Next, using a CW-THz spectroscopy system, the THz spectral response of an optimized Bragg waveguide-based sensor is studied for different values of the liquid analyte (different oils) refractive indices. By tracking the position of the spectral dip caused by the anticrossing phenomenon, our sensor sensitivity is found to be $\sim 110 \text{ GHz/RIU}$ near 0.23 THz , which is in good agreement with the theoretical result. By analyzing errors in the spectral response curves, we also find that our sensor resolution is $\sim 4.5 \cdot 10^{-3} \text{ RIU}$. We believe that our THz resonant fluidic sensors can be applied to a variety of practical applications that require monitoring of RI changes of the otherwise non-optically transparent liquid analytes in the $1.4 - 1.8 \text{ RIU}$ range.

4.2 Theoretical analysis of the THz hollow-core Bragg waveguides

4.2.1 Hollow-core Bragg waveguide with a perfectly periodic reflector

Over the past twenty years, a number of Bragg fibers were fabricated using the fiber drawing technique and offering operation in the visible [95, 97, 98, 200, 201], near-infrared (IR) [92, 202]

and mid-IR [203] spectral ranges. Such fibers typically operate within the photonic bandgap of a periodic reflector in the fiber cladding by confining the guided light in the fiber hollow core. In the reflector region, Bragg fibers feature periodic multilayers with the individual layer thicknesses in the sub- μm (visible) to several μm (mid-IR) range. A typical size of the fiber hollow core is in the several hundred μm range [92, 95, 97, 98, 200-203]. Most recently, several hollow-core Bragg waveguide designs were demonstrated in the THz spectral range using mechanical rolling [99, 204] and 3D printing fabrication techniques [100]. Due to much longer THz wavelengths compared to the IR wavelengths, Bragg fibers designed for THz applications are much easier to fabricate as they feature much larger core sizes and reflector layer thicknesses.

While most Bragg fibers in the visible and IR spectral ranges feature circular cross section, which is the shape most suitable for fiber drawing, in the THz spectral range this might not be the optimal shape for fabrication. This is due to the fact that THz Bragg waveguides are more convenient to fabricate using various 3D printing techniques such as FDM and SLA, which tend to produce linear structures (lines, planes, and walls) of much higher quality than curved structures (circles, spheres, etc.). This is related to the fact that most FDM printers are built with a Cartesian system in mind with mechanical parts (extruders and a built plane) that move naturally along the three orthogonal directions [205]. At the same time, most of the tabletop SLA devices are built around a projection system that defines a pattern of UV exposed resin at the built plane using a rectangular matrix or micromirrors (DLP chip) [206]. Therefore, a linear pattern aligned with the principal axis of a 3D printer hardware tends to give the highest build quality. In what follows, we, therefore, focus on studying square-shaped Bragg waveguides with the choice of the waveguide geometry mostly motivated by the employed fabrication method.

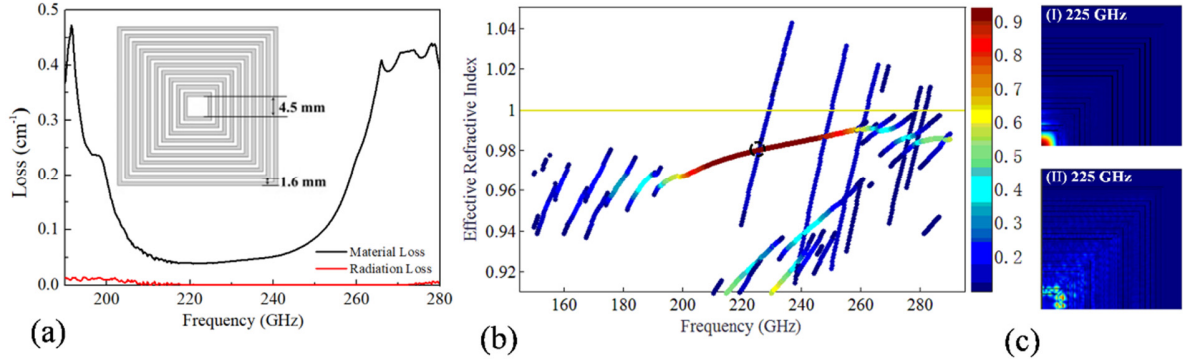


Figure 4.1 Numerical simulation of THz PBG Bragg waveguide

- (a) Spectral dependence of the material absorption and radiation loss for the fundamental core-guided mode of a hollow-core Bragg waveguide. Inset: schematic of the waveguide cross section. The grey and white layers represent the high- (plastic) and low- (air) RI materials, respectively. (b) Band diagram of the guided modes in the hollow-core Bragg waveguide featuring perfectly periodic reflector. The color scale defines the fraction of the modal power confined to the waveguide hollow core. Only the modes with over 10% of power guided in the core are presented. (c) Modal field distributions of the core guided mode (I) and a surface state supported by the Bragg reflector (II) at 225 GHz near the point of their accidental degeneracy.

Particularly, the hollow-core Bragg waveguide studied in our work features a hollow core of 4.5 mm size surrounded by a periodic reflector in the cladding region consisting of twenty alternating layers of plastic and air. Each of the ten bilayers consists of a high-RI Polylactic Acid (PLA) layer and a low-RI air layer ($n_a = 1$ [100]) with equal thicknesses of 0.8 mm (see inset in Fig. 4.1(a)). First, we numerically study the modes of a defect-free Bragg waveguide using the finite element COMSOL Multiphysics software. In our simulations, we use the experimental value of the PLA material RI $n_{PLA} = 1.63$ and loss $\alpha_{PLA} = 0.95 \text{ cm}^{-1}$ in the vicinity of 0.2 THz as measured using the cut-back method and a CW-THz system [100, 207, 208].

With these defined geometrical and materials parameters, in the 205 GHz - 255 GHz spectral range, the hollow-core Bragg waveguide features a Gaussian-like core-guided mode (see band diagram in Fig. 4.1(b)) with a slowly varying effective RI slightly smaller than that of air. Moreover, the modal absorption and transmission losses show a clear presence of a photonic bandgap (see Fig. 4.1(a))

with material absorption being the dominant loss mechanism. At the same time, the predicted modal absorption loss ($\sim 0.05 \text{ cm}^{-1}$) at the bandgap center frequency is considerably smaller than the PLA bulk absorption loss of $\sim 0.95 \text{ cm}^{-1}$ as the modal field is mainly confined to the low-loss air-filled hollow core, thus enabling efficient guiding of THz light while using high-loss materials that are typically employed in 3D printing. Further reduction of the waveguide transmission losses is possible by using lower-loss thermoplastic materials such as Polypropylene derivatives, however, finetuning of extrusion parameters for such materials is more difficult than it is for more standard FDM materials such as PLA or ABS. Alternatively, one can use waveguides with larger core sizes, however, larger cores also support a larger number of modes. As it is important for our waveguides to operate in the effectively single-mode regime (in order for a sensor to have a well-defined spectral response), waveguides of larger core diameters also tend to be longer in order to leak out higher-order modes. Finally, we note that a larger number of bi-layers in the reflector will not reduce Bragg fiber material loss as the number of bi-layers mostly affects the modal radiation loss, which is already smaller than the material loss. On the other hand, thicknesses of the individual layers in a Bragg reflector can be optimized to reduce the overall modal loss, however, fabrication of such layers with optimized thicknesses would require finer resolution of the additive manufacturing systems.

The band diagram in Fig. 4.1(b) also features an undesired surface state at the core/reflector interface with dispersion relation intersecting the fundamental mode one within the photonic bandgap. The field distribution of this surface state, however, is mostly localized in the reflector region (see Fig. 4.1(c) II) and overlaps only slightly with that of the fundamental core-guided mode (see Fig. 4.1(c) I), thus being largely irrelevant for the Bragg waveguide operation. In principle, such undesired surface states can be suppressed by the design of the first few layers of the Bragg reflector.

4.2.2 Hollow-core Bragg waveguide with a defect in the reflector

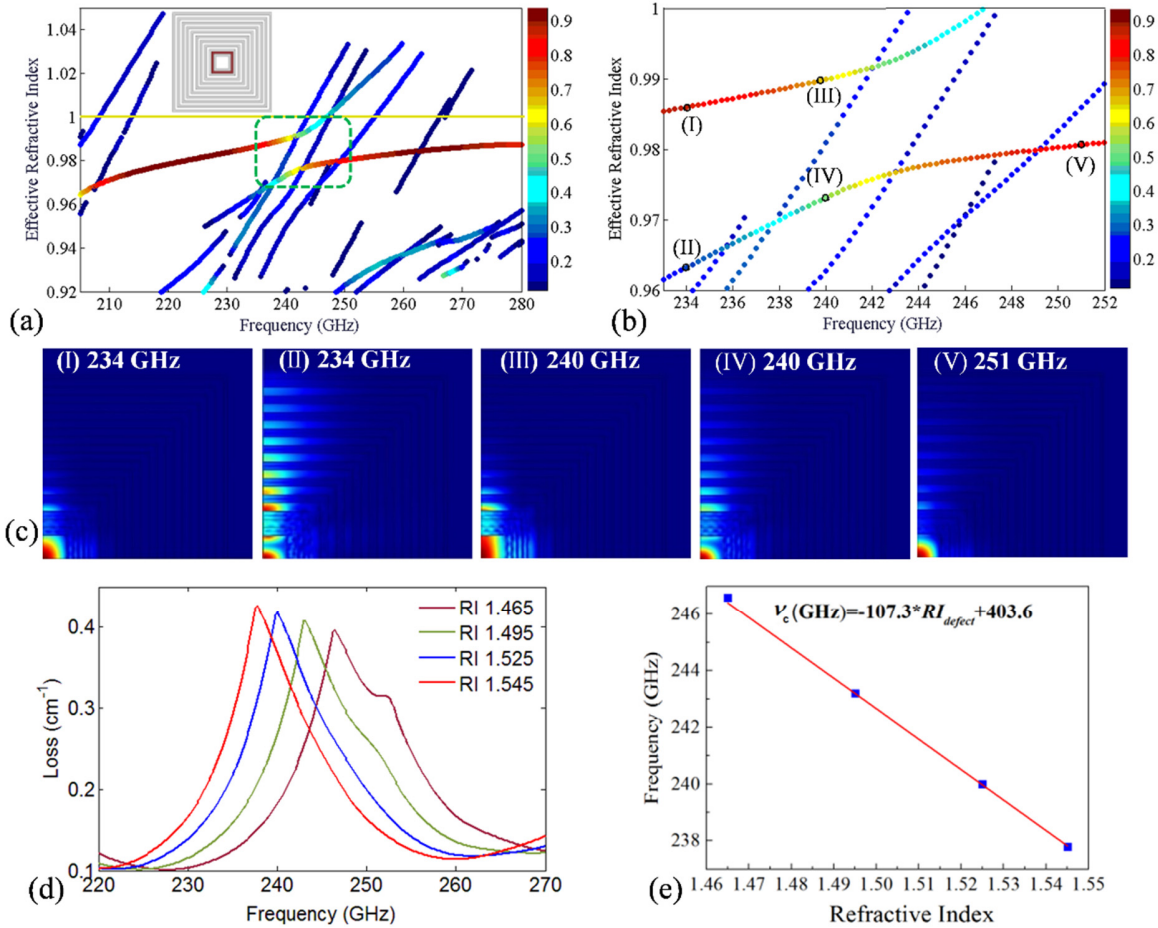


Figure 4.2 Numerical simulation of THz PBG Bragg waveguide with a defect in the reflector

(a) Band diagram of the hollow-core Bragg waveguide with a defect in the reflector second layer. The color scale defines the fraction of the modal power confined to the waveguide core. Only the modes with over 10% of power guided in the core are presented. Inset: schematic of the cross section of a Bragg waveguide with a defect. Red color indicates the position of the first air layer filled with liquid analyte. (b) A zoom into the spectral region of anticrossing between dispersion relations of the fundamental and the defect-guided modes. (c) Field distributions corresponding to the two hybridized modes in the anticrossing region (only a quarter of the computation cell is shown). Insets I, V and II show the core mode and the defect mode at the edges of the anticrossing region, where modal hybridization is small. Insets III and IV show the two

hybridized modes at the center of the anticrossing region. (d) The total transmission loss of the fundamental (lowest loss) mode propagating through the Bragg waveguides with a defect, for various values of the defect RI. The frequency with the highest loss of the fundamental mode approximately corresponds to the frequency of phase matching between the core-guided and defect modes (mid-range of the anticrossing spectral region). (e) Relation between the RI of the defect layer and the frequency with the highest loss (anticrossing frequency). The red line is a linear fit of the numerical data. Theoretical sensitivity deduced from the line slope is 107.3 GHz/RIU.

Next, we perform numerical studies of a Bragg waveguide with a defect in its reflector structure. Particularly, the RI of the air layer closest to the waveguide core is increased to 1.525, which corresponds to the RI of a typical analyte used in our experiments. Due to anticrossing of the dispersion relations of the core-guided and the defect-bound modes, the waveguide band diagram (Fig. 4.2(a)) is significantly different from the one for the waveguide with no defect (Fig. 4.1(b)). In the anticrossing region, the two modes are strongly hybridized with the modal fields of the resultant supermodes presenting both in the hollow core and in the defect layer (Figs. 4.2(b) and 4.2(c) III, IV), while at the edges of the anticrossing region, the supermodes have a predominant concentration of their fields either in the hollow core (Figs. 4.2(b) and 4.2(c) I, V) or in the defect layer (Figs. 4.2(b) and 4.2(c) II).

Moreover, transmission losses of the supermodes increase strongly inside of the anticrossing region as in this spectral region the low-loss hollow core-bound mode is strongly hybridized with a much lossy and tightly confined leaky mode that is bound to the defect layer. Experimentally, this leads to a sharp increase of the waveguide propagation losses inside of the anticrossing region. Theoretically, this phenomenon can be visualized by plotting spectral losses of the lowest-loss mode with effective RI smaller than one, which also happens to be the mode with the highest field presence in the waveguide core (see Fig. 4.2(d)). The resultant loss curve features a sharp loss peak whose spectral position corresponds to the center frequency of the anticrossing region (the frequency at which the difference between propagation constants of the two supermodes is smallest). Furthermore, similar loss curves can be plotted for various values of the defect RI (see Fig. 4.2(d)), from which it follows that the spectral position of the loss peak is highly sensitive to the real value of the defect RI and it moves towards lower frequencies for higher values of the

defect RI. When plotting the peak spectral position as a function of the defect layer RI, one finds a linear dependence between these two parameters in the whole operational range of the sensor (frequencies in the waveguide bandgap) (see Fig. 4.2(e)). The sensitivity of thus defined Bragg waveguide-based sensor is calculated as 107.3 GHz/RIU, while the spectral width of the loss peaks (defined as the full width at half maximum) is over 10 GHz, which is easy to resolve using both THz TDS and CW-THz setups.

4.3 Fabrication of the hollow-core THz Bragg waveguides using FDM and SLA techniques

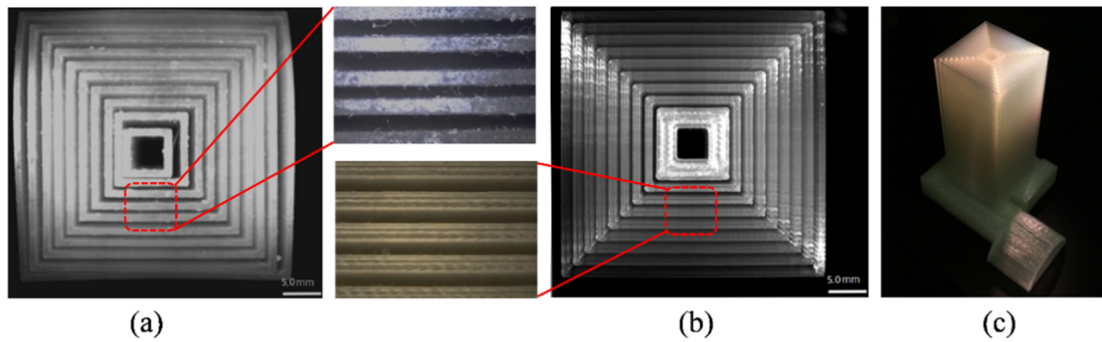


Figure 4.3 Photos of 3D printed THz PBG Bragg waveguide

(a) The cross section of the 3D-printed Bragg waveguide-based sensor fabricated using SLA and photosensitive resin. The structure is shown without the cover sheet that is used to seal the gap (defect) between the first and the second resin layers. (Dotted red region) The enlarged view of the reflector multilayers features layers of variable thickness and inconsistent periods. (b) The cross section of a 3D-printed Bragg waveguide-based sensor (FDM, PLA) with a cover sheet that seals the air gap of a defect layer. (Dotted red region) The enlarged view of the reflector multilayers features a well-defined structure with consistent period and layer thickness. (c) A 3D-printed (FDM, PLA) hollow-core Bragg waveguide-based THz fluidic sensor that includes a waveguide with a defect, and a fluidic delivery system.

Among various fabrication techniques, 3D printing technology has been proven to be an effective method for the fabrication of THz waveguides and guided wave components. A number of plastic THz optical components fabricated by SLA and FDM 3D printing technologies have been recently

reported [57, 100, 115, 116, 198, 199]. In the SLA, the photosensitive resin is cured layer by layer using spatially modulated UV radiation at the build plane. In the FDM, the plastic filament is first softened and then extruded through a nozzle as it is displaced in space to build the desired structure layer by layer. Within the FDM approach, the geometrical precision of the printed models as well as the roughness of its features are mainly decided by the nozzle size which is, typically, much larger ($\sim 200 - 400 \mu\text{m}$) than the beam spot of the UV laser used in the SLA ($10 - 50 \mu\text{m}$). Therefore, when higher resolution (smaller roughness) is required, one normally resorts to SLA, while FDM is rather used for rapid prototyping of coarse models. At the same time, FDM single material print can be used as is, while SLA prints require removal of the unreacted photosensitive resin (normally using isopropanol), as well as final UV curing of the remaining prints. The postprocessing of SLA prints with solvents can cause significant problems due to surface tension effects when printing porous structures or long slender channels. As our waveguides contain multiple air channels in their reflector, we used both FDM and SLA techniques for their fabrication in order to compare these two methods.

In this work the main challenge was a single-shot fabrication of the whole waveguide structure that includes both the fluidic part and a relatively long (10 cm or more) waveguide. Such a long waveguide length is required to realize an effectively single-mode guidance regime where a single Gaussian-like core-bound mode with the lowest modal transmission loss dominates. In such a waveguide, higher-order modes characterized by higher modal losses would either radiate out or be attenuated before reaching the waveguide end, thus having a negligible effect on the measured transmission spectrum. Our theoretical simulations show that at the bandgap center frequency of 235 GHz, the two lowest-loss core-bound modes (fundamental and a higher-order one) have the corresponding losses of $\alpha_f = 12.845 \text{ m}^{-1}$ and $\alpha_h = 24.707 \text{ m}^{-1}$. Therefore, effectively single-mode guidance regime can be realized by choosing waveguide length longer than $L_w > 1/(\alpha_h - \alpha_f) = 8.3 \text{ cm}$. Inspired by our prior work, we first attempted a 10-cm long Bragg waveguide fabrication using the SLA technique (ASIGA Pro 2 with PlasClear photosensitive resin) with the result shown in Fig. 4.3(a). For comparison, we also used FDM with PLA filament (MakerBot Replicator) to fabricate the same structure (see Figs. 4.3(b) and 4.3(c)).

When comparing the two prints we observe that the resultant structure of the waveguide fabricated using SLA is inferior to the one fabricated using FDM mainly due to the resin being much softer

and pliable compared to PLA. As a result, the relative position of the printed resin layers separated by air gaps is easily affected by even small internal stresses during manufacturing and postprocessing, as well as external stresses when handling. In addition, as postprocessing, we used the isopropanol washing followed by the airflow drying to remove the uncured resin that fills voids in the fabricated model. The uncontrollable effects of the surface tension during washing as well as apparent swelling of the resin when exposed to the washing agent have a significant effect on the internal porous structure of a long Bragg waveguide, thus resulting in pronounced dislocations and deformations of the individual resin layers. As observed under the microscope, the thicknesses of the resin layers and the air gaps in a cleaned structure vary between 0.7 and 1.0 mm, whereas both layer thickness in the printed structure before resin removal is around the designed 0.8 mm. Therefore, the standard cleaning process with isopropanol used in SLA printing results in a high degree of structural nonuniformity in long and highly porous Bragg waveguides studied in this work, thus limiting the utility of this postprocessing method to fabrication of shorter several-cm-long waveguides [100]. As a result, due to significant variations in the geometry of the printed Bragg reflector from that of the theoretical one, SLA printed waveguides after cleaning show relatively small and shallow bandgaps, while the anticrossing resonant phenomenon is not observed at all as both rely on light interference within waveguide structural elements and require precise geometry for the defect layer and the Bragg reflector layers. As structural element definition is considerably more precise in the shorter several-cm-long SLA printed waveguides (see [100], for example), in principle, longer waveguides can be constructed by joining together smaller SLA-printed sections. Finally, due to the challenges associated with the extraction of the unreacted resin from the waveguide porous structure, the sensor could not be printed as a single piece and it requires post-printing assembly of at least four components (the waveguide, fluidic conduits, and a cover sheet).

Next, we have attempted a single-step fabrication of the Bragg waveguide-based fluidic sensors using the FDM technique with a PLA filament. Compared to the Asiga Pro 2 SLA printer that offers z-axis resolution of 10 μm and x-y axis resolution of 50 μm , the FDM Makerbot Replicator printer offers 100 μm resolution along the z-axis and 400 μm resolution along the x-y axis. At the same time, the PLA material used in FDM is more rigid than the resin used in SLA, and the whole sensor structure can be printed in a single run without the need for any postprocessing. As a result,

while the structures created using FDM feature rougher surfaces and potentially higher scattering losses, at the same time, relative rigidity of the PLA material and the lack of post-processing result in highly repeatable Bragg waveguide-based sensors with well-defined geometries (see Fig. 4.3(b)). Particularly, we find that the FDM Bragg reflectors consistently feature PLA layer and air gap thicknesses in the range of 0.75 – 0.85 mm compared to the designed 0.8 mm. Additionally, unlike the corresponding SLA fabricated structures, the FDM fabricated hollow-core Bragg waveguides feature deeper bandgaps and anticrossing resonant phenomenon when the liquid analyte is placed into the first air gap.

Theoretically, the linewidth of the absorption peak caused by the anticrossing phenomenon is decided by the degree of the field overlap between the core-guided and defect modes. In principle, to achieve higher sensing resolution, it is desirable to reduce the spectral width of the absorption peak, which can be achieved by placing the defect in the Bragg reflector (liquid analyte-filled air gap) further away from the hollow core [100]. Thus, according to our simulations, when the defect layer is moved from the first to the second air gap, the spectral width of the loss peak (defined as the full width at half maximum) induced by the anticrossing resonant phenomenon decreases from ~10 GHz to ~5 GHz, while a further reduction in the peak width is possible by moving the defect layer farther away from the core. Experimentally, while the absorption peak is consistently and readily observable with a defect in the first layer, when moving the defect into the air gaps farther away from the core, it becomes harder to detect due to considerably less pronounced intensity variation. The decrease in the dip strength when placed into the farther air gaps can be explained by the variation in the reflector layer thicknesses and the scattering loss caused by the layer roughness, which are both known to reduce spatial coherence of the standing waves in the Bragg reflector that is needed for the manifestation of any resonant phenomenon (see detailed discussion of this phenomenon in [209]). These decoherence effects are more pronounced for sharper resonances that are expected when placing the defect layer farther away from the waveguide core.

4.4 Characterizing of the hollow-core THz Bragg waveguide-based sensors using CW-THz spectroscopy

In what follows, we study the hollow-core THz Bragg waveguide-based fluidic sensor with a defect in the first air gap of the Bragg reflector (analyte-filled air gap). In order to place the liquid analyte

into the defect layer, we have sealed the first air gap on both sides of a waveguide, while a fluidic conduit was placed into the gap to inject and maintain the flow of the liquid analyte through the channel (see Fig. 4.4(a)). In our experiments, different analytes were injected into the reflector gap, while optical measurements were performed in a static regime (no flow) with the defect layer being fully and slowly filled with the injected analyte starting from an empty system. The path of the liquid flow in the waveguide-based sensor is shown in Fig. 4.4(a). We have also verified in a separate experiment that the fluid occupied completely the gap space by using colorants and dissecting the model after filling and then draining the sensor structure.

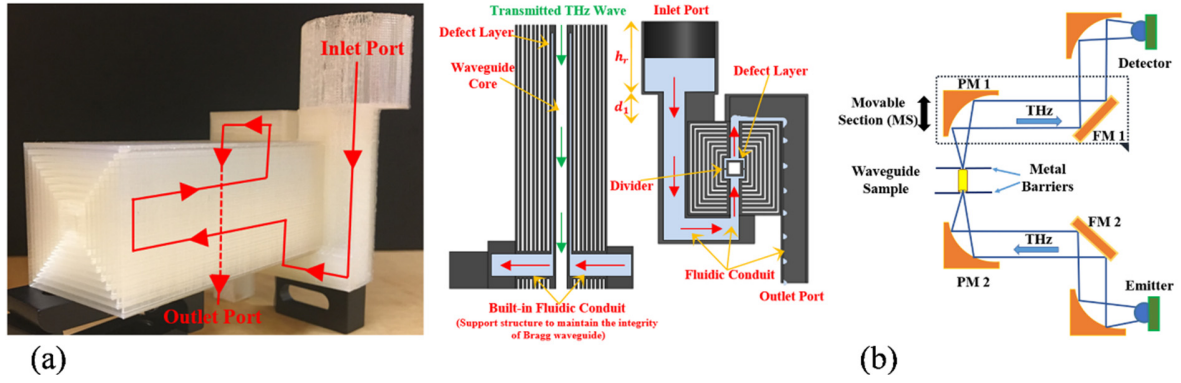


Figure 4.4 PBG Bragg waveguide-based THz fluidic sensor

(a) The fabricated hollow-core THz Bragg waveguide-based fluidic sensor and its schematics. In grey color — PLA material, in blue color — the liquid analyte, in white — air. Red arrows show the flow direction of the liquid analyte. Green arrows show the direction of THz propagation. (b) Schematic of the CW-THz spectroscopy system used to characterize the sensors.

Both the transmitted amplitude and phase spectra of the fabricated THz Bragg waveguide-based sensor (Fig. 4.3(c)) were studied by using the CW-THz spectroscopy system (TOPTICA Photonics) (Fig. 4.4(b)) [182, 184]. Transmitted THz spectra of the hollow-core THz Bragg waveguide sensors are measured in the following processes. First, the reference spectrum is recorded by placing a metallic aperture with an opening identical to that of the waveguide core at the joint focal point of the two parabolic mirrors PM1 and PM2 (see Fig. 4.4(b)). Note that PM1 and a flat mirror FM1 are both mounted onto a rail, and represent a movable section (MS) of the spectroscopy system, thus allowing measuring waveguides of various sizes, as well as a reference signal without a waveguide. Next, the Bragg waveguide is inserted with its input and output facets at the focal points

of PM1 and PM2 via adjusting the MS position. Additionally, two metallic apertures with opening identical to that of a hollow core are placed adjacent to both facets in order to block excitation of the cladding modes. Finally, the waveguide transmission amplitude and phase are extracted by comparing the measurements with and without (reference) a waveguide.

4.4.1 Choosing the optimal length of the hollow-core Bragg waveguide

Transmission spectra of the hollow-core Bragg waveguides depend strongly on the waveguide length. This is related to the well-known fact that large hollow-cores of most PBG waveguides support a large number of leaky modes that feature greatly different propagation losses. Thus, by choosing a long enough waveguide so that only the lowest-loss (fundamental) mode remains at the waveguide output end, one observes the well-defined transmission bandgaps. In contrast, for shorter waveguides, the contribution of the higher-loss modes remains important, which results in transmission bandgaps that tend to broaden and become shallow. Clearly though, when the waveguide is too long, transmission loss of the fundamental mode can be significant, thus resulting in the low signal-to-noise ratio. Therefore, ideally, the hollow-core Bragg waveguide has to be long enough to result in effective single-mode guidance, while not too long in order to avoid excessive transmission loss. Therefore, we first studied the optimal size of the hollow-core THz Bragg waveguide to be used in our sensors.

In Fig. 4.5(a), we plot the normalized transmission loss spectra (by field) for the PBG Bragg waveguides with the lengths of 5 cm, 7.5 cm, 10 cm, and 12.5 cm as:

$$Loss(\nu) = 10 \cdot \log_{10}(T_{\text{waveguide}}(\nu) / T_{\text{ref}}(\nu)) \quad (4.1)$$

From this data, we see that the photonic bandgap spectral position (frequencies of the transmission maximum ~ 230 GHz and the two adjacent minima at ~ 200 GHz and ~ 280 GHz), as well as its spectral shape stabilizes for waveguides of 10 cm and longer.

Furthermore, in the transmission data, we also see intensity ripples superimposed onto the waveguide transmission spectra. In fact, there are two sets of ripples, one is caused by the multiple reflections inside of the two silicon lenses (size $d \sim 10$ mm, $n_{\text{Si}} \sim 3.42$ [38]) that are integrated into the THz photomixers in the emission and detection arms of our setup. The corresponding frequency of these ripples is:

$$\Delta\nu_1 = \frac{c}{2dn_{si}} \sim 4 \text{ GHz} \quad (4.2)$$

Another set of ripples with higher frequencies is due to standing waves excited in the spectrometer cavity of length $L \approx 80$ cm (distance between the detector and emitter) with the characteristic frequency of:

$$\Delta\nu_2 = \frac{c}{2Ln_{cavity}} \sim 0.2 \text{ GHz} \quad (4.3)$$

In Fig. 4.5(b), we present Fourier transform into time domain $T(t)$ of the measured transmission spectra $T_{ref}(\nu)$ of an empty system (reference):

$$T_{ref}(t) = \int T_{ref}(\nu) * \exp(-i\nu t) d\nu \quad (4.4)$$

$$T_{ref}(\nu) = \int T_{ref}(t) * \exp(i\nu t) dt \quad (4.5)$$

The FFT shows clearly the presence of five peaks, one at $t=0$, and four others at $\pm t_1$ and $\pm t_2$ respectively. This means that the transmission spectrum contains among other frequencies the two sinusoidal contributions that define spectral ripples as:

$$T_{ref}(\nu) = T_0 + T_1 \cos(\nu t_1 + \varphi_1) + T_2 \cos(\nu t_2 + \varphi_2) + \dots \quad (4.6)$$

From Eq. 4.6 we thus find two characteristic ripple frequencies, one associated with standing waves inside silicon lenses as:

$$\Delta\nu_1 = \frac{2\pi}{t_1} \sim 4 \text{ GHz} \quad (4.7)$$

while another one corresponding to the standing waves in the spectrometer cavity as:

$$\Delta\nu_2 = \frac{2\pi}{t_2} \sim 0.2 \text{ GHz} \quad (4.8)$$

Although the intensity of these spectral oscillations can be somewhat mitigated by normalizing with respect to the reference, even the normalized data features spectral ripples that ultimately limit the sensor resolution.

Next, we study the spectral shape of the transmission dip due to enhanced absorption as a function of the Bragg waveguide length when introducing a defect into the structure of a Bragg reflector. In

Fig. 4.5(c), we present transmission spectra through waveguides of different lengths with the first air gap filled with mineral oil of $n_{oil} \sim 1.455$. The spectra are normalized with respect to the transmission spectra of the corresponding waveguides but without an analyte (empty sensor). Similar to the case of a waveguide without defect (Fig. 4.5(a)), we observe that the shape of the absorption peak (transmission dip), its depth and spectral position, stabilize for the waveguides longer than 10 cm.

Finally, we note that the volume of the analyte filling the first gap is estimated as ~ 2 mL.

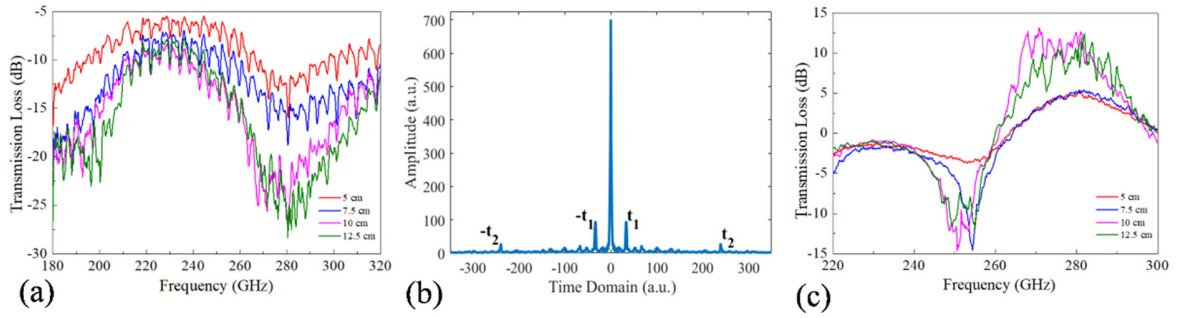


Figure 4.5 Spectral performance of THz PBG Bragg waveguides with different lengths

(a) Normalized transmission spectra of the FDM fabricated hollow-core Bragg waveguides (no defect) featuring different lengths. Normalization is with respect to the transmission spectra of the empty system. (b) Fourier transform of the measured transmission spectrum through the empty spectrometer (reference). (c) Resonant absorption enhancement (transmission dip) due to anticrossing phenomenon between the core-guided mode and a reflector defect state when filling the first air gap of the Bragg waveguide with a liquid analyte. Different transmission spectra are for waveguides (with a defect) of different lengths. Normalization is with respect to the transmission spectra of a waveguide of the same length without a defect (no analyte).

4.5 The performance of the THz PBG Bragg waveguide-based fluidic sensor

In this section, we characterize sensitivities of our THz fluidic sensors using mixtures of oils with RI in the range between 1.465 and 1.545 as liquid analytes. Firstly, the RIs of the mineral oil (Johnson & Johnson Inc) and cinnamon essential oil (Simply Essentials, Walmart Inc) were measured as 1.455 and 1.555 using a THz TDS system in a cutback configuration [207, 208]. Then, nine sets of liquid analytes with RI of 1.465, 1.475, 1.485, 1.495, 1.505, 1.515, 1.525, 1.535, and

1.545 were prepared by mixing thoroughly these two kinds of oils with volume ratios of 9:1, 8:2, 7:3, 6:4, 5:5, 4:6, 3:7, 2:8, and 1:9 respectively. Finally, two sets of measurements were performed to characterize sensor sensitivity, one using amplitude detection modality and another using phase detection modality. In what follows, we use interchangeably the terms “transmission dip” and “absorption peak”, meaning that in the vicinity of the anticrossing frequency between the dispersion relations of the core-guided mode and the reflector defect state, increased modal loss (absorption peak) manifests itself as a dip the waveguide transmission spectrum (transmission dip).

4.5.1 Amplitude detection modality

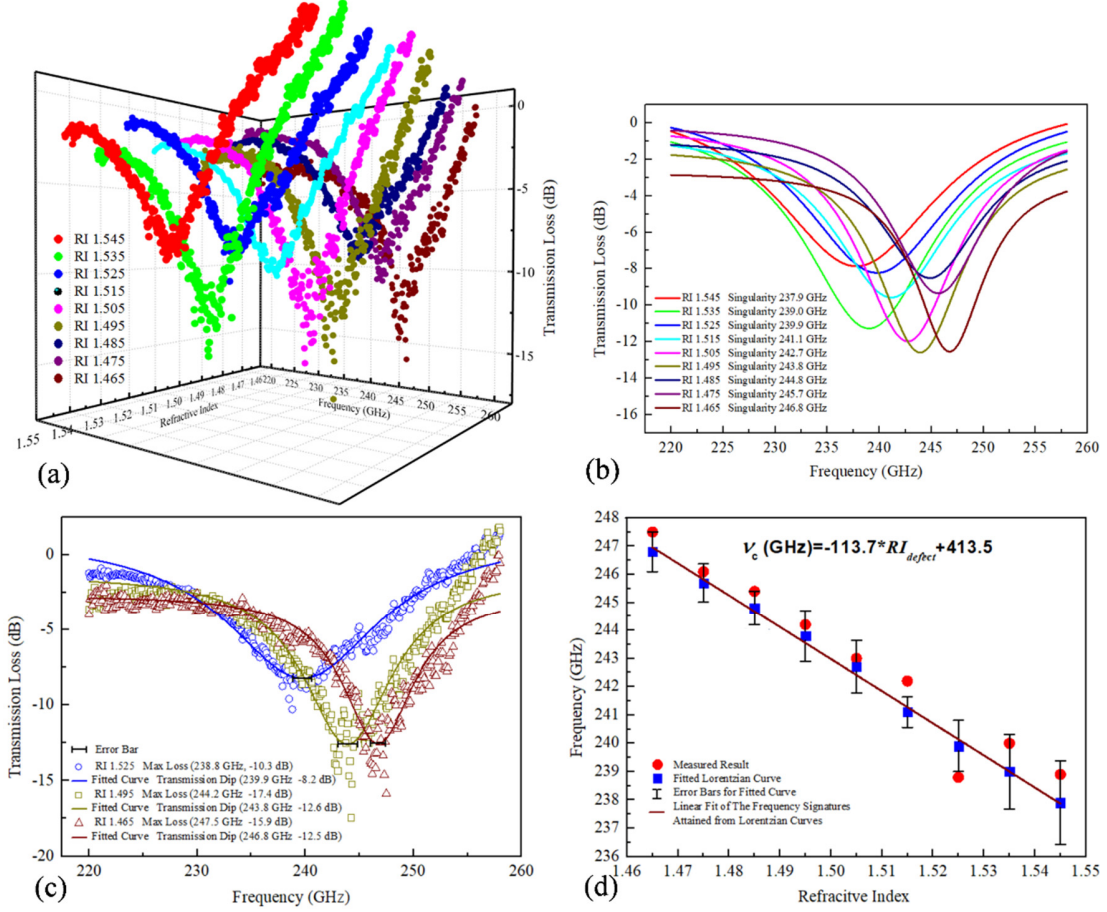


Figure 4.6 Sensing using amplitude detection modality

(a) Normalized transmission in the vicinity of absorption peak for different values of the analyte RI. (b) Lorentzian fit of the experimental curves. (c) Estimation of error in the position of a spectral dip using the mean square deviation of the Lorentzian fit and the raw data; shown are examples for the analyte refractive indices of 1.525, 1.495, and 1.465. (d) Dependence of the spectral position of the absorption peak on the analyte RI. Blue dots and error bars are computed using Lorentzian fitting curve and mean square error estimation. Red dots correspond to the maxima of the transmission losses.

In the first experiment, sensor sensitivity was deduced from the spectral position of the absorption peak (transmission dip) as detected from the normalized transmission spectra (by field) of the Bragg waveguide with an analyte-filled defect. To obtain a normalized spectrum, we have divided

the transmission spectrum of a waveguide with an analyte-filled gap (defect) by that of an empty waveguide (no analyte). In our measurements, we used 100 MHz frequency resolution. In Fig. 4.6(a), the raw normalized transmission data is presented in a 3D plot as:

$$T(\nu) = 10 \cdot \log_{10}(T_{\text{analyte}}(\nu) / T_{\text{empty}}(\nu)) \quad (4.9)$$

In Fig. 4.6(b), we present analytical fitting of the raw data using Lorentzian lineshapes:

$$T_L(\nu, \nu_c, \Delta\nu, A, T_0) = T_0 + A \frac{\Delta\nu}{4(\nu - \nu_c)^2 + \Delta\nu^2} \quad (4.10)$$

This is accomplished by minimizing the weighting function defined as a mean square error of the fit:

$$MSE(\nu_c, \Delta\nu, A, T_0) = \sum_{\nu_{\min}}^{\nu_{\max}} (T_L(\nu) - T_{\text{exp}}(\nu))^2 \quad (4.11)$$

Using data fitting with Lorentzian lineshapes allows efficient filtering of the spectral ripples from the raw normalized data, as well as to deduce spectral position ν_c and spectral width $\Delta\nu$ of the absorption peak. Particularly, we find that the spectral position of the absorption peak ν_c is strongly sensitive to the analyte RI by varying between 239.9 GHz – 246.8 GHz when changing RI in the 1.465 – 1.525 range. At the same time, the peak spectral widths $\Delta\nu$ also show some moderate variation between 10.1-13.7 GHz in the same range of the RIs. Experimentally measured peak positions and bandwidths are in good agreement with the results of theoretical simulations shown in Fig. 4.2.

Furthermore, comparing the raw data with its Lorentzian fit (Fig. 4.6(c)) also allows us to define the error in the definition of the absorption peak position. Numerically, the errors in the spectral dip position ($\pm\delta\nu_c$) can be found using the following definitions:

$$MSE(\nu_c, \Delta\nu, A, T_0) = \sum_{\nu_c - \text{dip width}/2}^{\nu_c + \text{dip width}/2} (T_L(\nu) - T_{\text{exp}}(\nu))^2 \quad (4.12)$$

$$MSE(\nu_c \pm \delta\nu_c, \Delta\nu, A, T_0) = (e-1) \cdot MSE(\nu_c, \Delta\nu, A, T_0) \quad (4.13)$$

The values of the absorption peak position (blue dots) as a function of the analyte RI, and the corresponding error bars are presented in Fig. 4.6(d), from which we observe that absorption peak moves to lower frequencies with increasing analyte RI. The average error in the peak position is

$\delta\nu_c \sim 0.9$ GHz, which is attributed to the noise due to standing wave resonances in the CW-THz spectroscopy system as described earlier in the paper. Additionally, in Fig. 4.6(d), for each value of the analyte RI, we plot the frequency of highest transmission loss (red dots) which can also be used as an alternative definition of the spectral position of the absorption peak. We note that the red dots generally fall within the error bars of the blue dots, thus indicating that the definition of the spectral position of an absorption peak based on fitting to Lorentzian lineshape is comparable in accuracy to the definition based on the highest transmission loss.

Finally, from Fig. 4.6(d), we conclude that the sensor response is linear with the value of the analyte RI with the corresponding sensitivity of $S=113.7$ GHz/RIU. Considering the ~ 50 GHz bandgap bandwidth and the ~ 12 GHz linewidth of the absorption peak, our sensor is able to detect liquid analytes with RI in the range between 1.4 and 1.8, which covers most of the common organic solvents and liquids for chemical and biological applications [210]. Sensor resolution using amplitude detection modality can be estimated from the average value of the error in the absorption peak position as:

$$\delta n = \delta\nu_c / S \sim 8.0 \cdot 10^{-3} \text{ RIU} \quad (4.14)$$

4.5.2 Phase detection modality

In the second experiment, sensor sensitivity was deduced from the spectral position of the anticrossing frequency between the core mode of a Bragg waveguide and a mode of an analyte-filled defect as deduced from the rapid change in the phase of transmitted light. The phase was retrieved from the complex normalized transmission spectrum (by field) obtained by dividing the transmission spectrum of a waveguide with an analyte-filled gap (defect) by that of an empty waveguide (no analyte). In our measurements, we used 100 MHz frequency resolution. In Fig. 4.7(a), the raw phase data is presented in a 3D plot. In Fig. 4.7(b), we present analytical fitting of the raw data using sigmoid lineshape:

$$\varphi(\nu, \nu_c, \Delta\nu, \varphi_0, \Delta\varphi) = \varphi_0 + \frac{\Delta\varphi}{1 + \exp(\frac{\nu - \nu_c}{\Delta\nu})} \quad (4.15)$$

which allows us to deduce the spectral width of the anticrossing region $\Delta\nu$ and the anticrossing frequency ν_c . This is accomplished by minimizing the weighting function defined as a mean square error of the fit similarly to Eq. 4.11. Spectral bandwidth of the anticrossing region is found to be weakly dependent on the analyte RI and equal to $\Delta\nu \sim 2$ GHz, which is significantly smaller than the 12GHz-spectral width of a resonant dip as defined using the amplitude-based methodology. Thus deduced anticrossing frequency ν_c generally corresponds to the anticrossing region midpoint frequency at which both modes that participate in anticrossing are equally excited in the waveguide core (see Fig. 4.2(b)). Sensor phase response has a narrow bandwidth because it involves a sudden change in the dominant mode effective refractive index when going through the anticrossing region. Particularly, while approaching the anticrossing region from lower frequencies, the light is propagating predominantly in a single core-guided mode 1 of refractive index n_1 . In the anticrossing region, two modes with similar refractive indices are excited, and the overall phase response of a sensor is a function of both the individual mode effective refractive indices, as well as relative powers in the two modes. Finally, at higher frequencies, the light is again predominantly propagating in a single core-guided mode 2 with refractive index n_2 that can be significantly different from n_1 , which is the reason for a step-like shape of the sensor phase response.

Furthermore, similarly to Eqs. 4.12 and 4.13, comparing the raw data with its fits using sigmoid lineshapes (Fig. 4.7(c)) allows us to define the error $\pm\delta\nu_c$ in the position of the anticrossing frequency. In Fig. 4.7(d), we present the value of the anticrossing frequency (blue dots) as a function of the analyte RI, and the corresponding error bars. The average error in the anticrossing frequency is found to be $\delta\nu_c \sim 0.5$ GHz, which is almost twice as small as in the case of amplitude-based detection described in the previous section. We attribute this to the fact that negative effects of the standing wave oscillations in a CW-THz system are more efficiently mitigated when working with a normalized signal phase rather than a normalized signal amplitude. This is also confirmed by comparing the quality of the raw data and its fits using the amplitude-based detection (Fig. 4.6(c)) with those of the phase-based detection (Fig. 4.7(c)), with a phase-based approach showing considerably smaller data spread and fit errors than the amplitude-based one.

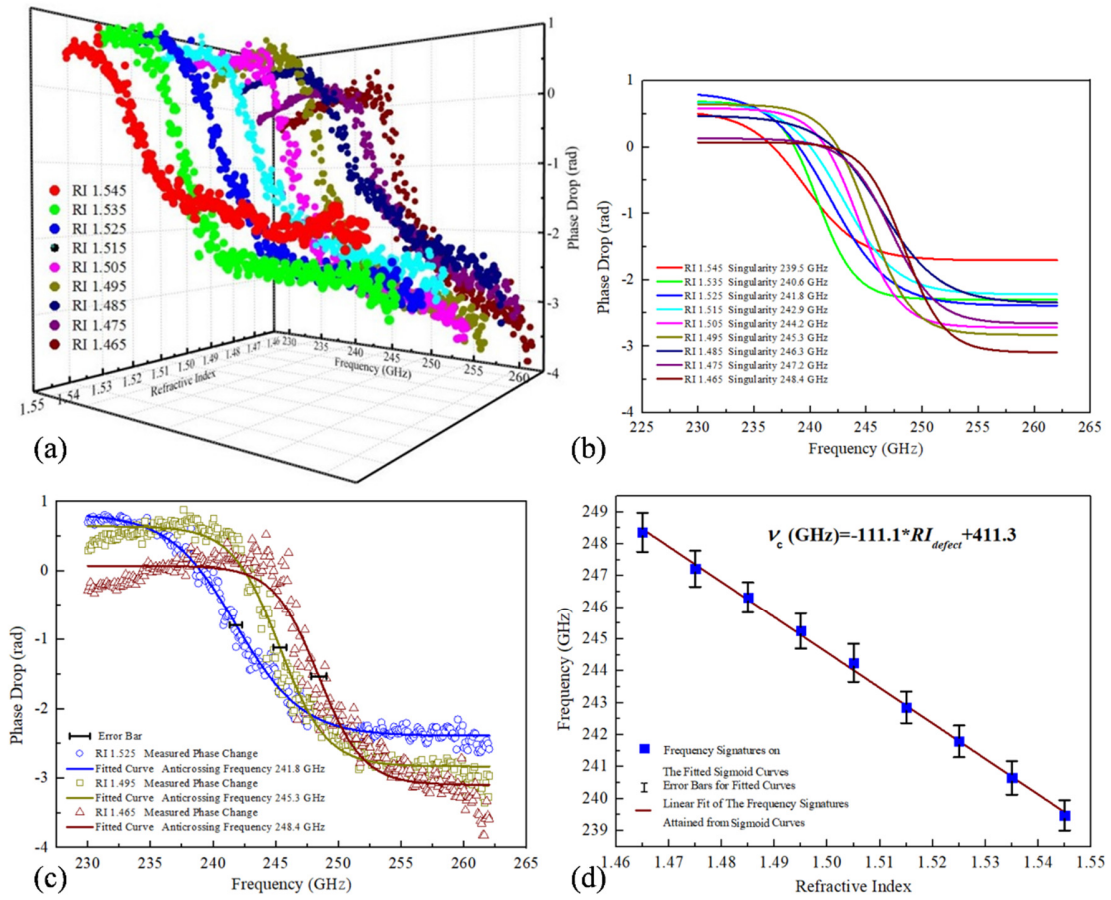


Figure 4.7 Sensing using phase detection modality

(a) Phase dependence extracted from the complex normalized transmission in the vicinity of the absorption peak (anticrossing frequency) for analytes featuring different values of RIs. (b) Sigmoid fit of the experimental curves. (c) Estimation of error in the position of the anticrossing frequency using mean square deviation of the Sigmoid fit and the raw data; shown are examples for the analyte refractive indices of 1.525, 1.495, and 1.465. (d) Dependence of the anticrossing frequency on the analyte RI. Blue dots and error bars are computed using Sigmoid fitting curve and a mean square error estimation.

Finally, from Fig. 4.7(d) we conclude that the sensor response is linear with the value of the analyte RI with the corresponding sensitivity of $S=111.1 \text{ GHz/RIU}$, which is almost identical to that of the amplitude-based detection method. At the same time, sensor resolution using phase detection modality is superior to that of the amplitude detection modality and can be estimated as:

$$\delta n = \delta v_c / S \sim 4.5 \cdot 10^{-3} \text{ RIU} \quad (4.16)$$

4.5.3 Real-time RI monitoring using fluidic sensor

In this section, we discuss applications of the proposed resonant fluidic sensor in real-time monitoring of the fluid RI in motion. All the measurements presented so far were conducted in a static regime in which different analytes (oils with calibrated RIs) were slowly loaded into an empty sensor. Moreover, we have ensured that the analytes occupied all the volume in a defect layer by referencing it to the volume of the used oil. Additionally, we have dissected several waveguides after following this filling procedure using oil with a colorant and observed that the inner surfaces of all the conduits and a sensing layer were colored. When using fluidic sensors for real-time monitoring of flowing liquids, one has to ensure that the analyte liquid injected from the inlet opening flows through the whole sensing layer channel before arriving at the outlet. This can be accomplished by placing into the channel two square dividers of sizes equal to that of the air gap and lengths slightly smaller than the waveguide length in order to force the fluid to go through the whole length of a waveguide and back, rather than choosing the shortest distance between the inlet and outlet openings of a sensing layer (see Fig. 4.4(a)). In this design, the total effective length of a fluidic channel in the sensing layer (along the x-axis) is $L_c = 17.4$ cm, the effective channel width is $W_c = 1.3$ cm, while the channel height is $D_c = 0.8$ mm (air gap size), with the total sensor channel volume $V_c \sim 1.81 \text{ cm}^3$. The sensor is fed from a semi-cylinder-shaped fluid reservoir of height $h_r = 2.6$ cm and base area $A_r = 4 \text{ cm}^2$, which is connected to the inlet opening of a sensing channel via a square cross-section conduit of height $d_l = 1.1$ cm located below the reservoir but above the level of the output fluidic port.

In the following experiments, we used the time-dependent hydrostatic pressure of the fluid column of the total height $h(t) + d_l$ ($h(t)$ is the height of liquid in the reservoir $0 < h(t) < h_r$ at the time t) to drive the analyte flow through the sensing layer. The density of the liquid analyte (Blandol and Carnation white oil mixture) is measured as $\rho = 857 \text{ kg/m}^3$ and viscosity is $\mu = 0.012 \text{ Pa}\cdot\text{s}$.

The flow is purely gravity driven with the time-dependent hydrostatic pressure $P(h(t)) = \rho g(h(t) + d_l)$ and assumed as laminar and viscosity-driven ($Re \ll 1$), we use the well-known expression for fluid velocity profile of creeping flow in parallel plate geometry (along the Y-direction) [211]:

$$v(y, h) = \frac{\rho g (h + d_1)}{2\mu L_c} y (D_c - y) \quad (4.17)$$

Further using the electric-hydraulic analogy, we define a pressure - flow rate relationship in the form of $P(h(t)) = R_{hyd} \cdot Q(h(t))$ [212], where:

$$R_{hyd} = \frac{12\mu}{D_c^3} \cdot \frac{L_c}{W_c} \quad (4.18)$$

is the channel hydraulic resistance, which for our system is estimated as $R_{hyd}^{th} \sim 3.8 \text{ kPa} \cdot \text{s/mL}$. Assuming that the liquid is incompressible, and using Eq. 4.18 along with a mass balance between the reservoir and main channel, we can find the dependence of the liquid height in the reservoir as a function of time:

$$-A_r \frac{dh}{dt} = Q(h) = \frac{\rho g (h + d_1)}{R_{hyd}} \quad (4.19)$$

Furthermore, assuming that the reservoir is completely filled at the beginning of the measurement $h(0) = h_r$, Eq. 4.19 has the following exponential solution:

$$h(t) = (h_r + d_1) \cdot \exp\left(-\frac{\rho g}{A_r R_{hyd}} t\right) - d_1 \quad (4.20)$$

$$Q(h) = \frac{\rho g (h_r + d_1)}{R_{hyd}} \cdot \exp\left(-\frac{\rho g}{A_r R_{hyd}} t\right) \quad (4.21)$$

that are valid for $0 < h(t) < h_r$. From Eq. 4.20 we can relate the reservoir voiding time t_r to the channel hydraulic resistance R_{hyd} as:

$$h(t_r) = 0 \rightarrow t_r = \frac{A_r R_{hyd}}{\rho g} \cdot \ln\left(1 + \frac{h_r}{d_1}\right) \quad (4.22)$$

Using the values of geometrical and material parameters presented above, we now find the theoretical estimate of the reservoir voiding time $t_r = 211 \text{ s}$.

Additionally, when operating a sensor with a fully filled reservoir, the filling time of a sensing layer can be estimated as:

$$t_s = \frac{R_{hyd} V_c}{\rho g (h_0 + d_1)} = \frac{12\mu}{\rho g (h_0 + d_1)} \cdot \left(\frac{L_c}{D_c}\right)^2 \sim 21 \text{ s} \quad (4.23)$$

which is also comparable to the scanning time $\sim 10\text{--}30$ s (depending on the resolution and averaging constant) of our CW spectroscopy system over the spectral range covered by the Bragg waveguide bandgap. Note that the filling time of a sensing layer as defined by Eq. 4.23 does not depend on the channel width but rather on the ratio of the channel length to the channel size. This time can also be considered as a characteristic response time of the sensor under continuous non-forced (no external pressure) liquid flow. This means that if the RI of an analyte at the input port of a sensing channel is suddenly changed to another value, the sensor spectral response will stabilize to a new reading after $\sim t_s$. Experimentally, sensor response time can be measured by simply introducing a new analyte into the reservoir and then marking the time it takes the sensor to stabilize to a new reading after changes start appearing in the sensor spectral response.

Finally, the maximum Reynolds number $Re = \rho UL_{ch}/\mu$ for the liquid flow within the sensing channel can be computed. We use the highest possible flow rate value (full reservoir) to compute the characteristic velocity $U \sim Q_{max}L_c/V_c$ in conjunction with the well-known characteristic length $L_{ch} \sim D_c^2/L_c$ for creeping flows in the elongated channel [212]. For the current design, the maximum Reynolds number within the sensing channel gives:

$$Re_{max} = \frac{\rho \frac{Q_{max}}{V_c} L_c \frac{D_c^2}{L_c}}{\mu} \sim 0.002 \quad (4.24)$$

which validates our initial creeping flow assumption.

Next, we experimentally measure the voiding time of the analyte reservoir, as well as sensor response time in order to verify if the channel volume used by the liquid flow corresponds to that of the physical volume of a sensor. This is important as sensor response time and its sensitivity will be directly affected by the speed and extent to which a new analyte could substitute the old analyte already present in the waveguide structure. In particular, we compare the performance of the two sensors, one using a divider as shown in Fig. 4.4(a), while another without a divider. While both sensors have a virtually identical optical response in the static regime (no liquid flow during measurement), they behave rather distinctly in the dynamic regime.

For a sensor without a divider, the reservoir voiding time is found to be $t_r^{no\ div} \sim 30$ s, which is seven times smaller than the theoretical one $t_r = 211$ s. Furthermore, using experimentally measured value

of the reservoir voiding time together with Eq. 4.22, we can find the channel hydraulic resistance $R_{hyd}^{no\ div} \sim 0.5 \text{ kPa}\cdot\text{s/mL}$, which is much smaller than the value derived from the theoretical analysis $R_{hyd}^{th} \sim 3.8 \text{ kPa}\cdot\text{s/mL}$. From the definition of the R_{hyd} we find that for a channel without a divider the effective channel aspect ratio $(L_c/W_c)^{no\ div} \sim 1.9$, which is much smaller than the geometrical value of $L_c/W_c \sim 13.4$. This indicates that in a sensor without a divider the liquid flows along the shortest path from the inlet to the outlet mostly perpendicularly to the waveguide rather than along its length. As a result, when attempting measurement of the sensor dynamic response, instead of the theoretically predicted $t_s = 21 \text{ s}$, it takes the sensor without a divider $t_s^{no\ div} \sim 3\text{--}5 \text{ min}$ to stabilize to a new value indicating that the flow of a new analyte does not efficiently displace the old analyte from the sensing channel.

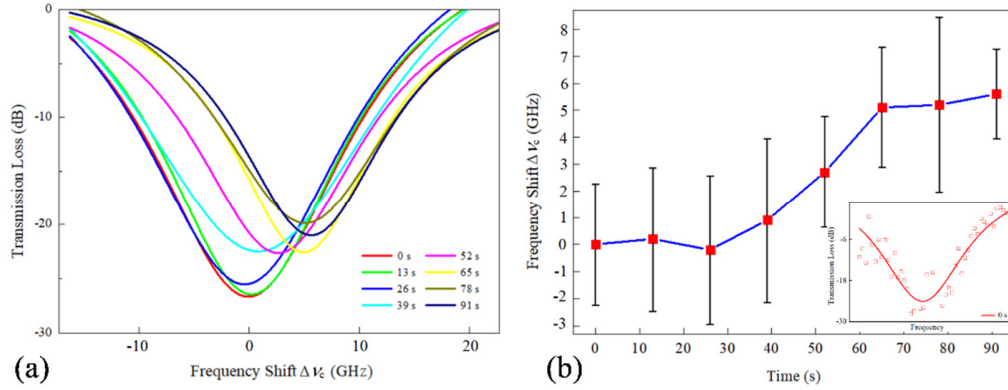


Figure 4.8 Real-time monitoring analyte RI change using PBG Bragg waveguide-based sensor

(a) Lorentzian fits of the time-dependent normalized transmission spectra of a sensor during displacement of an old analyte with RI of 1.505 with a new one with RI of 1.455 in the sensing layer. (b) Corresponding time dependence of the spectral position of the absorption peak. Error bars are computed by using the mean square deviation of the Lorentzian fits of the raw data.

Inset: example of the raw data and the corresponding Lorentzian fit at 0 s.

In contrast, for a sensor with dividers, the voiding time of the reservoir is measured as $t_r^{div} \sim 195 \text{ s}$, while channel hydraulic resistance is found as $R_{hyd}^{div} \sim 3.4 \text{ kPa}\cdot\text{s/mL}$, which both agree closely with the theoretically estimated ones. Finally, when performing dynamic spectral measurement by introducing the analyte of a distinct RI into the sensor reservoir, it takes $t_s^{div} \sim 30 \text{ s}$ for the sensor spectral response to stabilize (see Fig. 4.8), which agrees well with the theoretically predicted value

of $t_s=21$ s. A somewhat larger value of the sensor response time can be due to the inherent latency of the CW spectroscopy system that uses lock-in acquisition and data integration can add an additional 10—30 s to the response time depending on the spectral resolution of a scan. Additionally, further optimization of the fluidic design is necessary to make sensor operation more consistent and reliable. Namely, due to very low rates of the gravitationally driven fluid flow, the output port of a relatively large size ($0.84\text{ cm} \times 0.84\text{ cm}$) is largely empty (see Fig. 4.4(a) right) with droplets forming on the port inner walls. Therefore, the hydrostatic pressure taken as $\rho g(h+d_l)$ can be somewhat different from this value as the d_l parameter can vary by several mm due to dynamic droplet formation and the fluid outlet. As the d_l parameter is used to relate the experimentally measured reservoir voiding time to the channel resistance, we expect that the values of the channel resistance and estimates for the channel filling times can also be affected.

4.6 Conclusion

In this work, a 3D printed THz Bragg waveguide-based resonant fluidic sensor has been investigated theoretically and experimentally. The sensor features a sealed fluidic channel placed into the reflector of a 10cm-long hollow-core Bragg waveguide, and it is fabricated in a single step using a low-resolution ($400\text{ }\mu\text{m}$ in X-Y, $200\text{ }\mu\text{m}$ in Z) FDM printer and a PLA filament. Then, CW-THz spectroscopy in the $0.1 - 0.3\text{ THz}$ spectral range is used to characterize the sensitivity and resolution of the sensor via tracking of the spectral position of the resonant absorption peak as a function of the RI of the analyte in the fluidic channel. Both amplitude detection and phase detection methods are used for monitoring of the absorption peak position, with the phase detection method resulting in higher quality data and lower noise. The spectral position of the transmission dip is found to depend linearly on the analyte RI, while moving towards lower frequencies for higher values of the analyte RI. The sensitivity of our THz Bragg waveguide-based fluidic sensor is measured to be $\sim 110\text{ GHz/RIU}$, which also matches well the theoretical simulations. Finally, sensor resolution using phase detection modality is estimated to be $\delta n \sim 4.5 \cdot 10^{-3}\text{ RIU}$ and is mostly due to the negative effect of the standing waves in various optical elements of the CW-THz spectrometer cavity. We believe that due to the ease of fabrication and good optical characteristics, this proposed fluidic sensor can find its applications in real-time monitoring of the analyte RI.

Acknowledgments

This work was supported by the Canada Research Chairs I of Prof. Skorobogatiy in “Ubiquitous THz photonics” (34633), as well as China Scholarship Council funding of the doctoral fellowship of Y. Cao (201706250016). We also thank Mr. Jayesh Sadasivan for his contributions to setting up the numerical simulations at the start of the project.

Contributions

All authors conceived these experiments and contributed to their design. Y. C performed the numerical simulations and measurements. Y. C, K. N, H. G, T. G, and M. S contributed to writing the manuscript.

CHAPTER 5 ARTICLE 2: ADDITIVE MANUFACTURING OF HIGHLY RECONFIGURABLE PLASMONIC CIRCUITS FOR TERAHERTZ COMMUNICATIONS

Yang Cao¹, Kathirvel Nallappan^{1,2}, Hichem Guerboukha¹, Guofu Xu¹,
and Maksim Skorobogatiy¹

¹Génie physique, Polytechnique Montréal

²Génie électrique, Polytechnique Montréal

Optica, vol. 7, no. 9, p. 1112-1125 (2020)

Abstract: While in most existing terahertz communication systems, the THz carrier wave is transmitted via free-space channels, the THz waveguide-based integrated solutions can be of great utility at both the transmitter and receiver ends, thus simplifying miniaturization and mass production of the cost-effective THz communication systems. Here we present a new type of modular THz integrated circuits based on the two-wire plasmonic waveguide components fabricated using a novel combination of stereolithography 3D printing, wet chemistry metal deposition, and hot stamping techniques. Particular attention is paid to the design of optical circuits based on the two-wire waveguides suspended inside of a protective micro-sized enclosure. Such waveguides feature low transmission and bending losses, as well as low dispersion. Using such waveguides as basic building blocks, we then demonstrate several key optical subcomponents such as low-loss broadband 2 x 1 THz couplers that use two coalescing two-wire waveguide bends, as well as broadband waveguide Bragg gratings (WBGs) that feature a paper sheet with a periodic sequence of metal strips inserted into the air gap of a two-wire waveguide. Finally, using thus developed subcomponents, a two-channel ADM is demonstrated for the operation at 140 GHz. We believe that the reported micro-encapsulated two-wire waveguide-based modular platform can have a strong impact on the field of THz signal processing and sensing due to the ease of device fabrication and handling, high degree of reconfigurability, as well as high potential for real-time tunability.

5.1 Introduction

The explosive growth of data traffic over the past decades has placed increasing demands on communication systems. With data rates in excess of 100 Gbps, the terahertz (THz) wireless communications are poised to become an enabling technology for the next-generation communications networks [213]. The high directionality and limited propagation range of THz radiation offer enhanced security and resistance to eavesdropping. At the same time, the high directionality of THz radiation poses many challenging engineering problems such as complexity in discovering the THz network (homing to emitter location) [214], as well as the necessity of precise alignment between the transmitter and receiver modules, thus requiring the use of advanced beam steering solutions [26, 215]. While mechanical solutions to beam steering are available in various forms (ex. Galva mirror scanners), a more reliable and robust solution would ideally forgo the use of moving parts and rather employ integrated solutions such as passive and active leaky waveguides and leaky wave antennas [139, 216-219]. In the microwave and THz range, such structures often employ metallic waveguides [220, 221] as well as modes propagating along conductive surfaces [176, 179, 222] (which in THz range are also known as Sommerfeld waves or Zenneck waves depending on the material of a surface). In this respect, the development of integrated metallic waveguides supporting various types of plasmonic modes is of great interest. Beyond the use in advanced beam steering and detection, integrated THz optical circuits provide a remarkable technological platform for signal processing in THz communications [39, 223]. Unlike the cumbersome and prone to time drift assemblies of discrete free-space components, the use of integrated circuits improves long-term reliability, results in a smaller footprint, and is better suitable for mass production. Therefore, the development of THz integrated optical circuits is a promising direction for signal processing at THz frequencies.

One promising low-loss material that was identified for building THz circuits is silicone. Both total internal reflection waveguides and slab photonic crystal-based waveguides were explored to build THz integrated optical circuits [12]. Various optical elements such as ring resonators, filters, and couplers on silicon substrates have been demonstrated in the THz range [43, 224-228]. However, the fabrication of silicon optical circuits generally requires the use of costly top-of-the-line fab infrastructure (lithography systems, deep reactive ion etchers, etc.) as well as high-cost materials (gold, etc.) in a multi-stage fabrication process. Furthermore, high refractive index contrast

normally associated with silicone photonics results in challenging fabrication tolerances even for longer THz wavelengths [38]. Finally, silicone integrated photonics is inherently planar, with very limited capacity for 3D integration, and out-of-plane inter-chip connectorization.

Alternatively, the inherently 3D AM presents an interesting alternative to the mostly planar silicone photonics. Thus, large-scale THz waveguide-based circuits can be rapidly manufactured with deeply subwavelength precision using readily available low-cost SLA (Stereo Lithography) or filament deposition modeling tools. While featuring lower refractive index contrast material combinations than silicone photonics, AM results in more relaxed fabrication tolerances and less stringent alignment requirements. Owing to the ubiquitous availability of hardware, the low threshold for entering into production, as well as the ease of 3D integration and out-of-plane inter-chip interconnect solutions, AM emerges as a promising platform for manufacturing waveguide-based optical integrated circuits in the THz spectral range. One of the challenges for AM technique in THz is the lack of low-loss materials to fabricate optical elements with high precision. Particularly, most resins compatible with high-resolution SLA are strong absorbers of the THz light. While some relatively low-loss thermoplastics such as Polypropylene [26] are compatible with filament deposition modeling, the resolution of such devices is generally not adequate for the fabrication of THz signal processing components that require small fabrication tolerances (ex. ADM). In this respect, the search for new materials or novel waveguide designs is of critical importance for 3D printed THz integrated circuits.

Compared to other reported THz waveguides that were developed for THz communication applications, such as subwavelength fibers [26, 27], porous fibers [114, 229, 230], hollow-core waveguides [99, 231], and parallel plate waveguides (PPWG) [117, 121], the two-wire THz plasmonic waveguides have advantages of low transmission loss, negligible GVD, no cut-off frequency, and high coupling coefficient with the conventional linear-polarized THz sources [126]. Most of the two-wire waveguides that were studied earlier featured short sections of straight metallic wires fixed in bulky holders, were inconvenient to use, and unsuitable for building integrated circuits. Although handling and mechanical stability of the two-wire waveguides can be improved by embedding them into foams or other types of porous dielectric claddings [124-126, 132], the interaction of the modal fields with lossy materials of the cladding results in increased

GVD and transmission losses, thus limiting the utility of classic two-wire waveguides in communication applications.

In this paper, we develop a novel type of quasi-two-wire waveguides, as well as optical components based on such waveguides using optically thick metal layers deposited onto complex-shaped 3D printed mechanical supports. In fact, the principal goal of this work is to explore THz optical component fabrication using complex metalized 3D shapes that can be readily manufactured using standard SLA 3D printers. The idea is to ultimately go out of plane and pursue 3D optical integration of THz components, which is simply impossible using standard lithographic techniques used in the fabrication of most microwave and optical components. Additionally, for sensing applications as well as for the design of highly tunable THz components we want to have access to the modal fields, which is especially simple to achieve when using two-wire waveguides [87, 131]. Finally, using 3D printing allows seamless integration between the enabling optical elements (waveguides, resonators, etc.) as well as mechanical support and environmental isolation (protective cage around the waveguide, holders, alignment features and connectors, etc.) that ultimately results in convenient to handle, highly modular systems that are easy to assemble and maintain.

Owing to the relatively high resolution ($\sim 25\text{ }\mu\text{m}$), large build volumes ($\sim 15\text{cm} \times 15\text{cm}$), superior reproducibility, as well as due to wide availability, low infrastructure, and maintenance costs, the SLA 3D printing technique is perfectly suitable for the fabrication of THz components. As a result, a considerable amount of 3D printing work has been reported for the fabrication of THz dielectric components [100, 115, 173, 198]. At the same time, fabrication of THz plasmonic structures is more subtle and less studied due to the necessity of the metallization step that has to produce high quality optically thick films (several 100-300 nm for THz frequencies [1]) on complex-shaped polymer surfaces. Recently, efficient metallization and coating techniques for 3D printed parts were reported using standard sputtering techniques [57], as well as more advanced wet or aerosol chemistries with resulting metallic coatings performing comparably to the components machined from bulk metals [116, 232].

In what follows, we present the in-depth theoretical and experimental studies of the 3D printed two-wire THz plasmonic waveguide-based components and modular optical circuits based on such

components. The highly reconfigurable nature of the developed THz plasmonic circuits is demonstrated by assembling nontrivial optical components (ex., ADM) using basic building blocks such as waveguides, bends, Y-splitters, and WBGs, all based on the encapsulated two-wire plasmonic waveguides.

This paper is organized as follows. First, we present the fundamental building block of the proposed plasmonic optical circuits – a two-wire waveguide that is encapsulated into a protective micro-sized cage that can be handled directly and that has various self-alignment features. We start with a numerical study and optimization of the optical guidance properties of such waveguides including their loss, GVD, and coupling efficiency to the WR6.5 flange waveguide for the operation frequency of ~ 140 GHz set by our experimental setup. Then, the two-wire waveguides are fabricated using SLA 3D printing and wet chemistry deposition techniques, and their performance is experimentally characterized using the CW-THz spectroscopy and a cut-back method. Experimentally found waveguide transmission loss and GVD of the straight two-wire waveguide sections (WSs) were measured as ~ 6 m $^{-1}$ and -1.5 ps/THz \cdot cm at 140 GHz, respectively. Next, bending losses of the curved two-wire encapsulated waveguides with different bend radiuses and axis of rotation were studied numerically and experimentally. We find that the resin cage significantly reduces the bending loss of a two-wire encapsulated waveguide compared to that of a free-standing two-wire waveguide due to modal field enhancement within the cage. We also find that even relatively tight bends with the bending radii of 5 cm result in an only modest increase in the modal propagation loss of less than 10 m $^{-1}$. Next, we explore the design and fabrication of paper-based symmetric metal gratings that are made using a low-cost hot stamping technique involving a laser jet printer and metallic thermofoils. Resonant transmission properties of such WBGs can be readily explained by the destructive interference between the fundamental mode of a two-wire waveguide and the fundamental mode of a planar metallic waveguide formed by the metallic grating elements. Experimentally measured transmission dips with 25 dB suppression factor and spectral widths as large as 32 GHz (FWHM) at 140 GHz were obtained with thus designed 5 cm-long, 1.5 mm period WBGs. Finally, we present two reconfigurable THz plasmonic circuits as demonstrators for signal processing in the THz transmitter and receiver circuits, including a THz splitter/multiplexer and an ADM prototype. Thus, at first a Y-shaped splitter/multiplexer was fabricated using a combination of two 90° waveguide bends of 4cm bend

radius; in fact, the splitter is assembled using two 45° waveguide bend sections and a Y-coupler element. Experimentally, we find that the splitter introduces a negligible insertion loss (<0.5 dB) and very small crosstalk (<-20 dB). Finally, we use a WBG in one of the arms of a Y-splitter and demonstrate a two-channel ADM with In, Through and Drop ports operating at ~ 140 GHz and having a spectral width of ~ 2.8 GHz. We believe that the reported modular platform based on the micro-encapsulated two-wire waveguides can have a strong impact on the field of integrated optical circuits for THz signal processing and potentially sensing due to ease of device fabrication, modular design, and high degree of reconfigurability, low-loss and low-dispersion of the underlying waveguides, as well as high potential for the real-time tunability of the optical circuits due to ease of access of the modal fields inside the controlled in-cage environment.

5.2 Two-wire waveguides

5.2.1 The design of the micro-encapsulated two-wire waveguide

The main difference between the proposed micro-encapsulated and conventional two-wire waveguides is the presence of dielectric support. Such a support serves several functions, such as shielding the modal field from the influence of the environment during the handling, while also incorporating various alignment features to simplify system integration of several plasmonic components. Particularly, the resin cage with dielectric supports used for wire encapsulation keeps the two wires parallel to each other, while maintaining the gap between the two with high precision due to high definition of the 3D printing process (660 ± 15 μm gap over 6cm-long WS). Moreover, several mechanical alignment features are integrated into the cage structure to simplify waveguide coupling to the external sources (horn antennas, etc.), as well as between different sections of the plasmonic waveguides or other components. With the proper design, the cage surrounding the two wires has only a small impact on the THz SPP wave, which is mainly confined to the air region between the two wires.

The THz rectangular metallic waveguides (waveguide flanges) have been widely used in the THz transmitter and receiver circuits. When developing the two-wire waveguide-based plasmonic circuits for THz communications, the parameters of a two-wire waveguide are chosen at first to optimize butt-coupling efficiency with a standard WR6.5 waveguide flange (hollow rectangular

waveguide with sizes of $hzWR6=825.5 \mu m$, $hyWR6=1651 \mu m$) used for operation at 140 GHz. Fig. 5.1(a) is a schematic of the two waveguides at the coupling plane. To characterize coupling efficiency between these two waveguides, the mode-matching method is employed that computes the overlap integral between the fundamental mode of the output two-wire waveguide and the excitation mode supported by the input WR6.5 waveguide flange [1, 233, 234]. Particularly, the vectorial modal electric and magnetic field amplitude distributions of these two butt-coupled waveguides are obtained using the finite element COMSOL Multiphysics. Assuming that all the incoming power is in the fundamental TE_{10} mode of the WR6.5 waveguide $|F_{in}^+\rangle$ with the electric field polarized along the shorter side of a waveguide, then ignoring reflections, complex field coupling coefficient C into the fundamental mode of the two-wire waveguide $|F_{out}^+\rangle$ can be found using the following field averages with respect to the longitudinal flux operator \hat{S}_z as:

$$C = \frac{\langle F_{out}^+ | \hat{S}_z | F_{in}^+ \rangle}{\sqrt{\langle F_{out}^+ | \hat{S}_z | F_{out}^+ \rangle \langle F_{in}^+ | \hat{S}_z | F_{in}^+ \rangle}} = \frac{\frac{c}{16\pi} \int_{wc} dx dy (E_{t,out}^*(x, y) \times H_{t,in}(x, y) + E_{t,in}(x, y) \times H_{t,out}^*(x, y))}{\sqrt{\frac{c}{8\pi} \text{Re} \int_{wc} dx dy (E_{t,out}^*(x, y) \times H_{t,out}(x, y) \cdot \frac{c}{8\pi} \text{Re} \int_{wc} dx dy (E_{t,in}^*(x, y) \times H_{t,in}(x, y))}} \quad (5.1)$$

where integrals are performed over the whole waveguide cross-sectional plane using transverse modal fields. Note that the modal excitation coefficient (by power) is given by $|C|^2$. In simulations, the metallic wires are modeled using Impedance Boundary Condition (IBC) at the wire surface together with the Drude-Lorentz model for the dielectric constant ϵ_m of silver in THz spectral range taken from [235]:

$$\epsilon_m = 1 - \frac{\omega_p^2}{\omega^2 + i\omega\gamma} \quad (5.2)$$

where $\omega_p=2\pi \cdot 2.185e15$ Hz is the plasma frequency, and $\gamma=2\pi \cdot 0.5138e13$ Hz is the damping coefficient for the bulk Ag metal.

Fig. 5.1(b) shows the modal electric field distribution of the THz SPP wave supported by the stand-alone two-wire waveguide. The field is mainly confined to the air gap between the two wires, while extending somewhat in the transverse direction from the wires. To optimize the power coupling coefficient between the modes of a WR6.5 waveguide and a two-wire waveguide, we vary the gap size between the wires, as well as the wire diameter. The values of the power coupling coefficient $|C|^2$ and modal losses (by field) are shown in Figs. 5.1(e) and 5.1(f) as blue stars. The maximal

power coupling coefficient of 45.43% is obtained using wires featuring the diameter of $D=0.4\text{hyWR6}$ and the gap size of $AG=0.8\text{hzWR6}$. Then, using the modal field distribution of the fundamental mode of a stand-alone two-wire waveguide, the geometry of the resin cage encapsulating the wires (see Fig. 5.1(c)) was chosen so that the electric field intensity at the internal horizontal and vertical boundaries of a cage do not exceed 3% of the maximal value in the waveguide gap. The plasmonic waveguide losses, as well as the power coupling coefficient between the WR6.5 waveguide flange and micro-encapsulated two-wire waveguides, were then recomputed to study the effect of the cage on the waveguide modal properties. The corresponding values of the coupling coefficient and modal losses are shown in Figs. 5.1(e) and 5.1(f) as red stars. In numerical simulations, the refractive index of resin used in 3D printing and its losses are taken from the experimental studies presented in [39]. Particularly, at 140 GHz, their values are 1.644 and 0.225 cm^{-1} (by field), respectively.

By comparing the transverse electric field distributions of the THz SPP waves supported by the two-wire waveguides with and without the resin cage (Figs. 5.1(b) and 5.1(d)), it is noted that the presence of a resin cage leads to somewhat tighter confinement of the fundamental mode in the waveguide gap. This, in turn, leads to a somewhat higher power excitation efficiency of the encapsulated waveguide fundamental mode (47.61% as seen from Fig. 5.1(e)) in case of an encapsulated waveguide, while also result in the higher propagation losses of such waveguides due to presence of the modal fields in the lossy material of a cage (see Fig. 5.1(f)). Increased modal confinement due to the presence of a cage can be explained by “squeezing” of the modal field in the vertical direction (Z-axis) due to discontinuity of the electric field component at the top and bottom horizontal boundaries between the cage and the air regions. Particularly, at these boundaries the Z component of the electric field dominates. At such boundaries, the Z displacement field is continuous across the interface, therefore, the dominant Z component of the electric field in the plastic cage of dielectric constant ϵ_{pl} is going to be smaller than that in the air (with dielectric constant ϵ_{air}) by the fraction $\epsilon_{air}/\epsilon_{pl}$, which forces redistribution of the modal field towards the inside of the cage, hence higher presence of the modal field in the gap between the wires.

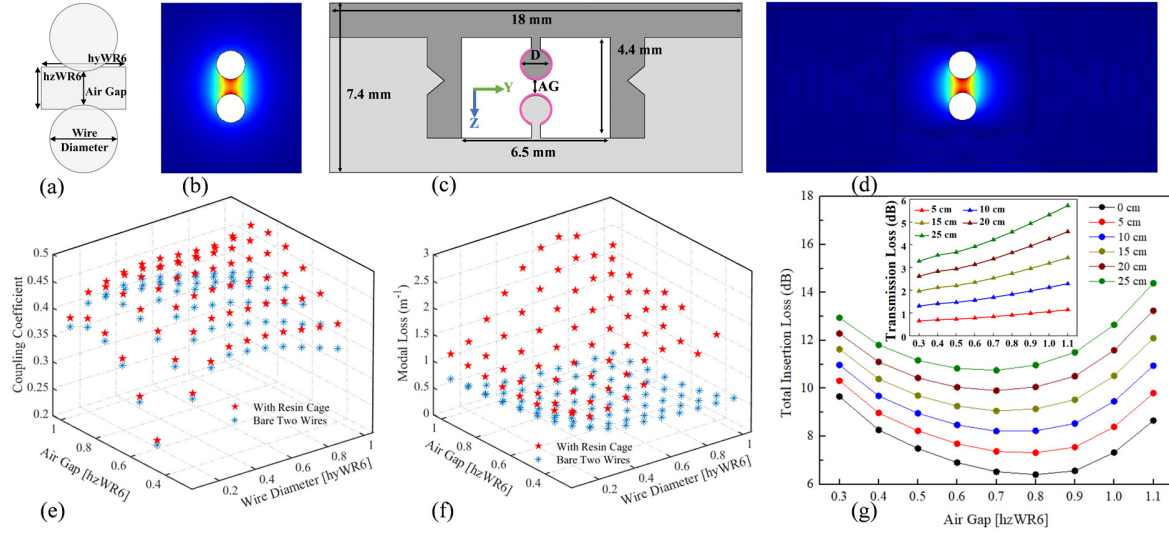


Figure 5.1 Design of micro-encapsulated two-wire waveguide

(a) Schematic of the butt-coupling arrangement between a two-wire waveguide and a WR6.5 waveguide flange. (b) Transverse modal electric field amplitude distribution $|E_t|$ of the THz SPP wave supported by the stand-alone two-wire waveguide at 140 GHz of 0.8hyWR6 wire diameter and 0.8hzWR6 inter-wire separation. (c) Schematic of the micro-encapsulated two-wire waveguide cross-section featuring two 3D printed parts (different shades of gray) each featuring a plastic cylinder covered with a silver layer (magenta) that are suspended in air (white) using dielectric supports and encapsulated within a plastic cage (grey). (d) Transverse modal electric field amplitude distribution $|E_t|$ at 140 GHz for a 3D printed two-wire waveguide with a silver layer coated wires placed inside of a resin enclosure. The two-wire waveguide geometry is the same as in Fig. 5.1(b), the cage size is the same as indicated in Fig. 5.1(c). (e) Dependence of the power coupling coefficient between the fundamental modes of a WR6.5 waveguide flange and a two-wire waveguide (with and without cage) as a function of the wire diameter and inter-wire separation at 140 GHz. (f) Dependence of the fundamental mode propagation loss (by field) of a two-wire waveguide (with and without cage) as a function of the wire diameter and the inter-wire separation at 140 GHz. (g) Total insertion losses (in-coupling, out-coupling, and propagation losses by power) of the micro-encapsulated two-wire waveguides featuring different lengths as a function of the inter-wire separation at 140 GHz. Inset: Propagation losses (by power) of the

micro-encapsulated two-wire waveguides of different lengths as a function of the inter-wire separation at 140 GHz.

Moreover, as seen from Fig. 5.1(f) (red stars), when increasing the wire diameter or the inter-wire separation (while keeping cage size the same) modal size also increases, thus leading to an increase in the modal propagation losses due to its stronger overlap with the lossy cage material. This is in contrast to the fundamental mode of a stand-alone two-wire waveguide whose modal losses decrease when using larger diameter wires or larger inter-wire separations (see Fig. 5.1(f) blue stars), due to the lower presence of the modal fields in the lossy metal material of the wires [122].

As seen from Fig. 5.1(e), the two-wire waveguide excitation efficiency is strongly sensitive to the value of the inter-wire separation with an optimal value $AG \approx 0.8 \cdot \lambda_{WR6} = 660 \text{ } \mu\text{m}$ regardless of the wire diameter. Setting the size of the air gap much smaller or much larger than the optimal value will result in a considerable vector field mismatch between the modes of a two-wire waveguide and a WR6.5 waveguide flange, which is clearly seen from Fig. B.2 in Appendix B, where we show modal intensity distributions for the flange waveguide and the two-wire waveguide featuring different sizes of the air gap. Significant modal mismatch, in turn, will result in weak coupling between the two waveguides as excitation efficiency is proportional to the overlap integral between two modes (see Eq. 5.1). At the same time, excitation efficiency is only weakly sensitive to the wire diameter, as long as it is larger than $D > 0.4 \cdot \lambda_{WR6} = 660 \text{ } \mu\text{m}$. From the fabrication point of view, the inter-wire distance is defined by the vertical resolution of the printer and is superior to $25 \text{ } \mu\text{m}$ for the SLA printer that we used (Asiga[®] Freeform PRO2). At the same time, the wire shape is rather defined by the transverse resolution of the printer, which is on the order of $50\text{-}100 \text{ } \mu\text{m}$, and thus, fabrication of the larger wire diameters is more reliable. In experiments, we found that we can reliably and consistently manufacture waveguides with the optimal inter-wire separation $0.8 \cdot \lambda_{WR6} = 660 \text{ } \mu\text{m}$, while somewhat larger wire diameters of $0.8 \cdot \lambda_{WR6} = 1.32 \text{ mm}$. As expected, at 140 GHz, the resultant waveguide has relatively a high excitation efficiency of 47.61% (by power) with the WR6.5 flange, which is close to that of the theoretical maximal value of 48.16%. Moreover, from numerical modeling, we observe that the transverse modal field distributions of the two-wire waveguide and the WR6.5 waveguide flange change little within the operational frequency range (110 GHz-170 GHz) (see Fig. B.3 in Appendix B). Therefore, the same high excitation efficiency can be maintained with only $\sim 6\%$ variation across all frequencies in this range.

Employing the damping coefficient of bulk silver in numerical simulations, theoretical loss (by field) of a straight waveguide is estimated at $\sim 2.3 \text{ m}^{-1}$, which is higher than that of a stand-alone two-wire waveguide $\sim 0.25 \text{ m}^{-1}$, while still small enough for the design of practical THz circuits.

For completeness, considering the potential importance of the developed waveguides in applications as interconnects between THz devices in the THz communication systems, the total insertion losses (comprising in-coupling, out-coupling, and propagation losses) of short micro-encapsulated two-wire waveguides featuring different inter-wire separations are computed by using the numerically modeled modal losses and excitation efficiency. The corresponding results are summarized in Fig. 5.1(g). Particularly, we find that the value of the total in/out-coupling loss (black solid line in Fig. 5.1(g)) is much larger than the propagation loss of the THz light due to material absorption for waveguides shorter than $\sim 15 \text{ cm}$. Thus, for shorter micro-encapsulated two-wire waveguides (also the ones used in our work), the minimal total insertion loss is achieved for the inter-wire separation of $AG \approx 0.8 \cdot \text{hzWR6}$. For longer waveguides, however, the lowest total insertion loss is observed for smaller inter-wire separation, which has to be taken into account when designing larger THz circuits.

5.2.2 The fabrication of the micro-encapsulated two-wire waveguide

For the convenience of fabrication, the encapsulated two-wire waveguide features two complementary parts, each one comprising one wire attached to a half cage using a deeply subwavelength dielectric support ridge with a width of $150 \text{ }\mu\text{m}$ (see Fig. 5.1(c)). Although printing along Z-axis can greatly reduce the fabrication time, printing large-diameter overhanging wire on a slender support ridge was proved to be challenging. Therefore, each part was printed along the waveguide propagation direction (X-axis) using $25 \text{ }\mu\text{m}$ layer thickness. After polishing the ends of a fully cured structure, the inside of a cage was protected with masking tape, while leaving only the plastic wire support surface exposed. Next, a silver layer was deposited on top of the plastic using wet chemistry to form conductive surfaces. A two-wire waveguide was finally obtained by assembling the two metalized parts by sliding them into each other using V-grooves and V-ridges that were printed onto the cage to simplify alignment and connectorization (see Fig. 5.1(c)). High-quality 6 cm -long WSs were then printed, while longer waveguides were assembled from such sections using another set of alignment and connectorization elements imprinted onto the cage end

facets (see Figs. 5.2(a) I and 5.2(b)). Position and size mismatch between the two wires in the adjacent WSs is mostly due to precision of the SLA printer and polishing imperfections, which is on the order of several tens of microns (example of a two-wire junction is shown in Fig. 5.2(c)). While this can bring additional coupling losses, it is expected that they will be small as the mode is mostly guided in the gap between the wires, which is almost a hundred times larger in size than potential misalignment and size mismatch of the wires. Additionally, precise alignment of the encapsulated two-wire waveguide with the WR6.5 waveguide flange (of a conical horn antenna) can be realized by aligning precision screw holes in a flange with judiciously positioned holes in a 3D printed cage (Fig. 5.2(a) II and 5.2(b)).

Additionally, the grain size of the deposited silver layer is on the order of several tens of nanometers [236], while the metal layer is several microns thick. Thus, metal surface roughness would be mostly determined by the roughness of the printed wire-shaped support, which is on the order of several tens of microns. While surface roughness of the metal layer that supports SPP can bring additional scattering loss, such roughness is on a scale much smaller than the wavelength of THz light, thus it is expected that waveguide losses will be mostly defined by the quality of the nanostructured metallic coating rather than by the imperfections in the shape of printed wire support.

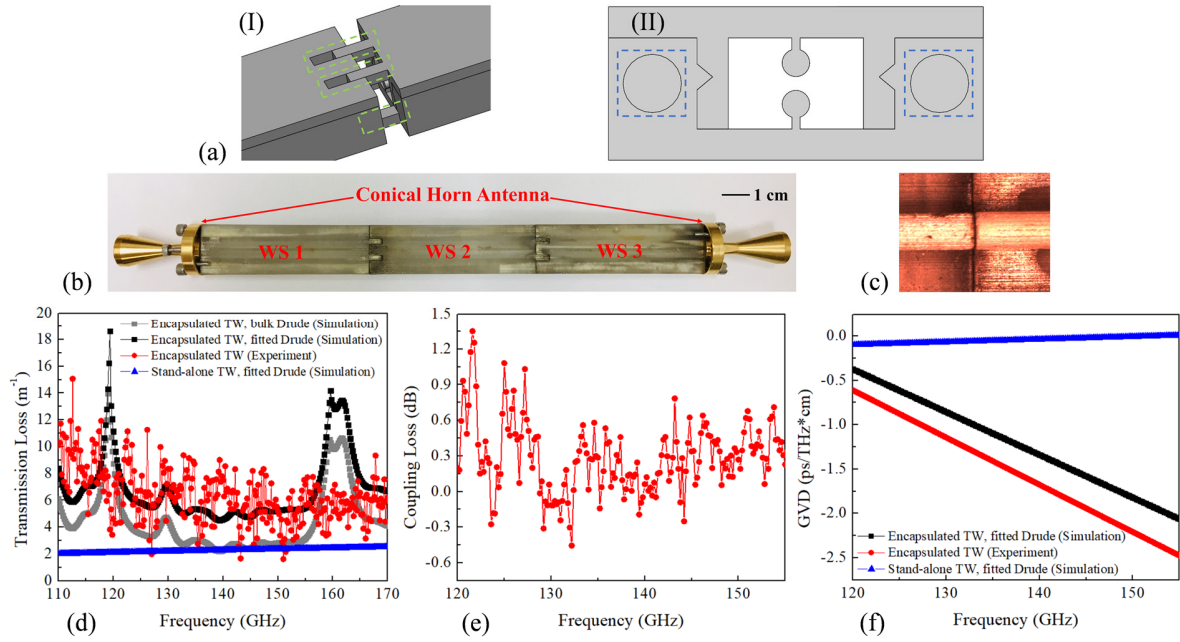


Figure 5.2 Characterization of straight micro-encapsulated two-wire waveguides

(a) I: Schematic of an interconnect between two plasmonic waveguides. In green dotted region are shown the alignment elements. II: Schematic of the end face of an encapsulated two-wire waveguide. In the blue dotted regions shown are the screw holes with depths of 5 mm for precision alignment and connectorization with the WR6.5 waveguide flange (of conical horn antenna). (b) An 18 cm-long straight two-wire waveguide assembled by connecting three 6 cm-long sections. The two ends of the composite waveguide are fitted with the WR6.5 conical horn antennas (Virginia Diodes, Inc.). (c) An enlarged view of the junction between the two wires in a butt-coupling arrangement between the two neighboring WSs. (d) Comparison of the numerical modal losses (by field) for the THz SPP wave and the measured transmission loss (by field) of a straight two-wire waveguide using cut-back measurements. (e) Experimentally measured insertion loss (by power) for two butt-coupled waveguides. (f) Numerical simulation and experimental results for the modal GVD for a straight two-wire waveguide.

5.3 Optical characterization of the 3D printed two-wire waveguide components

5.3.1 Straight two-wire waveguides

The two-wire waveguide transmission losses (see Fig. 5.2(d)) and coupling losses (see Fig. 5.2(e)) were deduced from the cut-back measurement using composite three-section waveguides similar to the one shown in Fig. 5.2(b) (see Appendix B.1 for details). The measured transmission loss (by field) is almost constant $\sim 6 \text{ m}^{-1}$ in the 120-170 GHz frequency range (red curve in Fig. 5.2(d)), which is almost twice as high as losses predicted by numerical simulations using the Drude model of bulk silver (grey curve in Fig. 5.2(d)). A significant difference between experimentally measured surface plasmon losses in THz and theoretically computed ones using the Drude-Lorentz model of bulk metals is a well-known problem, which is attributed to the surface imperfections and limitations of a Drude model at the metal surfaces [237-240]. In the case of silver layers deposited using wet chemistry (as used in this work), their metal conductivity can be significantly smaller than that of a fine silver sheet because of the nano/micro-crystallization and oxidation effects. While it was demonstrated that for such nanostructured surfaces Drude-Smith model of metal permittivity could provide more accurate numerical results for THz surface waves, this model is experiment-specific and lacks universality [222, 241]. To make a comparison between experimental and numerical work more realistic, and considering that experimentally characterized operational frequency range of the devices is relatively narrow (~ 110 -170 GHz), we retain the simple Drude-Lorentz model of silver for simulations, while simply fitting the damping factor to achieve the best fit of numerical simulations with the experiment (black and red curves in Fig. 5.2(d)). In particular, we find that to reproduce experimental loss of a straight plasmonic waveguide, the damping factor in the Drude-Lorentz model Eq. 5.2 should be increased by a factor of 50, the value $\gamma = 2\pi \cdot 2.69 \text{e}14 \text{ Hz}$ that is used in all following simulations. We then compare the losses of a stand-alone two-wire waveguide with that of an encapsulated waveguide of identical geometry (blue and black curves in Fig. 5.2(d)). We find that stand-alone two-wire waveguides (where ohmic losses dominate) have somewhat smaller, while nevertheless comparable losses to those of encapsulated waveguides that feature additional loss contribution due to resin cage absorption.

One significant discrepancy between the numerical simulations and loss measurements of micro-encapsulated two-wire plasmonic waveguides is the presence of two strong absorption peaks as predicted theoretically at 119 GHz and 161 GHz with spectral widths of 1.7 GHz and 3.1 GHz (full width at half maximum (FWHM)) respectively. These peaks are due to accidental degeneracy of the dispersion relations of the SPP mode and the high-loss bulk modes of a resin cage. In the vicinity of the degenerate frequency (phase-matching point), the SPP mode hybridizes with the mode of a resin cage, and the resultant dispersion relations of the supermodes exhibit classic avoided crossing behavior. The bandwidth of a loss peak is proportional to the coupling strength between the SPP and a cage mode. The exact shapes of such peaks and their positions are highly sensitive to the scattering losses and structure inhomogeneities (surface roughness) and can easily disappear completely (especially for the narrow peaks) due to decoherence brought by such imperfections [19]. Therefore, we are not surprised by the absence of such peaks in the measured spectra due to narrow bandwidths of peaks, which is most probably caused by the effects of roughness of the printed structures, as well as cage surface contamination with silver residue during wet chemistry processing. In fact, a more careful implementation of a waveguide with polishing and better controlled wet chemistry deposition of metal layer allows for observation of avoided crossing resonances, thus making us confident about the good correspondence between the theoretical and experimental results, as well as about our overall understanding of a system (see Appendix B.1 for details).

In addition to waveguide losses, one can also extract inter-waveguide coupling losses due to a mismatch in the relative size and positions of the neighboring WSs (see Appendix B.3.1 for details). The coupling loss (by power) data is measured in the 120 - 155 GHz range (see Fig. 5.2(e)), with a typical power loss value in the ~ 0.4 dB per connection, which is significantly smaller than a single WS transmission loss (~ 3 dB by power for a 6 cm-long section). This allows connecting ~ 8 sections (total waveguide length of ~ 0.5 m) before it can start significantly affecting the power budget, thus making us confident that connectorization of many two-wire waveguide-based components is feasible when designing complex THz processing photonic circuits.

Finally, Fig. 5.2(f) presents experimental data and numerical simulation of the GVD of the SPP mode of a two-wire encapsulated waveguide in the 120 – 155 GHz spectral range by using the following definition:

$$GVD = \frac{\partial^2 \beta(\omega)}{\partial \omega^2} = \frac{\partial^2 (n(\omega) \cdot \omega / c)}{\partial \omega^2} \quad (5.3)$$

One reason for pursuing the development of the plasmonic THz circuits is because of the very small GVDs of the THz SPP waves guided by the classical stand-alone two-wire waveguides [36], which potentially allows the processing of extreme data bitrates without scrambling the signal due to temporal pulse dispersion. In the case of encapsulated two-wire waveguides, the GVD of an SPP mode will be higher than that of a stand-alone two-wire waveguide due to partial overlap of the SPP modal fields with the cage. As shown in Fig. 5.2(f), the measured GVD of an encapsulated two-wire waveguide is in the 1-2 ps/THz·cm, which is also in agreement with the results of numerical simulations. While this value is significantly higher than that of a stand-alone two-wire waveguide (less than 0.1 ps/THz·cm) which is shown (blue curve) in Fig. 5.2(f), it is nevertheless much smaller than the GVD of most alternative THz waveguides, which is normally in the 10's ps/THz·cm range. For all these reasons, we believe that encapsulated two-wire waveguides offer a viable platform for building signal processing THz photonic circuits.

5.3.2 Two-wire waveguide bends

The curved waveguides are of critical importance for building practical photonic circuits and they are an integral part of various components such as splitters, couplers, ring resonators, optical delay lines, etc. [51, 115, 119, 242]. Moreover, curved waveguides serve as interconnects between various components of the high-density photonic circuit. Unfortunately, modes guided by curved waveguides are often leaky, and they are prone to higher radiation losses for tighter bends [243]. Additionally, the mode of a bent waveguide has somewhat different field distribution from that of a straight waveguide, thus coupling between straight and bent waveguides also leads to back reflections and radiative insertion loss, which again is more pronounced for tighter bends. All these negative effects associated with waveguide bends are typically mitigated by increasing the mode confinement which can be achieved, for example, by employing high refractive index contrast waveguides (ex. silicon photonics) [244, 245]. Importantly, plasmonic modes of a two-wire waveguide show relatively strong confinement in the gap between the two metallic wires, while the effect of bending in such waveguides is less pronounced compared to many other THz waveguides such as single wires [246], hollow-core waveguides [247] and subwavelength fibers

[26]. In what follows we present numerical and experimental studies in bending loss of the encapsulated two-wire waveguides and demonstrate that it is significantly smaller than that in the case of stand-alone two-wire waveguides. We attribute this finding to stronger confinement of the plasmonic mode in the case of encapsulated wires.

Figs. 5.3(a) and 5.3(b) show schematics of the two types of bends that differ from each other by the relative orientation of the bend rotation axis and the two wires. When plotting the modal electric field distributions $|E|$, it is noted that their maxima are somewhat shifted from the center of the gap between the two wires and away from the rotational axis, which is a well-known effect of the bend on modal fields, and is also the principal reason for the bend insertion losses. The transmission t (by field) through a waveguide bend that is connectorized on both sides to straight sections of the same waveguide can be quite generally written as:

$$t = |C(R)| \cdot |C(R)| \cdot \exp(-\alpha_{st} l_b) \exp(-\alpha_b(R) \cdot l_b) \quad (5.4)$$

Where R is the bend radius of the two-wire waveguide bend, l_b is the length of the waveguide bend, α_{st} is the transmission loss (by field) of a straight waveguide, $\alpha_b(R)$ is an additional loss (by field) due to bending. $|C(R)|$ is the coupling coefficient (by field) between the bent and straight waveguides, while $1-|C(R)|^2$ is the insertion loss (by power) on each side of the bent/straight waveguide connection.

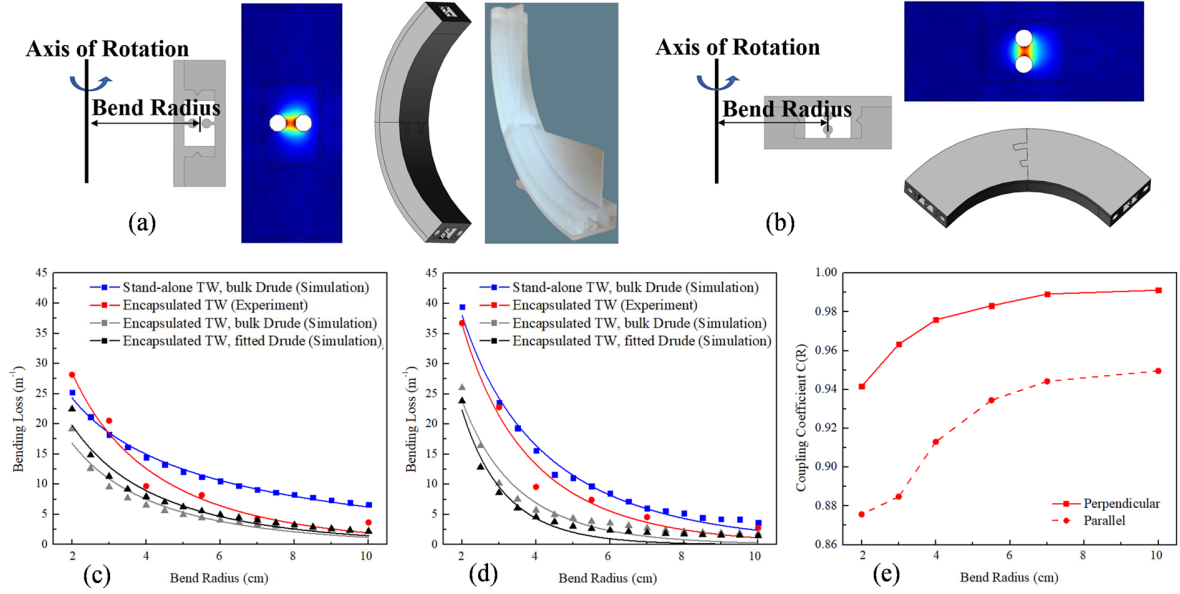


Figure 5.3 Micro-encapsulated two-wire waveguide bends

(a) and (b) Schematics and a photo of the two types of the two-wire waveguide 90° bends of 4 cm bend radius and the corresponding modal field distributions $|E(x,y)|$ of the THz SPP waves at 140 GHz. (c) and (d) Bending losses (by field) of the two types of waveguide bends. (e) The coupling coefficient $|C(R)|^2$ (by power) between the encapsulated two-wire waveguide bends and the straight one.

The curved two-wire waveguides were studied using 2D axisymmetric models in COMSOL finite element modeling software that allows computing complex effective refractive indices of the bend modes. The Ag layer was modeled using IBC with the Drude-Lorentz model in Eq. 5.2. Figs. 5.3(c) and 5.3(d) show the results of numerical simulations of bending losses as a function of bending radius of stand-alone and encapsulated two-wire waveguides as well as their corresponding analytical fit using [248, 249]:

$$\alpha_b(R) = A \cdot \exp(-B \cdot R) / \sqrt{R} \quad (5.5)$$

Compared to the stand-alone two-wire waveguide bends, the encapsulated two-wire waveguide bends show considerably lower bending losses due to enhanced modal confinement brought by the resin cage (blue and gray curves in Figs. 5.3(c) and 5.3(d)), as explained in Chapter 5.2.1. Moreover, bending loss is not sensitive to the value of the damping constant (gray and black curves in Figs.

5.3(c) and 5.3(d) computed using η_b and η_r , respectively). Finally, Fig. 5.3(e) shows the power coupling coefficient $|C(R)|^2$ that was computed using modal matching approach Eq. 5.1 [1], by expanding the mode of a straight encapsulated waveguide into the modes of a bent one (assuming no back reflections).

As a result, bends with the axis of rotation perpendicular to the line connecting the two-wire centers (see Fig. 5.3(a)) feature somewhat smaller bending losses and larger coupling coefficient with the straight waveguides than the other bend type (see Fig. 5.3(b)). This is due to tighter confinement of the guided mode in the case of the first bend type. Indeed, the effect of the bend is to shift the modal field away from the rotational axis of the bend toward infinity. In the case of a bend in Fig. 5.3(a), in doing so the mode encounters a metal surface of a wire, while in the case of a bend in Fig. 5.3(b) there is nothing to limit such a shift. Therefore, modes of such a bend show stronger confinement in the core (inter-wire gap), which also results in lower bending losses.

Next, we experimentally studied the losses of the two bend types using 90° bend sections for the bend radii in the range of 2-10 cm at 140 GHz. Due to the limitation of SLA 3D printing, 90° bends were realized by assembling two 45° sections of the same bend radius (see Figs. 5.3(a) and 5.3(b)). The measurements are summarized in Figs. 5.3(c) and 5.3(d) (see details in Appendix B.3.2). While the experimental loss is somewhat higher than the theoretical one, the overall tendency is well reproduced. Discrepancies between the experimental and numerical results can be attributed to the effect of printing imperfections such as discrete shape definition by the SLA printer, as well as surface warping during the postprocessing curing step.

5.3.3 Two-wire waveguide Bragg gratings

THz WBGs are of great value for building signal processing components for THz communications. WBGs are often used as band-reject filters, while WBGs with defects are used as band-pass filters. Thus, integration of even the simplest WBGs into THz photonic circuits can enable such advanced signal processing functionalities as noise filtering or channel adding or dropping when using frequency division multiplexing. In what follows, we demonstrate the design and fabrication of strong two-wire WBGs with a stopband of up to 20 GHz for applications in THz communications within the FDM paradigm. With the operation frequency in the lower THz band of 0.1 – 0.3 THz, one can pack ~10 of 20 GHz-wide channels each, supporting up to 20 GBs data rates. The lower

THz band is easily accessible both with electronics [185, 250] and optics-based THz communication systems [251] with data modulation rates per channel as high as 40 GBs. We, therefore, believe that the frequency division multiplexing approach in the lower THz band can be a viable approach for multi-channel data transmission with total data rates exceeding several 100s GBs.

To fabricate strong WBGs based on the two-wire waveguides, a low-loss dielectric substrate featuring a periodic pattern of metallic stripes is placed into the gap between the two wires. This arrangement results in strong overlap of the waveguide modal fields with the grating region, and as a consequence, wide stopbands of up to 10% (of the center frequency) can be achieved. While a variety of methods exist for the fabrication of metal patterns on dielectric substrates including laser engraving, lithography, and etching [252-254], such techniques require relatively expensive infrastructure. In this work, we explored an alternative low-cost and simple hot stamping technique for WBG fabrication. The main advantage of this technique is its similarity to 3D printing as it allows rapid prototyping and extensive fine-tuning of the grating geometry with only minimal time and material expenditures. Particularly, 100 μm -thick printing paper (Premium Laser Print, Hammermill Inc, $n_p=1.45$, $\alpha_p[\text{cm}^{-1}] = 20.67 \cdot (\omega[\text{THz}])^2 + 1.019$ (by field) [131]) was used as the substrate for the metal grating. The periodic metal pattern was deposited by first printing the required pattern in ink on both sides of the paper symmetrically (laser printer Xerox Phaser 6180MFP), and then transferring the metal/polymer composite from the thermofoil sheet (Deco foil, Thermoweb Inc) onto the ink-covered paper region. The transfer was achieved by placing the paper in direct contact with thermofoils and heating inside the thermal laminator (Fusion 1100L, Swingline Inc). The end result is a periodic pattern of a few μm -thick aluminum/thermoplastic composite transferred on top of the printed ink pattern [181]. To accommodate thus fabricated grating, the enclosure of a 3D printed two-wire waveguide shown in Fig. 5.1(c) was slightly modified to include two narrow slits in the resin cage throughout the whole length of a waveguide. The grating was then inserted into the slits and self-aligned to be in the center of the air gap between the wires (see Fig. 5.4(a)).

Operation of thus fabricated gratings is easy to understand using coupled-mode theory by considering three principal modes propagating in the two sections of the WBG. Particularly, Fig. 5.4(b) I shows the schematic of the two sections comprising a single period of the WBG. The first

section of width w_1 features a two-wire waveguide with a blank paper sheet in between. The first section transverse cross-section is shown in Fig. 5.4(b) II. As the optical thickness of a blank paper ($\sim 145 \mu\text{m}$) is much smaller than the gap size ($\sim 660 \mu\text{m}$) and the wavelength of light used in experiments (at 140 GHz $\lambda \sim 2 \text{ mm}$), the paper substrate itself does not modify significantly the modal field distribution in the gap between the two wires. Therefore, the effective RI of the fundamental mode propagating in section 1 (propagation constant of β_1) is still close to 1 and the modal field distribution resembles that of an empty two-wire waveguide (compare Figs. 5.4(b) IV and 5.1(d)). At the same time, due to the paper orientation, the modal electric field is mostly perpendicular to the paper surface, thus the amplitude of the electric field in the paper is reduced compared to that in the air $|E_p| \approx |E_a|/n_p^2 \sim |E_a|/2$. Transmission spectrum through a two-wire waveguide with the inserted paper is therefore close to the one without the inserted paper, as seen in Fig. 5.4(e) (orange curve).

The second section of width w_2 additionally features thin metal plates on both sides of a paper sheet. The second section transverse cross-section is shown in Fig. 5.4(b). III. In Section 2 of the grating, two kinds of modes are supported. As the paper dielectric substrate is sandwiched by two metal plates, one of the modes (see Fig. 4(b) V) with propagation constant β_2 propagates directly between the metal plates, thus resembling a TEM-like mode of a PPWG. As the corresponding modal field is mainly localized in the paper, mode 2 effective RI is close to that of the paper 1.45. The other mode propagating in section 2 (mode 3 with β_3) is mostly confined to the air region between the metal wires and metal plates. Its modal field distribution and effective RI are similar to those of mode 1 of section 1 (compare Figs. 5.4(b) IV and VI). At the interface between two sections of a single period, the power coupling coefficient δ between highly dissimilar modes 1 and 2 can be computed using the mode-matching method Eq. 5.1 [1]. For geometries considered in this paper, we find $\delta \sim 0.03\text{--}0.06$ depending on the configuration. At the same time, the power coupling coefficient between two similar modes 1 and 3 is high, and assuming small reflection and negligible scattering (radiation) loss at the interface between two sections it is $\sim 1 - \delta$. It can be then shown using a rigorous coupled-mode theory that the forward propagating modal fields at the beginning of any period $|F(x)\rangle$ will be related to the corresponding fields at the beginning of the next period $|F(x+P)\rangle$ as:

$$\begin{aligned} |F(x+P)\rangle &\approx |F(x)\rangle \cdot \exp(i\beta_1 w_1) \cdot [\delta \cdot \exp(i\beta_2 w_2) + (1-\delta) \cdot \exp(i\beta_3 w_2)] = \\ &= |F(x)\rangle \cdot \exp(i\beta_1 w_1 + i\beta_3 w_2) \cdot [1 - \delta \cdot (1 - \exp(i(\beta_2 - \beta_3) w_2))] \end{aligned} \quad (5.6)$$

Physically this means that mode 1 of section 1 excites two modes 2 and 3 in section 2, which then propagate with different phase velocities (see Fig. 5.4(b)). If modes 2 and 3 recombine destructively at the end of the period, this will result in the strong back-reflection, and the grating will be at the stop band. As phase difference between the two copropagating modes after propagation over one grating period is given by $(\beta_2 - \beta_3)w_2$, then, to minimize transmitted power of THz light at the desired Bragg frequency ω_B one has to choose the width w_2 of section 2 to result in destructive interference between the two modes:

$$[\beta_2(\omega_B) - \beta_3(\omega_B)]w_2 = \pi \cdot (2m_w + 1), \quad m_w \in \mathbb{N} \quad (5.7)$$

Additionally, remembering that the modes 1 and 3 are similar (Figs. 5.4(b) IV and VI) and have very similar propagation constants $\beta_1 \approx \beta_3$, and that the grating period is $P = w_1 + w_2$, then, for the forward propagating field we can write:

$$\begin{aligned} |F(x+P)\rangle &\approx |F(x)\rangle \cdot \exp(i\beta_1 P) \cdot [1 - 2\delta] = |F(x)\rangle \cdot \exp(i\beta_g P) \\ \beta_g &= \beta_1 + i \frac{2\delta}{P} \end{aligned} \quad (5.8)$$

which shows exponential decay of the fields along the grating, and it also satisfies the Bloch form assuming complex propagation constant of the WBG. Finally, as propagation along the grating is mostly dominated by the modes 1 and 3 with propagation constant β_1 , then the reciprocal wavevector of the grating has to match the difference between WBG forward and backward propagating modes, thus resulting in additional condition for the grating design:

$$2\beta_1 = \frac{2\pi}{P} m_p, \quad m_p \in \mathbb{N} \quad (5.9)$$

Example of the numerical study of gratings designed using resonant design conditions Eqs. 5.7 and 5.9 is presented in Appendix B.4. Results of transmission and reflections simulations using COMSOL finite element formulation with ports confirm the validity of our understanding of the grating operation principles. Note that the resonant conditions Eqs. 5.7 and 5.9 result in the most pronounced stop bands and strong reflections, while there are other resonant conditions possible when phase matching the forward propagating mode of a two-wire waveguide with that of forward

or backward propagating modes in a metal plate waveguide. The design complexity and numerous possible resonances in a three-mode grating merit a separate paper, while what follows just aims at presenting some examples of WBGs based on the combination of two-wire and PPWGs.

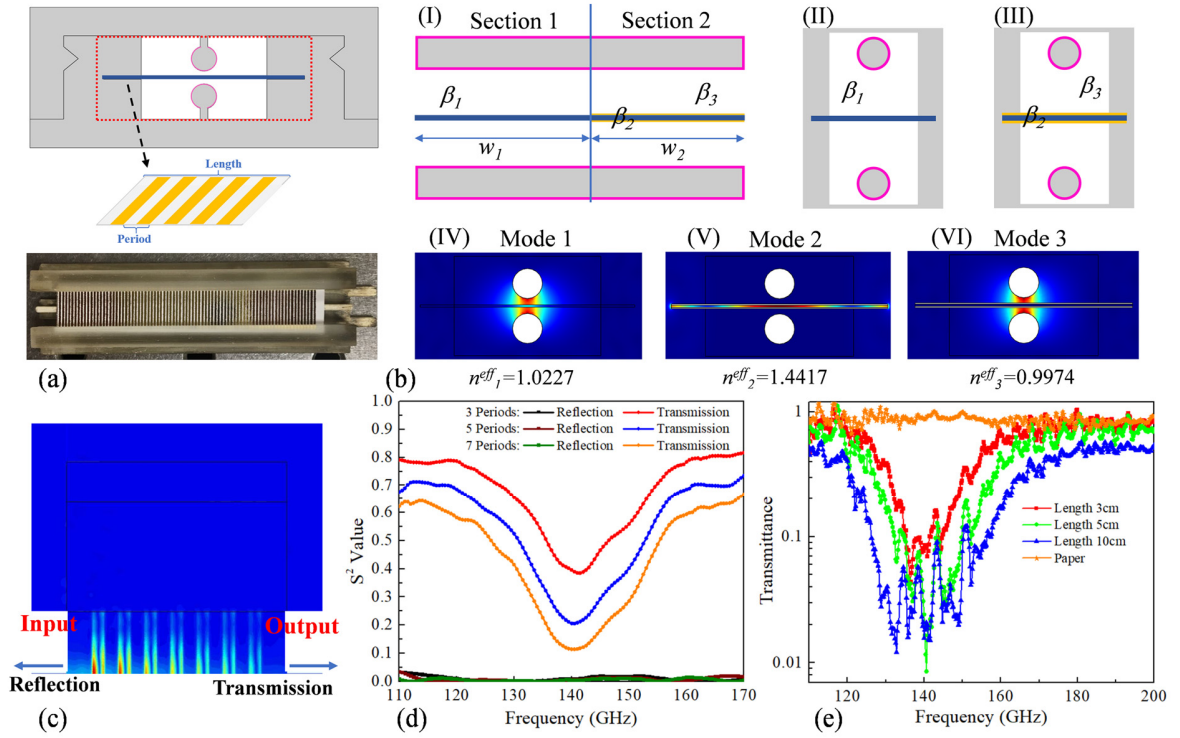


Figure 5.4 Paper-based two-wire waveguide Bragg gratings

- (a) Schematic of the two-wire WBG (top) and a photo from the top with half of the cage removed (bottom). (b) (I) Schematic of a single period of the WBG that comprises two sections, one containing a blank paper sheet, and the other one containing metalized paper with the corresponding transverse cross-sections shown in (II) and (III). The electric field distributions ($|E|$) of principal modes propagating in section 1 - Mode 1 (IV), and section 2 - Mode 2 (V), and Mode 3 (VI) at 140 GHz. (c) The simulated modal electric field distribution ($|E|$) of a WBG in the symmetry plane in the mid-gap between the two wires at 140 GHz. (d) The simulated power transmission $|S_{21}|^2$ and reflection $|S_{11}|^2$ coefficients for WBGs with different number of periods. (e) Experimentally measured transmittance of the paper/metal WBGs of different lengths inserted into a 10 cm-long two-wire waveguide. Transmittance is computed by dividing the grating transmission spectra (by field) by that of an empty two-wire waveguide (reference).

Next, the two-wire WBGs featuring broad and pronounced transmission dips at 140 GHz are detailed. Such WBGs can serve as efficient band-rejection filters in the THz communication circuits. The WBGs are first studied using a 3D modeling frequency domain tool with ports within COMSOL Multiphysics. Because of two reflection symmetry planes, only a quarter of a structure together with Perfect Electrical Conductor (PEC) and Perfect Magnetic Conductor (PMC) boundary conditions can be used. The metalized patterns on paper are defined using the IBC boundary condition with Drude-Lorentz model for bulk Aluminum ($\omega_{AI}=2\pi\cdot 3.57\text{e}15$ Hz, $\gamma_{AI}=2\pi\cdot 1.94\text{e}13$). In simulations, the THz light is launched using port boundary condition at the input facet of the WBGs containing 7 periods. By monitoring the power transmission coefficient at the other facet of the WBGs ($|S_{21}|^2$), it is noted that gratings with a period of 1.5 mm and a metalized-paper section width w_2 of 0.7 mm feature pronounced transmission dips at 140 GHz (see Figs. 5.4(d) and 5.4(e)). At the same time, the power reflection coefficient ($|S_{11}|^2$) in such a design is small (less than 3%). A more detailed analysis shows that in such a grating the forward propagating mode of a metal plate waveguide is matched to the backward propagating mode of a metal plate waveguide, which has only a small coupling with a backward propagating mode of a two-wire waveguides. Thus, such a grating, while featuring a large stopband, is also characterized by low reflection into a two-wire waveguide that feeds it.

In experiments we used gratings of different lengths that featured a periodic sequence with 19, 32, and 65 metal strips on a paper substrate that was placed into a gap of a 10-cm two-wire waveguide. It was then characterized in a setup detailed in Appendix B.3.1. The grating transmittance was obtained by comparing the transmission spectra (by field) of the two-wire waveguide with and without the gratings (see Fig. 5.4(e)). A pronounced transmission dip at 140 GHz featuring a spectral width of 32 GHz (FWHM) and a minimum relative transmittance below 10^{-2} is obtained using the grating with a length of 5 cm. Additionally, when increasing the grating length to 10 cm, such transmission dip becomes even more pronounced.

In passing, we note the presence of ripples in the measured transmission spectra (see for example Figs. 5.2, 5.4, 5.5, and 5.6). The origin of these ripples is a standing-wave phenomenon, which is particular to the coherent CW-THz spectroscopy setup used in our experiments. In fact, there are two types of ripples. The most pronounced ones are caused by the multiple reflections inside of the two silicon lenses (size $d\sim 10$ mm, $n_{Si}\sim 3.42$) that are integrated into the THz photomixers in the

emission and detection arms. The corresponding frequency separation between the two ripples of this kind is given by $\Delta\nu_I = c/2dn_{Si} \sim 4$ GHz. The second type of ripples is due to standing-waves formed between reflections on the free-space optical components (ex. parabolic mirrors and plano-convex lenses). These ripples have smaller amplitudes and are more closely spaced in the frequency domain. Although the effect of the first type of ripples can be somewhat mitigated by normalizing the measured spectra with respect to the reference [19], the effect of the second type of ripples is more difficult to alleviate as the free-space path within the setup normally changes during measurements.

5.4 The THz plasmonic circuits

In this section, we demonstrate the possibility of building highly reconfigurable plasmonic circuits using as an example THz splitter/multiplexer and a two-channel ADM.

5.4.1 THz splitter/multiplexer

A Y-shaped THz splitter/multiplexer was fabricated by fusing two 90° two-wire waveguide bends of 4 cm bending radius (axis of rotation parallel to the line connecting the wire centers) as shown in Fig. 5.5(a). Furthermore, the two curved sections are terminated with short 0.5-cm sections of a straight waveguide for the ease of connectorization with other components. Such a coupler can be used either as a broadband 50/50 splitter or a multiplexer of two data streams.

In the first experiment, we test the Y-coupler operation in the splitter mode. The THz light is launched into port 1 via a WR6.5 conical horn antenna, then divided in the Y-shaped splitter, and finally registered at ports 2 and 3 (each featuring a WR6.5 conical horn antenna). Fig. 5.5(b) shows the transmittances of the output ports, which are obtained by dividing the transmission spectra (by field) of light coming out from ports 2 and 3 by that of the THz light launched into port 1 (for more details, see Appendix B.5). The data shows that transmittances of the two output ports are very similar with the difference of only a few percentages in the 100-200 GHz operation frequency range.

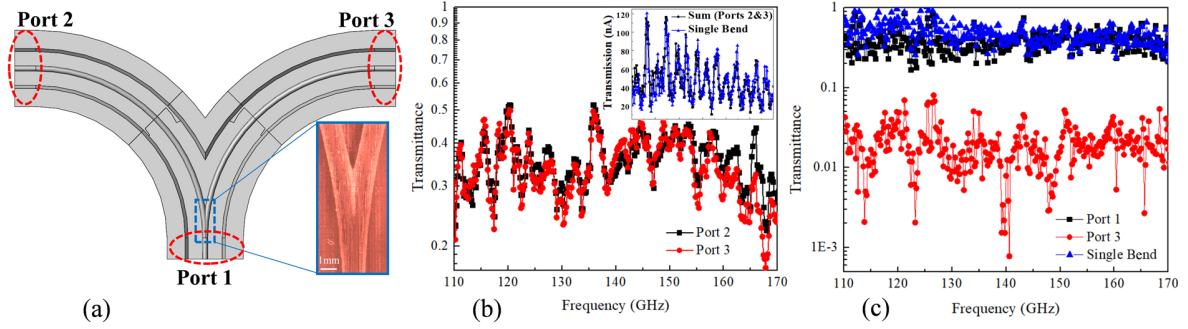


Figure 5.5 Two-wire waveguide-based coupler

(a) Schematic (half) of a Y-shaped splitter/multiplexer that uses two fused two-wire waveguide bends. In red dotted regions are the 0.5-cm section of straight waveguides. Inset: photo of the two fused wires in a blue dotted region of a schematic. (b) Transmittance of the output ports 2 and 3 with the incident THz light in port 1. It is computed by dividing the transmission spectra (by field) of the THz light received at the corresponding output ports of a splitter by the one launched into port 1. Inset: comparison of the two transmission spectra (by field), one (black) is obtained by summing the outputs of the ports 2 and 3 when light is launched into port 1, while the other one (blue) is obtained by measuring a single bend section with the equivalent geometry of a half splitter (shown in Fig. 5.3(b)), thus signifying a minimal scattering loss at a Y-junction. (c) Transmittance of the output ports 1 (black) and 3 (red) when the THz light is launched into port 2, comparison with the transmittance of a single bend section of the equivalent geometry (blue) shown in Fig. 5.3(b). The transmittance is computed by dividing the transmission spectra (by field) of the THz light recorded at the output ports of a multiplexer by that of the incident THz light.

In the second experiment, we test the Y-coupler operation in the multiplexer mode. The THz light is launched into port 3 (or port 2), then travels through the Y-junction, and finally leaves the component through port 1 and partially through unused port 2 (or port 3, correspondently). For example, Fig. 5.5(c) shows transmittances of ports 1 and 3, which are obtained by dividing the transmission spectra (by field) measured at these ports by the spectrum of the THz light launched into port 2. Note that parasitic transmission through port 2 (due to back-scattering at the Y-junction) is much weaker (on average by -50 dB by power) than intended forward signal transmission through port 1, which signifies that the developed component can be used as a 2 x 1 multiplexer.

Furthermore, by comparing the net (sum) intensity of THz light measured at the output ports 1 (and 2) of the Y-coupler to the light intensity transmitted through a single bend of identical geometry (see blue curves in Figs. 5.5(b) inset and 5.5(c)), we conclude that the average insertion loss brought by the Y-junction is small ~ 0.3 dB at ~ 140 GHz.

5.4.2 THz add-drop multiplexer (ADM)

The ADM is a key building block in any communication systems that uses frequency division multiplexing. Many ADM designs in the near-infrared telecommunication band use fiber Bragg gratings and circulators [255], a concept that is translated in our current work into the THz range. Alternatively, THz ADMs were also built using photonic band gap materials and ring resonators [256, 257]. Such devices, however, were obtained using complex and costly microfabrication processes in which a high-resistivity float zone silicon wafer was machined to obtain the periodically arranged posts, and then such array was sandwiched by two metal plates using eutectic bonding.

In this section, as a proof of concept, we demonstrate a simple ADM of ~ 2.8 GHz bandwidth (FWHM) that operates at ~ 140 GHz by integrating a Y-coupler and a WBG based on two-wire waveguide technology detailed earlier. The ADM is shown in Fig. 5.6(a). A signal featuring several mixed stand-alone channels at different frequencies (frequency division multiplexing modality) is launched into the In port. After propagation through a curved waveguide of a Y-coupler, the signal arrives at a WBG where the channel in the grating stopband is back-reflected, while the rest of the channels continue into the Through port. In the absence of a THz circulator, the reflected channel is then split 50/50 by the Y-coupler and it finally arrives at the Drop port. Note that THz circulators have been demonstrated earlier (ex. [258]) and they are fully compatible with the two-wire waveguide base technology used in this work.

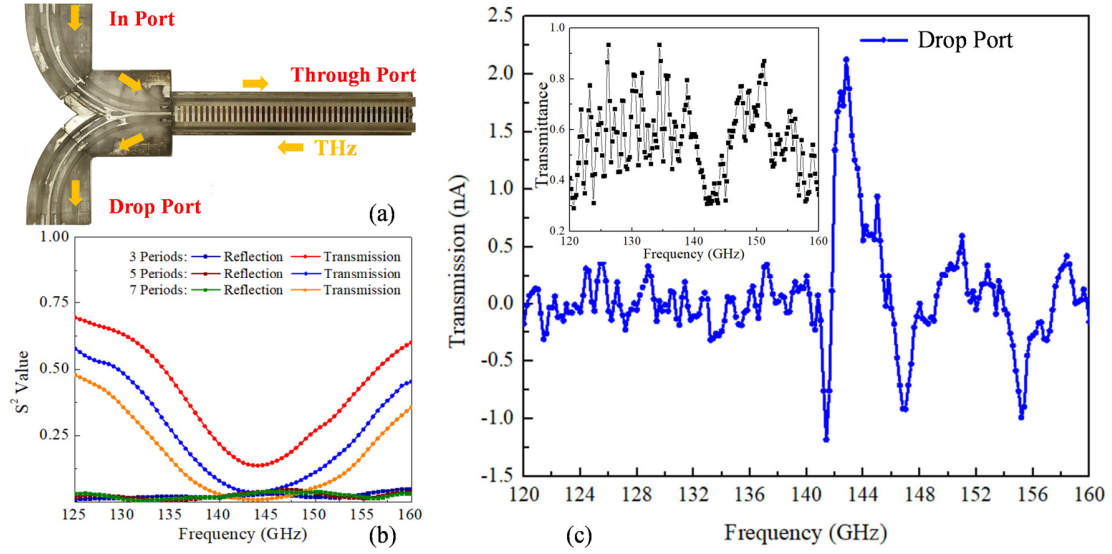


Figure 5.6 Two-wire waveguide-based ADM

- (a) Schematic of ADM composed of a Y-coupler and a WBG. (b) The numerical results of the transmission ($|S_{21}|^2$) and reflection ($|S_{11}|^2$) of WBGs with a period of 2.3 mm and a duty cycle of 55%. (c) Recorded spectrum (field amplitude) of the ADM measured at the Drop port. Inset: the transmittance (by field) of the stand-alone WBG that is integrated into the ADM.

At first, we study the WBGs used in the ADM prototype with COMSOL Multiphysics. By analyzing the transmission and reflection spectra of gratings featuring different pitches, we find that transmission dips and reflection peaks can be obtained at ~ 140 GHz using gratings with a period of 2.3 mm and a duty cycle of 55% ($w_2=1.27$ mm) (see Fig. 5.6(b)). Here we present simulation using lossy versus loss-less paper substrate material. Compared with the grating of 1.5 mm period discussed earlier (see Fig. 5.4(d)), gratings used in the ADM prototype feature somewhat narrower stop bands, while at the same time they feature significant reflected power in the stop band ($|S_{11}|^2 \sim 30\%$ loss-less paper, and $|S_{11}|^2 \sim 6\%$ lossy paper), which makes them suitable for building ADMs. It is noted that paper loss has a significant negative effect on the reflected power, and in future work alternative substrates will be used in gratings. Experimentally, a 6.9 mm-wide paper sheet featuring 43 grating periods of 2.3 mm pitch and symmetric arrangement of metal stripes on both sides of the paper substrate was prepared as described in Chapter 5.3.3. A resultant 10 cm-long WBG was measured and showed a minimal relative transmittance (by field) of 0.3 with

~ 4 GHz (FWHM) transmission dip at the Bragg frequency of 142.6 GHz (see Fig. 5.6(c) Inset). Finally, Fig. 5.6(c) shows the measured spectra at the Drop port of the ADM that uses the abovementioned WBG in the Through arm of the device (for details of the measurement see Appendix B.6). The dropped target range ~ 141 -145 GHz is clearly visible at the Drop port of the ADM despite the low reflection efficiency of the grating.

Finally, the simulations suggest that considerably more efficient (in reflection) gratings can be designed using classic quarter-wave condition for each section in the period, or even using more relaxed design criteria Eqs. 5.7 and 5.9, however, such gratings cannot be reliably manufactured using a simple hot stamping technique that was explored in this paper as they require significantly smaller metallic features and lower-loss substrates. We, therefore, consider the results of this section as a proof of principle with a clear path for optimization to be pursued in future works.

5.5 Conclusion

In this work, 3D printed micro-encapsulated two-wire THz plasmonic waveguide components and circuits have been investigated theoretically and experimentally. Modular THz components and reconfigurable circuits are built based on two-wire waveguides featuring two metalized plastic wire substrates suspended in air on deeply subwavelength supports and encapsulated inside a protective resin cage. Such components are fabricated using highly precise, efficient, and low-cost SLA 3D printing enhanced with wet chemistry metal deposition technique. Using CW-THz spectroscopy, we first characterized the transmission loss and the GVD of straight waveguides at 140 GHz, which are ~ 6 m⁻¹ (by field) and -1.5 ps/THz cm respectively. Next, the bending loss of bent two-wire waveguides was characterized experimentally as a function of bending radii for two different types of bend geometry. It was concluded that the presence of encapsulating cage significantly reduces bending loss due to stronger confinement of light in the gap between the two wires compared to the case of stand-alone two-wire waveguides. We find that even for a small bending radius ~ 5 cm, experimental bending loss does not exceed ~ 10 cm⁻¹ (by field). Next, we detailed two-wire WBGs that feature a thin paper sheet with a periodic sequence of metal strips placed in the gap between two wires. Metalized gratings were fabricated using a rapid prototyping hot stamping technique using thermofoils, laser printed templates, and a laminator. Experimentally, we find that even short 5 cm-long WBGs of this design can exhibit transmission dips with minimal relative transmittance

below 10^{-2} and a spectral width of 32 GHz. Finally, two kinds of THz plasmonic circuit prototypes were demonstrated, including a Y-shaped THz splitter/multiplexer that employs two coalescing waveguide bends, as well as an ADM that employs a reflective WBG. Experimentally, we find that the Y-shaped coupler features a negligible insertion loss (<0.5 dB) and transmission loss almost identical to that of a stand-alone bend section employed in its design. Finally, we found experimentally that an ADM exhibits a designed drop functionality with a spectral bandwidth of 2.8 GHz at the Bragg frequency of ~ 140 GHz. Based on these findings we, therefore, conclude that proposed 3D printed THz two-wire waveguides and components based on such waveguides present a viable technology for the robust, cost-effective, and highly reconfigurable THz optical circuits for signal processing, and sensing applications.

Acknowledge

This work was supported by the Canada Research Chairs I of Prof. Skorobogatiy in “Ubiquitous THz photonics” (34633), as well as China Scholarship Council funding of the doctoral fellowship of Y. Cao (201706250016).

Contributions

All authors conceived these experiments and contributed to their design. Y. C performed the numerical simulations and measurements. Y. C, K. N, H. G, G. X, and M. S contributed to writing the manuscript.

CHAPTER 6 ARTICLE 3: ADD DROP MULTIPLEXERS FOR TERAHERTZ COMMUNICATIONS USING TWO-WIRE WAVEGUIDE BASED PLASMONIC CIRCUITS

Yang Cao, Kathirvel Nallappan, Guofu Xu, and Maksim Skorobogatiy*

Génie physique, Polytechnique Montréal

*maksim.skorobogatiy@polymtl.ca

Submitted to Nature Communications

Abstract: Terahertz (THz) band is considered to be the next frontier in wireless communications. The emerging THz multiplexing techniques are expected to dramatically increase the information capacity of THz communications far beyond a single channel limit. In this work, we explore the THz frequency-division multiplexing modality enabled by novel ADM design. Based on modular two-wire plasmonic waveguides fabricated using AM and metallization techniques, we demonstrate four-port THz ADMs containing grating-loaded side couplers for operation at ~ 140 GHz carrier frequency. Particular attention is paid to the design of plasmonic WBGs and directional couplers capable of splitting broadband THz light in spectral and spatial domains, respectively. Finally, we demonstrate multiplexing and demultiplexing of THz signals with bit rates up to 6 Gbps using the developed ADMs. We believe that proposed plasmonic circuits hold strong potential to provide robust integrated solutions for analog signal processing in the upcoming THz communications.

6.1 Introduction

The global mobile data traffic is expected to reach 77.49 exabytes per month by the year 2022 [259]. According to the Shannon-Hartley theorem [260], in the presence of noise, the maximal bit rate supported by the transmission channel is proportional to the available bandwidth. Currently, most of the wireless systems operate in the overcrowded microwave band, which is not sufficient to meet the bandwidth demand of the near future. Shifting the carrier wave towards higher frequencies is inevitable in order to accommodate the imminent surge in data volume [261, 262]. Therefore, the terahertz (THz) frequency band (0.1-10 THz) is considered as the next frontier in

wireless communications [213, 263]. To date, there are already several demonstrations of free-space ultra-high bit rate data transmission (> 100 Gbps) using a single-channel THz link having a carrier frequency in 0.3-0.4 THz together with various optical multiplexing (ex. optical frequency and polarization division multiplexing) and modulation techniques (ex. quadrature amplitude modulation and quadrature phase-shift keying (PSK)) [133-135]. The capacity of the THz communication system can be further increased by using various THz multiplexing techniques [136, 137, 140]. Among them, frequency-division multiplexing, in which several discrete carrier frequencies support distinct users, is routinely used in fiber optic communications to multiply the data-throughput capacity. In optical networks, one typically uses carrier waves in C-band (infrared) with channel spacing less than 10 GHz, thus allowing simultaneous transmission of hundreds of channels with hundred MHz bandwidth each [264]. In THz communications, the current studies place the carrier wave frequency in the 100 – 300 GHz range with a single channel bandwidth of $\sim 10 - 40$ GHz, which can allow spectral allocation and simultaneous utilization of several tens of communication channels within this spectral range.

The key component in designing frequency division multiplexing systems is the ADM. It allows multiple carrier frequencies to share the same frontend, thus reducing the overall size and complexity of the communication networks [9, 39]. In optical frequency division multiplexing networks, the add-drop multiplexing is usually realized by the combination of mature optical elements such as ring resonator, phase-shifted grating, Bragg grating, arrayed waveguide grating, circulator, and coupler on the platform of silica-based planar lightwave circuits and fiber arrays [141-143, 145]. However, the ADMs capable of operation at THz frequencies are still in the early development due to the lack of universal standards for the THz communication components, as well as the relative abundance of possible, while untested, fabrications routes.

Using the directional coupling between two adjacent waveguides or the leaky wave of a single deformed waveguide, THz ADMs have been proposed based on parallel-plate waveguides and silicon substrates [39, 43, 44, 120, 138, 139]. Particularly, the silicon substrates also have great potential in developing several feasible THz ADM designs, such as diplexer and bandpass filters [265], ring resonators [42], and topological insulators [40]. Nevertheless, add/drop frequency tunability is problematic, and the top-of-the-line expensive fab infrastructure is required to fabricate silicon-based circuits. Besides, a THz ADM prototype composed of a lossy Y-coupler

and an external low-reflectivity Bragg grating was also fabricated using two-wire plasmonic waveguides [20, 180]. However, most of the reported THz ADMs contain only three ports, while to implement both channel dropping and adding of THz carrier waves, cascaded ADMs or four-port ADMs have to be employed in the communication networks.

In what follows, we report the design and characterization of four-port THz ADMs for frequency division multiplexing communications. The core of our system is modular micro-encapsulated two-wire plasmonic waveguides fabricated using stereolithography (SLA) 3D printing and wet chemistry metal deposition techniques reported recently in [20]. Due to the low-cost and wide availability of the fabrication infrastructure, the two-wire photonic circuits in which the plastic surfaces are selectively metalized are highly suitable for rapid prototyping and reproduction. Such waveguide features low transmission and bending loss, low GVD, broadband operation, as well as high coupling coefficient between connected Ws and with the conventional linearly polarized THz sources [122, 126]. Additionally, this two-wire waveguide provides a versatile platform to build highly reconfigurable and convenient to handle THz circuits, including the desired ADMs that enable advanced signal processing functionalities in THz communications. By replacing the decisive modular element of ADM circuits, the drop/add frequencies and the corresponding channel bandwidths can be readily changed without affecting the rest of the circuits. Furthermore, thermal and mechanical tuning of the proposed circuits is readily achievable as modal fields of air-core two-wire waveguides are easily accessible. This opens an important opportunity for such structures toward meeting the requirement of dynamic band allocation in THz communication networks [266].

One key element of our system is a WBG that serves as a wavelength-selective mirror [267]. By integrating the WBG into optical circuits, a tunable stopband and passband in the transmission and reflection spectra can be achieved. Hindered by the lack of THz circulators compatible with circuits [258, 268], the directional coupler is used as an alternative diplexer to combine THz signals in spatial domain, which is another key element of the proposed ADM circuit. Particularly, we develop an interferometric THz ADM where uniform Bragg grating is symmetrically added on two side coupled two-wire waveguides, which is a concept adapted from the mid-infrared range [269-271]. Compared with other ADM designs of similar configurations, such as grating-assisted contra-directional coupler [272] and grating-loaded Mach-Zehnder interferometer [273], the

aforementioned design has advantages of compact structure, simple design criteria, single-mode operation, while allowing relatively relaxed fabrication tolerances. Additionally, due to the low reflectance at the resonant frequency of a distributed feedback reflector (quarter-wave defect) inserted into the proposed two-wire WBG, another ADM design that is universal in the mid-infrared band where phase-shifted gratings are placed on directional coupler sections is not a promising alternative for our circuit [144, 145].

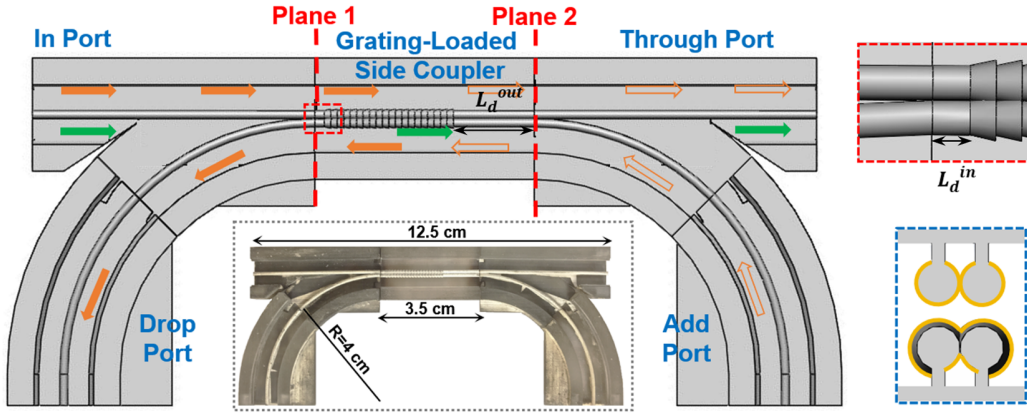


Figure 6.1 Schematic of the proposed four-port ADM circuit (top part is not shown) comprising a grating-loaded side coupler placed between two Y splitters

L_d^{in} and L_d^{out} are the distances between the grating end-facets and the side coupler edges (see an Insert in the red dotted box). The orange arrows indicate the path of a THz carrier wave that falls within the grating stopband (dropped or added signals). The green arrows indicate the path of a THz carrier wave outside of the grating stopband (through signal). The arrows of solid colors correspond to the waves launched into the In port and then either dropped or guided through. The hollow arrows correspond to the waves launched into the Add port and then added to the Through port. Insert in the blue dotted box presents a cross section of the grating-loaded side coupler.

Insert in the black dotted box presents an experimental four-port ADM circuit (top part is not shown).

This paper is organized as follows. Firstly, we develop high-reflectivity WBGs based on the two-wire THz plasmonic waveguides, with one of the wires featuring a periodic array of end-to-end connected truncated cones. As a result, we experimentally demonstrate stopbands of up to 14 GHz with a center wavelength that can be positioned anywhere in the 120-160 GHz range. Secondly,

we design and fabricate directional couplers based on two adjacent two-wire waveguides, and then confirm experimentally that a several centimeter-long coupler is capable of full-cycle coupling at 140 GHz carrier frequency over a broad bandwidth exceeding 60 GHz. Finally, we propose a four-port THz ADM circuit, where the grating-loaded side coupler plays the crucial role, which allows to spatially separate (drop) and add the THz wavelengths that fall within the grating stopband, while let all the other wavelengths within the coupler bandwidth to pass through. Two wideband Y splitters connected with the coupler are used to guide THz signals to/from the grating-loaded side coupler section from/to the desired ports of ADM circuits (see Fig. 6.1). Channel dropping and adding functionalities of ADMs for several THz carrier waves in the vicinity of ~140 GHz modulated up to 6 Gbps were demonstrated in experiments.

6.2 Results

6.2.1 Two-wire waveguide-based Bragg grating

The two-wire WBGs studied in this work are introduced by periodically varying the cross section of a single wire inside a micro-encapsulated two-wire waveguide [20]. The choice of end-to-end connected truncated cones in the grating structure (see Fig. 6.2(a)) was experimentally found to be the most reliable and stable for printing compared to other alternative designs (see Appendix C.1 for details on the design and fabrication of two-wire WBGs). Such WBGs typically feature high grating strengths and wide stopbands $\Delta\lambda \sim 0.1 - 0.2 \cdot \lambda_{Bragg}$ as their strong geometrical overlap with the modal field confined in the gap between two wires. The spectral position of the grating stopband can be estimated using standard quarter-wave condition $\lambda_{Bragg} \approx 2\lambda_{eff}$, where the effective refractive index of the grating mode for two-wire waveguides is close to that of air $n_{eff} \sim 1.1$.

As we will see in what follows, the operational bandwidth of the ADM is determined by that of the WBGs used in its design. In this work, by comparing optical properties of WBGs we find the optimal ridge height of truncated cones to be $H=0.21$ mm to ensure large operational bandwidth, reproducible optical performance, and manageable loss of ADMs. With the period length of a 20-periods WBG set to $\Lambda=1.03$ mm, the resultant stopband center frequency is 140 GHz with the corresponding bandwidth of ~18 GHz (FWHM) in numerical simulations.

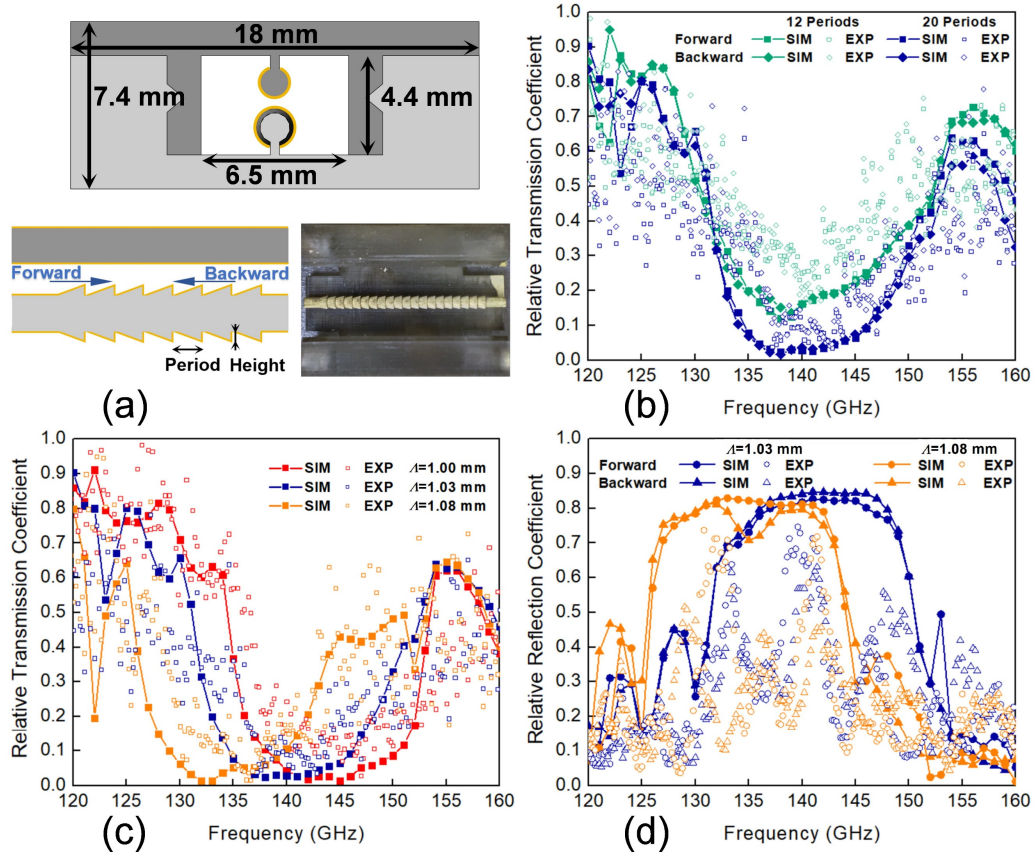


Figure 6.2 Numerical and experimental studies on the two-wire WBGs

(a) Schematic of the cross section of a two-wire WBG comprising two 3D-printed parts (different shades of gray), its side view, as well as the photograph of a fabricated WBG (top half (dark gray) removed). The gratings featuring a periodic sequence of truncated cones (light gray) are suspended in air (white) on dielectric supports and encapsulated within a plastic cage (light and dark gray). Both the cylindrical wire (dark gray) and the gratings are covered with a silver layer (gold) by wet chemistry deposition. (b) The numerical and experimental relative transmission coefficients of 2.5cm-long WBG sections comprising 12 and 20 periods ($\lambda = 1.03$ mm, $H = 0.21$ mm) with two possible traveling directions of the THz light. (c) The numerical and experimental relative transmission coefficients of 2.5cm-long WBGs containing 20 periods ($H = 0.21$ mm) as a function of the period length λ . The THz light travels in the forward direction along WBG (see Fig. 6.2(a)). (d) The numerical and experimental relative reflection coefficients of 2.5cm-long

WBG sections containing 20 periods ($H=0.21$ mm) for two different grating period lengths, and two possible propagation directions along WBGs.

Fig. 6.2(b) compares the numerical and experimental results for the relative transmission coefficient of two-wire WBGs containing different numbers of periods, and two possible directions of the THz light propagation. While more periods result in deeper transmission dips, experimental WBGs show somewhat shallower transmission spectra compared to the numerical simulations, which is attributed to imperfections in the geometrical structure of 3D printed gratings. Nevertheless, the experimental WBG with 20 periods exhibits a pronounced transmission dip near 140 GHz featuring a bandwidth of ~ 14 GHz (FWHM) and a minimal transmittance (by power) of less than 1%. Additionally, WBG transmission spectra are virtually symmetric when switching the input and output ports despite the WBG nonsymmetric structure. Furthermore, we confirm the designability of the WBG spectral response by varying grating periodicity (see Fig. 6.2(c)). Reducing the grating period from 1.08 mm to 1 mm shifts the center frequency of WBG stopband from 134 GHz to 145 GHz, while measured WBG bandwidth remains largely unaffected (~ 14 GHz).

The reflection spectra of WBGs were experimentally characterized using a CW-THz spectroscopy system together with a two-wire waveguide-based Y-coupler. Although there is a qualitative agreement between the measurements and theoretical predictions with spectral reflection peaks located within the WBG stopband, we also note strong ripples that are presented in the experimental reflection spectra (see Fig. 6.2(d)). These result from the standing waves formed in the cavity of the CW-THz spectroscopy setup, as well as inside of a photomixer silicon lens. Although such spectral oscillations can be somewhat mitigated via normalization with respect to a reference, they are, nevertheless, notoriously difficult to eliminate. This is especially true when the effective cavity length of the spectrometer changes during experiments, which is the case for measurements in the reflection mode when using different WBGs [19, 274]. Even though, we can still see that the relative reflection coefficient of a WBG with 20 periods and $A=1.03$ mm is ~ 0.7 in the spectral range between 133 GHz and 147 GHz.

6.2.2 Two-wire waveguide-based directional coupler circuit

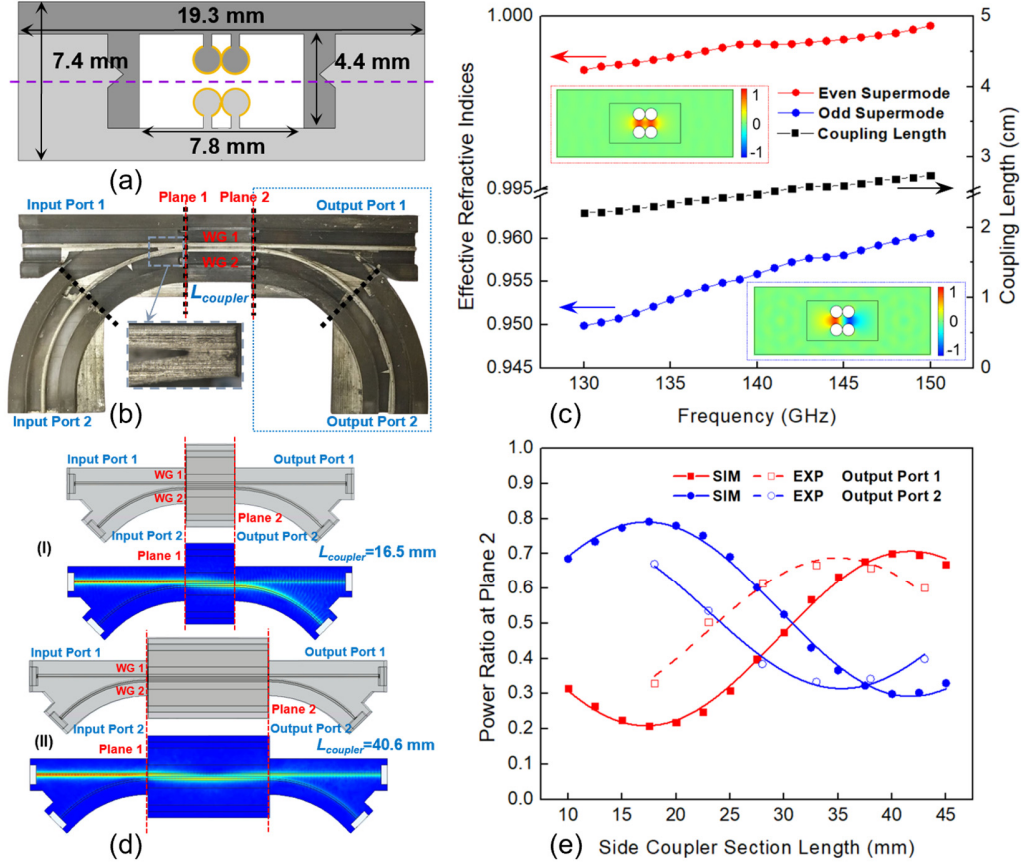


Figure 6.3 Numerical and experimental studies on two-wire directional coupler circuit

(a) Schematic of the cross section of a straight side coupler featuring two touching two-wire waveguides that are suspended in air on thin dielectric supports and encapsulated within a plastic cage. Gold defines the metallic layer, light and dark gray correspond to the two halves of a device printed separately in photosensitive resin. (b) A photo of the assembled directional coupler circuit (top half removed) comprising a side coupler section placed between two Y splitters. The black dashed lines define interfaces between distinct modular sections of the circuit. Insert: the enlarged view of the Y splitter end where curved and straight waveguides meet. (c) The numerical effective refractive indices of the odd and even supermodes that are supported by the side coupler section, as well as the corresponding coupling length. Inserts: the X-component of electric field distributions for the even and odd supermodes, which is in the direction that is the

same as the polarization direction of the supported modes. (d) 3D models of the directional coupler circuits, and the computed electric field distributions in the circuits when using the fundamental mode of IP 1 at 140 GHz as the excitation condition. (I) Case of the half-cycle coupler $L_{coupler}=16.5$ mm that results in the maximal power transfer from Waveguide 1 to Waveguide 2. (II) Case of the full-cycle coupler $L_{coupler}=40.6$ mm that results in the maximal power transfer from Waveguide 1 to Waveguide 2 and then back to Waveguide 1. (e) The numerical derived and experimentally measured power transmittance ratio of the OP 1 and OP 2 at Plane 2 as a function of the side coupler section length $L_{coupler}$.

Experimental realization of directional coupling using free-standing THz waveguides is typically challenging. This is due to the need for precise alignment of such waveguides to maintain a fixed inter-waveguide separation (normally on a sub-mm scale), which necessitates the use of cumbersome holders, spacers, etc. [124, 125, 131, 132]. In contrast, using high-definition 3D printing allows fabrication of the monolithic solutions that integrate waveguides, holders, and enclosure in a single step with precise control over the inter-waveguide separation. In the case of micro-encapsulated two-wire waveguides, the field of the fundamental mode is predominantly confined in the air gap between two wires [20]. Therefore, directional coupling between two separate waveguides is weak. To enhance the inter-waveguide coupling, we placed the cylindrical wires belonging to two different two-wire waveguides to touch each other and increased the enclosure width (by a single wire diameter) to accommodate these two waveguides (see Figs. 6.3(a) and 6.3(b)).

The effective refractive indices (n_e and n_o) of the even and odd supermodes supported by the side coupler are computed using the 2D mode solver tool of COMSOL Multiphysics, while the corresponding coupling length L_c between the two modes is estimated as $L_c = \lambda/2(n_e - n_o)$ (see Fig. 6.3(c)). For the presented design, the coupling length is $L_c \sim 24.5$ mm at ~ 140 GHz operational frequency, while even smaller coupling lengths (stronger coupling strengths) are possible to realize by allowing the two wires to partially overlap.

To spatially separate the THz light at the output end (Plane 2) and allow a two-port input (Plane 1), two Y splitters were added at both ends of the side coupler element (see Fig. 6.3(b)). This configuration was then used to build the four-port ADMs. The Y splitter features a curved two-

wire waveguide gradually approaching a straight one, while joining in a wedge configuration at Plane 2 (see the blue dotted region in Fig. 6.3(b)).

The optical performance of the complete directional coupler circuit as a function of the side coupler length (distance between Planes 1 and 2) was studied using a 3D module with ports of COMSOL Multiphysics. Particularly, we are interested in finding the relative signal intensities at Output ports 1 and 2 (OP 1,2) of the directional coupler circuit containing side couplers featuring different lengths when assuming that all the power is launched into Input port 1 (IP 1). An immediate complication is that two branches of the Y splitter used at the output side of the side coupler have significantly different losses as one of them is curved and longer compared to the straight one. Therefore, instead of simply plotting the power transmittance in the OP 1 and OP 2 assuming excitation at the IP 1 expressed via the corresponding elements of the scattering matrix ($T_{op\ 1,2}=|S_{OP\ 1,2; IP\ 1}|^2$) (see Appendix C.2), we characterize the performance of side coupler section by estimating the ratio of power carried by the two waveguides (Waveguide 1 and Waveguide 2) at its end (Plane 2) using:

$$T_{CW\ 1,2} = |S_{OP\ 1,2; IP\ 1}|^2 / T_{Y-branch\ 1,2} \quad (6.1)$$

$$Ratio_{CW\ 1,2} = \frac{T_{CW\ 1,2}}{T_{CW\ 1} + T_{CW\ 2}} \quad (6.2)$$

where $T_{Y-branch\ 1,2}$ are numerically computed power transmittances of the two stand-alone branches of a Y splitter (see Appendix C.3). The maximum power of THz light at 140 GHz operational frequency transfer from Waveguide 1 to Waveguide 2 is achieved by a 16.5 mm-long coupler, while the power is cycled back into Waveguide 1 in a 40.6 mm-long coupler. The corresponding electric field distributions of the two directional coupler circuits on the plane that is marked by violet dashed line in Fig. 6.3(a) are shown in Fig. 6.3(d).

Compared to the beat length between the two supermodes ($2L_c \sim 49$ mm), which is computed theoretically using a 2D model solver, we find that the full-cycle coupling is realized by the directional coupler circuit containing a side coupler with a somewhat smaller length (40.6 mm) (see Fig. 6.3(e)). This difference mainly stems from the fact that coupling action between two waveguides persists over some distance in Y splitters as in this element the curved and straight waveguides run almost in parallel to each other over a certain distance. Finally, the incomplete

power transfer in the coupler is due to the significant loss difference of the two supermodes that have different field overlapping with the lossy resin cage (see Appendix C.2). Additionally, due to the asymmetric structure of Y splitters, the directional coupler circuit is no longer symmetric, thus breaking the phase-matching condition between the two co-propagating modes that is required for the complete power transfer.

Experimental characterization of such circuits confirms sinusoidal behavior of the power coupling coefficients as a function of the side coupler length (see Fig. 6.3(e)). The experimentally found maximum power ratio for Waveguide 1 was obtained by a 35mm-long side coupler section, which is somewhat shorter than the predicted one. This is most probably related to the deviation of the experimental geometry of Y splitters from the ideal ones used in numerical modeling. As seen from the Insert of Fig. 6.3(b), due to the limited resolution of the 3D printer, the two waveguides remain joint for several mm at the entrance of a Y splitter, which results in stronger than expected inter-waveguide coupling in the fabricated Y splitters.

Due to the contribution of Y splitters to the coupling between the bus and dropping waveguides, we design the ADM circuit using a 35mm-long side coupler section that enables the full-cycle coupling at ~ 140 GHz operational frequency with a broadband operation of over 60 GHz owing to the modest variation in the coupling length (see Appendix C.2).

6.2.3 Grating-loaded side couplers for ADMs

The THz ADM circuits feature a grating-loaded side coupler placed between two Y splitters. Particularly, the directional coupler circuit enabling full-cycle coupling is modified by inscribing two Bragg gratings on a single set of two joint wires of the side coupler section (see Figs. 6.1 and 6.4(a)). While propagating in the grating-loaded side coupler, the THz signal within the grating stopband that is launched into In port on Waveguide 1 (Add port on Waveguide 2) is back-reflected by the gratings, and then transferred to Waveguide 2 (1) by the side coupler. The THz signal within the grating passband when launched into In port propagates through the grating-loaded side coupler and into Through port. Within the coupler bandwidth, the variation in the coupling length is moderate (see Fig. 6.3(c)), thus allowing high signal amplitude to be recorded at Through port. Separate numerical and experimental studies of Y splitters (see Appendix C.3) reveal that in such structures THz light mostly propagates in the forward direction regardless of the launching port

with only a minimal amount of back-reflections and cross-talk (larger than 30 dB by power for any port). When integrating Y splitters into ADM circuits, their contribution to the crosstalk is negligible, with the main negative effect being additional propagation loss incurred by the signals propagating through the curved arms. Therefore, instead of using the actual powers at the different ports of ADM circuits after propagation through Y splitters, it is more convenient for the design purposes to use powers right at the output of grating-loaded side coupler element (Planes 1 and 2), which can be estimated by using Eq. 6.1 in numerical simulations (see examples in Fig. 6.4(a) and Appendix C.4 for detailed information).

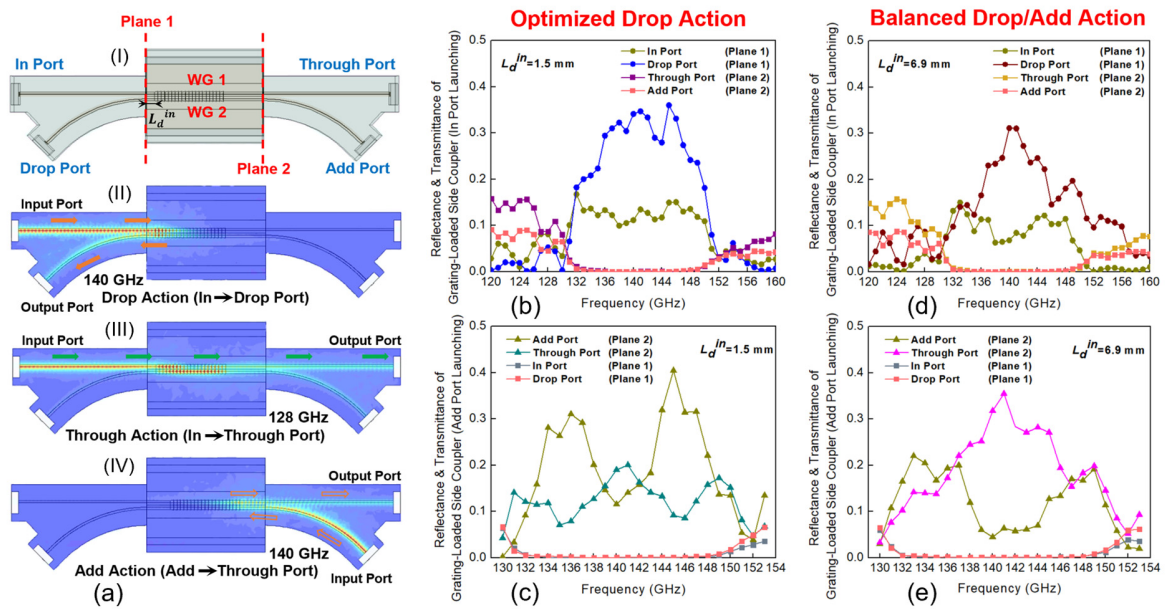


Figure 6.4 Numerical study on the grating-loaded side coupler sections

(a) (I) Schematic of the ADM circuit used in numerical simulations of the experimental ADM shown in Fig. 6.1. It is composed of two Y splitters and a 35mm-long grating-loaded side coupler containing 20 periods with $A=1.03$ mm, $H=0.21$ mm. The computed electric field distributions in the ADM circuit with optimized drop action ($L_d^{in}=1.5$ mm) when using the fundamental mode of In Port (II) at 140 GHz (within grating stopband), and (III) at 128 GHz (within grating passband) as the excitation condition, and (IV) that in the ADM circuit with balanced drop/add action ($L_d^{in}=6.9$ mm) when using the fundamental mode of Add Port at 140 GHz (within grating stopband) as the excitation condition. Numerical transmittances and reflectance (by power) of

grating-loaded side coupler with $L_d^{in}=1.5$ mm at Planes 1 and 2 of the ADM with optimized drop action when using the fundamental mode of (b) In port (Plane 1), and (c) Add port (Plane 2) as the excitation condition. Numerical transmittances and reflectance (by power) of grating-loaded side coupler with $L_d^{in}=6.9$ mm at Planes 1 and 2 of the ADM with balanced drop/add action when using the fundamental mode of (b) In port (Plane 1), and (c) Add Port (Plane 2) as the excitation condition. Figs. 6.4(b-e) are computed using Eq. 6.1 and numerical 3D models shown in Fig. 6.4(a).

It should be noted that the relative position of the 20.6mm-long gratings inside the 35mm-long side coupler section (controlled by the L_d^{in} parameter) gives rise to different interference conditions between the two supermodes of a coupler, which we use to find optimal coupler designs. Particularly, to optimize the drop action we choose L_d^{in} that results in the highest power at Drop port (Plane 1) within the grating stopband. Defining L_g to be the light penetration distance into gratings, the desired relative position of the grating section L_d^{in} can be found from:

$$L_d^{in} + L_g \approx L_c / 2 \quad (6.3)$$

Another optimal ADM design is to reduce the difference between spectral performance of the add and drop action at expense of their absolute performance, thus resulting in the balanced ADM. In this optimization, one minimizes the difference between transmission through the Through port under Add port launching and transmission through the Drop port under In port launching.

By comparing the ADM circuits featuring different L_d^{in} , the grating-loaded side couplers featuring L_d^{in} of 1.5 mm and 6.9 mm are chosen to enable the ADM circuits with optimized drop action and balanced drop/add action, correspondingly. Figs. 6.4(b-e) show the numerically computed transmittance and reflectance of these two grating-loaded side couplers when the light is launched at In port (Plane 1) and Add port (Plane 2). We note that L_g and L_c parameters are frequency-dependent across the grating stopband. Therefore, ripples in transmittance and reflectance spectra of various ports are observed even for these optimal designs.

These two ADM designs were then experimentally characterized using a CW-THz spectroscopy system. Firstly, we present the normalized power transmittances at Planes 1 and 2 to characterize the performance of the grating-loaded side coupler section while decoupling it from the losses incurred in Y splitters of an ADM. By using lower loss Y splitters one can significantly improve

the loss characteristics of complete ADM devices, which are ultimately limited by those of the grating-loaded side coupler sections. While in this work, we use relatively lossy Y splitters comprising straight and curved branches. Further research is to develop more performant splitters, which is, however, beyond the scope of this paper.

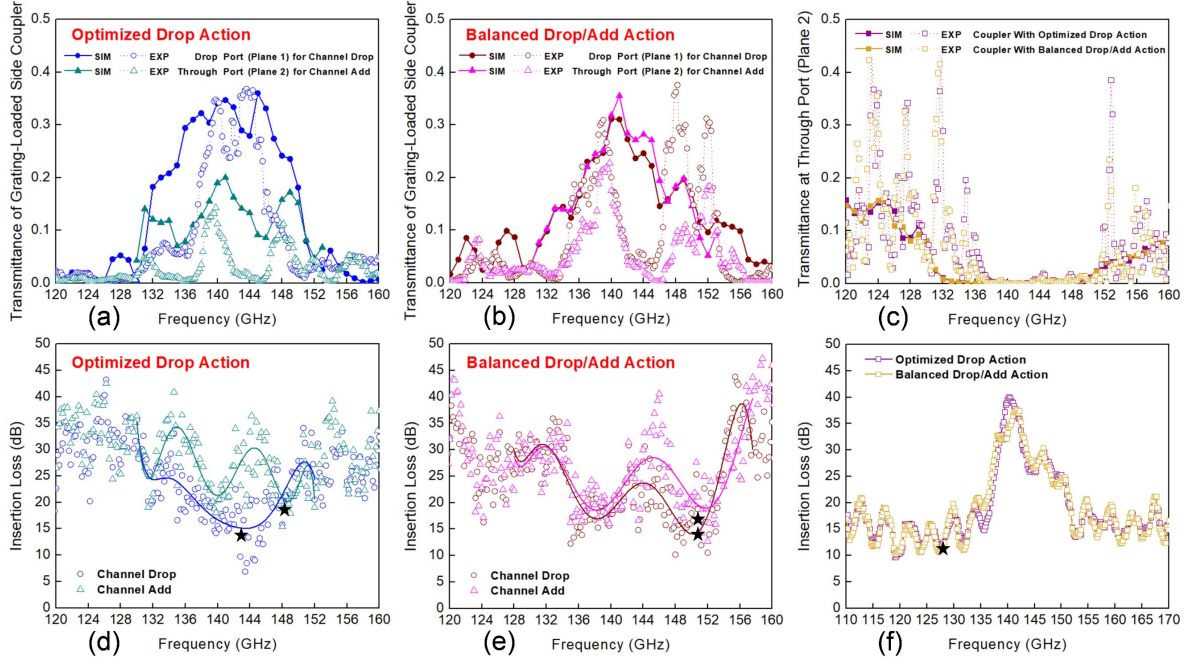


Figure 6.5 Power transmittances of grating-loaded side couplers and insertion losses of complete ADM circuits

Numerical simulation and experimental results for the power transmittances of the grating-loaded side couplers that enable (a) the ADM with optimized drop action ($L_d^{in}=1.5$ mm) and (b) the ADM with balanced drop/add action ($L_d^{in}=6.9$ mm) under In port launching (Plane 1) and Add port launching (Plane 2) conditions. (c) Numerical simulation and experimental results for the power transmittances of these two grating-loaded side couplers at Through port (Plane 2) under In port launching (Plane 1) condition. The measured insertion losses (by power) under In (Add) port launching conditions as registered at Drop (Through) port of the complete ADM circuit (see Fig. 6.1) exhibiting (d) optimized drop action, and (e) balanced drop/add action. Solid lines are the 8th-degree polynomial fits. (f) The measured insertion losses (by power) under In port launching condition as registered at Through port of the complete ADM circuits.

In Fig. 6.5(a) we present experimental and numerical transmittances at Drop port (Plane 1) under In port launching (Plane 1) and transmittances at Through port (Plane 2) under Add port launching (Plane 2) of the grating-loaded side coupler that enables the ADM circuit with optimized drop action. While an overall good correspondence between numerical and experimental data is observed, we also note that experimental transmittances show more pronounced ripples in their spectra, as well as somewhat lower bandwidths. This can be attributed to the suboptimal performance of the imperfect Bragg gratings due to manufacturing imperfections, as well as under-optimized (with respect to the Drop port) functioning of the Add port.

Additionally, compared with the numerical Bragg gratings featuring ideal geometry, the geometrical nonuniformity of the fabricated structure leads to the variation in the frequency-dependent L_g . As a result, it gives rise to the discrepancy in the interference of THz signal within the grating stopband propagating in the numerically and experimentally studied ADM circuits (Eq. 6.3), thus resulting in the different transmittance of Drop port under In port launching (Through port under Add port launching). This inconsistency becomes pronounced for the grating-loaded side coupler designed for the ADM circuit with balanced drop/add action (see Fig. 6.5(b)). However, it is noted that similar transmittances were measured at Drop port (Plane 1) for channel dropping and Through port (Plane 2) for channel adding in experiments. Furthermore, Fig. 6.5(c) shows that the measured power transmittances at Through port (Plane 2) under In port launching (Plane 1) condition for these two grating-loaded side couplers in optimal designs are similar.

When inserting the complete ADM circuits containing these two grating-loaded side couplers (see Fig. 6.1) into two-wire waveguide-based THz communication networks, the insertion losses of THz light registered at different ports under In and Add port launching conditions are shown in Figs. 6.5(d-f) (see Appendix C.5 for details).

6.2.4 Characterization of ADMs using THz communication system

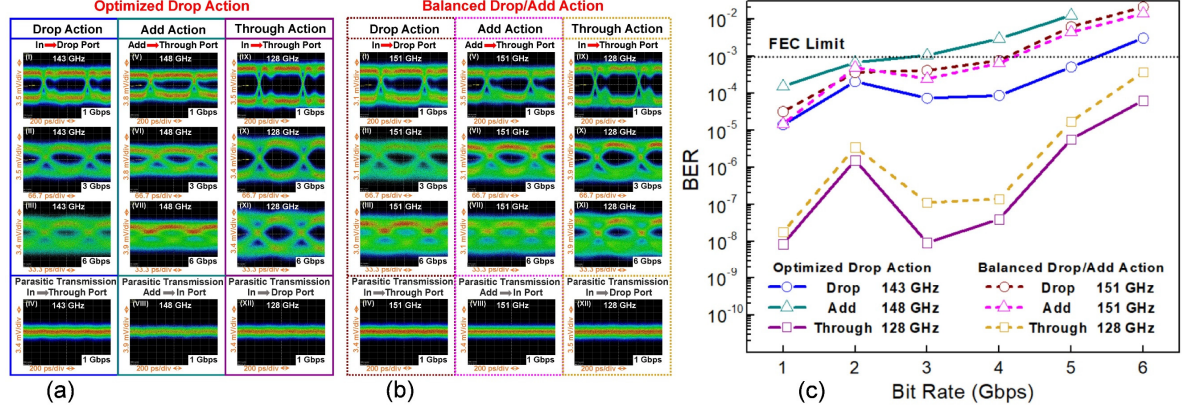


Figure 6.6 Experimental study of two-wire ADM circuits for THz communications

(a) Eye patterns for the THz signals of different bit rates and different carrier frequencies propagating through the THz ADM circuit with optimized drop action. Measurements at (I-III) Drop port and (IV) Through port (In port launch, 143 GHz carrier), (V-VII) Through port and (VIII) In Port (Add port launch, 148 GHz carrier), as well as (IX-XI) Through port and (XII) Drop port (In port launch, 128 GHz carrier). (b) Eye patterns for the THz signals of different bit rates and different carrier frequencies propagating through the THz ADM circuit with balanced add/drop action. Measurements at (I-III) Drop port and (IV) Through port (In port launch, 151 GHz carrier), (V-VII) Through port and (VIII) In Port (Add port launch, 151 GHz carrier), as well as (IX-XI) Through port and (XII) Drop port (In port launch, 128 GHz carrier). The eye patterns featuring obvious eye opening were obtained by characterizing the response of these two ADMs at different ports in the spectral positions that are marked by black stars in Figs. 6.5(d-f).

(c) Measured BER versus bit rate of the THz carrier wave propagating through two ADM circuits.

Finally, we experimentally characterized the two THz ADM circuits, one with optimized drop action ($L_d^{in}=1.5$ mm) and the other one with balanced add/drop action ($L_d^{in}=6.9$ mm), using an in-house photonics-based THz communication system with amplitude-shift-keying modulation format. The eye patterns are recorded at different ports of ADM circuits for THz signals within the grating stopband (add/drop action), as well as within the grating passband (through action) for various data rates as shown in Figs. 6.6(a) and 6.6(b). Due to the relatively high insertion loss of

our devices and low power of the optical THz source, the operational data rates are limited to ~6 Gbps.

For the ADM with optimized drop action, the minimal insertion loss (~14 dB) for channel dropping is observed in the middle of the grating stopband at 143 GHz (see Fig. 6.5(d)). Therefore, when the THz signal with the carrier frequency of 143 GHz is launched into In port, the eye pattern recorded at Drop port shows the highest eye amplitude within the grating stopband (see Fig. 6.6(a) I-III), while the eye diagram for the parasitic transmission into Through port is shown in Fig. 6.6(a) IV. As only the drop action has been optimized, the performance of the add action of this ADM is not symmetric with respect to that of the drop action. Thus, the highest efficiency of the add action is achieved within the grating stopband at 148 GHz (insertion loss of ~18 dB). In experiments, THz signal was launched into Add port and measured at Through port for different data rates (see Fig. 6.6(a) V-VII), while parasitic transmission into In port is shown in Fig. 6.6(a) VIII. The corresponding BERs for the added (Through port) and dropped (Drop port) signals are shown in Fig. 6.6(c), from which it is clear that a nonsymmetric ADM also features nonsymmetric BER performances for the add and drop actions.

For the THz ADM with balanced drop/add performance, the lowest insertion loss (~15 dB) is at 151 GHz within the grating stopband (see Fig. 6.5(e)). Unsurprisingly, the resultant eye patterns for add and drop functions are similar and so are the corresponding BER curves (see Figs. 6.6(b) I-III & V-VII and 6.6(c)). In Fig. 6.6(b) IV and VIII we also show the parasitic transmission in Through port for the drop action and In port for the add action, correspondingly.

Despite the difference in the channel dropping and adding functions of these two ADMs, the through function of both ADMs in the grating passband is remarkably similar (see Fig. 6.5(f)). This is manifested by the similar eye patterns (see Figs. 6.6(a) and 6.6(b) IX-XI) and BER curves (see Fig. 6.6(c)) for THz signals within the grating passband (ex. 128 GHz). Such similar performance in the passband is expected as the main difference between these two designs is the relative position of gratings within the side coupler sections of a fixed length. In the passband, though, transmitted light will only see the total length of the coupler circuit, while being somewhat modified by the presence of gratings. Parasitic transmissions into Drop port when the signal in the grating passband is launched into In port for through action are shown in Figs. 6.6(a) and 6.6(b) XII. It is found that

the crosstalk for the drop/add function in the stopband and through function in the passband is below the system noise level.

Finally, we present the BER response of these two ADM circuits (see Fig. 6.6(c)). In the analysis, we have to distinguish the through action in the grating passband from the drop/add actions in the grating stopband. For the through action, it is the dispersion and transmission losses of the straight Ws along the In – Through path of ADMs, as well as dispersion and losses of the Bragg gratings in the passband that limit the data rates. For the drop/add action, it is the dispersion and losses in the straight and curved branches of a Y splitter, as well as dispersion and losses of the Bragg gratings in the stopband that limit the data rates. Generally, modal dispersion leads to signal scrambling that manifests itself in the eye diagram distortion and closing of the eye pattern. From Fig. 6.6(c) we conclude that the through action in grating passband can support signal bandwidth greater than 6 Gbps as the maximal bitrate is mainly limited by the dispersion of a straight waveguide (assuming operation away from the edge of grating stopband). At the same time, it is also clear that the signal bandwidth for the drop/add action is rather limited by the size of the grating stopband, which limits useful bitrates to ~2-5 Gbps (see Appendix C.6 for details).

Additionally, losses of various ADM subcomponents significantly affect the BER of the device due to the negative effect of the noise on the detection accuracy. We observe that the highest loss in our device of ~9 dB comes from the 6.3cm-long curved branch of a Y splitter. This loss is mainly due to radiation from a curved waveguide and ohmic losses of plasmonic modes. Next, the grating-loaded side coupler section typically results in ~7 dB loss for operation in the grating passband (for through action), as well as >4 dB loss for operation in grating stopband (for drop and add action). This loss is mainly due to the mismatch between the modal fields of straight two-wire waveguides and gratings, ohmic losses, as well as imperfections in the grating structure. Next, there is butt-coupling loss of ~3 dB at each interface between ADM and waveguide-coupled THz emitter and detector [20], which has not been counted in Figs. 6.5(d-f). Finally, there are relatively low losses of straight waveguides, (0.4 dB/cm) which are mostly due to ohmic losses in the deposited silver layer incurred by the plasmonic modes. As a result, our ADMs feature relatively high insertion losses and a modest signal-to-noise ratio value (see Appendix C.7 for details).

6.3 Discussion

We demonstrated four-port ADM circuits capable of channel adding and dropping for applications in THz communication systems operating within frequency division multiplexing modality. We used 3D-printed two-wire plasmonic waveguide as a base technology to develop reconfigurable plasmonic circuits comprising WBGs, directional couplers, grating-loaded side couplers, and Y splitters. We believe that the air-core two-wire waveguides offer many advantages for THz circuit development, including: low losses due to the high modal presence in air, device tunability due to ease of access to modal fields, 3D integration potential, modular nature, and low coupling loss between modules, as well as the capability for robust and cost-effective prototyping and fabrication. Two ADM types were studied, one is a drop action optimized design, the other one is a balanced drop/add design, both featuring experimental bandwidths of 12 GHz (grating stopband) in the vicinity of 143 GHz. For the drop optimized ADM circuit, drop action with data rates of up to 5 Gbps at 143 GHz carrier and add action with data rates of up to 3 Gbps at 148 GHz carrier were confirmed to result in bit error rates lower than 10^{-3} (forward error correction (FEC) limit). For the balanced add/drop multiplexer design, both add and drop actions supported data rates of up to 4 Gbps at 151 GHz carrier with $\text{BER} < 10^{-3}$. Through action in the grating passband (ex. 128 GHz) was shown to support bitrates exceeding 6 Gbps for both designs.

The main challenge for the proposed ADM designs was relatively high insertion losses (~ 10 dB for through action and larger than 14 dB for drop and add action) together with the butt-coupling loss of ~ 6 dB. The main reasons for such losses, in order of importance, are: suboptimal Y splitter (~ 9 dB), insertion losses of Bragg gratings, and scattering in gratings due to fabrication imperfections (~ 7 dB for grating passband and > 4 dB for grating stopband), butt-coupling loss at each interface (~ 3 dB), transmission losses of straight two-wire waveguides (~ 0.4 dB/cm). We believe that further work on relatively straightforward optimization of ADM circuits, including employing more efficient splitter design and better fabrication strategies, as well as reducing coupling losses to detector and emitter by geometry optimization of output ports, could reduce the insertion loss by 5-10 dB. It can also improve and balance the performance of add and drop actions, thus rendering ADM devices highly suitable for ultra-fast analog signal processing in THz communications.

6.4 Methods

6.4.1 Fabrication of two-wire waveguide components

For the ease of fabrication, each proposed micro-encapsulated two-wire plasmonic waveguide component such as straight and curved WS, WBG module, directional coupler, and grating-loaded side coupler, is split into two complementary parts. Each part comprises of one or two joint wires (depends on the waveguide component) that are attached to a half cage using deeply subwavelength dielectric support ridges of width $150\text{ }\mu\text{m}$ (see Figs. 6.1, 6.2(a), and 6.3(a)) [20]. These structures were then fabricated using an SLA 3D printer (Asiga[®] Freeform PRO2) that features an XY-axis resolution of $50\text{ }\mu\text{m}$. It is noted that the length of the waveguide is fabricated along the Z-axis of the 3D printer. To ensure high geometrical precision, the parts of the waveguide component with periodic variation in cross sections were printed using the finest resolution in the Z-axis (layer thickness of $10\text{ }\mu\text{m}$). While the parts with smooth surfaces were fabricated with the Z-axis resolution of $25\text{ }\mu\text{m}$ to reduce the fabrication duration and moreover it does not affect the overall performance of the component. After fabrication, the inner surface of the cage was covered using masking tape leaving the plastic wire uncovered. Then, a silver layer was deposited on top of the plastic wires using wet chemistry deposition to form conductive surfaces. Finally, the two-wire waveguide components were obtained by assembling the two selectively metalized parts by sliding the corresponding parts into each other using V-grooves and V-ridges that were printed onto the cage. The proposed THz circuits (directional coupler and ADM circuits) were assembled from these two-wire waveguide components using another set of alignment and connectorization elements that are imprinted onto the cage end facets for seamless connectorization (see Figs. 6.1 and 6.3(b)).

6.4.2 Characterization of two-wire WBGs

The proposed micro-encapsulated two-wire WBGs were characterized using the CW-THz spectroscopy system (Toptica Photonics) [182-184]. The schematic of the experimental setup is shown in Appendix C.8 and briefly explained as follows. Two distributed feedback (DFB) lasers with the power of $\sim 30\text{ mW}$ each, operating in the infrared C-band with slightly different emission wavelengths are used as the source of THz generation. A 50:50 fiber coupler is used to combine

the two laser beams and split into both emission and detection arms, respectively. By applying AC bias voltage to the emitter photomixer, the THz radiation corresponding to the beat frequency between the two DFB lasers is generated. The output THz frequency can be varied by simply tuning the emission wavelengths of the lasers. A similar photomixer (without bias voltage) and a lock-in amplifier are used in the THz detection arm. The focused linearly-polarized CW-THz beam transmitting through the waveguide components is re-collimated and the amplitude of the THz signal is recorded using lock-in detection. The phase of the THz signal is simultaneously recorded by using the fiber stretchers of equal lengths that are connected to both emitter and detector arms.

The relative transmission coefficient of WBG was characterized as follows. Firstly, a two-wire WS featuring the same length as the WBGs (2.5 cm) was placed between two WSs (3 cm). The assembled two-wire waveguide was connected with WR6.5 conical horn antennas (Virginia Diode, Inc.) at both ends, and then inserted into the THz beam path of the spectroscopy system with the input and output planes of the waveguide flanges at the focal points of plano-convex lenses (PCL1 and PCL2). It is noted that a metal barrier is placed around the horn antenna at the input port to block the residual THz signal from entering the detector. Then, the transmission spectrum (by field) of the assembled waveguide was measured as the reference. Next, the 2.5cm-long WS was replaced by the WBG element, and the transmission spectrum of the assembled waveguide component was recorded. The relative transmission coefficient (by field) of WBG was finally obtained by dividing the measured spectrum with WSs by the reference.

The relative reflection coefficient of WBG was characterized as follows. Firstly, the two-wire Y-coupler and the WBG were assembled using the interconnects at the end facets of both components. Then, two WR6.5 conical horn antennas were connected to the unused ports, namely input and output ports of the Y-coupler. The THz light was launched into the input port of the Y-coupler, guided through a curved arm of the coupler, and reflected from the WBG under study. The reflected light was then divided equally by the Y junction and directed towards both the input and output ports. The transmission spectrum of THz light at the output port was recorded. Next, the WBG was replaced by a planar-metallic mirror to completely reflect the THz signal at the Y-junction. The transmission spectrum recorded at the output port was used as the reference. Finally, the relative reflection coefficient (by field) of WBG was obtained by comparing these two measured transmission spectra.

6.4.3 Characterization of side coupler section

The THz side coupler containing two two-wire waveguides was characterized as follows. Firstly, the side coupler was placed between two Y splitters (see Fig. 6.3(b)). Each port of the assembled THz circuit was connected to a WR6.5 conical horn antenna, and then inserted into the CW-THz spectroscopy system (see Appendix C.9). Initially, the THz signal was launched into IP 1 and the transmitted power received at OP 2 was recorded. Then, by rotating the rotary section by 90° in the clockwise direction, the transmitted power at OP 1 was recorded. The power of THz light in the Waveguide 2 and 1 at the output plane of the side coupler section (Plane 2) (see Fig. 6.3(b)) was obtained by dividing the transmitted power recorded at OP 2 and OP 1 by the insertion loss of the curved and straight two-wire waveguide in the two arms of Y splitter (see Appendix C.3), correspondingly. The power ratio of each waveguide was then computed by dividing its derived output power by the sum of these two values. By subsequently abrading the side coupler section to reduce its length and repeating the similar measurements, the power ratios of the two two-wire waveguides of straight side coupler sections featuring different lengths were obtained.

6.4.4 Characterization of two-wire ADM circuits using CW-THz spectroscopy system

The transmittance (by power) of grating-loaded side couplers and the insertion loss (by power) of complete THz ADM circuits (see Fig. 6.1) were characterized using a CW-THz spectroscopy system. The grating-loaded side coupler section was placed between two Y splitters. Each port of the assembled THz ADM circuit was then connected with a WR6.5 conical horn antenna. Firstly, to measure the transmittance of Drop port under In port launching at Plane 1 of grating-loaded side coupler for channel dropping, the ADM circuit was inserted into the CW-THz spectroscopy system with the input and output planes of waveguide flanges connected with In and Drop ports at the focal points of PCL1 and PCL2 (see Appendix C.9). The transmitted power spectrum of Drop port was recorded when the THz light was launched into In port. Next, the ADM circuit was replaced by a two-wire waveguide assembled by straight and curved WSs, which features the same length with the sum of the two arms of a Y splitter. Its transmitted power spectrum was recorded as the reference. The transmittance of Drop port at Plane 1 of the grating-loaded side coupler was then

obtained by dividing the measured transmitted power spectrum at Drop port of the complete THz ADM circuit by this reference spectrum to decouple it from the losses incurred in the Y splitter.

Next, the reference spectrum that is used to characterize the insertion loss of a complete THz ADM circuit when it is inserted into a two-wire waveguide-based communication system was obtained by dividing the measured transmitted power spectrum of a straight two-wire waveguide by its transmission loss [20]. The insertion loss (by power) of the THz carrier wave for channel dropping was then computed by dividing the measured transmitted power spectrum at Drop port of THz ADM under In port launching condition by this reference. The transmittance of Through port of grating-loaded side coupler under Add port launching condition at Plane 2 for channel adding and the corresponding insertion loss of complete ADM circuit were characterized using the similar processes after placing the input and output planes of waveguide flanges connected with Add and Through ports at the focal points of PCL1 and PCL2 in CW-THz spectroscopy system.

To characterize the transmittance of Through port at Plane 2 of the grating-loaded side coupler section under In port launching (Plane 1) condition, the THz ADM circuit was placed inside the CW-THz spectroscopy system with the input and output planes of waveguide flanges connected with In and Through ports at the focal points of PCL1 and PCL2. Then the transmitted power spectrum of Through port was recorded when the THz light was launched into In port. Next, the transmitted power spectrum of a two-wire waveguide having the same length with the sum of straight arms in two Y splitters was recorded as a reference spectrum. The transmittance of Through port at Plane 2 was obtained by dividing the transmitted power spectrum recorded at Through port of ADM by this reference. The insertion loss of the THz carrier wave propagating from In port to Through port of the complete ADM circuit was then computed by comparing the transmitted power spectrum recorded at Through port and the reference spectrum which has been used to measure the insertion loss of ADM for channel dropping and adding.

6.4.5 Characterization of ADM circuits using THz communication system

The two-wire plasmonic ADM circuits were also characterized using an in-house photonics-based THz communication system. The schematic diagram of the experimental setup is shown in Appendix C.10 and briefly explained as follows. In the transmitter section, two independently tunable DFB lasers (Toptica Photonics) operating in the infrared C-band with slightly different

center frequencies are combined using a 3 dB coupler as the source of THz generation. The baseband signal source of pseudorandom bit sequence (PRBS) with a varying bit rate from 1 Gbps to 6 Gbps and pattern length of $2^{31}-1$ is generated by the pulse pattern generator (PPG) unit integrated in the test equipment (Anritsu-MP2100B). The baseband signal is then amplified using the RF amplifier (Thorlabs-MX10A) which drives the Mach-Zehnder modulator (Thorlabs-LN81S-FC) to modulate the intensity of laser beams. Then the modulated laser beams are amplified using an erbium-doped fiber amplifier (EDFA) (Calmar laser-AMP-PM-18) and injected into a waveguide coupled uni-traveling-carrier-photodiode (UTC-PD) photomixer (NTT Electronics) to generate modulated THz carrier wave with operation frequency corresponding to the beat frequency of the two tunable DFB lasers. In the receiver section, the THz carrier wave is detected and demodulated by a zero bias Schottky diode (Virginia Diodes-WR6.5-ZBD-F), and then amplified using a high gain low noise amplifier (LNA) (Fairview Microwave-SLNA-030-32-30-SMA). Finally, the eye pattern and BER are recorded using the test equipment (Anritsu-MP2100B) [26, 185].

In experiments, the THz carrier wave within the spectral range of 110 -170 GHz having the power in the range between 125 μ W and 250 μ W was butt-coupled into the THz ADM circuit via a 1-inch-long WR6.5 rectangular waveguide (Virginia Diodes WR6.5). A similar arrangement was used to connect the output port of the THz ADM circuit and the Schottky diode (see Appendix C.10). We switched the ports of ADM circuits connected with the THz transmitter and receiver, and characterized the THz carrier wave featuring operation frequencies in the stopband and passband of gratings that are loaded on the side coupler section subsequently. Three scenarios, that are, the transmitter and receiver are connected to In and Drop ports, In and Through ports, as well as Add and Through ports, correspondingly, were mainly studied. In each case, the eye pattern and the corresponding BER measurements of different bit rates were carried out for the carrier frequencies in the grating stopband and passband of the ADM circuits, respectively. It is noted that, during BER measurements, the decision threshold was optimized to equalize the insertion error (digital 0 is mistaken as digital 1) and omission error (digital 1 is mistaken as digital 0). It is then recorded within the duration of $1/(\text{target BER} \times \text{bit rate})$, where the target BER was set as 10^{-12} (error-free).

6.4.6 Numerical simulation

The numerical studies of the proposed WBGs, directional coupler circuits, and ADM circuits were carried out using the commercial finite element software COMSOL Multiphysics within the 3D finite element frequency domain module with ports. Within this formulation, transmission and reflection can be characterized by using scattering matrix coefficients (S-parameters) related to each defined port. In our simulations we used frequency-dependent refractive index ($n_{resin}(f)=1.654-0.07f$ [THz]) and material absorption ($\alpha(f)$ [cm^{-1}]= $0.64+13.44(f$ [THz])²) of resin (used in 3D printing) in THz spectral range of 0.1-0.3 THz, which were obtained in a prior experimental study detailed in Ref. [100]. The metallic wires were modeled using IBC at the wire surface together with the Drude-Lorentz model for the dielectric constant of silver obtained from [20, 235]:

$$\epsilon_m = 1 - \frac{\omega_p^2}{\omega^2 + i\omega\gamma_b} \quad (6.4)$$

where $\omega_p=2\pi \cdot 2.185\text{e}15$ Hz is the plasma frequency of silver, and $\gamma_b=2\pi \cdot 2.69\text{e}14$ Hz is the fitted value of the damping coefficient of the Ag layer deposited on resin support in THz spectral range.

Due to the geometrical symmetry of the two-wire WBG module, only half of this structure together with PEC boundary condition was used in numerical simulations. When the THz light is launched using port boundary condition at the input facet of the WBG, the reflection coefficient at the same port (S_{11}) and transmission coefficient at the port on the other end facet (S_{21}) were computed (see Appendix C.11 for example).

By following the similar procedure discussed above, the directional coupler and ADM circuits were studied using numerical simulations. Different from the WBG models, the complete structure of the directional coupler and ADM circuits were studied using 3D models due to their asymmetric structures. The scattering matrix coefficient (S^2) at the four defined ports are computed under various launching conditions, i.e., OP 1 and OP 2 under IP 1 launching for directional coupler circuit (see Fig. 6.3(d)), as well as In, Drop, Add, and Through ports under In port launching and Add port launching conditions for ADM circuit (see Fig. 6.4(a)). The transmittance and reflectance (by power) of side couplers at Planes 1 and 2 were then obtained using Eq. 6.1.

Acknowledge

This work was supported by Prof. Skorobogatiy Canada Research Chair I in Ubiquitous THz photonics (34633); China Scholarship Council (201706250016).

Contributions

All authors conceived these experiments and contributed to their design. Y. C and K. N performed the numerical simulations and measurements. Y. C, K. N, G. X, and M. S contributed to writing the manuscript.

CHAPTER 7 GENERAL DISCUSSION

In this chapter, we discuss the limitations of the AM techniques employed in THz waveguide fabrication and corresponding further optimizations, as well as explore the potential of the proposed quasi-two-wire plasmonic waveguide in THz communications.

7.1 Limitation of employed manufacturing techniques and further optimization

In this thesis, we explored the design, fabrication, and characterization of two types of THz waveguide components, that is, dielectric hollow-core fiber and plasmonic waveguide. In contrast to the numerically studied model with an ideal geometry, owing to the limited resolution and inherent defects of the manufacturing techniques, the obtained THz components suffer deformation and malfunction to a certain degree, thus resulting in the deterioration of optical performance in experiments (e.g., larger insertion loss, less pronounced or absent spectral singularity, and a shift in the operation frequency). In this section, we summarize the limitations of the manufacturing techniques used in this thesis, their impact on the fabrication and optical performance of THz waveguide components, and possible optimization and alternative methods.

For the hollow-core PBG Bragg waveguide, the geometrical deviation of the structure obtained from that of the ideal one is primarily attributed to the limited resolution of the FDM 3D printer. Although the sub-micrometer step size of mechanical parts ensures a small error in the relative position of the extruder and the built plane during 3D printing, the mismatch of the key printing parameters, such as the filling ratio, layer thickness, and printing speed, results in deformation on a scale of tens of micrometers. Consequently, the resultant rough surface and variation in the thickness of the PLA layers in the cladding region leads to the high scattering loss and narrow bandgap of the PBG Bragg waveguide. The desired components with higher precision can be obtained by finely tailoring these printing parameters further, which is a time-consuming process.

For the fabricated micro-encapsulated two-wire plasmonic waveguide components, their difference from the corresponding numerical ones with two metal wires in optical performance is primarily associated with certain intrinsic defects of SLA 3D printing and employed metallization techniques. Although the high resolution (50 μm on the XY-axis) of the SLA 3D printer theoretically enables

the reproduction of designed objects with high accuracy, the cure-through effect in printing, surface tension effect in post-processing, and errors in end facet polishing usually result in the uncontrollable deformation of dielectric supports of two-wire waveguide components in experiments.

The cure-through effect induces the solidification of photosensitive resin with a larger thickness than expected in a single UV curing time. The resultant deformation becomes pronounced for objects having cross sections that change rapidly along the printing direction, such as the two-wire WBG with different printed patterns for two consecutive UV curing times. To obtain a smooth surface of the desired truncated cones, thereby reducing the scattering loss associated with surface roughness, we used the minimum layer thickness of the SLA 3D printer (finest Z-axis resolution, 10 μm) to fabricate the dielectric support of two-wire WBGs in this thesis. However, utilizing this layer thickness may also exacerbate the cumulative deformation caused by the cure-through effect, thus damaging the periodicity of the index change and reducing the grating strength of the Bragg gratings. Therefore, to mitigate the cure-through effect, the photosensitive resin chemistry must be carefully chosen, and the printing parameters should be finely adjusted, including the light intensity and exposure time of the UV laser, to match the desired layer thickness.

Compared with SLA 3D printed hollow-core PBG Bragg waveguides (see Chapter 4.3), the dielectric support of two-wire waveguide components with a solid structure undergoes less noticeable deformation during cleaning of the remaining uncured resin using isopropanol washing and airflow drying. Nevertheless, a deeply subwavelength pillar with a small width (e.g., less than 0.2 mm) tends to become pliable and easily collapses owing to surface tension. The resultant misalignment of the two wires leads to a substantial increase in the insertion loss of the two-wire waveguide component (see Chapter 5.2). Therefore, the optimal pillar width must be chosen to fix the cylinder wire on the enclosure firmly and simultaneously minimize its influence on the transmitted SPP wave. In this study, the pillar width was set to 0.35 mm. A slender pillar can be available when using rigid resin and optimized post-processing procedures.

In addition, a tree-like support structure was used to fix the SLA 3D prints on the building platform during printing in most cases. However, its debris attached to 3D prints is notoriously difficult to remove completely, even for the dielectric support of a two-wire waveguide component whose base is on a flat plane. Theoretically, the ideally horizontal end facet can be achieved by polishing,

thus enabling seamless connectorization between two two-wire WSs with no coupling loss. However, the inclined end facet due to the inevitable error in polishing adds extra insertion loss to the two-wire plasmonic circuits with an average value of ~ 0.4 dB per connection in experiments, which can be further reduced by optimizing the polishing process.

In this work, it was found that the performance of the metalized dielectric wire support is comparable to the conventional component in bulk metal as THz plasmonic waveguides. The transmission of the SPP wave confined in the air gap between two wires is highly reliant on the conductive surface deposited on the wire supports. Compared with most alternative metallization techniques, the wet chemistry deposition employed in this study is cost-effective, easy to use, and suitable for mechanical supports with complicated structures, thus emerging as a superior method for low-yield production in the laboratory. However, the uncontrollable deposition parameters (e.g., the layer thickness and surface roughness), as well as nano/micro-crystallization and oxidation effects, induce geometric defects in the deposited silver layer. The resultant decrease in conductivity leads to a high transmission loss of the two-wire waveguides in the experiments. In addition, the deposited metal layer is fragile, and its adhesion to the SLA 3D printed resin support is not resistant to certain types of organic solvents (e.g., isopropanol and ethanol), which restricts the potential application of micro-encapsulated two-wire waveguide components in gas and fluidic sensing. We believe that advanced metallization techniques [150, 275], such as sputtering, can be further used to obtain high-quality metal layer and facilitate the reproduction of the proposed THz plasmonic circuits.

Moreover, we increased the working temperature of the two-wire waveguide components using positive temperature coefficient heaters from room temperature to $70\text{ }^{\circ}\text{C}$ in the experiments, which is slightly lower than the glass transition temperature of the cured resin ($85\text{ }^{\circ}\text{C}$). By monitoring the spectral position of the stopband of a two-wire WBG, it was found that increasing the working temperature leads to a larger effective refractive index of the THz SPP wave. We believe that this variation is related to the RI change of the resin enclosure, whose impact on the transmitted THz SPP wave can be attenuated by using resin with higher thermostability or increasing the distance between the wires and resin enclosure.

7.2 Application of 3D-printed two-wire waveguide in THz communications

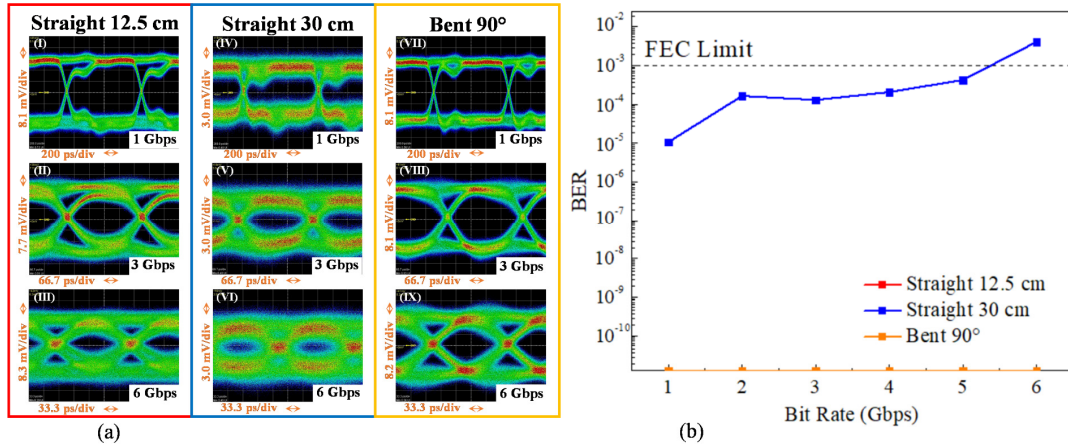


Figure 7.1 Experimental study of two-wire waveguides for THz communications

(a) Eye patterns for the THz signals of different bit rates propagating through the straight and bent two-wire plasmonic waveguides. (I-III) A 12.5 cm-straight waveguide. (IV-VI) A 30 cm-straight waveguide. (VII-IX) A 90° bent waveguide. (b) Measured BER versus bit rate of the THz carrier wave propagating through two-wire waveguides.

We demonstrate that the proposed micro-encapsulated two-wire waveguide features moderate transmission loss and low GVD in Chapter 5.3 and performs as the base of four-port ADM circuits for THz frequency division multiplexing communications in Chapter 6.2.3. The THz ADM was characterized using a THz communication system (see Chapter 6.2.4). It was found that the ADM performance is restricted by the transmission loss and dispersion of both the Bragg gratings and the two-wire waveguide. Moreover, to rule out the influence of Bragg grating and explore applications of two-wire waveguides in THz signal transmission, the straight and bent two-wire waveguides were characterized using the same THz communication system, and the experimental results are concluded as follows.

In experiments, the input and output end facets of the two-wire waveguides were connected to the THz transmitter and receiver via WR6.5 waveguide flanges. The characterized eye pattern and corresponding BER of different bit rates for a carrier frequency of 140 GHz are shown in Fig. 7.4. In contrast to the In – Through path in an ADM circuit, error-free data transmission was found by

a two-wire waveguide with the same length due to the absence of the Bragg gratings and directional coupling. However, restricted by the low power of the THz transmitter, the power of the THz signal reaching the THz receiver after propagation through a straight two-wire waveguide with a length exceeding 35 cm is lower than the threshold to be detected. It is found that when using a straight two-wire waveguide with a length less than 25 cm as the interconnect between THz transmitter and receiver, the received THz power can reach the limit for the error-free data transmission. In addition, a two-wire waveguide bend with a bend radius of 4 cm which is the same as that used in Y splitters of THz ADM circuits, was characterized. Despite the additional bending loss of $\sim 10 \text{ m}^{-1}$ and larger GVD ($\sim 8 \text{ ps}/(\text{THz}\cdot\text{cm})$) at 140 GHz when compared with the straight waveguide, we found that error-free signal propagation with a data rate of 6 Gbps is still possible for a 90° bend.

CHAPTER 8 CONCLUSION

To conclude, we introduced the development of a THz PBG Bragg waveguide-based resonant sensor and demonstrated real-time liquid RI monitoring using amplitude and phase detection modalities. Thereafter, we proposed a novel type of THz two-wire plasmonic waveguide and developed various THz optical components and ADM circuits based on this waveguide for THz communications. It is worth highlighting the important role of AM techniques in the fabrication of proposed THz optical components. The applications, advantages, limitations, and further optimization of the employed AM techniques were discussed in this thesis.

First, in Chapter 4, we demonstrated a THz fluidic sensor based on an FDM 3D printed hollow-core PBG Bragg waveguide. The waveguide features a square hollow core surrounded by a periodic sequence of PLA/air bilayers. The resonant sensor was built by integrating a fluidic channel into the waveguide cladding. The liquid analyte flowing through the channel supported a resonant defect state that can be spectrally probed. It utilizes the high transmission loss of the supermode in the vicinity of the phase-matching wavelength as a result of the strong hybridization between the low-loss core-guided mode and the lossy one bound to the defect layer. The anticrossing phenomenon manifests itself as an amplitude dip and rapid phase change in the measured complex normalized transmission spectra of PBG Bragg waveguides. It was found that the spectral position of these singularities depended linearly on the real part of the liquid analyte RI. The proposed fluidic sensor sensitivity was derived as ~ 110 GHz/RIU. In addition, because the liquid analyte flows through the entire sealed sensing layer before reaching the outlet, real-time RI monitoring with a response time of ~ 21 s can be realized by the proposed sensor. It is noted that a smaller bandwidth of the spectral singularity is required for a higher sensing resolution, which can be accomplished by moving the analyte layer further away from the core. Compared with the noise caused by the standing wave oscillation in the CW-THz spectroscopy system for characterization, the structural nonuniformity of the PBG Bragg waveguide as a result of the limited resolution of FDM 3D printing is the primary hurdle to obtaining the detectable anticrossing phenomenon for the designed sensor in experiments.

Second, in Chapter 5, we developed a new type of reconfigurable THz quasi-two-wire plasmonic circuit for application in THz communications and sensing. The basic building block, namely the

two-wire THz waveguide, comprises two metalized parallel wires suspended inside a protective micro-sized dielectric enclosure. High-resolution SLA 3D printing and wet chemistry metal deposition techniques were employed to print the complex-shaped mechanical supports in resin and subsequently, selectively deposited an optically thick silver conductive layer onto wire substrates. With a proper design, this fabricated waveguide features low transmission ($\sim 6 \text{ m}^{-1}$) and bending loss (less than 10 m^{-1} for bending radius above 5 cm), small GVD ($-1.5 \text{ ps}/(\text{THz}\cdot\text{cm})$), as well as high power coupling coefficient with rectangular waveguide flange ($\sim 50 \%$) for operation around 140 GHz. With the assistance of the hot-stamping technique, we also developed two-wire WBGs by inserting paper-based metal gratings in the air gap center of the underlying two-wire waveguides. Moreover, 3D printing allowed seamless integration of two-wire WSs using the alignment and connectorization elements imprinted on their enclosures, thus endowing the two-wire waveguide components with a modular nature. Consequently, to prove the potential of two-wire waveguide components in developing THz optical circuits, we demonstrated a Y-shaped THz splitter/multiplexer and ADM.

Third, in Chapter 6, we proposed four-port ADM circuits for THz frequency-division multiplexing communication networks. The 3D-printed micro-encapsulated two-wire waveguide proposed in Chapter 5 forms the platform of the ADM circuits. A high-reflectivity two-wire WBG with one wire with periodic variation in cross sections was developed using a quarter-wave condition. Further, we developed side couplers featuring two touching two-wire waveguides sharing the same enclosure to enable efficient directional coupling. Subsequently, coupled with two Y splitters, we proposed two-wire ADM circuits using a combination of these two elements that are capable of splitting broadband THz light in the spectral and spatial domains. The addition of the Bragg gratings to the side coupler of a directional coupler circuit enabled full-cycle coupling, and thus the THz carrier frequencies that fall within the grating stopband could be dropped from and added to the bus waveguide, whereas all the other wavelengths within the broad bandwidth of the coupling circuit were guided through the bus waveguide with small distortion. Next, the study of two optimal ADMs for operation at ~ 140 GHz carrier frequency, that is, one with optimized drop action, and the other exhibiting balanced drop/add performance were focused upon. Consequently, characterized by a THz communication system, the low crosstalk between channels, clear eye

diagrams, and moderate bit error rate for THz signals with high data rates for both drop/add and through actions revealed the great potential of the proposed two-wire ADM circuit in THz communications. However, certain intrinsic limitations and defects of SLA 3D printing and metallization techniques have a negative impact on the optical properties of the obtained two-wire waveguide components. Consequently, optimizing the manufacturing processes can further improve the application of two-wire plasmonic circuits in THz science.

In conclusion, we explored the application of 3D printed THz waveguide components in THz sensing and communications in this thesis, which reveals the great potential of additive manufacturing techniques in the THz regime. However, it is noted that the insufficient resolution (hundreds and tens of micrometers for commercial desktop FDM and SLA 3D printers, respectively) as well as some intrinsic defects of 3D printing (ex. the model wrapping and high material absorption of conventional thermoplastics for FDM 3D printing, cure-through resin and surface tension effects, together with errors in end polishing as a post-printing process for SLA 3D printing) restrict the design and fabrication of THz optical components. The THz waveguides for operation in the higher part of the THz spectrum and the THz optical components with deeply subwavelength features are largely unexplored fields for 3D printing techniques. Nevertheless, with the continuous advance in hardware and applicable material of 3D printing, together with proper waveguide design, we believe that 3D printing will bring a revolution for THz optical components with advanced functionalities among the whole THz band.

REFERENCES

- [1] M. Skorobogatiy, *Nanostructured and Subwavelength Waveguides: fundamentals and applications*. John Wiley & Sons, 2012.
- [2] C. Fattinger and D. Grischkowsky, "Terahertz beams," *Applied Physics Letters*, vol. 54, no. 6, pp. 490-492, 1989.
- [3] N. Katzenellenbogen and D. Grischkowsky, "Efficient generation of 380 fs pulses of THz radiation by ultrafast laser pulse excitation of a biased metal-semiconductor interface," *Applied Physics Letters*, vol. 58, no. 3, pp. 222-224, 1991.
- [4] R. A. Lewis, "A review of terahertz sources," *Journal of Physics D: Applied Physics*, vol. 47, no. 37, p. 374001, 2014.
- [5] R. Lewis, "A review of terahertz detectors," *Journal of Physics D: Applied Physics*, vol. 52, no. 43, p. 433001, 2019.
- [6] J.-H. Son, S. J. Oh, and H. Cheon, "Potential clinical applications of terahertz radiation," *Journal of Applied Physics*, vol. 125, no. 19, p. 190901, 2019.
- [7] T. W. Crowe, T. Globus, D. L. Woolard, and J. L. Hesler, "Terahertz sources and detectors and their application to biological sensing," *Philosophical Transactions of the Royal Society of London. Series A: Mathematical, Physical and Engineering Sciences*, vol. 362, no. 1815, pp. 365-377, 2004.
- [8] M. Walther, B. M. Fischer, A. Ortner, A. Bitzer, A. Thoman, and H. Helm, "Chemical sensing and imaging with pulsed terahertz radiation," *Analytical and Bioanalytical Chemistry*, vol. 397, no. 3, pp. 1009-1017, 2010.
- [9] S. Koenig *et al.*, "Wireless sub-THz communication system with high data rate," *Nature photonics*, vol. 7, no. 12, pp. 977-981, 2013.
- [10] M. Van Exter, C. Fattinger, and D. Grischkowsky, "Terahertz time-domain spectroscopy of water vapor," *Optics Letters*, vol. 14, no. 20, pp. 1128-1130, 1989.
- [11] X. C. Zhang, A. Shkurinov, and Y. Zhang, "Extreme terahertz science," *Nature Photonics*, vol. 11, no. 1, pp. 16-18, 2017.
- [12] K. Tsuruda, M. Fujita, and T. Nagatsuma, "Extremely low-loss terahertz waveguide based on silicon photonic-crystal slab," *Optics Express*, vol. 23, no. 25, pp. 31977-31990, 2015.
- [13] D. Headland, W. Withayachumnankul, X. Yu, M. Fujita, and T. Nagatsuma, "Unclad microphotronics for terahertz waveguides and systems," *Journal of Lightwave Technology*, vol. 38, no. 24, pp. 6853-6862, 2020.
- [14] S. Atakaramians, S. Afshar, T. M. Monro, D. Abbott, and Photonics, "Terahertz dielectric waveguides," *Advances in Optics*, vol. 5, no. 2, pp. 169-215, 2013.
- [15] X. Zhang *et al.*, "Terahertz surface plasmonic waves: a review," *Advanced Photonics*, vol. 2, no. 1, p. 014001, 2020.
- [16] B. Zhang, W. Chen, Y. Wu, K. Ding, and R. Li, "Review of 3D printed millimeter-wave and terahertz passive devices," *International Journal of Antennas and Propagation*, vol. 2017, 2017.

- [17] J. Sun and F. Hu, "Three-dimensional printing technologies for terahertz applications: a review," *International Journal of RF and Microwave Computer-Aided Engineering*, vol. 30, no. 1, p. e21983, 2020.
- [18] B. You, T.-A. Liu, J.-L. Peng, C.-L. Pan, and J.-Y. Lu, "A terahertz plastic wire based evanescent field sensor for high sensitivity liquid detection," *Optics Express*, vol. 17, no. 23, pp. 20675-20683, 2009.
- [19] Y. Cao, K. Nallappan, H. Guerboukha, T. Gervais, and M. Skorobogatiy, "Additive manufacturing of resonant fluidic sensors based on photonic bandgap waveguides for terahertz applications," *Optics Express*, vol. 27, no. 20, pp. 27663-27681, 2019.
- [20] Y. Cao, K. Nallappan, H. Guerboukha, G. Xu, and M. Skorobogatiy, "Additive manufacturing of highly reconfigurable plasmonic circuits for terahertz communications," *Optica*, vol. 7, no. 9, pp. 1112-1125, 2020.
- [21] Y. Cao, K. Nallappan, G. Xu, and M. Skorobogatiy, "Add drop multiplexers for terahertz communications using two-wire waveguide based plasmonic circuits," *arXiv preprint arXiv:14090*, 2021.
- [22] Y. Yang, A. Shutler, and D. Grischkowsky, "Measurement of the transmission of the atmosphere from 0.2 to 2 THz," *Optics Express*, vol. 19, no. 9, pp. 8830-8838, 2011.
- [23] J. Knight, T. Birks, P. S. J. Russell, and D. Atkin, "All-silica single-mode optical fiber with photonic crystal cladding," *Optics Letters*, vol. 21, no. 19, pp. 1547-1549, 1996.
- [24] Y.-S. Jin, G.-J. Kim, and S.-G. Jeon, "Terahertz dielectric properties of polymers," *Journal of the Korean Physical Society*, vol. 49, no. 2, pp. 513-517, 2006.
- [25] L.-J. Chen, H.-W. Chen, T.-F. Kao, J.-Y. Lu, and C.-K. Sun, "Low-loss subwavelength plastic fiber for terahertz waveguiding," *Optics Express*, vol. 31, no. 3, pp. 308-310, 2006.
- [26] K. Nallappan, Y. Cao, G. Xu, H. Guerboukha, C. Nerguizian, and M. Skorobogatiy, "Dispersion-limited versus power-limited terahertz communication links using solid core subwavelength dielectric fibers," *Photonics Research*, vol. 8, no. 11, pp. 1757-1775, 2020.
- [27] M. Roze, B. Ung, A. Mazhorova, M. Walther, and M. Skorobogatiy, "Suspended core subwavelength fibers: towards practical designs for low-loss terahertz guidance," *Optics Express*, vol. 19, no. 10, pp. 9127-9138, 2011.
- [28] G. Xu, K. Nallappan, Y. Cao, and M. Skorobogatiy, "Fabrication of low loss and near zero dispersion suspended core polypropylene fibers for terahertz communications using infinity 3D printing technique," 2020.
- [29] Y. Geng, X. Tan, P. Wang, and J. Yao, "Transmission loss and dispersion in plastic terahertz photonic band-gap fibers," *Applied Physics B*, vol. 91, no. 2, pp. 333-336, 2008.
- [30] Z. Wu, W.-R. Ng, M. E. Gehm, and H. Xin, "Terahertz electromagnetic crystal waveguide fabricated by polymer jetting rapid prototyping," *Optics Express*, vol. 19, no. 5, pp. 3962-3972, 2011.
- [31] J. Yang *et al.*, "3D printed low-loss THz waveguide based on Kagome photonic crystal structure," *Optics Express*, vol. 24, no. 20, pp. 22454-22460, 2016.

- [32] L. Van Putten, J. Gorecki, E. N. Fokoua, V. Apostolopoulos, and F. Poletti, "3D-printed polymer antiresonant waveguides for short-reach terahertz applications," *Applied Optics*, vol. 57, no. 14, pp. 3953-3958, 2018.
- [33] J. Sultana, M. S. Islam, K. Ahmed, A. Dinovitser, B. W.-H. Ng, and D. Abbott, "Terahertz detection of alcohol using a photonic crystal fiber sensor," *Applied Optics*, vol. 57, no. 10, pp. 2426-2433, 2018.
- [34] B. You *et al.*, "Subwavelength film sensing based on terahertz anti-resonant reflecting hollow waveguides," *Optics Express*, vol. 18, no. 18, pp. 19353-19360, 2010.
- [35] G. Hasanuzzaman, S. Rana, and M. S. Habib, "A novel low loss, highly birefringent photonic crystal fiber in THz regime," *IEEE Photonics Technology Letters*, vol. 28, no. 8, pp. 899-902, 2016.
- [36] Y.-F. Zhu, M.-Y. Chen, H. Wang, H.-B. Yao, Y.-K. Zhang, and J.-C. Yang, "Design and analysis of a low-loss suspended core terahertz fiber and its application to polarization splitter," *IEEE Photonics Journal*, vol. 5, no. 6, pp. 7101410-7101410, 2013.
- [37] M. A. Kabir, K. Ahmed, M. M. Hassan, M. M. Hossain, and B. K. Paul, "Design a photonic crystal fiber of guiding terahertz orbital angular momentum beams in optical communication," *Optics Communications*, vol. 475, p. 126192, 2020.
- [38] J. Dai, J. Zhang, W. Zhang, and D. Grischkowsky, "Terahertz time-domain spectroscopy characterization of the far-infrared absorption and index of refraction of high-resistivity, float-zone silicon," *JOSA B*, vol. 21, no. 7, pp. 1379-1386, 2004.
- [39] W. Withayachumnankul, M. Fujita, and T. Nagatsuma, "Integrated silicon photonic crystals toward terahertz communications," *Advanced Optical Materials*, vol. 6, no. 16, p. 1800401, 2018.
- [40] Y. Yang *et al.*, "Terahertz topological photonics for on-chip communication," *Nature Photonics*, vol. 14, no. 7, pp. 446-451, 2020.
- [41] C. M. Yee and M. S. Sherwin, "High-Q terahertz microcavities in silicon photonic crystal slabs," *Applied Physics Letters*, vol. 94, no. 15, p. 154104, 2009.
- [42] J. Xie, X. Zhu, X. Zang, Q. Cheng, L. Chen, and Y. Zhu, "Terahertz integrated device: high-Q silicon dielectric resonators," *Optical Materials Express*, vol. 8, no. 1, pp. 50-58, 2018.
- [43] M. Yata, M. Fujita, and T. Nagatsuma, "Photonic-crystal diplexers for terahertz-wave applications," *Optics Express*, vol. 24, no. 7, pp. 7835-7849, 2016.
- [44] D. Headland, W. Withayachumnankul, M. Fujita, and T. Nagatsuma, "Gratingless integrated tunneling multiplexer for terahertz waves," *Optica*, vol. 8, no. 5, pp. 621-629, 2021.
- [45] J. Xie *et al.*, "A Review on Terahertz Technologies Accelerated by Silicon Photonics," *Nanomaterials*, vol. 11, no. 7, p. 1646, 2021.
- [46] G. Gallot, S. Jamison, R. McGowan, and D. Grischkowsky, "Terahertz waveguides," *JOSA B*, vol. 17, no. 5, pp. 851-863, 2000.
- [47] G. Chattopadhyay, J. S. Ward, N. Llombert, and K. B. Cooper, "Submillimeter-wave 90° polarization twists for integrated waveguide circuits," *IEEE Microwave and Wireless Components Letters*, vol. 20, no. 11, pp. 592-594, 2010.

- [48] S. M. Lewis, E. A. Nanni, and R. J. Temkin, "Direct machining of low-loss THz waveguide components with an RF choke," *IEEE Microwave and Wireless Components Letters*, vol. 24, no. 12, pp. 842-844, 2014.
- [49] H. J. Tang, W. Hong, G. Q. Yang, and J. X. Chen, "Silicon based THz antenna and filter with MEMS process," in *2011 International Workshop on Antenna Technology (iWAT)*, 2011, pp. 148-151: IEEE.
- [50] W. Zhu, A. Agrawal, and A. Nahata, "Planar plasmonic terahertz guided-wave devices," *Optics Express*, vol. 16, no. 9, pp. 6216-6226, 2008.
- [51] B. Wang and G. P. Wang, "Plasmonic waveguide ring resonator at terahertz frequencies," *Applied Physics Letters*, vol. 89, no. 13, p. 133106, 2006.
- [52] P. Padhy, P. K. Sahu, and R. Jha, "Metal wire waveguide based all plasmonic refractive index sensor for terahertz frequencies," *Sensors and Actuators B: Chemical*, vol. 225, pp. 115-120, 2016.
- [53] H. Zhan, R. Mendis, and D. M. Mittleman, "Superfocusing terahertz waves below $\lambda/250$ using plasmonic parallel-plate waveguides," *Optics Express*, vol. 18, no. 9, pp. 9643-9650, 2010.
- [54] S.-H. Kim, E. S. Lee, Y. B. Ji, and T.-I. Jeon, "Improvement of THz coupling using a tapered parallel-plate waveguide," *Optics Express*, vol. 18, no. 2, pp. 1289-1295, 2010.
- [55] Y. Zhang *et al.*, "Terahertz spoof surface-plasmon-polariton subwavelength waveguide," *Photonics Research*, vol. 6, no. 1, pp. 18-23, 2018.
- [56] M. A. Unutmaz and M. Unlu, "Terahertz spoof surface plasmon polariton waveguides: a comprehensive model with experimental verification," *Scientific Reports*, vol. 9, no. 1, pp. 1-8, 2019.
- [57] S. Pandey, B. Gupta, and A. Nahata, "Terahertz plasmonic waveguides created via 3D printing," *Optics Express*, vol. 21, no. 21, pp. 24422-24430, 2013.
- [58] F. Zhang, K. Tominaga, M. Hayashi, and H.-W. Wang, "Low-frequency vibration study of amino acids using terahertz spectroscopy and solid-state density functional theory," in *Infrared, Millimeter-Wave, and Terahertz Technologies III*, 2014, vol. 9275, p. 92750D: International Society for Optics and Photonics.
- [59] R. Knipper *et al.*, "THz absorption in fabric and its impact on body scanning for security application," *IEEE Transactions on Terahertz Science and Technology*, vol. 5, no. 6, pp. 999-1004, 2015.
- [60] D. Mittleman, *Sensing with terahertz radiation*. Springer, 2013.
- [61] P. Rodríguez-Ulibarri and M. Beruete, "Sensing at terahertz frequencies," in *Fiber Optic Sensors*: Springer, 2017, pp. 301-327.
- [62] W. Xu, L. Xie, and Y. Ying, "Mechanisms and applications of terahertz metamaterial sensing: a review," *Nanoscale*, vol. 9, no. 37, pp. 13864-13878, 2017.
- [63] T. Driscoll *et al.*, "Tuned permeability in terahertz split-ring resonators for devices and sensors," *Applied Physics Letters*, vol. 91, no. 6, p. 062511, 2007.
- [64] H. Yoshida *et al.*, "Terahertz sensing method for protein detection using a thin metallic mesh," *Applied Physics Letters*, vol. 91, no. 25, p. 253901, 2007.

- [65] X. Wu *et al.*, "Alkanethiol-functionalized terahertz metamaterial as label-free, highly-sensitive and specific biosensor," *Biosensors and Bioelectronics*, vol. 42, pp. 626-631, 2013.
- [66] X. Hu *et al.*, "Metamaterial absorber integrated microfluidic terahertz sensors," *Laser and Photonics Reviews*, vol. 10, no. 6, pp. 962-969, 2016.
- [67] K. Shih, P. Pitchappa, M. Manjappa, C. P. Ho, R. Singh, and C. Lee, "Microfluidic metamaterial sensor: Selective trapping and remote sensing of microparticles," *Journal of Applied Physics*, vol. 121, no. 2, p. 023102, 2017.
- [68] A. Sadeqi, H. R. Nejad, R. E. Owyung, and S. Sonkusale, "Three dimensional printing of metamaterial embedded geometrical optics (MEGO)," *Microsystems and Nanoengineering*, vol. 5, no. 1, pp. 1-10, 2019.
- [69] R. Mendis, V. Astley, J. Liu, and D. M. Mittleman, "Terahertz microfluidic sensor based on a parallel-plate waveguide resonant cavity," *Applied Physics Letters*, vol. 95, no. 17, p. 171113, 2009.
- [70] V. Astley, K. S. Reichel, J. Jones, R. Mendis, and D. M. Mittleman, "Terahertz multichannel microfluidic sensor based on parallel-plate waveguide resonant cavities," *Applied Physics Letters*, vol. 100, no. 23, p. 231108, 2012.
- [71] J. S. Melinger, N. Laman, S. S. Harsha, and D. Grischkowsky, "Line narrowing of terahertz vibrational modes for organic thin polycrystalline films within a parallel plate waveguide," *Applied Physics Letters*, vol. 89, no. 25, p. 251110, 2006.
- [72] J. F. O'Hara, W. Withayachumnankul, and I. Al-Naib, "A review on thin-film sensing with terahertz waves," *Journal of Infrared, Millimeter, and Terahertz Waves*, vol. 33, no. 3, pp. 245-291, 2012.
- [73] J. S. Melinger, N. Laman, and D. Grischkowsky, "The underlying terahertz vibrational spectrum of explosives solids," *Applied Physics Letters*, vol. 93, no. 1, p. 011102, 2008.
- [74] J. S. Melinger, N. Laman, S. S. Harsha, S. Cheng, and D. Grischkowsky, "High-resolution waveguide terahertz spectroscopy of partially oriented organic polycrystalline films," *The Journal of Physical Chemistry A*, vol. 111, no. 43, pp. 10977-10987, 2007.
- [75] N. Laman, S. S. Harsha, D. Grischkowsky, and J. S. Melinger, "High-resolution waveguide THz spectroscopy of biological molecules," *Biophysical Journal*, vol. 94, no. 3, pp. 1010-1020, 2008.
- [76] M. Walther, M. R. Freeman, and F. A. Hegmann, "Metal-wire terahertz time-domain spectroscopy," *Applied Physics Letters*, vol. 87, no. 26, p. 261107, 2005.
- [77] Y. Huang, S. Zhong, T. Shi, Y.-C. Shen, and D. Cui, "HR-Si prism coupled tightly confined spoof surface plasmon polaritons mode for terahertz sensing," *Optics Express*, vol. 27, no. 23, pp. 34067-34078, 2019.
- [78] J. Yang, Y. Francescato, D. Chen, J. Yang, and M. Huang, "Broadband molecular sensing with a tapered spoof plasmon waveguide," *Optics Express*, vol. 23, no. 7, pp. 8583-8589, 2015.
- [79] Z. Ma *et al.*, "Terahertz particle-in-liquid sensing with spoof surface plasmon polariton waveguides," *APL Photonics*, vol. 2, no. 11, p. 116102, 2017.
- [80] B. Ng *et al.*, "Broadband terahertz sensing on spoof plasmon surfaces," *Acs Photonics*, vol. 1, no. 10, pp. 1059-1067, 2014.

- [81] S. Sen, M. Abdullah-Al-Shafi, A. S. Sikder, M. S. Hossain, and M. M. Azad, "Zeonex based decagonal photonic crystal fiber (D-PCF) in the terahertz (THz) band for chemical sensing applications," *Sensing and Bio-Sensing Research*, vol. 31, p. 100393, 2021.
- [82] M. S. Islam, J. Sultana, A. A. Rifat, A. Dinovitser, B. W.-H. Ng, and D. Abbott, "Terahertz sensing in a hollow core photonic crystal fiber," *IEEE Sensors Journal*, vol. 18, no. 10, pp. 4073-4080, 2018.
- [83] A. Hassani and M. Skorobogatiy, "Surface Plasmon Resonance-like integrated sensor at terahertz frequencies for gaseous analytes," *Optics Express*, vol. 16, no. 25, pp. 20206-20214, 2008.
- [84] A. Mazhorova *et al.*, "Label-free bacteria detection using evanescent mode of a suspended core terahertz fiber," *Optics Express*, vol. 20, no. 5, pp. 5344-5355, 2012.
- [85] B. You, J.-Y. Lu, C.-P. Yu, T.-A. Liu, and J.-L. Peng, "Terahertz refractive index sensors using dielectric pipe waveguides," *Optics Express*, vol. 20, no. 6, pp. 5858-5866, 2012.
- [86] L. Cheng *et al.*, "Terahertz-wave absorption in liquids measured using the evanescent field of a silicon waveguide," *Applied Physics Letters*, vol. 92, no. 18, p. 181104, 2008.
- [87] G. Yan, A. Markov, Y. Chinifooroshan, S. M. Tripathi, W. J. Bock, and M. Skorobogatiy, "Resonant THz sensor for paper quality monitoring using THz fiber Bragg gratings," *Optics Letters*, vol. 38, no. 13, pp. 2200-2202, 2013.
- [88] F. Fan *et al.*, "Terahertz transmission and sensing properties of microstructured PMMA tube waveguide," *Optics Express*, vol. 23, no. 21, pp. 27204-27212, 2015.
- [89] P. Yeh, A. Yariv, and E. Marom, "Theory of Bragg fiber," *JOSA*, vol. 68, no. 9, pp. 1196-1201, 1978.
- [90] S. G. Johnson *et al.*, "Low-loss asymptotically single-mode propagation in large-core OmniGuide fibers," *Optics Express*, vol. 9, no. 13, pp. 748-779, 2001.
- [91] J. Li, "Hollow core photonic Bragg fibers for industrial sensing applications," Ecole Polytechnique, Montreal (Canada), 2017.
- [92] Y. Wang, G. Yan, Z. Lian, C. Wu, and S. He, "Liquid-level sensing based on a hollow core Bragg fiber," *Optics Express*, vol. 26, no. 17, pp. 21656-21663, 2018.
- [93] S. Février *et al.*, "High-power photonic-bandgap fiber laser," *Optics Letters*, vol. 33, no. 9, pp. 989-991, 2008.
- [94] X. Peng, M. Mielke, and T. Booth, "High average power, high energy 1.55 μm ultra-short pulse laser beam delivery using large mode area hollow core photonic band-gap fiber," *Optics Express*, vol. 19, no. 2, pp. 923-932, 2011.
- [95] H. Qu and M. Skorobogatiy, "Liquid-core low-refractive-index-contrast Bragg fiber sensor," *Applied Physics Letters*, vol. 98, no. 20, p. 201114, 2011.
- [96] K. J. Rowland, S. Afshar, A. Stolyarov, Y. Fink, and T. M. Monro, "Bragg waveguides with low-index liquid cores," *Optics Express*, vol. 20, no. 1, pp. 48-62, 2012.
- [97] J. Li, H. Qu, and M. Skorobogatiy, "Simultaneous monitoring the real and imaginary parts of the analyte refractive index using liquid-core photonic bandgap Bragg fibers," *Optics Express*, vol. 23, no. 18, pp. 22963-22976, 2015.

- [98] J. Li, H. Qu, and M. Skorobogatiy, "Squeezed hollow-core photonic Bragg fiber for surface sensing applications," *Optics Express*, vol. 24, no. 14, pp. 15687-15701, 2016.
- [99] A. Dupuis, K. Stoeffler, B. Ung, C. Dubois, and M. Skorobogatiy, "Transmission measurements of hollow-core THz Bragg fibers," *JOSA B*, vol. 28, no. 4, pp. 896-907, 2011.
- [100] J. Li, K. Nallappan, H. Guerboukha, and M. Skorobogatiy, "3D printed hollow core terahertz Bragg waveguides with defect layers for surface sensing applications," *Optics Express*, vol. 25, no. 4, pp. 4126-4144, 2017.
- [101] B. Hong *et al.*, "Low-loss asymptotically single-mode THz Bragg fiber fabricated by digital light processing rapid prototyping," *IEEE Transactions on Terahertz Science and Technology*, vol. 8, no. 1, pp. 90-99, 2017.
- [102] M. Skorobogatiy and A. Dupuis, "Ferroelectric all-polymer hollow Bragg fibers for terahertz guidance," *Applied Physics Letters*, vol. 90, no. 11, p. 113514, 2007.
- [103] T. Kürner and S. Priebe, "Towards THz communications-status in research, standardization and regulation," *Journal of Infrared, Millimeter, and Terahertz Waves*, vol. 35, no. 1, pp. 53-62, 2014.
- [104] P. Yang, Y. Xiao, M. Xiao, and S. Li, "6G wireless communications: Vision and potential techniques," *IEEE Network*, vol. 33, no. 4, pp. 70-75, 2019.
- [105] X. Li *et al.*, "132-Gb/s photonics-aided single-carrier wireless terahertz-wave signal transmission at 450GHz enabled by 64QAM modulation and probabilistic shaping," in *Optical Fiber Communication Conference*, 2019, p. M4F. 4: Optical Society of America.
- [106] M. H. Rahaman, A. Bandyopadhyay, S. Pal, and K. P. Ray, "Reviewing the scope of THz communication and a technology roadmap for implementation," *IETE Technical Review*, pp. 1-14, 2020.
- [107] K. Nallappan *et al.*, "Terahertz Waveguides for Next Generation Communication Network: Needs, Challenges and Perspectives," in *Next Generation Wireless Terahertz Communication Networks*: CRC Press, pp. 379-410.
- [108] <https://www.vadiodes.com/en/products/directional-couplers>.
- [109] W. Xin, Z. Binzhen, W. Junlin, and D. Junping, "100 GHz waveguide band-pass filter employing UV-LIGA micromachining process," *Microelectronics Journal*, vol. 69, pp. 101-105, 2017.
- [110] J. Hu, S. Xie, and Y. Zhang, "Micromachined terahertz rectangular waveguide bandpass filter on silicon-substrate," *IEEE Microwave and Wireless Components Letters*, vol. 22, no. 12, pp. 636-638, 2012.
- [111] W. Withayachumnankul, R. Yamada, C. Fumeaux, M. Fujita, and T. Nagatsuma, "All-dielectric integration of dielectric resonator antenna and photonic crystal waveguide," *Optics Express*, vol. 25, no. 13, pp. 14706-14714, 2017.
- [112] G. Xu, K. Nallappan, Y. Cao, and M. Skorobogatiy, "Microstructured fiber links for THz communications and their fabrication using infinity printing," *arXiv preprint arXiv:2004.04578*, 2021.
- [113] N. Van Thienen, Y. Zhang, M. De Wit, and P. Reynaert, "An 18Gbps polymer microwave fiber (PMF) communication link in 40nm CMOS," in *ESSCIRC Conference 2016: 42nd European Solid-State Circuits Conference*, 2016, pp. 483-486: IEEE.

- [114] K. Nallappan, H. Guerboukha, Y. Cao, C. Nerguizian, and M. Skorobogatiy, "Experimental demonstration of 5 Gbps data transmission using long subwavelength fiber at 140 GHz," in *2019 IEEE Radio and Wireless Symposium (RWS)*, 2019, pp. 1-4: IEEE.
- [115] M. Weidenbach *et al.*, "3D printed dielectric rectangular waveguides, splitters and couplers for 120 GHz," *Optics Express*, vol. 24, no. 25, pp. 28968-28976, 2016.
- [116] T. Ma, K. Nallapan, H. Guerboukha, and M. Skorobogatiy, "Analog signal processing in the terahertz communication links using waveguide Bragg gratings: example of dispersion compensation," *Optics Express*, vol. 25, no. 10, pp. 11009-11026, 2017.
- [117] R. Mendis and D. Grischkowsky, "Undistorted guided-wave propagation of subpicosecond terahertz pulses," *Optics Letters*, vol. 26, no. 11, pp. 846-848, 2001.
- [118] R. Mendis and D. Grischkowsky, "THz interconnect with low-loss and low-group velocity dispersion," *IEEE Microwave and Wireless Components Letters*, vol. 11, no. 11, pp. 444-446, 2001.
- [119] K. S. Reichel, R. Mendis, and D. M. Mittleman, "A broadband terahertz waveguide T-junction variable power splitter," *Scientific Reports*, vol. 6, no. 1, pp. 1-6, 2016.
- [120] K. S. Reichel *et al.*, "Electrically reconfigurable terahertz signal processing devices using liquid metal components," *Nature Communications*, vol. 9, no. 1, pp. 1-6, 2018.
- [121] R. Mendis and D. M. Mittleman, "Comparison of the lowest-order transverse-electric (TE₁) and transverse-magnetic (TEM) modes of the parallel-plate waveguide for terahertz pulse applications," *Optics Express*, vol. 17, no. 17, pp. 14839-14850, 2009.
- [122] K. Wang and D. M. Mittleman, "Metal wires for terahertz wave guiding," *Nature*, vol. 432, no. 7015, pp. 376-379, 2004.
- [123] N. C. Van der Valk and P. C. Planken, "Effect of a dielectric coating on terahertz surface plasmon polaritons on metal wires," *Applied Physics Letters*, vol. 87, no. 7, p. 071106, 2005.
- [124] A. Markov, H. Guerboukha, and M. Skorobogatiy, "Hybrid metal wire–dielectric terahertz waveguides: challenges and opportunities," *JOSA B*, vol. 31, no. 11, pp. 2587-2600, 2014.
- [125] J. Anthony, R. Leonhardt, and A. Argyros, "Hybrid hollow core fibers with embedded wires as THz waveguides," *Optics Express*, vol. 21, no. 3, pp. 2903-2912, 2013.
- [126] M. Mbonye, R. Mendis, and D. M. Mittleman, "A terahertz two-wire waveguide with low bending loss," *Applied Physics Letters*, vol. 95, no. 23, p. 233506, 2009.
- [127] M. K. Mridha *et al.*, "Active terahertz two-wire waveguides," *Optics Express*, vol. 22, no. 19, pp. 22340-22348, 2014.
- [128] D. Teng, Q. Cao, S. Li, and H. Gao, "Tapered dual elliptical plasmon waveguides as highly efficient terahertz connectors between approximate plate waveguides and two-wire waveguides," *JOSA A*, vol. 31, no. 2, pp. 268-273, 2014.
- [129] H. Gao, Q. Cao, M. Zhu, D. Teng, and S. Shen, "Nanofocusing of terahertz wave in a tapered hyperbolic metal waveguide," *Optics Express*, vol. 22, no. 26, pp. 32071-32081, 2014.
- [130] G. Balistreri *et al.*, "Time-Domain Integration of Broadband Terahertz Pulses in a Tapered Two-Wire Waveguide," *Laser and Photonics Reviews*, vol. 15, no. 8, p. 2100051, 2021.

- [131] G. Yan, A. Markov, Y. Chinifooroshan, S. M. Tripathi, W. J. Bock, and M. Skorobogatiy, "Low-loss terahertz waveguide Bragg grating using a two-wire waveguide and a paper grating," *Optics Letters*, vol. 38, no. 16, pp. 3089-3092, 2013.
- [132] A. Markov and M. Skorobogatiy, "Two-wire terahertz fibers with porous dielectric support," *Optics Express*, vol. 21, no. 10, pp. 12728-12743, 2013.
- [133] S. Jia *et al.*, "0.4 THz photonic-wireless link with 106 Gb/s single channel bitrate," *Journal of Lightwave Technology*, vol. 36, no. 2, pp. 610-616, 2018.
- [134] S. Jia *et al.*, "Integrated dual-DFB laser for 408 GHz carrier generation enabling 131 Gbit/s wireless transmission over 10.7 meters," in *Optical Fiber Communication Conference*, 2019, p. Th1C. 2: Optical Society of America.
- [135] K. Liu *et al.*, "100 Gbit/s THz photonic wireless transmission in the 350-GHz band with extended reach," *IEEE Photonics Technology Letters*, vol. 30, no. 11, pp. 1064-1067, 2018.
- [136] N. Oshima, K. Hashimoto, S. Suzuki, and M. Asada, "Terahertz wireless data transmission with frequency and polarization division multiplexing using resonant-tunneling-diode oscillators," *IEEE Transactions on Terahertz Science and Technology*, vol. 7, no. 5, pp. 593-598, 2017.
- [137] Q. Wang *et al.*, "Polarization and frequency multiplexed terahertz meta-holography," *Advanced Optical Materials*, vol. 5, no. 14, 2017.
- [138] J. Ma, N. J. Karl, S. Bretin, G. Ducournau, and D. M. Mittleman, "Frequency-division multiplexer and demultiplexer for terahertz wireless links," *Nature Communications*, vol. 8, no. 1, pp. 1-8, 2017.
- [139] N. J. Karl, R. W. McKinney, Y. Monnai, R. Mendis, and D. M. Mittleman, "Frequency-division multiplexing in the terahertz range using a leaky-wave antenna," *Nature Photonics*, vol. 9, no. 11, pp. 717-720, 2015.
- [140] H. Zhao, B. Quan, X. Wang, C. Gu, J. Li, and Y. Zhang, "Demonstration of orbital angular momentum multiplexing and demultiplexing based on a metasurface in the terahertz band," *ACS Photonics*, vol. 5, no. 5, pp. 1726-1732, 2017.
- [141] I. Baumann, J. Seifert, W. Nowak, and M. Sauer, "Compact all-fiber add-drop-multiplexer using fiber Bragg gratings," *IEEE Photonics Technology Letters*, vol. 8, no. 10, pp. 1331-1333, 1996.
- [142] Y. Tachikawa, Y. Inoue, M. Kawachi, H. Takahashi, and K. Inoue, "Arrayed-waveguide grating add-drop multiplexer with loop-back optical paths," *Electronics Letters*, vol. 29, no. 24, pp. 2133-2134, 1993.
- [143] B. E. Little *et al.*, "Ultra-compact Si-SiO₂ microring resonator optical channel dropping filters," *IEEE Photonics Technology Letters*, vol. 10, no. 4, pp. 549-551, 1998.
- [144] H. A. Haus and Y. Lai, "Narrow-band distributed feedback reflector design," *Journal of Lightwave Technology*, vol. 9, no. 6, pp. 754-760, 1991.
- [145] H. A. Haus and Y. Lai, "Narrow-band optical channel-dropping filter," *Journal of lightwave technology*, vol. 10, no. 1, pp. 57-62, 1992.
- [146] T. D. Ngo, A. Kashani, G. Imbalzano, K. T. Nguyen, and D. Hui, "Additive manufacturing (3D printing): A review of materials, methods, applications and challenges," *Composites Part B: Engineering*, vol. 143, pp. 172-196, 2018.

- [147] Q. Yan *et al.*, "A review of 3D printing technology for medical applications," *Engineering*, vol. 4, no. 5, pp. 729-742, 2018.
- [148] <https://www.museumnext.com/article/how-museums-are-using-3d-printing/>.
- [149] M. Ahmadloo and P. Mousavi, "A novel integrated dielectric-and-conductive ink 3D printing technique for fabrication of microwave devices," in *2013 IEEE MTT-S International Microwave Symposium Digest (MTT)*, 2013, pp. 1-3: IEEE.
- [150] J. A. Byford, M. I. M. Ghazali, S. Karuppuswami, B. L. Wright, and P. Chahal, "Demonstration of RF and microwave passive circuits through 3-D printing and selective metalization," *IEEE Transactions on Components, Packaging and Manufacturing Technology*, vol. 7, no. 3, pp. 463-471, 2017.
- [151] M. I. M. Ghazali, E. Gutierrez, J. C. Myers, A. Kaur, B. Wright, and P. Chahal, "Affordable 3D printed microwave antennas," in *2015 IEEE 65th Electronic Components and Technology Conference (ECTC)*, 2015, pp. 240-246: IEEE.
- [152] S.-W. Qu, H. Yi, C. H. Chan, and K. B. Ng, "Low-cost discrete dielectric terahertz lens antenna using 3D printing," in *2014 IEEE Conference on Antenna Measurements & Applications (CAMA)*, 2014, pp. 1-3: IEEE.
- [153] X. Wei *et al.*, "Generation of arbitrary order Bessel beams via 3D printed axicons at the terahertz frequency range," *Applied Optics*, vol. 54, no. 36, pp. 10641-10649, 2015.
- [154] A. Hernandez-Serrano *et al.*, "Design and fabrication of 3-D printed conductive polymer structures for THz polarization control," *Optics Express*, vol. 27, no. 8, pp. 11635-11641, 2019.
- [155] F. Zhou, W. Cao, B. Dong, T. Reissman, W. Zhang, and C. Sun, "Additive manufacturing of a 3D terahertz gradient-refractive index lens," *Advanced Optical Materials*, vol. 4, no. 7, pp. 1034-1040, 2016.
- [156] S. S. Crump, "Apparatus and method for creating three-dimensional objects," ed: Google Patents, 1992.
- [157] S. Wickramasinghe, T. Do, and P. Tran, "FDM-based 3D printing of polymer and associated composite: A review on mechanical properties, defects and treatments," *Polymers*, vol. 12, no. 7, p. 1529, 2020.
- [158] S. Busch, M. Weidenbach, M. Fey, F. Schäfer, T. Probst, and M. Koch, "Optical properties of 3D printable plastics in the THz regime and their application for 3D printed THz optics," *Journal of Infrared, Millimeter, and Terahertz Waves*, vol. 35, no. 12, pp. 993-997, 2014.
- [159] W. Talataisong *et al.*, "Singlemoded THz guidance in bendable TOPAS suspended-core fiber directly drawn from a 3D printer," *Scientific Reports*, vol. 10, no. 1, pp. 1-10, 2020.
- [160] W. Talataisong *et al.*, "Hollow-core antiresonant terahertz fiber-based TOPAS extruded from a 3D printer using a metal 3D printed nozzle," *Photonics Research*, vol. 9, no. 8, pp. 1513-1521, 2021.
- [161] C. W. J. U. S. P. Hull, Appl., No. 638905, Filed, "Apparatus for production of three-dimensional objects by stereolithography," 1984.
- [162] H. Quan, T. Zhang, H. Xu, S. Luo, J. Nie, and X. Zhu, "Photo-curing 3D printing technique and its challenges," *Bioactive Materials*, vol. 5, no. 1, pp. 110-115, 2020.

- [163] M. D'Auria *et al.*, "3-D printed metal-pipe rectangular waveguides," *IEEE Transactions on Components, Packaging and Manufacturing Technology*, vol. 5, no. 9, pp. 1339-1349, 2015.
- [164] J. Shen and D. S. Ricketts, "Additive manufacturing of complex millimeter-wave waveguides structures using digital light processing," *IEEE Transactions on Microwave Theory and Techniques*, vol. 67, no. 3, pp. 883-895, 2019.
- [165] B. Zhang and H. Zirath, "Metallic 3-D printed rectangular waveguides for millimeter-wave applications," *IEEE Transactions on Components, Packaging and Manufacturing Technology*, vol. 6, no. 5, pp. 796-804, 2016.
- [166] <https://formlabs.com/3d-printers/fuse-1/>.
- [167] M. A. Skylar-Scott, J. Mueller, C. W. Visser, and J. A. Lewis, "Voxelated soft matter via multimaterial multinozzle 3D printing," *Nature*, vol. 575, no. 7782, pp. 330-335, 2019.
- [168] X. Kuang *et al.*, "Advances in 4D printing: Materials and applications," *Advanced Functional Materials*, vol. 29, no. 2, p. 1805290, 2019.
- [169] E.-S. Wu, J. H. Strickler, W. R. Harrell, and W. W. Webb, "Two-photon lithography for microelectronic application," in *Optical/Laser Microlithography V*, 1992, vol. 1674, pp. 776-782: International Society for Optics and Photonics.
- [170] A. Standaert, L. Brancato, B. Lips, F. Ceyssens, R. Puers, and P. Reynaert, "Three techniques for the fabrication of high precision, mm-sized metal components based on two-photon lithography, applied for manufacturing horn antennas for THz transceivers," *Journal of Micromechanics and Microengineering*, vol. 28, no. 3, p. 035008, 2018.
- [171] T. Sörgård *et al.*, "Broadband infrared and THz transmitting silicon core optical fiber," *Optical Materials Express*, vol. 10, no. 10, pp. 2491-2499, 2020.
- [172] C. S. Ponseca Jr *et al.*, "Transmission of terahertz radiation using a microstructured polymer optical fiber," *Optics Letters*, vol. 33, no. 9, pp. 902-904, 2008.
- [173] T. Ma, H. Guerboukha, M. Girard, A. D. Squires, R. A. Lewis, and M. Skorobogatiy, "3D Printed Hollow-Core Terahertz Optical Waveguides with Hyperuniform Disordered Dielectric Reflectors," *Advanced Optical Materials*, vol. 4, no. 12, pp. 2085-2094, 2016.
- [174] A. L. Cruz, C. Cordeiro, and M. A. Franco, "3D printed hollow-core terahertz fibers," *Fibers*, vol. 6, no. 3, p. 43, 2018.
- [175] J.-Y. Lu *et al.*, "Terahertz air-core microstructure fiber," *Applied Physics Letters*, vol. 92, no. 6, p. 064105, 2008.
- [176] T.-I. Jeon, J. Zhang, and D. Grischkowsky, "THz Sommerfeld wave propagation on a single metal wire," *Applied Physics Letters*, vol. 86, no. 16, p. 161904, 2005.
- [177] A. Treizebré, T. Akalin, and B. Bocquet, "Planar excitation of Goubau transmission lines for THz bioMEMS," *IEEE Microwave Wireless Components Letters*, vol. 15, no. 12, pp. 886-888, 2005.
- [178] S. Kaur, S. Kaur, M. Kaur, and G. Kumar, "Numerical analysis of terahertz surface plasmon polaritons propagating in a parallel plate configuration," in *Journal of Physics: Conference Series*, 2016, vol. 759, no. 1, p. 012049: IOP Publishing.

- [179] C. R. Williams, S. R. Andrews, S. Maier, A. Fernández-Domínguez, L. Martín-Moreno, and F. García-Vidal, "Highly confined guiding of terahertz surface plasmon polaritons on structured metal surfaces," *Nature Photonics*, vol. 2, no. 3, pp. 175-179, 2008.
- [180] H. Guerboukha, Y. Amarasinghe, R. Shrestha, A. Pizzuto, and D. M. Mittleman, "High-volume rapid prototyping technique for terahertz metallic metasurfaces," *Optics Express*, vol. 29, no. 9, pp. 13806-13814, 2021.
- [181] T. Rossner, R. Sarwar, A. Lyashenko, E. Dörsam, and R. Werthschützky, "Hot stamped conductors on nano-micro wires made by electroplating for medical sensors and micro-implants," *Proceedings SENSOR*, pp. 248-251, 2013.
- [182] A. Roggenbuck *et al.*, "Coherent broadband continuous-wave terahertz spectroscopy on solid-state samples," *New Journal of Physics*, vol. 12, no. 4, p. 043017, 2010.
- [183] A. Roggenbuck *et al.*, "Using a fiber stretcher as a fast phase modulator in a continuous wave terahertz spectrometer," *JOSA B*, vol. 29, no. 4, pp. 614-620, 2012.
- [184] D. Stanze, A. Deninger, A. Roggenbuck, S. Schindler, M. Schlak, and B. Sartorius, "Compact cw terahertz spectrometer pumped at 1.5 μm wavelength," *Journal of Infrared, Millimeter, and Terahertz Waves*, vol. 32, no. 2, pp. 225-232, 2011.
- [185] K. Nallappan, H. Guerboukha, C. Nerguizian, and M. Skorobogatiy, "Live streaming of uncompressed HD and 4K videos using terahertz wireless links," *IEEE Access*, vol. 6, pp. 58030-58042, 2018.
- [186] J. F. Federici *et al.*, "THz imaging and sensing for security applications—explosives, weapons and drugs," *Semiconductor Science and Technology*, vol. 20, no. 7, p. S266, 2005.
- [187] J. H. Wade and R. C. J. A. c. Bailey, "Refractive index-based detection of gradient elution liquid chromatography using chip-integrated microring resonator arrays," vol. 86, no. 1, pp. 913-919, 2014.
- [188] M. Brucherseifer, M. Nagel, P. Haring Bolivar, H. Kurz, A. Bosserhoff, and R. Büttner, "Label-free probing of the binding state of DNA by time-domain terahertz sensing," *Applied Physics Letters*, vol. 77, no. 24, pp. 4049-4051, 2000.
- [189] V. Matvejev, Y. Zhang, and J. Stiens, "High performance integrated terahertz sensor for detection of biomolecular processes in solution," *IET Microwaves, Antennas and Propagation*, vol. 8, no. 6, pp. 394-400, 2014.
- [190] J. Qin, L. Xie, and Y. Ying, "A high-sensitivity terahertz spectroscopy technology for tetracycline hydrochloride detection using metamaterials," *Food Chemistry*, vol. 211, pp. 300-305, 2016.
- [191] W. Xu *et al.*, "Terahertz sensing of chlorpyrifos-methyl using metamaterials," *Food chemistry*, vol. 218, pp. 330-334, 2017.
- [192] M. Skorobogatiy, "Microstructured and photonic bandgap fibers for applications in the resonant bio-and chemical sensors," *Journal of Sensors*, vol. 2009, 2009.
- [193] X. Chen and W. Fan, "Ultrasensitive terahertz metamaterial sensor based on spoof surface plasmon," *Scientific Reports*, vol. 7, no. 1, pp. 1-8, 2017.
- [194] W. Wang, F. Yan, S. Tan, H. Zhou, and Y. Hou, "Ultrasensitive terahertz metamaterial sensor based on vertical split ring resonators," *Photonics Research*, vol. 5, no. 6, pp. 571-577, 2017.

- [195] P. Russell, "Photonic crystal fibers," *Science*, vol. 299, no. 5605, pp. 358-362, 2003.
- [196] C. Lin, W. Zhang, Y. Huang, and J. Peng, "Zero dispersion slow light with low leakage loss in defect Bragg fiber," *Applied Physics Letters*, vol. 90, no. 3, p. 031109, 2007.
- [197] L. Shang and K. Zheng, "Design of hollow core Bragg fibers for a compact fluorescence sensing scheme," *IEEE Photonics Journal*, vol. 9, no. 2, pp. 1-15, 2017.
- [198] A. Squires, E. Constable, and R. Lewis, "3D printed terahertz diffraction gratings and lenses," *Journal of Infrared, Millimeter, and Terahertz Waves*, vol. 36, no. 1, pp. 72-80, 2015.
- [199] D. Jahn *et al.*, "3D printed terahertz focusing grating couplers," *Journal of Infrared, Millimeter, and Terahertz Waves*, vol. 38, no. 6, pp. 708-716, 2017.
- [200] B. Gauvreau *et al.*, "Color-changing and color-tunable photonic bandgap fiber textiles," *Optics Express*, vol. 16, no. 20, pp. 15677-15693, 2008.
- [201] E. Pone *et al.*, "Drawing of the hollow all-polymer Bragg fibers," *Optics Express*, vol. 14, no. 13, pp. 5838-5852, 2006.
- [202] H. T. Bookey *et al.*, "Experimental demonstration of spectral broadening in an all-silica Bragg fiber," *Optics Express*, vol. 17, no. 19, pp. 17130-17135, 2009.
- [203] M. Zhu *et al.*, "Fabrication of an IR hollow-core Bragg fiber based on chalcogenide glass extrusion," *Applied Physics A*, vol. 119, no. 2, pp. 455-460, 2015.
- [204] K. Stoeffler, C. Dubois, A. Ajji, N. Guo, F. Boismenu, and M. Skorobogatiy, "Fabrication of all-polymeric photonic bandgap Bragg fibers using rolling of coextruded PS/PMMA multilayer films," *Polymer Engineering and Science*, vol. 50, no. 6, pp. 1122-1127, 2010.
- [205] B. Huang and S. Singamneni, "Adaptive slicing and speed-and time-dependent consolidation mechanisms in fused deposition modeling," *Proceedings of the Institution of Mechanical Engineers, Part B: Journal of Engineering Manufacture*, vol. 228, no. 1, pp. 111-126, 2014.
- [206] M. P. Lee, G. J. Cooper, T. Hinkley, G. M. Gibson, M. J. Padgett, and L. Cronin, "Development of a 3D printer using scanning projection stereolithography," *Scientific Reports*, vol. 5, no. 1, pp. 1-5, 2015.
- [207] P. U. Jepsen, D. G. Cooke, and M. Koch, "Terahertz spectroscopy and imaging—Modern techniques and applications," *Laser and Photonics Reviews*, vol. 5, no. 1, pp. 124-166, 2011.
- [208] H. Guerboukha, K. Nallappan, and M. Skorobogatiy, "Toward real-time terahertz imaging," *Advances in Optics and Photonics*, vol. 10, no. 4, pp. 843-938, 2018.
- [209] B. Ung, A. Dupuis, K. Stoeffler, C. Dubois, and M. Skorobogatiy, "High-refractive-index composite materials for terahertz waveguides: trade-off between index contrast and absorption loss," *JOSA B*, vol. 28, no. 4, pp. 917-921, 2011.
- [210] A. M. Adbul-Munaim, M. Reuter, M. Koch, and D. G. Watson, "Distinguishing gasoline engine oils of different viscosities using terahertz time-domain spectroscopy," *Journal of Infrared, Millimeter, and Terahertz Waves*, vol. 36, no. 7, pp. 687-696, 2015.
- [211] R. Fitzpatrick, *Theoretical fluid mechanics*. IOP Publishing Bristol, 2017.
- [212] H. Bruus, *Theoretical microfluidics*. Oxford university press Oxford, 2008.

- [213] T. Kleine-Ostmann and T. Nagatsuma, "A review on terahertz communications research," *Journal of Infrared, Millimeter, and Terahertz Waves*, vol. 32, no. 2, pp. 143-171, 2011.
- [214] Y. Ghasempour, R. Shrestha, A. Charous, E. Knightly, and D. M. Mittleman, "Single-shot link discovery for terahertz wireless networks," *Nature Communications*, vol. 11, no. 1, pp. 1-6, 2020.
- [215] Z. Chen *et al.*, "A survey on terahertz communications," *China Communications*, vol. 16, no. 2, pp. 1-35, 2019.
- [216] S. Taravati and C. Caloz, "Mixer-duplexer-antenna leaky-wave system based on periodic space-time modulation," *IEEE Transactions on Antennas and Propagation*, vol. 65, no. 2, pp. 442-452, 2016.
- [217] A. Al-Bassam, S. Otto, D. Heberling, and C. Caloz, "Broadside dual-channel orthogonal-polarization radiation using a double-asymmetric periodic leaky-wave antenna," *IEEE Transactions on Antennas and Propagation*, vol. 65, no. 6, pp. 2855-2864, 2017.
- [218] L. Liu, C. Caloz, and T. Itoh, "Dominant mode leaky-wave antenna with backfire-to-endfire scanning capability," *Electronics Letters*, vol. 38, no. 23, pp. 1414-1416, 2002.
- [219] C. Caloz, T. Itoh, and A. Rennings, "CRLH metamaterial leaky-wave and resonant antennas," *IEEE Antennas and Propagation Magazine*, vol. 50, no. 5, pp. 25-39, 2008.
- [220] B. Bowden, J. A. Harrington, and O. Mitrofanov, "Low-loss modes in hollow metallic terahertz waveguides with dielectric coatings," *Applied Physics Letters*, vol. 93, no. 18, p. 181104, 2008.
- [221] J. A. Harrington, R. George, P. Pedersen, and E. Mueller, "Hollow polycarbonate waveguides with inner Cu coatings for delivery of terahertz radiation," *Optics Express*, vol. 12, no. 21, pp. 5263-5268, 2004.
- [222] M. Poulin, S. Giannacopoulos, and M. Skorobogatiy, "Surface wave enhanced sensing in the terahertz spectral range: modalities, materials, and perspectives," *Sensors*, vol. 19, no. 24, p. 5505, 2019.
- [223] B. Vidal, T. Nagatsuma, N. J. Gomes, and T. E. Darcie, "Photonic Technologies for Millimeter-and Submillimeter-Wave Signals," *Advances in Optical Technologies*, 2012.
- [224] J. Li, J. He, and Z. Hong, "Terahertz wave switch based on silicon photonic crystals," *Applied Optics*, vol. 46, no. 22, pp. 5034-5037, 2007.
- [225] S. Li, H. Liu, Q. Sun, and N. Huang, "A tunable terahertz photonic crystal narrow-band filter," *IEEE Photonics Technology Letters*, vol. 27, no. 7, pp. 752-754, 2015.
- [226] H.-W. Hübers, "Towards THz integrated photonics," *Nature Photonics*, vol. 4, no. 8, pp. 503-504, 2010.
- [227] X. Yu, R. Yamada, J.-Y. Kim, M. Fujita, and T. Nagatsuma, "Integrated circuits using photonic-crystal slab waveguides and resonant tunneling diodes for terahertz communication," in *2018 Progress in Electromagnetics Research Symposium (PIERS-Toyama)*, 2018, pp. 599-605: IEEE.
- [228] F. Fan, Y. Hou, Z.-W. Jiang, X.-H. Wang, and S.-J. Chang, "Terahertz modulator based on insulator-metal transition in photonic crystal waveguide," *Applied optics*, vol. 51, no. 20, pp. 4589-4596, 2012.
- [229] A. Hassani, A. Dupuis, and M. Skorobogatiy, "Low loss porous terahertz fibers containing multiple subwavelength holes," *Applied Physics Letters*, vol. 92, no. 7, p. 071101, 2008.

- [230] A. Hassani, A. Dupuis, and M. Skorobogatiy, "Porous polymer fibers for low-loss Terahertz guiding," *Optics Express*, vol. 16, no. 9, pp. 6340-6351, 2008.
- [231] H. Bao, K. Nielsen, O. Bang, and P. U. Jepsen, "Dielectric tube waveguides with absorptive cladding for broadband, low-dispersion and low loss THz guiding," *Scientific Reports*, vol. 5, no. 1, pp. 1-9, 2015.
- [232] D. A. Kovacevich *et al.*, "Self-limiting electrospray deposition for the surface modification of additively manufactured parts," *ACS Applied Materials and Interfaces*, vol. 12, no. 18, pp. 20901-20911, 2020.
- [233] H. Pahlevaninezhad, T. E. Darcie, and B. Heshmat, "Two-wire waveguide for terahertz," *Optics Express*, vol. 18, no. 7, pp. 7415-7420, 2010.
- [234] H. Pahlevaninezhad and T. E. Darcie, "Coupling of terahertz waves to a two-wire waveguide," *Optics Express*, vol. 18, no. 22, pp. 22614-22624, 2010.
- [235] X. Zhang, Y. L. Chen, R.-S. Liu, and D. P. Tsai, "Plasmonic photocatalysis," *Reports on Progress in Physics*, vol. 76, no. 4, p. 046401, 2013.
- [236] T. Wen, J. Gao, B. Bian, and J. Shen, "Investigation on roughness of silver thin films inside silica capillaries for hollow waveguides," *Materials Letters*, vol. 50, no. 2-3, pp. 124-128, 2001.
- [237] J. S. Jo, T.-I. Jeon, and D. R. Grischkowsky, "Prototype 250 GHz bandwidth chip to chip electrical interconnect, characterized with ultrafast optoelectronics," *IEEE Transactions on Terahertz Science and Technology*, vol. 3, no. 4, pp. 453-460, 2013.
- [238] N. Laman and D. Grischkowsky, "Reduced conductivity in the terahertz skin-depth layer of metals," *Applied Physics Letters*, vol. 90, no. 12, p. 122115, 2007.
- [239] M. Nazarov and J.-L. Coutaz, "Terahertz surface waves propagating on metals with sub-wavelength structure and grating reliefs," *Journal of Infrared, Millimeter, and Terahertz Waves*, vol. 32, no. 10, p. 1054, 2011.
- [240] A. J. Shutler and D. Grischkowsky, "Gap independent coupling into parallel plate terahertz waveguides using cylindrical horn antennas," *Journal of Applied Physics*, vol. 112, no. 7, p. 073102, 2012.
- [241] T. L. Cocker *et al.*, "Microscopic origin of the Drude-Smith model," *Physical Review B*, vol. 96, no. 20, p. 205439, 2017.
- [242] J. Ma, M. Weidenbach, R. Guo, M. Koch, and D. Mittleman, M, "Communications with THz waves: switching data between two waveguides," *Journal of Infrared, Millimeter, and Terahertz Waves*, vol. 38, no. 11, pp. 1316-1320, 2017.
- [243] J. Saijonmaa and D. Yevick, "Beam-propagation analysis of loss in bent optical waveguides and fibers," *JOSA*, vol. 73, no. 12, pp. 1785-1791, 1983.
- [244] Y. A. Vlasov and S. J. McNab, "Losses in single-mode silicon-on-insulator strip waveguides and bends," *Optics Express*, vol. 12, no. 8, pp. 1622-1631, 2004.
- [245] J. T. Kim, S. Park, J. J. Ju, S. Lee, and S. Kim, "Low bending loss characteristics of hybrid plasmonic waveguide for flexible optical interconnect," *Optics Express*, vol. 18, no. 23, pp. 24213-24220, 2010.

- [246] V. Astley, J. Scheiman, R. Mendis, and D. M. Mittleman, "Bending and coupling losses in terahertz wire waveguides," *Optics Letters*, vol. 35, no. 4, pp. 553-555, 2010.
- [247] J.-T. Lu, Y.-C. Hsueh, Y.-R. Huang, Y.-J. Hwang, and C.-K. Sun, "Bending loss of terahertz pipe waveguides," *Optics Express*, vol. 18, no. 25, pp. 26332-26338, 2010.
- [248] D. Marcuse, "Curvature loss formula for optical fibers," *JOSA*, vol. 66, no. 3, pp. 216-220, 1976.
- [249] R. T. Schermer and J. H. Cole, "Improved bend loss formula verified for optical fiber by simulation and experiment," *IEEE Journal of Quantum Electronics*, vol. 43, no. 10, pp. 899-909, 2007.
- [250] K. Nallappan, H. Guerboukha, C. Nerguizian, and M. Skorobogatiy, "Live streaming of uncompressed 4K video using terahertz wireless links," presented at the IEEE International Conference on Communications (ICC), 2018.
- [251] T. Nagatsuma and K. Kato, "Photonically-assisted 300-GHz wireless link for real-time 100-Gbit/s transmission," in *2014 IEEE MTT-S International Microwave Symposium (IMS2014)*, 2014, pp. 1-4: IEEE.
- [252] S. F. Zhou, L. Reekie, H. P. Chan, Y. T. Chow, P. S. Chung, and K. M. Luk, "Characterization and modeling of Bragg gratings written in polymer fiber for use as filters in the THz region," *Optics Express*, vol. 20, no. 9, pp. 9564-9571, 2012.
- [253] I. Yamada, K. Takano, M. Hangyo, M. Saito, and W. Watanabe, "Terahertz wire-grid polarizers with micrometer-pitch Al gratings," *Optics Letters*, vol. 34, no. 3, pp. 274-276, 2009.
- [254] Y. M. Shin, L. R. Barnett, D. Gamzina, N. C. Luhmann Jr, M. Field, and R. Borwick, "Terahertz vacuum electronic circuits fabricated by UV lithographic molding and deep reactive ion etching," *Applied Physics Letters*, vol. 95, no. 18, p. 181505, 2009.
- [255] H. Lee and G. P. Agrawal, "Add-drop multiplexers and interleavers with broad-band chromatic dispersion compensation based on purely phase-sampled fiber gratings," *IEEE Photonics Technology Letters*, vol. 16, no. 2, pp. 635-637, 2004.
- [256] E. I. Simakov, C. E. Heath, D. Y. Shchegolkov, M. J. Kelly, and B. D. Schultz, "Fabrication and testing of channel-drop filters at millimeter waves," in *2011 International Conference on Infrared, Millimeter, and Terahertz Waves*, 2011, pp. 1-3: IEEE.
- [257] E. I. Simakov, L. M. Earley, C. E. Heath, D. Y. Shchegolkov, and B. D. Schultz, "First experimental demonstration of a photonic band gap channel-drop filter at 240 GHz," *Review of Scientific Instruments*, vol. 81, no. 10, p. 104701, 2010.
- [258] M. Shalaby *et al.*, "Terahertz Faraday rotation in a magnetic liquid: High magneto-optical figure of merit and broadband operation in a ferrofluid," *Applied Physics Letters*, vol. 100, no. 24, p. 241107, 2012.
- [259] <https://www.statista.com/statistics/271405/global-mobile-data-traffic-forecast/>.
- [260] R. V. Hartley, "Transmission of information," *Bell System Technical Journal*, vol. 7, no. 3, pp. 535-563, 1928.
- [261] Y. Niu, Y. Li, D. Jin, L. Su, and A. V. Vasilakos, "A survey of millimeter wave communications (mmWave) for 5G: opportunities and challenges," *Wireless Networks*, vol. 21, no. 8, pp. 2657-2676, 2015.

- [262] J. Zhang, P. Tang, L. Tian, Z. Hu, T. Wang, and H. Wang, "6–100 GHz research progress and challenges from a channel perspective for fifth generation (5G) and future wireless communication," *Science China Information Sciences*, vol. 60, no. 8, pp. 1-18, 2017.
- [263] I. F. Akyildiz, J. M. Jornet, and C. Han, "Terahertz band: Next frontier for wireless communications," *Physical Communication*, vol. 12, pp. 16-32, 2014.
- [264] H. Toba, K. Inoue, and K. Nosu, "A conceptional design on optical frequency-division-multiplexing distribution systems with optical tunable filters," *IEEE Journal on Selected Areas in Communications*, vol. 4, no. 9, pp. 1458-1467, 1986.
- [265] X. Zhao *et al.*, "Silicon micromachined D-band diplexer using releasable filling structure technique," *IEEE Transactions on Microwave Theory and Techniques*, vol. 68, no. 8, pp. 3448-3460, 2020.
- [266] A. Sabharwal, A. Khoshnevis, and E. Knightly, "Opportunistic spectral usage: Bounds and a multi-band CSMA/CA protocol," *IEEE/ACM Transactions On Networking*, vol. 15, no. 3, pp. 533-545, 2007.
- [267] K. O. Hill and G. Meltz, "Fiber Bragg grating technology fundamentals and overview," *Journal of Lightwave Technology*, vol. 15, no. 8, pp. 1263-1276, 1997.
- [268] F. Fan, S. J. Chang, C. Niu, Y. Hou, and X.-H. Wang, "Magnetically tunable silicon-ferrite photonic crystals for terahertz circulator," *Optics Communications*, vol. 285, no. 18, pp. 3763-3769, 2012.
- [269] C. Riziotis and M. N. Zervas, "Novel full-cycle-coupler-based optical add-drop multiplexer and performance characteristics at 40-Gb/s WDM networks," *Journal of Lightwave Technology*, vol. 21, no. 8, p. 1828, 2003.
- [270] C. Riziotis and M. N. Zervas, "Performance comparison of Bragg grating-based optical add-drop multiplexers in WDM transmission systems," *IEE Proceedings-Circuits, Devices and Systems*, vol. 149, no. 3, pp. 179-186, 2002.
- [271] S. S. Orlov, A. Yariv, and S. Van Essen, "Coupled-mode analysis of fiber-optic add-drop filters for dense wavelength-division multiplexing," *Optics Letters*, vol. 22, no. 10, pp. 688-690, 1997.
- [272] W. Shi *et al.*, "Silicon photonic grating-assisted, contra-directional couplers," *Optics Express*, vol. 21, no. 3, pp. 3633-3650, 2013.
- [273] D. Johnson, K. Hill, F. Bilodeau, and S. Faucher, "New design concept for a narrowband wavelength-selective optical tap and combiner," *Electronics Letters*, vol. 23, no. 13, pp. 668-669, 1987.
- [274] D. I. Babic and S. W. Corzine, "Analytic expressions for the reflection delay, penetration depth, and absorptance of quarter-wave dielectric mirrors," *IEEE Journal of Quantum Electronics*, vol. 28, no. 2, pp. 514-524, 1992.
- [275] M. Dionigi, C. Tomassoni, G. Venanzoni, and R. Sorrentino, "Simple high-performance metal-plating procedure for stereolithographically 3-D-printed waveguide components," *IEEE Microwave and Wireless Components Letters*, vol. 27, no. 11, pp. 953-955, 2017.
- [276] G. P. Agrawal, *Lightwave technology: telecommunication systems*. John Wiley & Sons, 2005.

APPENDIX A SUPPLEMENTARY MATERIAL FOR: ADDITIVE MANUFACTURING OF RESONANT FLUIDIC SENSORS BASED ON PHOTONIC BANDGAP WAVEGUIDES FOR TERAHERTZ APPLICATIONS

A.1 The RI of PLA used in FDM-3D printing

The RI and absorption loss of the PLA material used in the PBG Bragg waveguide fabrication were measured by employing a cutback method and CW-THz spectroscopy. As shown in Fig. A.1(a), the printed PLA plates with a thickness of ~ 4 mm were first placed in a stack and then inserted in the path of a collimated THz beam. Then, several consecutive measurements of the transmitted complex field as a function of frequency were performed by removing the plates from the stack one after another. The RI and loss can then be extracted from the amplitudes and phases of the normalized transmission spectra by using transmission through an empty system as a reference (see Fig. A.1(b) and A.1(c)). Particularly, for the stack of length L and complex refractive index $n(\omega)$, the following equations were used to interpret the measured data:

$$T(\omega, L) = \frac{E_{stack}}{E_{ref}} = C_{in}(\omega) \cdot C_{out}(\omega) \cdot \exp\left(-\frac{\alpha(\omega)}{2} \cdot L\right) \cdot \exp(i\varphi(\omega, L)) \quad (A.1)$$

$$\varphi(\omega, L) = -\frac{\omega}{c} (\text{Re}(n(\omega)) - 1)L \quad (A.2)$$

$$\alpha(\omega) = \frac{2\omega}{c} \text{Im}(n(\omega)) \quad (A.3)$$

where E_{stack} and E_{ref} are the complex transmission spectra of the PLA stack and the reference spectrum. C_{in} and C_{out} are the coupling and outcoupling efficiencies of the probing THz beam at the two PLA stack/air interfaces, which are presumed the same for stacks of different lengths. The RI and absorption coefficient of the PLA plates were then deducted from Fig. A.1(d) and A.1(e) via standard interpretation of the cutback data to be the following:

$$n_{real}(\omega) = 1.636 - 0.0331 \cdot \omega [\text{THz}] \quad (A.4)$$

$$\alpha(\omega) [\text{cm}^{-1}] = 0.16482 + 19.695 \cdot (\omega [\text{THz}])^2 \quad (A.5)$$

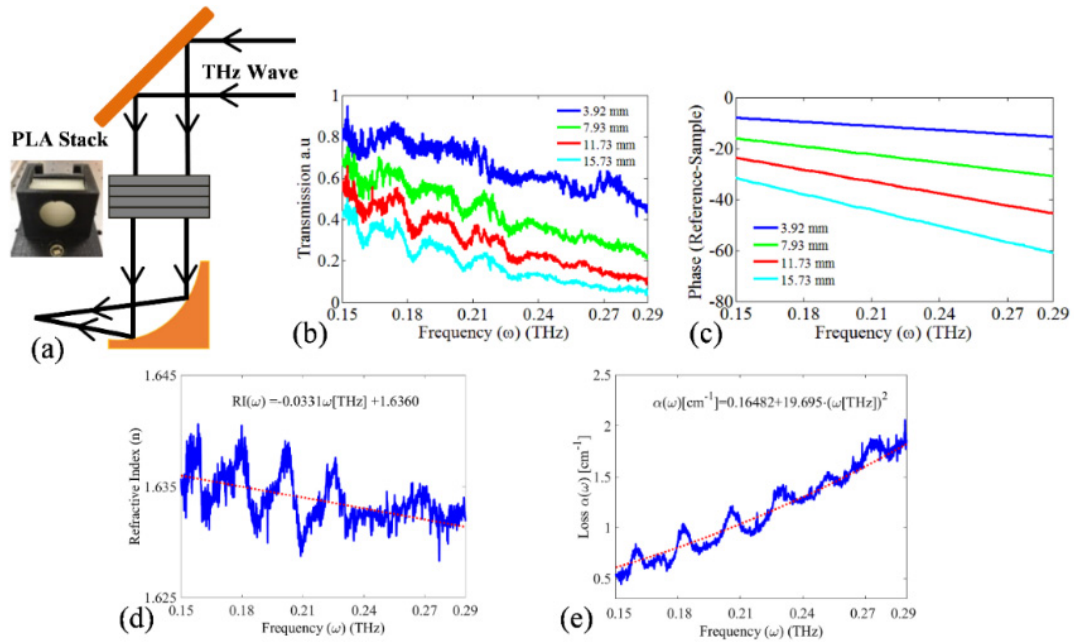


Figure A. 1 The measurement of complex RI of 3D printed PLA plates

(a) Schematic of the experimental setup to measure the RI and absorption loss of PLA material used in FDM. (b) Normalized transmission spectra of the PLA stack consisting of different numbers of PLA plates. (c) Unwrapped phase of the transmitted THz wave (relative to the reference spectrum) of the PLA stack consisting of different numbers of PLA plates. (d) Measured and fitted RI of the PLA in 0.15 – 0.29 THz frequency range. (e) Measured and fitted absorption loss of the PLA in 0.15 – 0.29 THz frequency range.

A.2 The RI of mineral and cinnamon essential oil

The RI of the mineral and cinnamon essential oil used as liquid analytes for sensing were measured by employing the cutback method and a THz-TDS system. As shown in Fig. A.2(a), a THz-transparent plastic container was first placed in the path of a collimated THz beam. Then, several consecutive measurements of the transmitted complex field as a function of frequency were performed by injecting oil analyte into the container successively. Based on the Eqs. A.1 and A.2, the analyte RI can then be deduced from the phases of the normalized transmission spectra using transmission through an empty container as a reference (see Fig. A.2(b) and A.2(c)). Under such condition, the RIs of the mineral and cinnamon essential oil were computed as 1.455 and 1.555, respectively (see Fig. A.2(d) and A.2(e)).

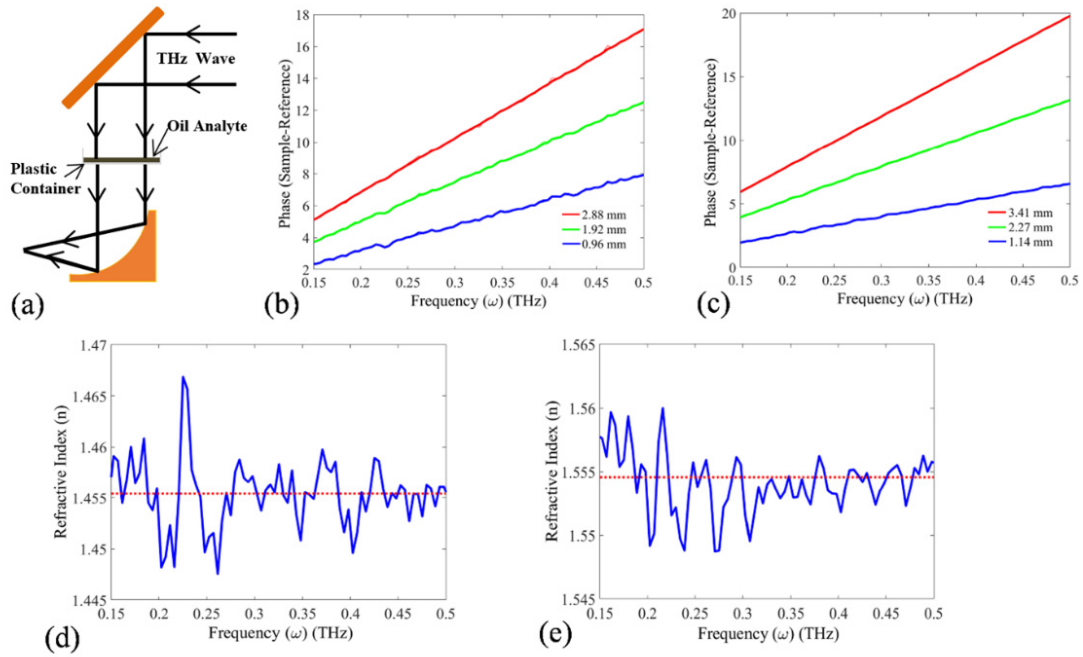


Figure A. 2 Measurement of RI of fluidic analytes for THz sensing

(a) Schematic of the experimental setup to measure the RI of mineral and cinnamon essential oil. (b) Unwrapped phase of the transmitted THz wave (relative to the reference spectrum) of the mineral oil with different thicknesses. (c) Unwrapped phase of the transmitted THz wave (relative to the reference spectrum) of the cinnamon essential oil with different thicknesses. (d) Measured RI of the mineral oil in the 0.15 – 0.5 THz frequency range. (e) Measured RI of the cinnamon essential oil in the 0.15 – 0.5 THz frequency range.

APPENDIX B SUPPLEMENTARY MATERIAL FOR: ADDITIVE MANUFACTURING OF HIGHLY RECONFIGURABLE PLASMONIC CIRCUITS FOR TERAHERTZ COMMUNICATIONS

B.1 The influence of the accidental degeneracy of the dispersion relations of the SPP mode and bulk modes of a resin cage

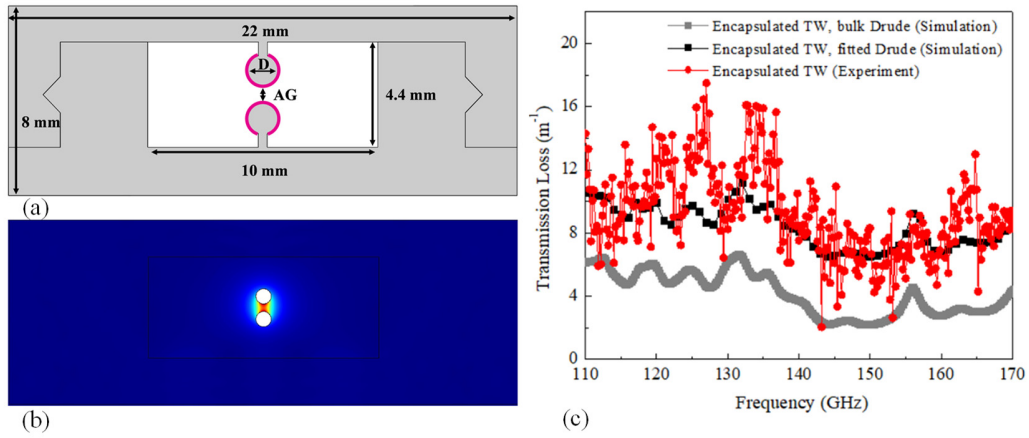


Figure B. 1 Micro-encapsulated two-wire waveguide in another design

(a). The schematic of a two-wire waveguide encapsulated by a resin cage featuring wider confined air area than the one indicated in the main text. (b). The modal electric amplitude field distribution of the supported THz SPP wave at 140 GHz. (c). The theoretical modal loss (by field) of the THz SPP wave and the measured transmission loss (by field) of the straight two-wire waveguide.

Here we studied a straight two-wire waveguide encapsulated by a resin cage featuring a wider internal dimension (the width of the air space is increased from 6.5 mm to 10 mm) than that of the two-wire waveguide indicated in the main-text (see Fig. B.1(a)). In these two designs, the geometries of the wire support including wire diameter and inter-wire separation are identical. As larger hollow space is left between the wires and the resin cage in this design, the presence of a portion of the supported THz SPP wave in the lossy resin is smaller than that of the waveguide studied in the main text (see Fig. B.1(b)). Therefore, the computed modal loss and measured transmission loss (by field) of this waveguide are somewhat smaller at 140 GHz. However, Fig. B.1(c) shows that the modal loss of the supported THz SPP wave in a broad spectral range of 110-135 GHz is larger than that of the other characterized frequencies,

and larger measured transmission loss appears in such spectral range in experiments. It is different from the two-wire waveguides indicated in main-text whose measured transmission loss maintains despite the presence of modal loss peak of the supported THz SPP wave featuring a narrow spectral width in numerical simulations. We believe that the observed modal loss increase is resulting from the hybridization between the THz SPP wave and a mode supported by the resin cage. The spectral position of the resonant frequency is related to the geometry of wires and the cage. In this design (Fig. B.1(a)), even with inaccuracy in 3D printed structure from the ideal model, the avoided crossing phenomenon is easy to be excited, thus resulting in the larger transmission loss in a broad spectral range. Therefore, different from the stand-alone two-wire waveguide that features a frequency-insensitive transmission loss, the proposed 3D printed waveguide has to be designed appropriately to avoid the presence of modal loss peaks featuring a large spectral width around the desired operation frequency.

B.2 The transverse electric field distribution of the fundamental modes of micro-encapsulated two-wire waveguides and WR6.5 waveguide flange

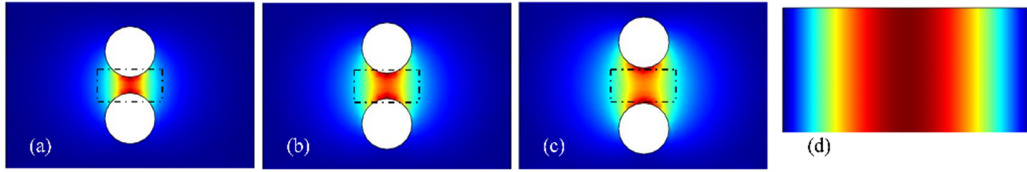


Figure B. 2 The transverse modal electric field distribution $|E_t|$ of the fundamental mode of the micro-encapsulated two-wire waveguides

Two-wire waveguides featuring different inter-wire separations at 140 GHz. The black dotted region represents the opening of the WR6.5 waveguide flange under the butt-coupling arrangement. (a) $AG=0.5 \cdot \lambda_{WR6}$. (b) $AG=0.8 \cdot \lambda_{WR6}$. (c) $AG=1.1 \cdot \lambda_{WR6}$. (d) The transverse modal electric field distribution $|E_t|$ of the fundamental mode of the WR6.5 waveguide flange at 140 GHz.

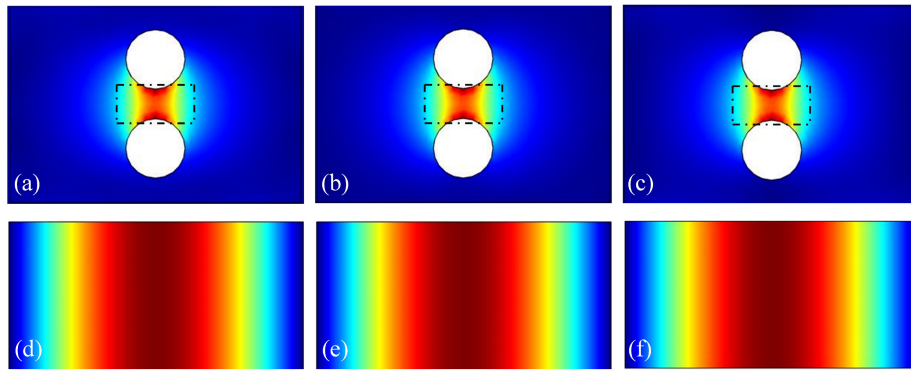


Figure B. 3 The transverse electric field distribution $|E_t|$ of the fundamental mode of a micro-encapsulated two-wire waveguide

Studied at operation frequencies of (a) 110 GHz (b)140 GHz and (c)170 GHz. The transverse modal electric field distribution $|E_t|$ of the TE_{10} mode of the WR6.5 waveguide flange at the operation frequencies of (d) 110 GHz (e)140 GHz and (f)170 GHz.

B.3 The characterization of the micro-encapsulated two-wire waveguide components and circuits

The proposed 3D printed micro-encapsulated two-wire waveguide components and circuits were studied by using the CW-THz spectroscopy system (TOPTICA Photonics) [182, 184]. The schematic of the experimental setup is shown in Figs. B.4(a), B.4(b), B.6(a), B.6(b) and B.7(a). The CW-THz spectroscopy system is briefly explained as follows. Two distributed feedback (DFB) lasers of power ~ 30 mW, operating in the infrared C-band with slightly different emission wavelengths are used as the source of THz generation. A 50:50 fiber coupler is used to combine the two laser beams and split into both emission and detection arms respectively. The THz radiation is generated in the emitter photomixer (under bias voltage) and corresponds to the beat frequency between the two DFB lasers. The output THz frequency can be varied by simply tuning the emission wavelengths of the lasers. A similar photomixer (without bias voltage) and a lock-in amplifier are used to detect the THz radiation. The focused linear-polarized CW-THz beam transmitting through the waveguides is re-collimated and the amplitude of the THz signal is recorded using lock-in detection.

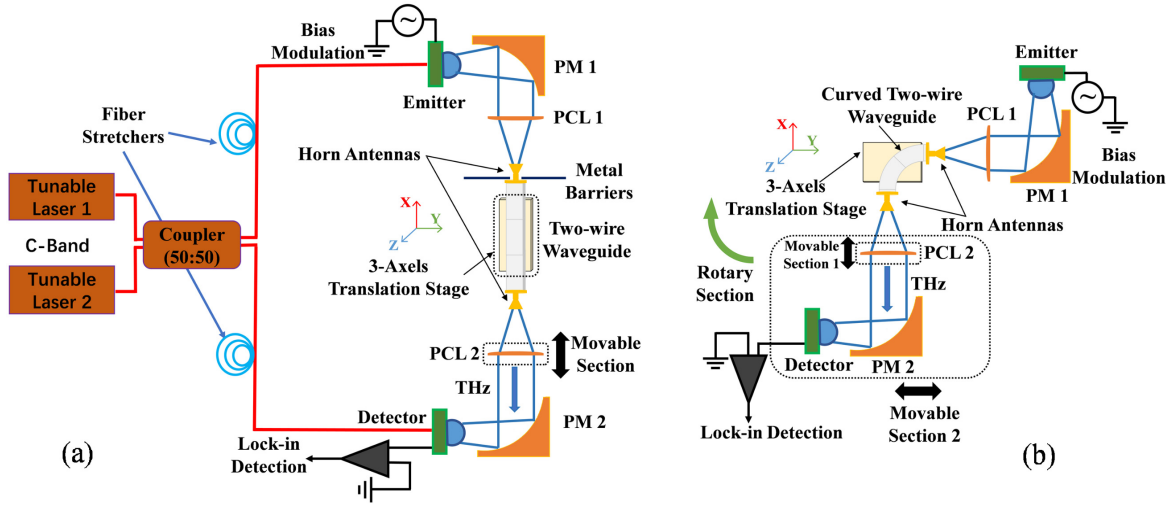


Figure B. 4 Experimental setup to characterize two-wire waveguides

- (a). The experimental setup to measure the propagation loss and the GVD of straight two-wire waveguides. The same setup is also used to characterize the two-wire WBGs. PM: off-axis parabolic mirror featuring a reflective focal length of 10.1 cm (MPD249-M01, Thorlabs, Inc.), PCL: PTFE plano-convex lens featuring a focal length of 7.5 cm (LAT075, Thorlabs, Inc.). (b). The experimental setup to measure the bending loss of the curved two-wire waveguides.

B.3.1 The measurement of the propagation loss and GVD of the straight two-wire waveguides and the characterization of the WBGs

The straight two-wire waveguides were characterized in the following processes. Firstly, the reference spectrum was recorded by placing two WR6.5 conical horn antennas (Virginia Diode, Inc.) between the two neighboring plano-convex lenses PCL1 and PCL2 with their focal points at the input and output plane of the connected waveguide flanges. Note that PCL2 is mounted onto an optical rail, and represents an MS of the spectrometer, thus allowing measuring two-wire waveguides of various lengths, as well as the reference signal. The assembled two-wire waveguide composed of multiple WSs was connected with WR6.5 conical horn antennas at both ends. The whole section was then inserted into the spectrometer with the input and output planes of the waveguide flanges at the focal points of PCL1 and PCL2 via adjusting the positions of the MS and 3-axels translation stage. The schematic of the characterization setup is shown in Fig. B.4(a). Finally, a cutback measurement was carried out by subsequently removing the WSs sandwiched

between the input and output WSs. The measured complex transmission spectra (by field) were then analyzed to estimate the transmission loss and coupling loss of the two-wire waveguide.

In experiments, two sets of waveguide samples were characterized to distinguish the transmission loss α_{st} and the coupling loss Cl (by field) between neighboring WSs. Each set includes the same number of WSs with the same length l . By comparing the measurements with the reference, the normalized transmittance (by field) t_{ml} of waveguides can be given as follow:

$$t_{ml} = |C_{in}| |C_{out}| Cl^{m-1} \cdot \exp(-\alpha_{st} ml) \quad (B.1)$$

where, $|C_{in}|$ and $|C_{out}|$ refer to the input and output field coupling coefficients which are assumed as a constant, while m refers to the number of measured WSs. By expressing the Eq. B.1 as the logarithms of e and comparing the transmittance of two waveguides integrated by the same number of sections from different sets of samples, the transmission loss α_{st} was derived by the following equation:

$$\log(t_{ml_1}) - \log(t_{ml_2}) = -m\alpha(l_1 - l_2) \quad (B.2)$$

Then, with the measured transmission loss α_{st} , the average coupling loss Cl was obtained by comparing the transmittance of waveguides exhibiting different lengths.

The phase measurement was performed by the CW-THz spectroscopy using an optical delay line in the form of polarization-maintaining fiber wound piezoelectric elements (see Fig. B.4(a)) [183]. The effective RI of the two-wire waveguide was computed from the normalized complex transmission spectrum (by field) and then fitted into a two-order polynomial function of angular frequency ω [208]. The GVD was computed as the second-order derivative of the derived waveguide propagation constant with respect to ω by Eq. 5.3.

To characterize the two-wire WBGs, a 3D printed two-wire waveguide with slits (the schematic diagram is shown in Fig. 5.4(a)) was placed with its two ends at the focal points of the PCL1 and PCL2. Firstly, the reference transmission spectrum (by field) was obtained by measuring the waveguide without the paper. After inserting the paper-based periodic metalized structure between wires, the transmission spectra (by field) of WBGs were recorded. The transmittances spectra were then obtained by dividing them by the reference data.

B.3.2 The measurement of the bending loss of the two-wire waveguide bends

The transmission spectra of the two-wire waveguide bends were measured by the following process. 90° bends having different bend radii were fabricated and characterized. In order to avoid the difference in the coupling coefficient between different waveguide bends with the WR6.5 waveguide flange, a 5mm-length straight WS is integrated at both ends of each waveguide bend. The schematic of the experimental setup is shown in Fig. B.4(b). It is noted that the straight waveguide can be measured by simply rotating the rotary section clockwise by 90° from its original position. Firstly, the reference transmission spectrum of a straight waveguide whose length is the same as the curved waveguide was measured. Next, the transmission spectrum of the curved two-wire waveguide with the axis of rotation parallel to the line connecting wire centers was measured by resetting the rotary section (see Fig. B.4(b)). Similarly, the curved waveguides with the axis of rotation perpendicular to the line connecting wire centers were measured by rotating the emitter and detector photomixers by 90°. Therefore, the polarization state of the THz light that was launched into two-wire waveguides was maintained for all the measurements.

In order to derive the bending loss α_b from the experimental results, the power coupling coefficient $|C(R)|^2$ between straight and bent waveguide was computed using the mode-matching method (the results are shown in Fig. 5.3(e)) [1]. Additionally, given the high similarity in the modal field distribution of the THz SPP wave supported by the bent and straight waveguides (see Figs. 5.1(d), 5.3(a), and 5.3(b)), the power coupling coefficient between the two bent WSs is assumed identical to the one between two straight WSs. Therefore, the bending loss α_b of waveguide bends can be extracted by comparing the measured transmission spectrum of the bend with that of the corresponding straight waveguides using:

$$\alpha_b = -\log(t_{\text{curve}} / t_{\text{straight}} / |C(R)|^2) / (0.5\pi R) \quad (\text{B.3})$$

where R refers to the bend radius of the waveguide bends, t_{curve} and t_{straight} refer to the transmittance (by field) of the curved and straight waveguides.

B.4 The theoretical analysis of a two-wire WBG

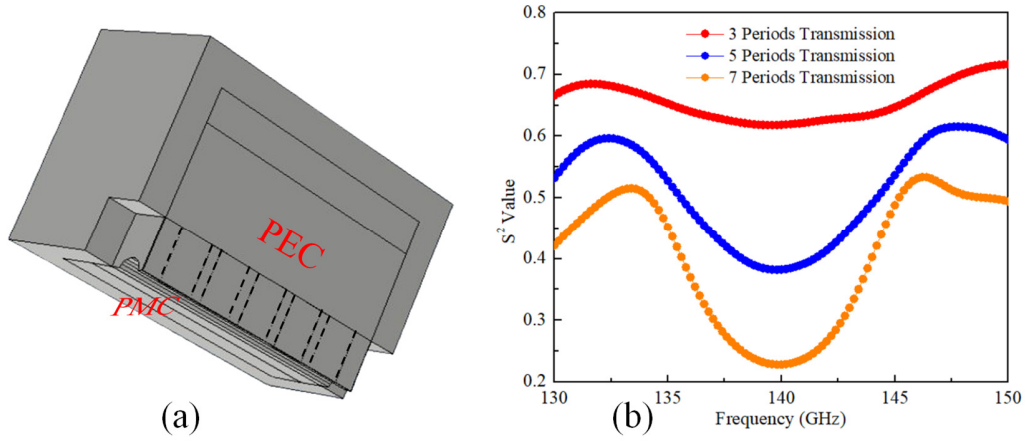


Figure B. 5 Numerical simulation of paper-based two-wire WBG

(a) The 3D model of a two-wire WBG to estimate the transmission and reflection coefficients using COMSOL Multiphysics. (b) The simulated power transmission $|S_{21}|^2$ for WBGs with the different number of periods.

In this section, we study both theoretically and numerically a two-wire WBG with the Bragg frequency of ~ 140 GHz. Theoretically, using Eqs. 5.7 and 5.9 with m_w of 0 and m_p of 3, the total period width of WBG and the width of section 2 in one period (see Fig. 5.4(b) I) are set as 3.21 mm and 2.46 mm respectively to realize the Bragg resonance at 140 GHz. WBGs featuring such a design were numerically studied using COMSOL Multiphysics by 3D models. (The geometry of a WBG consisting of five periods is shown in Fig. B.5(a)). The derived spectral position of the transmission dip is at 140 GHz (see Fig. B.5(b)), which agrees well with the theoretical results obtained by using Eqs. 5.7 and 5.9.

B.5 The characterization of two-wire waveguide-based THz coupler

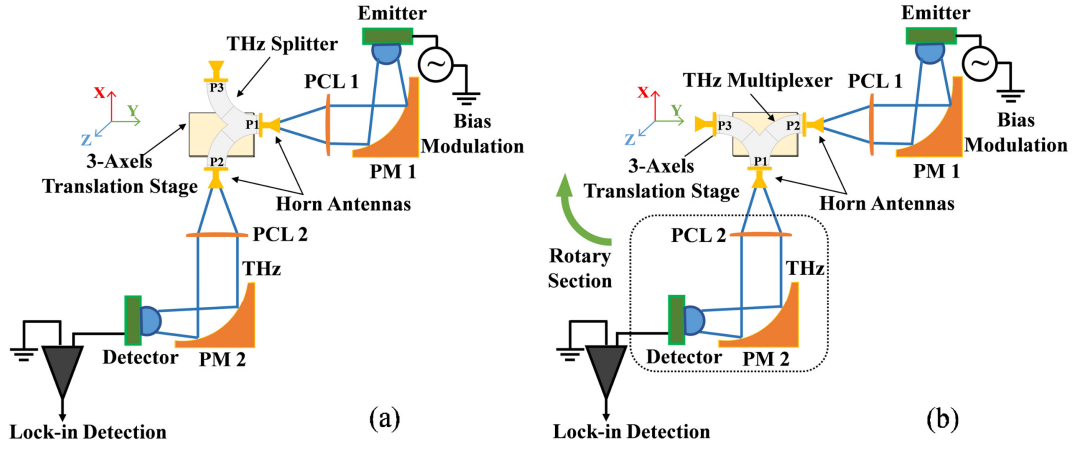


Figure B. 6 Experimental setup to characterize THz coupler

The experimental setup to characterize (a) THz splitter. (b) THz multiplexer.

The two-wire waveguide-based THz coupler containing three ports was characterized by the following processes. Firstly, each port of the THz coupler was connected with a WR6.5 conical horn antenna. When functioning as a THz splitter, the coupler was inserted into the CW-THz spectrometer system with the input and output planes of waveguide flanges connected with ports 1 and 2 at the focal points of PCL1 and PCL2 (see Fig. B.6(a)). The transmission spectrum received at the output port 2 was recorded when the THz light was launched into port 1. Then, the THz splitter was turned over to measure the transmission spectrum at the output port 3. When functioning as a THz multiplexer, the coupler was placed with the input and output planes of waveguide flanges connected with ports 2 and 1 at the focal points of PCL1 and PCL2 (see Fig. B.6(b)). The transmission spectrum received at the output port 1 was recorded when the THz light was launched into port 2. Then, by clockwise rotating the rotary section by 90°, the transmission spectrum at port 3 was measured. To estimate the amount of THz power that is coupled into the input port, the THz coupler was then replaced by a straight waveguide, and the transmission spectrum was measured with the same incident THz light (see Fig. B.6(b)) (The measurement process is detailed in Appendix B.3.1). The reference spectrum (i.e. the maximum amplitude of the coupled THz light) was derived from this transmission spectrum by:

$$t_{\text{ref}} = t_{\text{straight}} / \exp(-\alpha_{\text{st}} l_{\text{straight}}) / Cl \quad (\text{B.4})$$

Additionally, the transmission spectrum of a two-wire waveguide bend featuring the same geometry of half of a THz coupler (see Fig. 5.4(b)) was chosen as the control of that of the THz coupler. The transmission spectrum of the waveguide bend was measured with the same incident THz light (the process is detailed in Appendix B.3.2).

B.6 The characterization of two-wire waveguide-based Add-Drop Multiplexer

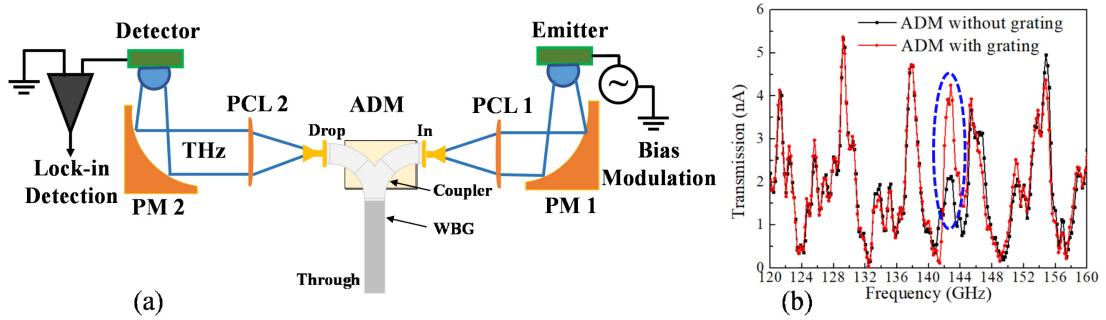


Figure B. 7 Characterization of two-wire ADM circuit

(a). The experimental setup to characterize the THz ADM. (b) Transmission amplitude of the ADM with and without paper-based metalized periodic pattern inserted into the integrated WBG. The characterization of the ADM was carried out as follows. Firstly, the THz coupler and WBG were assembled using the interconnects at the end facets of both waveguide components. Then, two WR6.5 conical horn antennas were connected to the In and Drop ports. The schematic of the experimental setup is shown in Fig. B.7(a). When the THz light was launched into the In port, the transmission spectra received at the Drop port with and without the paper-based metalized periodic structure inserted into the WBG were measured (see Fig. B.7(b)). For the purpose of clarity, the data points within the blue circle showing the resonance peak are presented in Fig. 5.6(c).

APPENDIX C SUPPLEMENTARY MATERIAL FOR: ADD DROP MULTIPLEXERS FOR TERAHERTZ COMMUNICATIONS USING TWO-WIRE WAVEGUIDE BASED PLASMONIC CIRCUITS

C.1 Design of two-wire waveguide Bragg gratings

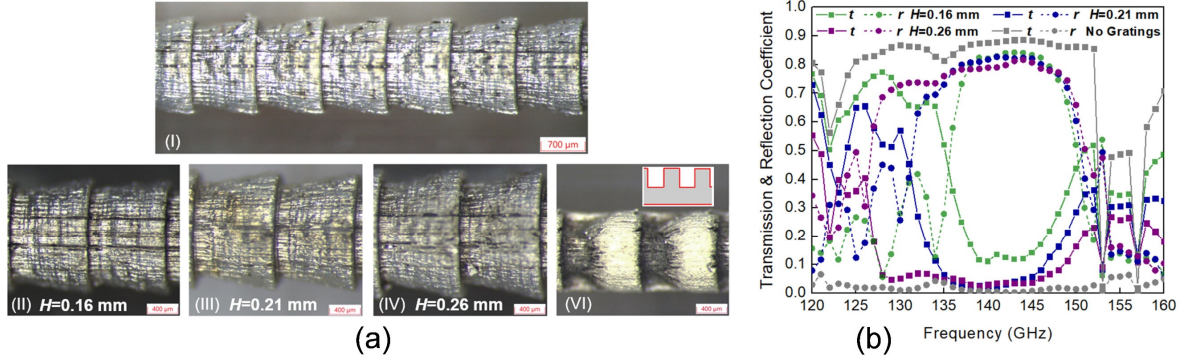


Figure C. 1 The design of two-wire WBGs

(a) (I) Photographs from the top of a fabricated WBG with a period of $\Lambda = 1.03$ mm and a ridge height of $H = 0.21$ mm (only the WBG half is shown). (II-IV) Enlarged view of the metalized gratings (truncated cones) of different ridge heights H . (V) Photograph of a metalized grating featuring rectangular grooves and its schematic. (c) The numerical transmission and reflection coefficients (by field) of the 2.5cm-long WBGs containing 20 periods with $\Lambda = 1.03$ mm as a function of the ridge height H .

The two-wire WBG features periodic variation in cross sections of one wire, while the other wire is uniform and has a fixed diameter of $D = 1.321$ mm. The periodic structure is a sequence of end-to-end connected truncated cones added on top of a uniform circular wire of diameter D (see Fig. C.1(a) (I-IV)). The choice of truncated cones in the grating structure was experimentally found to be the most reliable and stable for printing compared to other alternatives such as rectangular or sinusoidal ridges, or rectangular grooves on the wire surface. The deformations in these 3D printed structures are mainly attributed to the “cure-through” effect during 3D printing. Particularly, the UV radiation not only cures the resin within the top printed layer, but also leaks through the cured layer and solidifies some resin on the other side. This uncontrollable effect occurs repeatedly, thus resulting in the cumulative deformation of prints, which is most pronounced when the geometry

changes rapidly from one layer to another. For example, the ideal steep slope at the edge of a rectangular $\sim 600\mu\text{m}$ -deep groove engraved on a wire was deformed into a conical structure when printed (see Fig. C.1(a) V). This problem highlights the importance of carefully choosing the photosensitive resin chemistry to match the UV absorption depth with the desired layer thickness. Finally, we mention that gratings used in this work can only be printed along a single direction from the conus smaller base towards its larger base to avoid overhanging structures.

In Fig. C.1(b) we show computed transmission and reflection coefficients (by field) of THz light propagating through 2.5cm-long WBG sections as a function of the ridge height H , which effectively controls grating strength (stopband bandwidth). The gratings contain 20 periods of truncated cones with a grating period of $\Lambda=1.03\text{ mm}$. As a reference, transmission and reflection coefficients for a straight two-wire waveguide of the same length are also shown. Due to anticrossing of the waveguide fundamental modes with those of a resin cage, sharp dips in the reference waveguide transmission spectrum are present at 122 GHz and 155 GHz, while in-between these values waveguide transmission is relatively featureless. Similar anticrossing phenomenon is also observed numerically in the transmission spectra of WBGs. However, such spectral features are very sensitive to the surface roughness and other structural imperfections, and in fact not easily observed experimentally as reported earlier in Ref. [20]. We also note that increasing the ridge height H from 0.16 mm to 0.26 mm results in a strong increase in the size of the grating stopband from $\sim 12\text{ GHz}$ to $\sim 25\text{ GHz}$ calculated as an FWHM of the reflection coefficient curve. Additionally, an increase in the ridge height results in a smaller average gap size between the two wires, and as a consequence, a higher effective refractive index of a WBG mode, thus reducing the center frequency of the grating stopband. Considering the finite transverse resolution of the stereolithography (SLA) 3D printer ($50\text{ }\mu\text{m}$ in our case), the truncated cone-shaped grating section featuring larger ridge heights (Fig. C.1(a) IV) can be fabricated easier and more reliable than those with smaller heights (Fig. C.1(a) II). However, at the same time, larger ridge heights require tighter tolerances for the various sizes of the supporting cage due to smaller separation between the grating wire and the uniform wire. Using larger ridge heights also tends to result in lossier gratings due to the stronger scattering effect of imperfections in the grating structure on the guided modal fields. Therefore, an optimal ridge height of the gratings must be chosen to ensure large operational bandwidth, reproducible optical performance, and manageable loss. In this work, by comparing optical properties of several WBGs we find the optimal ridge height to be $H=0.21\text{ mm}$ (see Fig.

C.1(a) I and III). With the period of a WBG set to $\Lambda=1.03$ mm, the resultant stopband center frequency is 140 GHz with the corresponding bandwidth of ~ 18 GHz.

C.2 Numerical simulation results of directional coupler circuit

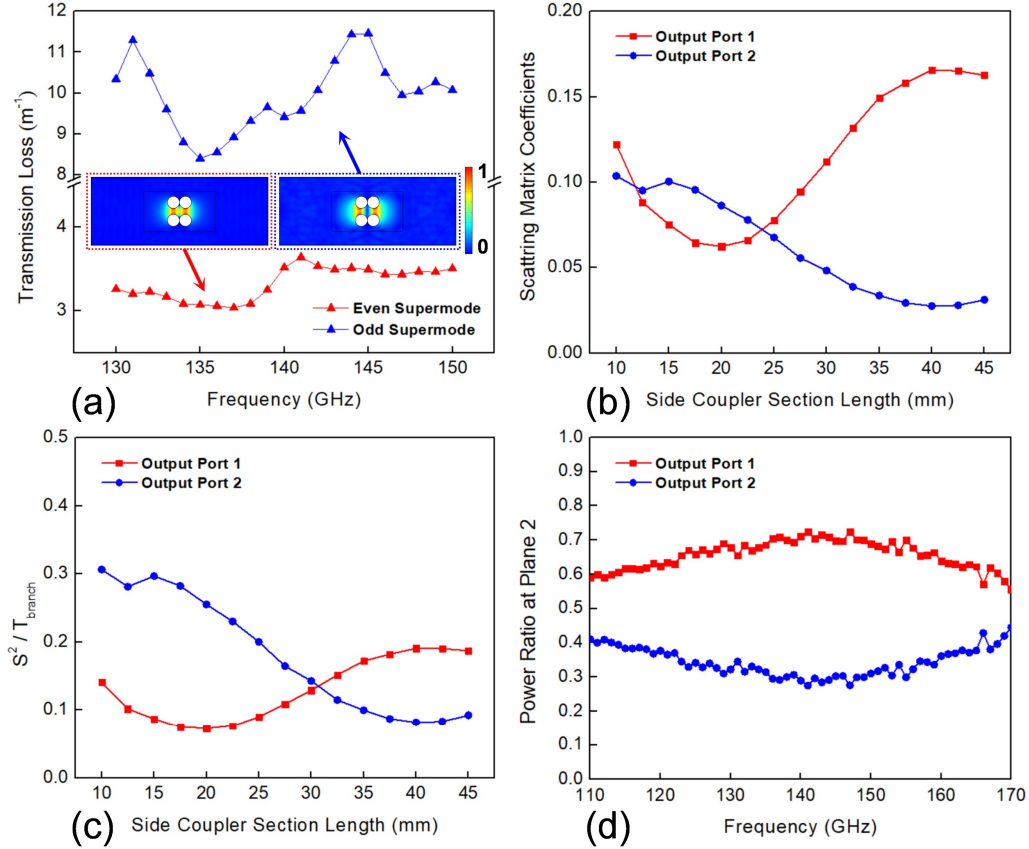


Figure C. 2 Numerical simulation results of directional coupler circuit

(a) The transmission loss (by field) of the even and odd supermode supported by the side coupler section that contains two two-wire waveguides. Insert: the modal electric field distribution of the two supermodes at 140 GHz operational frequency. (b) The numerically computed power transmittance at the Output port 1 and Output port 2 assuming excitation at the Input port 1 of the directional coupler circuit (see Fig. 6.3(d)) as a function of the length of the straight side coupler section. (c) The numerically computed power transmittance of the two waveguides (Waveguides 1 and 2) at the end (Plane 2) of the side coupler section assuming excitation at Input port 1 of the directional coupler circuit (see Fig. 6.3(d)) as a function of the length of the straight side coupler section (obtained by using Eq. 6.1). (d) The ratio of the power carried by the two two-wire

waveguides (Waveguides 1 and 2) at the end (Plane 2) of a 40.6mm-long side coupler section when it is integrated into the directional coupler circuit shown in Fig. 6.3(d), whose value is computed using Eqs. 6.1 and 6.2.

C.3 Characterization of Y splitters used in the directional coupler and ADM circuits

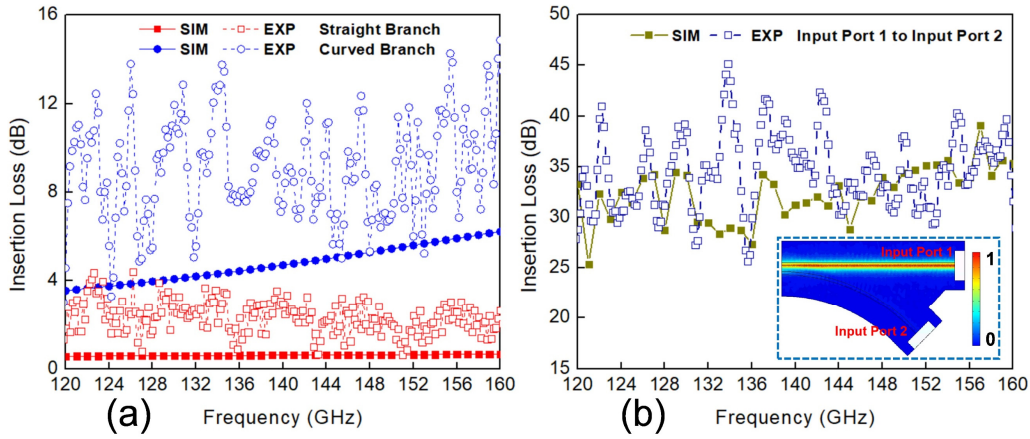


Figure C. 3 Characterization of two-wire Y splitters

(a) The insertion loss of the straight and curved arms of the Y splitters used in the directional coupler and ADM circuits for numerical and experimental studies. (b) The insertion loss of the THz light that is launched into Input port 1 and registered at Input port 2 of Y splitters. Insert: the computed electric field distributions in the Y splitter when using the fundamental mode of Input port 1 at 140 GHz as the excitation condition in numerical simulations.

In this work, the two-wire waveguide-based broadband Y splitter (see Figs. 6.1, 6.3(b), 6.3(d), and 6.4(a)) was used to guide THz signals to/from the side coupler section from/to the desired ports of the directional coupler and ADM circuits. It features a curved two-wire waveguide (circular arc of radius 4 cm) gradually approaching a 4.5cm-long straight two-wire waveguide, while joining in a wedge configuration at the end. In this work, the side coupler sections were connected with Y splitters at their two ends to form the complete directional coupler and ADM circuits. In the numerical simulation, the transmittance and reflectance of the side coupler section were computed by dividing the scattering matrix coefficient (S^2) of the desired port of the complete circuit by the insertion loss of the arms in Y splitters. In experiments, the transmittance of the side coupler section

was measured by dividing the transmitted power spectrum recorded at the desired port of the complete circuit by the transmitted power spectra of a two-wire waveguide having a length same with the arms in Y splitters which the THz carrier wave propagates through.

Additionally, Fig. C.3(b) shows that in Y splitter, the THz light that is launched into one port mostly propagates in the forward direction (larger than 30 dB by power) with only a minimal amount of crosstalk to the other port. Therefore, when using Y splitters in directional coupler and ADM circuits, their contribution to the crosstalk is negligible.

C.4 Numerical simulation of two-wire ADM circuits

In what follows we detail the design and optimization of the ADM circuit shown in Figs. 6.1 and 6.4(a). The orange arrows represent THz signals that are within the stopband of a grating, while green arrows correspond to those in the grating passband. The path of the THz light that is launched into In port (Waveguide 1) is marked by solid arrows, while that launched into Add port (Waveguide 2) is marked by hollow arrows. While propagating in the grating-loaded side coupler, the THz signal within the grating stopband that is launched into In port on Waveguide 1 (Add port on Waveguide 2) is back-reflected by the gratings, and then transferred to Waveguide 2 (Waveguide 1) by the coupler. The THz signal within the grating passband when launched into In port propagates through the grating-loaded side coupler and into Through port.

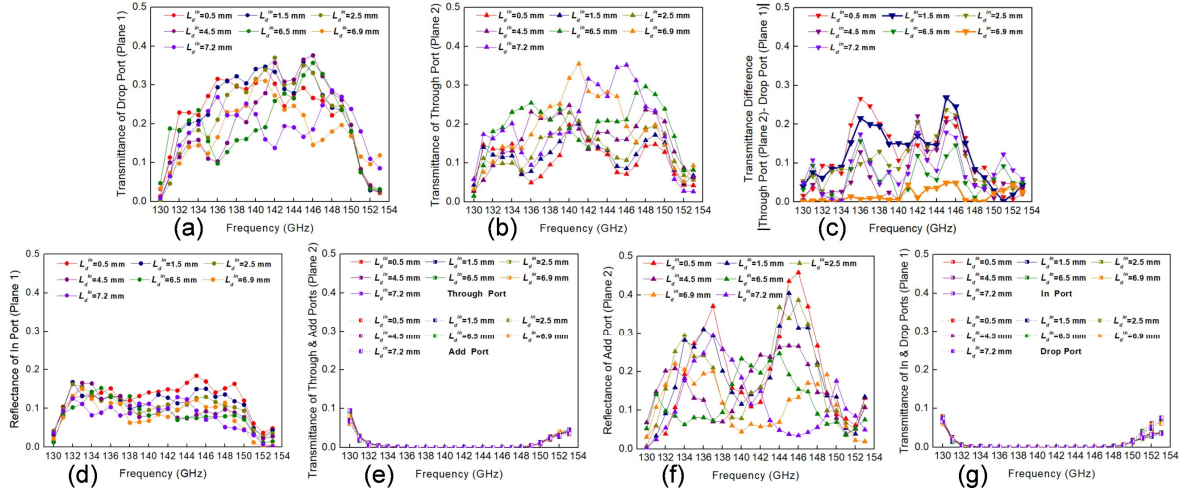


Figure C. 4 Numerical simulation results of 35mm-long grating-loaded side coupler sections containing 20 periods with $A=1.03$ mm, $H=0.21$ mm, and different L_d^{in} computed using Eq. 6.1

Numerical transmittances (by power) at (a) Plane 1 for Drop port under In port launching, and (b) Plane 2 for Through port under Add port launching conditions. (c) Minimizing the difference between the transmittance of Drop port at Plane 1 (drop function) and that of Through port at Plane 2 (add function) to equalize the drop and add functions. Numerical reflectance (by power) at (d) Plane 1 for In port, and (f) Plane 2 for Add port of ADM circuits. Parasitic transmittance (by power) at (e) Plane 2 for Through and Add ports under In port launching (Plane 1), and (g) Plane 1 for In and Drop ports under Add port launching (Plane 2) conditions.

Firstly, we numerically study transmittance and reflectance (by power) characteristics of the 35mm-long grating-loaded side couplers containing 20.6mm-long gratings using Eq. 6.1 and scattering matrix coefficients (S^2) at the In, Drop, Add, and Through ports for various launching conditions. By varying the L_d^{in} parameter, particular attention was paid to the design of two optimal grating-loaded side couplers that enable the ADM circuits with optimized drop and balanced drop/add actions, respectively.

Numerical simulations show that the maximum value of the transmittance of Drop port at Plane 1 for the operation frequency within the grating stopband ~ 140 GHz ± 6 GHz, which gives rise to the optimized drop action of ADM circuit, is obtained when $L_d^{in} \sim 0.5$ -2.5 mm (see Fig. C.4(a)). This shows the realistic tolerances when choosing the value of L_d^{in} for the optimized drop action considering that the SLA printer resolution is ~ 50 μ m.

For the design of the other optimal ADM with balanced drop/add action, one needs to minimize the difference between transmission through the Through port under Add port launching condition and transmission through the Drop port under In port launching condition. Particularly, we vary the L_d^{in} parameter to minimize the absolute difference between transmittances of the Through and Drop ports (see Figs. C.4(a-c)). Clearly, by choosing identical left and right grating offsets $L_d^{in} = L_d^{out}$ should result in the balanced performance of channel dropping and adding in case of the ADM with symmetric gratings [269, 270]. In our case, we observe that the balanced ADM performance is achieved when $L_d^{out} - L_d^{in} = 0.6$ mm ($L_d^{in}=6.9$ mm). This somewhat off-center positioning of gratings is attributed to the small asymmetry in the grating performance depending on the direction of propagation of light.

Additionally, we also present an analysis of parasitic transmissions into Through and Add ports (Plane 2) when light is launched into In port (Plane 1) within the grating stopband. In this case, most of the energy ($\sim 15\text{-}40\%$) is transferred into Drop port (Plane 1) (Fig. C.4(a)), some is reflected back into In port (Plane 1) ($\sim 5\text{-}15\%$) (Fig. C.4(d)), while parasitic transmissions to Through and Add ports (Plane 2) constitute $<1\%$ (Fig. C.4(e)). Similar conclusions are reached for the four ports when light is launched into Add port (Plane 2) within the grating stopband (see Figs. C.4(b), C.4(f), C.4(g)).

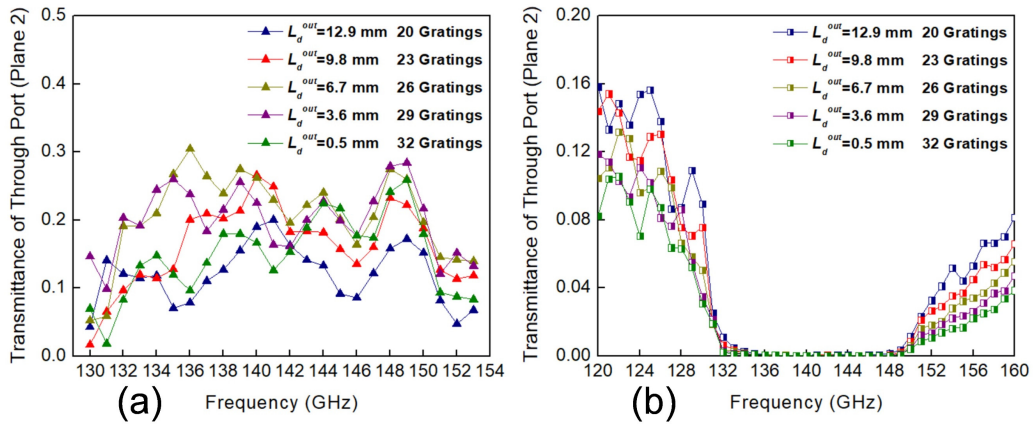


Figure C. 5 Numerical transmittances (by power) of the 35mm-long grating-loaded side coupler sections containing gratings featuring different numbers of periods with $\Lambda=1.03$ mm, $H=0.21$ mm, and $L_d^{in}=1.5$ mm computed using Eq. 6.1 at Plane 2 for Through port

(a) Under Add port launching (Plane 2), and (b) Under In port launching (Plane 1) conditions.

For the above-mentioned grating-loaded side couplers, the value of L_d^{out} might be suboptimal as it is not truly a free parameter. In fact, if N_g is the number of grating periods, then:

$$L_d^{out} = L_{coupler} - L_d^{in} - N_g \Lambda \quad (C.1)$$

Since L_d^{in} has been determined as 1.5 mm to enable the optimized drop action, L_d^{out} can be adjusted by varying the number of grating periods to optimize add action simultaneously. One usually can set $L_d^{out} \approx L_d^{in}$, which requires the use of longer gratings (ex. $N_g=30$) (see Fig. C.5). However, we found experimentally that longer Bragg gratings $N_g \sim 22-31$ result in high transmission losses due to scattering loss on the imperfectly printed grating structure. At the same time, one requires at least $N_g = 15-20$ in experiments to make sure that the grating length is longer than the light penetration depth into the grating L_g . Thus, for the ADM design with imperfect gratings, there is a tradeoff between the equivalently optimized performance of channel dropping and adding and the ADM loss. In experiments, we prioritized low ADM losses while somewhat sacrificing the optimized operation of both of Add and Drop ports by choosing $N_g=20$, which is mostly manifested by the elevated back reflection in the case of Add port (Plane 2) (see Fig. C.4(f)) which is more pronounced than back reflection into In port (Plane 1) for the drop action (see Fig. C.4(d)).

C.5 Measured insertion loss of two-wire ADM circuits

When inserting the complete ADM circuit (see Fig. 6.1) into two-wire waveguide-based THz communication networks, the insertion losses of THz light registered at different ports under In and Add port launching conditions are shown in Fig. 6.5(d-f). For the ADM with optimized drop action ($L_d^{in} = 1.5$ mm), the minimum insertion loss by power (within the Bragg grating stopband) as registered at Drop port under In port launching was measured as 14 dB at 143 GHz. While for the Through port under Add port launching, the minimal insertion loss was 18 dB at 148 GHz for channel adding (see Fig. 6.5(d)). Similarly, for the ADM circuit with balanced drop/add performance ($L_d^{in} = 6.9$ mm), the minimal insertion losses were measured at two spectral locations ~ 138 GHz and ~ 151 GHz with the corresponding values of ~ 16 dB and ~ 15 dB for Drop port under In port launching and ~ 18 dB and ~ 15 dB for Through port under Add port launching. Besides, an insertion loss peak appears around the center of the grating stopband on the fitted spectra (see Fig. 6.5(e)). Finally, insertion losses for the two ADM designs as registered at Through port under In port launching are shown in Fig. 6.5(f). The pronounced loss peaks corresponding to the drop action of ~ 12 GHz FWHM bandwidth are clearly observable in the vicinity of ~ 140 GHz.

C.6 Influence of dispersion of ADM on data transmission

To quantify the effect of the link dispersion on the maximal supported bit rate, we consider second-order modal dispersion β_2 . The maximum bit rate ‘ B ’ (for ASK modulation) supported by the waveguide of a length ‘ L ’ can be estimated using Eq. C.2, which is derived by requiring that ~95% of the power of the broadened pulse form still remains within the time slot allocated to logical “1” [276]:

$$B = \frac{1}{4\sqrt{|\beta_2|}L} \quad (\text{C.2})$$

In [20] it was demonstrated that in the 120-160 GHz spectral range, the two-wire waveguides (same as used in the ADMs of this paper) feature low GVD which are < 3 ps/(THz*cm) for the straight waveguide and < 10 ps/(THz*cm) for the bent waveguide with 4 cm bending radius. Thus, according to Eq. C.2, dispersion of the 12.5cm-long straight In-Through waveguide will only affect data rates exceeding 40 Gbps. It is noted that in this estimate we assumed that dispersion of a grating in the passband is similar to that of a straight waveguide, which is a valid assumption for the operational frequency far away from the edges of the grating stopband.

In contrast, for the drop/add action in the grating stopband, the reflective properties of the Bragg grating vary greatly within the stopband. Ultimately, it is the spectral size of the grating stopband that limits the signal bandwidth. Furthermore, due to fracturing of the stopband because of the fabrication imperfections and various interference effects (see Figs. 6.5(d) and 6.5(e)), signal bandwidth for the drop/add action in our ADMs is expected to be limited to ~2-4 GHz.

C.7 Signal-to-noise ratio (SNR) of THz ADM circuits

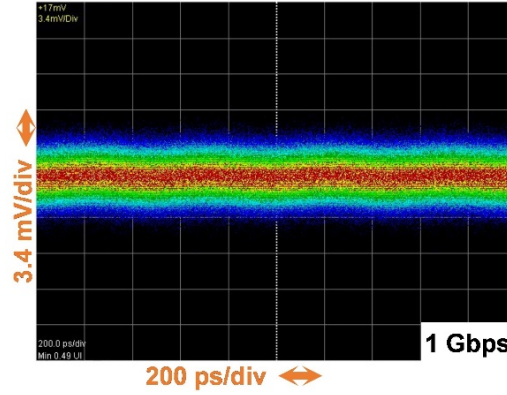


Figure C. 6 Eye diagram for the noise level of the THz communication system

Fig. C.6 shows the eye diagram for the noise level (no signal) of the THz communication system. Due to the relatively high insertion losses for both the drop/add actions and through action, our ADMs feature modest SNR as seen from Fig. 6.6. For example, for the response of ADM with balanced drop/add action to THz signal with a data rate of 1 Gbps, SNR for through action in the grating passband (THz light launched into In port and measured at Through port) and drop (add) action in grating stopband (THz light launched into In (Add) port and measured at Drop (Through) port) is approximately 11 dB and 5 dB, respectively. This is in good agreement with the insertion losses obtained from the spectroscopic measurements, in which the insertion loss is ~ 10 dB for through action and ~ 15 dB for drop and add action (see Figs. 6.5(e) and 6.5(f)).

C.8 Experimental setup to characterize two-wire WBGs

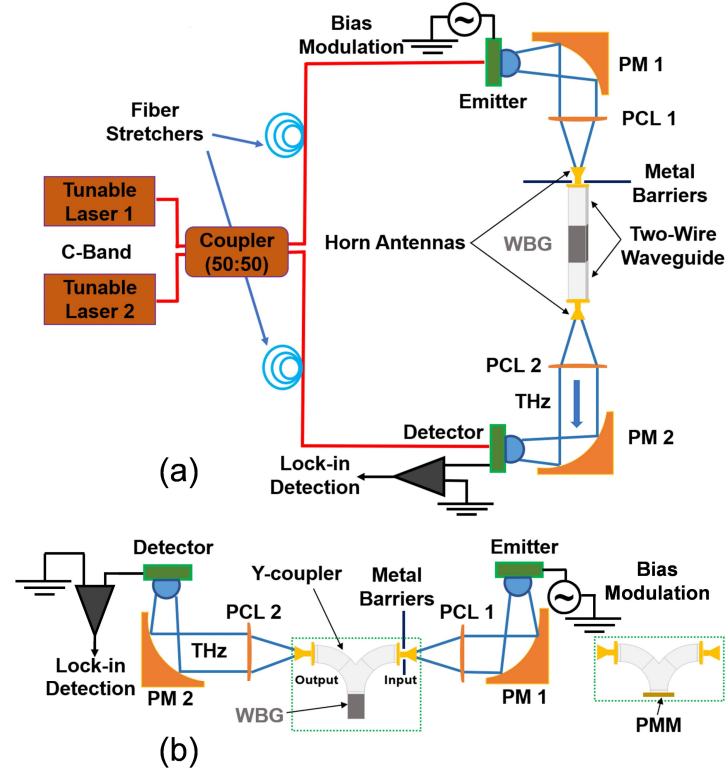


Figure C. 7 The CW-THz spectroscopy system to characterize two-wire WBGs

- (a) Experimental setup to measure the relative transmission coefficient of two-wire WBGs. PM: parabolic mirror, PCL: plano convex lens. (b) Experimental setup to measure the relative reflection coefficient of two-wire WBGs. Insert: the THz optical components to replace the ones that have been placed inside the CW-THz spectroscopy system (in green dotted region) for the reference spectrum. PMM: planar metallic mirror.

C.9 Experimental setup to characterize directional coupler and ADM circuits

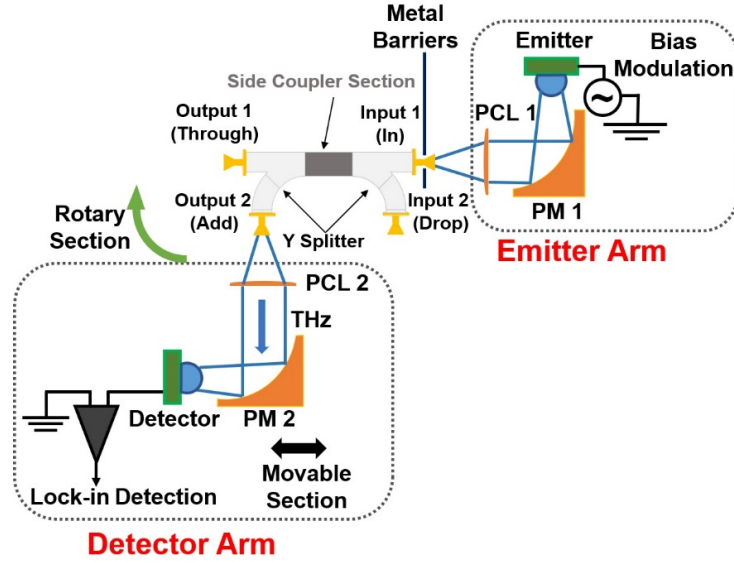


Figure C. 8 The CW-THz spectroscopy system to characterize the directional coupler and ADM circuits.

C.10 Characterization of the two-wire ADM circuits using THz communication system

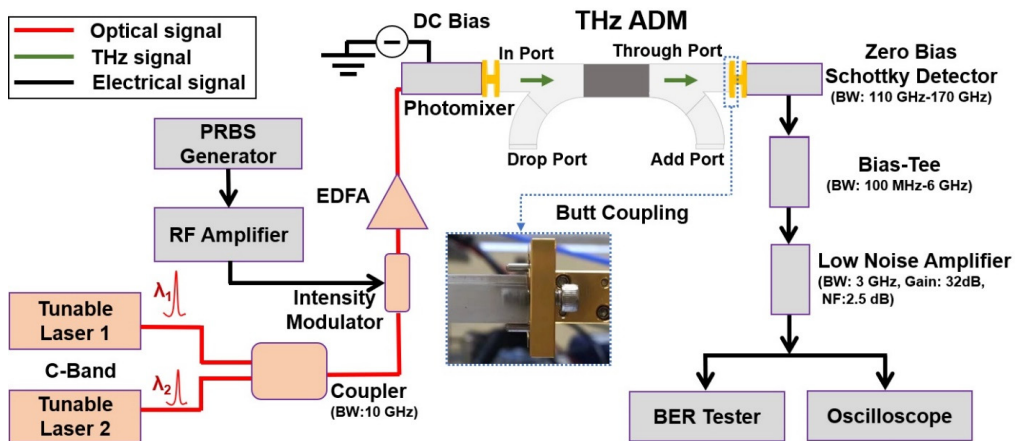


Figure C. 9 Schematic of the photonics-based THz communication system to characterize THz ADM circuits

Insert: Butt coupling of the THz ADM circuit and a WR6.5 waveguide connected to the Schottky detector.

C.11 Numerical simulation of two-wire WBGs

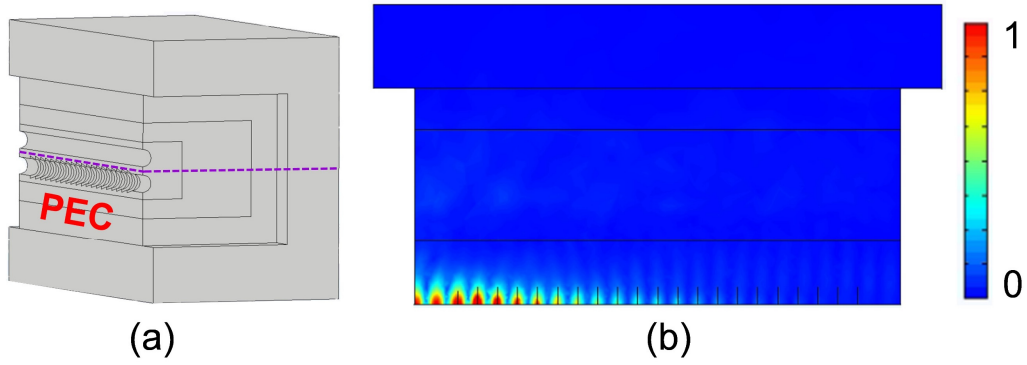


Figure C. 10 Numerical simulation of two-wire WBGs

(a) The 3D model built in COMSOL Multiphysics to study WBGs. (b) The electric field distribution of THz light within grating stopband (140 GHz) in a two-wire WBG on the plane noted by the violet dashed line in Fig. C.10(a)) when the THz light is launched using port boundary condition at the input facet of the WBG.

APPENDIX D SCIENTIFIC CONTRIBUTIONS

Peer-reviewed journals

1. **Y. Cao**, K. Nallappan, H. Guerboukha, T. Gervais, and M. Skorobogatiy, "Additive manufacturing of resonant fluidic sensors based on photonic bandgap waveguides for terahertz applications," *Optics Express*, 27(20), pp.27663-27681, 2019.
2. **Y. Cao**, K. Nallappan, H. Guerboukha, G. Xu, and M. Skorobogatiy, "Additive manufacturing of highly reconfigurable plasmonic circuits for terahertz communications," *Optica*, 7(9), pp.1112-1125, 2020.
3. **Y. Cao**, K. Nallappan, G. Xu, and M. Skorobogatiy, "Add drop multiplexers for terahertz communications using two-wire waveguide based plasmonic circuits." (Submitted to *Nature Communications*, under revision considering peer reviewers' comments)
4. H. Guerboukha, **Y. Cao**, K. Nallappan, and M. Skorobogatiy, "Super-resolution orthogonal deterministic imaging technique for terahertz subwavelength microscopy." *ACS Photonics*, 7(7), pp.1866-1875, 2020.
5. K. Nallappan, **Y. Cao**, G. Xu, H. Guerboukha, C. Nerguizian, and M. Skorobogatiy, "Dispersion-limited versus power-limited terahertz communication links using solid core subwavelength dielectric fibers," *Photonics Research*, 8(11), pp.1757-1775, 2020.
6. E. Zhang, **Y. Cao**, C. Caloz, and M. Skorobogatiy, "Improving thermo-optic properties of smart windows via coupling to radiative coolers," *Applied Optics*, 59(13), pp. 210-220, 2020.
7. H. Guerboukha, K. Nallappan, **Y. Cao**, M. Seghilani, J. Azaña, and M. Skorobogatiy, "Planar Porous Components for Low-Loss Terahertz Optics," *Advanced Optical Materials*, 7(15), p.1900236, 2019.

Conference proceedings

1. **Y. Cao**, K. Nallappan, H. Guerboukha, T. Gervais, M. Skorobogatiy, "Photonic Bandgap Bragg Waveguide-based Terahertz Microfluidic Sensor," IRMMW-THz, Tu-PM1-3-5, France, 2019.
2. **Y. Cao**, K. Nallappan, H. Guerboukha, T. Gervais and M. Skorobogatiy, "Photonic Bandgap Bragg Waveguide-based Terahertz Microfluidic Sensor," The 8th International Conference on Optical Terahertz Science and Technology, paper 135, We-P-47, USA, 2019.
3. **Y. Cao**, K. Nallappan, H. Guerboukha, G. Xu, M. Skorobogatiy, "3D Printed Two-wire Terahertz Waveguide," SPIE Photonics North, OT-2-27-8, Canada, 2020.

4. **Y. Cao**, K. Nallappan, H. Guerboukha, G. Xu, M. Skorobogatiy, "Additive manufacturing of highly reconfigurable plasmonic circuits for terahertz communications," APS March Meeting, H71.00057, USA, 2021
5. **Y. Cao**, K. Nallappan, H. Guerboukha, G. Xu, M. Skorobogatiy, "Modular 3D-Printed Plasmonic Circuits for Signal Processing in THz Communications," CLEO, STh2F.3, USA, 2021.

Book chapter

K. Nallappan, H. Guerboukha, **Y. Cao**, G. Xu, C. Nerguizian, D. M. Mittleman, and M. Skorobogatiy, "Fiber-based THz Communication Links within THz Wireless Networks: Needs, Challenges and Perspectives," in the Next Generation Wireless Terahertz Communication Networks Editors: S. Ghafoor, M. H. Rehmani, and A. Davy (CRC Press, Taylor and Francis Group, USA, 2021)